

MASTER OF SCIENCE THESIS

Hybrid Eulerian-Lagrangian Vortex Particle Method

**A fast and accurate numerical method for 2D Vertical-Axis
Wind Turbine**

L. Manickathan B.Sc.

Date TBD

Faculty of Aerospace Engineering · Delft University of Technology

Hybrid Eulerian-Lagrangian Vortex Particle Method

**A fast and accurate numerical method for 2D Vertical-Axis
Wind Turbine**

MASTER OF SCIENCE THESIS

For obtaining the degree of Master of Science in Aerospace
Engineering at Delft University of Technology

L. Manickathan B.Sc.

Date TBD



Copyright © L. Manickathan B.Sc.
All rights reserved.

DELFT UNIVERSITY OF TECHNOLOGY
DEPARTMENT OF
AERODYNAMICS AND WIND ENERGY

The undersigned hereby certify that they have read and recommend to the Faculty of Aerospace Engineering for acceptance a thesis entitled "**Hybrid Eulerian-Lagrangian Vortex Particle Method**" by **L. Manickathan B.Sc.** in partial fulfillment of the requirements for the degree of **Master of Science**.

Dated: Date TBD

Head of department:

prof.dr.ir. G.J.W. van Bussel

Academic Supervisor:

dr.ir. C.J. Simao Ferreira

Academic Supervisor:

dr.ir. A. Palha da Silva Clerigo

Summary

This is the summary of the thesis.

Acknowledgements

I wish to thank the following persons...

Delft, The Netherlands
Date TBD

L. Manickathan B.Sc.

Contents

Summary	v
Acknowledgements	vii
List of Figures	xix
List of Tables	xxi
Nomenclature	xxiii
1 Introduction	1
1.1 Motivation and Goal	2
1.2 Research Aim and Plan	4
1.3 Introduction to Hybrid Eulerian-Lagrangian Vortex Particle Method	5
1.3.1 Simple coupling strategy	6
1.4 Verification and Validation Test Cases	8
1.5 Thesis Outline	9
2 Lagrangian Subdomain: Vortex Particle Method	11
2.1 Introduction to the Vortex Particle Method	11
2.1.1 Vorticity	12
2.1.2 Velocity-Vorticity Formulation of the Navier-Stokes Equations . .	12
2.1.3 Viscous Splitting Algorithm	13
2.2 Spatial Discretization: Introduction to Vortex Blobs	13
2.2.1 Discrete Form of Vorticity Field	13
2.2.2 Biot-Savart Law	14
2.2.3 Mollified Vortex Kernels	15
2.2.4 Vortex Blob Initialization	16

2.2.5	Minimization of Particle Discretization Error	17
2.3	Convection in Vortex Particle Method	18
2.3.1	Remeshing Scheme: Treating Lagrangian Grid Distortion	18
2.4	Diffusion in Vortex Particle Method	21
2.4.1	Wee Remeshing Scheme	22
2.4.2	Tutty Remeshing Scheme	23
2.5	Boundary Conditions for Viscous Vortex Particle Method	25
2.5.1	Boundary Integral Equations	26
2.5.2	Discretization of Integral Equations using Vortex Panels	27
2.6	Evolution of the Lagrangian method	30
2.7	Validation of Lagrangian method	32
2.7.1	Error Analysis of Vortex Panels	32
2.7.2	Error Analysis of Vortex Blobs	34
2.7.3	Convergence Study of the Viscous Vortex Method	39
2.8	Summary	40
2.9	Chapter Nomenclature	42
3	Eulerian Subdomain: Finite Element Method	45
3.1	Introduction to the Finite Element Method	45
3.1.1	Finite Element Discretization	46
3.1.2	Finite Element Functions and Function Spaces	47
3.2	Solving the Finite Element Problem	50
3.2.1	Introduction to FEniCS Project	50
3.2.2	Mesh Generation using GMSH	52
3.3	Solving Incompressible Navier-Stokes Equations	52
3.3.1	Velocity-Pressure Formulation	52
3.3.2	Determining the Vorticity Field	52
3.3.3	Taylor-Hood Finite Element Family for Solving ICNS	54
3.3.4	Incremental Pressure Correction Scheme	55
3.3.5	Determining the Body Forces	58
3.4	Evolution of the Eulerian method	59
3.5	Validation of Eulerian Method	60
3.5.1	Lamb-Oseen Vortex	60
3.5.2	Clercx-Bruneau Dipole Collision at $Re = 625$	64
3.5.3	Impulsively started cylinder at $Re = 550$	70
3.6	Summary	75
3.7	Chapter Nomenclature	75

4 Hybrid Eulerian-Lagrangian Vortex Particle Method	79
4.1 Decomposition of the domain	80
4.1.1 Local to Global Transformation	81
4.2 Correction of Lagrangian domain	82
4.2.1 Approach from literature	82
4.2.2 Issues with the correction algorithm	84
4.2.3 Modified correction strategy	86
4.3 Evolution of the Lagrangian solution	93
4.4 Evolution of the Eulerian solution	93
4.4.1 Dirichlet boundary conditions	94
4.4.2 Multi-step evolution	94
5 Introduction to the Hybrid Solver: pHyFlow	97
5.1 Program structure	97
5.2 Hybrid class Hierarchy	100
6 Verification and Validation of Hybrid Method	101
6.1 Lamb-Oseen Vortex Evolution	102
6.1.1 Problem Definition	102
6.1.2 Results and Discussion	103
6.1.3 Conclusion	112
6.2 Clercx-Bruneau Dipole Convection	113
6.2.1 Problem Definition	113
6.2.2 Results and Discussion	114
6.2.3 Conclusion	117
6.3 Clercx-Bruneau Dipole Collision	117
6.3.1 Problem Definition	117
6.3.2 Results and Discussion	119
6.3.3 Conclusion	122
6.4 Impulsively Started Cylinder at $Re = 550$	122
6.4.1 Problem Definition	122
6.4.2 Results and Discussion	124
6.4.3 Conclusion	129
6.5 Stalled Elliptic Airfoil at $Re = 5000$	129
6.5.1 Problem Definition	129
6.5.2 Results and Discussion	130
6.6 Multi-body problem	133
6.6.1 Problem Definition	133
6.6.2 Results and Discussion	133

7 Conclusion and Recommendation	135
7.1 Conclusion	135
7.1.1 Lagrangian domain	135
7.1.2 Eulerian domain	135
7.1.3 Hybrid method	135
7.2 Recommendations	135
7.2.1 Lagrangian domain	135
7.2.2 Eulerian domain	135
7.2.3 Hybrid method	135
References	137
A pHyFlow Code Structure	143

List of Figures

1.1	VAWT vs. HAWT	1
1.2	3-D Unsteady Panel simulation of a Straight-bladed VAWT showing the strength of the shed vorticity. The VAWT blades interact with their own wake increasing the complexity of the wake geometry [26]	2
1.3	Eulerian formulation of the fluid. We observe a given volume \mathbf{V} and evaluate the change in properties of the fluid, velocity \mathbf{u} and pressure p at time passes.	3
1.4	Lagrangian formulation of the fluid. We track the path of the individual fluid elements as time passes.	4
1.5	Standard domain decomposition using Schwartz iteration for coupling the two methods. Eulerian subdomain Ω_E (near the body), and Lagrangian subdomain Ω_L (away from the body). Figure is based on Guermond (2000) [30]	6
1.6	Modified domain decomposition <u>without</u> Schwartz alternating method. Lagrangian subdomain extends up to the surface of the body. Figure is based on Daeninck (2006) [23].	7
1.7	Flowchart of the simple coupling strategy. The flowchart shows the procedure to evolve both methods from t_n to t_{n+1}	8
2.1	Definition of the circulation in the fluid.	12
2.2	The smoothing function ζ_σ for a gaussian distribution with $k = 2$, $\sigma = 1$	15
2.3	Vortex blob with an overlap ratio $\lambda = h/\sigma$	16
2.4	Mollified vorticity field of a Gaussian vorticity distribution by blobs with $\lambda = 1.0$, $\sigma = 0.19$, and $h = 0.19$. Vortex blob strengths were assigned using equation 2.21, sampling the exact vorticity [\bullet , red dot]. Figure depicts the exact vorticity distribution ω [—, solid black], the vorticity distribution of each blob ω_i [—, solid green], and the mollified vorticity field from the blobs ω^h [- -, dashed black].	16
2.5	Convergence of the spatial discretization h and λ of the initial vorticity distribution. Figure depicts the exact vorticity field ω [—, solid black], and various discretized vorticity distributions.	17

2.6	Lagrangian distortion of the vortex blobs after 100 time steps. The initial vorticity field is $\omega(\mathbf{x}, 0) = \exp(-12 \mathbf{x})$ with $\Delta t = 0.1$, $\sigma = 0.02$, and overlap = 1.0. Figure depicts (a) the initial distribution of the vortex blobs, and (b) the final distribution of the vortex blobs after 100 time steps.	19
2.7	Remeshing of a single vortex blob [•, green dot] onto a uniform grid defined by the (3×3) 2-D stencil.	19
2.8	M'_4 interpolation kernel, a third-order, piecewise smooth, B-spline kernel by Monaghan [46].	20
2.9	1D Tutty Remeshing Scheme (TRS), diffusing the vortex blobs at $x_i \leq x_\nu \leq x_{i+1}$, onto the four stencil points $k = i - 1, \dots, i + 2$, with a grid spacing h	23
2.10	Extended vorticity field separated into vorticity in the fluid and the vortex sheet distribution confined to the body.	26
2.11	Extended vorticity field: Vortex sheet being an extension to the vorticity field (resolved by the vortex blobs), capable of capturing the body bounded vorticity distribution.	27
2.12	The two coordinate system of the panel method problem. The figure depicts (a) the global panel coordinate system, and (b) the local panel coordinate system, as defined by Katz and Plotkin [36].	29
2.13	Multi-body panel problem: two bodies with different numbers of panels. The figure depicts a square body with 4 panels (a_1, a_2, a_3, a_4), and a triangular body with 3 panels (b_1, b_2, b_3).	30
2.14	Flowchart of the Lagrangian method. The flowchart shows coupling between vortex panels and vortex blobs to evolve from t_n to t_{n+1} (without taking into account of the vorticity generation at the boundary).	31
2.15	Panel method solution: the potential velocity field around a unit cylinder with $R = 1$, $\mathbf{u}_\infty = (1, 0)$, and $N_{\text{panels}} = 100$. The figure depicts the magnitude of velocity field $\ \mathbf{u}\ $, with a zero velocity inside the body. . . .	33
2.16	Comparison of the velocity field along the y -axis, $y = 0$ to $y = 10$. Figure (a) shows both the solutions, the numerical $\ \mathbf{u}^h\ $ [—, solid blue] and the analytical solution [—, solid black]. Figure (b) shows the relative error ϵ in velocity between the solution, given by equation 2.60.	33
2.17	Convergence plot of the Constant-Strength Straight Vortex panels. The figures depicts the converges of the relative error ϵ at an $\mathcal{O}(N^{-1})$	33
2.18	The vorticity ω distribution of the Lamb-Oseen vortex problem with $\Gamma_c = 1$ and $\nu = 5 \times 10^{-4}$ in the domain $[-0.5, 0.5] \times [-0.5, 0.5]$. The figure depicts distribution for various initial time constant τ , determining the peakiness of the distribution.	35
2.19	Relative error growth of Lamb-Oseen vorticity during the evolution (in logarithmic scale) using the parameters tabulated in table 2.2. The figure shows (a), the initial relative error at $t = 0$, and (b) the final relative error in vorticity at $t = 1$	37
2.20	Relative error growth of Lamb-Oseen vortex during the evolution from $t = 0$ to $t = 1$ using the parameters in table 2.2. This figure depicts the error in vorticity: maximum relative error [—, solid black], and the error in L^2 – norm [—, dashed black]; and error in velocity: maximum relative error [—, solid blue], and error in L^2 – norm [—, dashed blue].	38

2.21 Comparison of Tutty's scheme TRS, and Wee-Ghoniem scheme WRS for treating diffusion, depicting the evolution of maximum relative error in vorticity, equation 2.64 from $t = 0$ to $t = 1$. The Figure (a) shows TRS performing diffusion at every step, $\Delta t_d = \Delta t_c = 0.01$ and WRS performing diffusion at every 7 th step, $\Delta t_d = k_d \cdot \Delta t_c = 7 \times 0.01$; (b) shows TRS performing diffusion at every step, $\Delta t_d = \Delta t_c = 0.05$ and WRS performing diffusion at every step, $\Delta t_d = k_d \cdot \Delta t_c = 1 \times 0.05$	39
2.22 Convergence in spatial discretization of the vortex blobs. Figure (a) shows the convergence by fixing the core size σ and (b) shows the convergence when overlap ratio $\lambda = h/\sigma = 1$	39
2.23 Convergence of the error in velocity [—, solid] and the error in vorticity [---, dashed] due to temporal discretization of the vortex blobs. The figure compares the convergence rate of TRS (black) vs. WRS (blue)	40
3.1 A two-dimensional finite element geometry. The cell represents the area of the element, and vertices are the edges of the cell.	46
3.2 Delaunay triangulation of the fluid around a cylinder resulting in unstructured mesh with controllable cell sizes.	46
3.3 The Lagrange CG _q triangle for $q = 1, 2$. The triangles have 3 and 6 DOFs respectively (●, black dot).	48
3.4 DOLFIN VTK plot of the Poisson solution, given by the problem, source code listing 3.1.	50
3.5 Flowchart of the Eulerian method.	60
3.6 Eulerian domain Ω_E (gray) for the Lamb-Oseen vortex problem, bounded by the Dirichlet velocity boundary Σ_d (red), where the Dirichlet velocity boundary condition was applied. The parameters of the domain are tabulated in table 3.2.	62
3.7 Relative error in vorticity (in logarithmic scale) using the parameters tabulated in table 3.2. The figure shows (a), the initial relative error in vorticity at $t = 0$, and (b) the final relative error in vorticity at $t = 1$	63
3.8 Evolution of the maximum relative errors from $t = 0$ to $t = 1$ using the parameters in table 3.2. The figure depicts maximum relative error in velocity [—, solid blue] and the maximum relative error in vorticity [—, solid black].	63
3.9 Convergence in space and time. The figure depicts (a) convergence in space of $\mathcal{O}(\Delta h^2)$ and (b) convergence in time of $\mathcal{O}(\Delta t)$. The control parameters are tabulated in table 3.2.	63
3.10 Domain of the Clercx-Bruneau dipole collision problem. The figure depicts (a) the definition of the domain with the fluid domain (gray) and the no-slip boundary (blue); and (b) the unstructured mesh of the domain with $N_{\text{vert}} = 48k$	64
3.11 Vorticity contour plots of the Clercx-Bruneau dipole-wall collision at $Re = 625$ and $t = [0, 0.25, 0.5, 0.75, 1.0, 1.25]$ with vorticity contour levels at $[-320, -200, -100, -50, -10, 10, 50, 100, 200, 320]$. The figure depicts positive contours [—, solid black], and negative contours [---, dashed black].	66
3.12 Comparison of the vorticity contours at $t = 1$ with contour levels [..., -50, -30, -10, 10, 30, 50, ...]. The figure compares the plot obtained by (a) literature of Clercx and Bruneau [15] and (b) the present study.	68

3.13 Comparison of the fluid parameters from $t = 0$ to $t = 2$ with reference data obtained from Clercx and Bruneau [15] [\bullet , red dot]. The figure shows the evolution of (a) the kinetic energy $E(t)$, (b) the enstrophy $\Omega(t)$, and (c) the palinstrophy $P(t)$	69
3.14 The vorticity generated at the bottom-left wall ($y = -1$, $-0.6 \leq x \leq 0$) at $t = 0.4$ [—, solid blue], $t = 0.6$ [—, solid red] and $t = 1$ [—, solid green]. The results are compared with Clercx and Bruneau [15] (dotted).	69
3.15 Domain of the ISC problem. The figure depicts (a) the definition, (b) the full domain mesh, and (c) the mesh near the surface.	71
3.16 Comparison of the vorticity contours for $T = [1, 3, 5, 7]$ with contour levels $[-7, \dots, -2, -1, -0.5, -0.2, -0.1, 0.1, 0.2, 0.5, 1, 2, \dots, 7]$, showing negative vorticity (solid) and positive vorticity (dotted). The present study (right) is compared with plots obtained from Koumoutsakos and Leonard [39] (left).	73
3.17 Evolution of drag force. The figure depicts the total drag coefficient C_d [—, solid blue], the pressure drag coefficient $C_{d_{\text{pres}}}$ [—, solid red] and the friction drag coefficient $C_{d_{\text{fric}}}$ [—, solid green]. The dotted lines indicate the data obtained from literature, Koumoutsakos and Leonard [39].	74
3.18 Evolution of the lift coefficient C_l and the drag coefficient C_d from $T = 0$ to $T = 40$ with artificial perturbation [42]. The dotted lines represent the data obtained from literature, Rosenfeld et al. [52].	74
4.1 Schematic of the domain decomposition. The two subdomain are the Lagrangian domain $\Omega_L : \Omega_p \cup \Omega_b$ and the Eulerian domain Ω_E where $\Omega_E \subset \Omega_L$	80
4.2 Boundaries of the decomposed domains. No-slip boundary $\partial\Omega_{\text{body}}$, exterior vortex panel boundary $\partial\Omega_p$, exterior Eulerian boundary $\partial\Omega_E$	81
4.3 Elliptical geometry in (a) the local coordinate system and (b) the global coordinate system. The geometry is positioned using the displacement vector $[x_o, y_o]$ and rotated by θ_0 about the local origin point.	82
4.4 Result of hybrid coupling by Daeninck [23]. The figure shows artificial vorticity at the boundary of the Eulerian domain.	83
4.5 Definition of the interpolation region $\partial\Omega_{\text{int}}$ with the boundaries: $\partial\Omega_p$ and $\partial\Omega_{\text{int}}$	83
4.6 Structured interpolation grid \mathbf{x}_{str} (pink) covering the entire Eulerian mesh (gray).	87
4.7 Interpolated vorticity $\hat{\omega}$ on the structured grid \mathbf{x}_{str} from interpolating ω of the unstructured grid $\mathbf{x}_{\text{unstr}}$ with the interpolation weights W	88
4.8 The interpolation region Ω_{int} , bounded by the boundary polygons: panel region boundary $\partial\Omega_P$ near the wall, and exterior boundary $\partial\Omega_{\text{int}}$ near the outer region.	88
4.9 Particles inside the interpolation domain Ω_{int} located at \mathbf{x}_i coinciding the Lagrangian remeshing grid.	89
4.10 Interpolating the strengths from the structured grid \mathbf{x}_{str} onto the vortex blobs \mathbf{x}_i using a bilinear interpolation	90
4.11 Interpolated strengths α_i from the structured grid \mathbf{x}_{str} using bilinear interpolation.	91
4.12 Dirichlet boundary conditions at boundary of Eulerian domain $\mathbf{u} \in \partial\Omega_E$. We evaluate the induced velocities from the Lagrangian solution at the nodes of the boundary [\bullet , red dot].	94

4.13 Eulerian multi-stepping to match the Lagrangian Δt_L . The figures shows $\Delta t_L = 4\Delta t_E$ and required $k_E = 4$ iterations to time march from t_n to t_{n+1} .	95
5.1 Flowchart of the pHyFlow library structured into modules , option script files, and classes .	98
5.2 Flowchart of the HybridSolver hierarchy. The HybridSolver couples the LagrangianSolver class and the EulerianSolver class using the hybrid coupling schemes.	100
6.1 (<i>Not to scale</i>) The domain decomposition for the Lamb-Oseen vortex problem, $\Omega_E \subseteq \Omega_L$. The Eulerian domain is defined as $\Omega_E = [-0.5, 0.5] \times [-0.5, 0.5]$ with Dirichlet boundary $\partial\Omega_{dirichlet}$ [—, solid red]. The parameters of the discretization are tabulated in table 6.1.	103
6.2 Initial relative error at $t = 0$ inside the Eulerian domain Ω_E . The figure depicts (a) the relative error in velocity \mathbf{u} , and (b) the relative error in vorticity ω .	105
6.3 Evolution of the maximum relative error in velocity (dashed) and the maximum relative error in vorticity (solid), equation 2.64, from $t = 0$ to $t = 1$, using the parameters tabulated in table 6.1. The figure compares uncoupled case (black) vs. the one-way coupled case (blue) vs. the fully coupled case (red).	105
6.4 Plot of the relative error in velocity (<i>left</i>) and relative error in vorticity (<i>right</i>) in the Eulerian domain Ω_E at $t = 1$. The figure compares the error between (a)(b) the uncoupled, (c)(d) the one-way coupled, and (e)(f) the fully coupled cases.	106
6.5 Plot of the relative error in velocity (left) and the relative error in vorticity (right) in the Eulerian domain Ω_E at $t = 1$. The figure compares the error between (a)(b) without conservation of circulation, and (c)(d) with the conservation of circulation.	108
6.6 Plot of the maximum relative error in vorticity ϵ_ω [- -, dashed] and maximum relative error in vorticity ϵ_u [—, solid], equation 2.64, from $t = 0$ to $t = 1$, using the parameters tabulated in table 6.1. The figure compares the coupling scheme with conservation of circulation (red) vs. the coupling scheme without conservation of circulation (green).	109
6.7 Plot of the error in total circulation ϵ_Γ of the Lagrangian method from $t = 0$ to $t = 1$. The figure compares the scheme with conservation of circulation [—, solid red], and the scheme without conservation of circulation [—, solid green].	109
6.8 Evolution of the maximum relative error for various nominal blob spacing $h = [0.01, 0.02, 0.05, 0.1]$ from $t = 0$ to $t = 1$. The figures shows the maximum relative error in vorticity [- -, dashed] and maximum relative error in vorticity [—, solid].	110
6.9 Convergence of the maximum relative error in vorticity due to the nominal blob spacing $h = [0.01, 0.02, 0.05, 0.1]$.	111
6.10 Evolution of the maximum relative error for various overlap ratios $\lambda = [0.5, 0.75, 1.0, 1.5]$ from $t = 0$ to $t = 1$. The figures shows the maximum relative error in vorticity [- -, dashed] and the maximum relative error in vorticity [—, solid].	111

6.11 Evolution of the maximum relative error from $t = 0$ to $t = 1$ for various number of Eulerian sub-steps $k_E = [1, 2, 5, 10]$, modifying (a) the Lagrangian time step Δt_L , and (b) the Eulerian time step Δt_E . The figures shows the maximum relative error in vorticity [- -, dashed] and maximum relative error in vorticity [—, solid].	111
6.12 (<i>Not to Scale</i>) The domain decomposition for the Clercx-Bruneau convection problem, with the positive pole located at $p_+ = (x_1, y_1) = (-1, 0.1)$ and negative pole located at $p_- = (x_2, y_2) = (-1, -0.1)$. The parameters of the simulation are tabulated in table 6.2.	113
6.13 Plot of the Clercx-Bruneau dipole at $t = [0, 0.2, 0.4, 0.7]$ using parameters tabulated in table 6.2. The figure compares the hybrid simulation (top halves) against the FE only simulation (bottom halves).	115
6.14 Evolution of the maximum vorticity $\max\{\omega\}$ from $t = 0$ to $t = 0.7$. The solutions are compared with the benchmark results of FE only [—, solid black], and VPM only [- -, dashed black] simulations. The figure depicts (a) the maximum vorticity in the Eulerian and the Lagrangian sub-domain of the hybrid method, and (b) the maximum vorticity of hybrid method with nominal blob spacing $h = 0.01$ and $h = 0.005$	116
6.15 Vorticity contour plots of the dipole with levels ..., -50, -30, -10, 10, 30, 50, ... of the Eulerian and the Lagrangian sub-domains. The figure highlights the effect of the artificial vorticity at the boundary of the Eulerian domain.	116
6.16 Evolution of the (a) kinetic energy E and (b) enstrophy for the nominal blob spacing $h = 0.01$ and $h = 0.005$	116
6.17 [<i>Not to Scale</i>] The domain decomposition for the Clercx-Bruneau dipole collision problem, with the positive pole at $p_+ = (x_1, y_1) = (0.1, 0)$ and negative pole at $p_- = (x_2, y_2) = (-0.1, 0)$. The parameters of the simulation are tabulated in table 6.3.	118
6.18 Plot of the dipole at $t = [0, 0.2, 0.4, 0.6, 0.8, 1]$, comparing the hybrid simulation (left half) and FE only simulation (right half).	120
6.19 Comparison of the vorticity contours at $t = 1$. The figure compares the plot obtained by (a) literature, Clercx and Bruneau [15], and (b) the present study, the hybrid and FE only simulation.	121
6.20 Variation in the fluid parameters from $t = 0$ to $t = 1$. The figure compares the hybrid results [—, solid blue] with the FE only [—, solid black] results.	121
6.21 Compares the vorticity generated at the bottom-left wall ($y = -1, -0.6 \leq x \leq 0$) at $t = 0.4$ [—, solid blue], $t = 0.6$ [—, solid red] and $t = 1$ [—, solid green].	122
6.22 (<i>Not to Scale</i>) The domain decomposition for the Impulsively started cylinder. The parameters of the domain are tabulated in table 6.4.	123
6.23 Comparison of the vorticity contours for (a) $t = 1$, (b) $t = 3$, (c) $t = 5$ and (d) $t = 7$ with contour levels $[-7, \dots, -3, -2, -1, 0.5, -0.2, -0.1, 0.1, 0.2, 0.5, 1, 2, 3, \dots, 7]$. The figures compares the hybrid simulation (top half) with FE only simulation (bottom half).	125
6.24 Evolution of the drag coefficient during the initial stages $t = 0$ to $t = 4$ with total drag coefficient C_d (solid), pressure drag coefficient $C_{d_{pres}}$ (dashed) and friction drag coefficient $C_{d_{fric}}$ (dotted). The figure compares results of hybrid simulation (blue), FE only simulation (red) and reference data (black) of Koumoutsakos and Leonard [39]	125

6.25	Parameters sensitivity analysis on the drag evolution of the cylinder from $t = 0$ to $t = 4$, compared with literature data (black) obtained from Koumoutsakos and Leonard [39]	126
6.26	Evolution of the lift and drag coefficient from $t = 0$ to $t = 40$ with artificial perturbation [42]. The figure compares hybrid (blue), FE only (red), and the reference data (black) from Rosenfeld et al. [52].	126
6.27	Plot of the vorticity field at $t = [10, 20, 30, 40]$, comparing the hybrid simulation (left) with the FE only simulation (right).	127
6.28	Plot of the first shed vortex at $t = 40$, comparing (a) the hybrid simulation, and (b) the FE only simulation.	127
6.29	(<i>Not to scale</i>) The domain decomposition for the stalled elliptical airfoil. The parameters of the domain are tabulated in table 6.5.	129
6.30	hybrid ellipse HybridvsFE contourDeviation	131
6.31	Forces	132
6.32	hybrid ellipse Hybrid contours	132
6.33	(<i>Not to Scale</i>) The hybrid domain decomposition configuration of two impulsively started cylinder test case.	133
6.34	hybrid ellipse Hybrid contours	134

List of Tables

2.1	Panel study parameters	32
2.2	Summary of the parameters for the Lamb-Oseen vortex evolution. This table shows also the parameters of Tutty's diffusion method	36
3.1	Summary of the Lagrange element CG_q of order q , that was used for solving the incompressible Navier-Stokes problem. The variable names of the function space, the trial functions, and the test functions are tabulated together.	55
3.2	Summary of the parameters for the Lamb-Oseen vortex evolution.	61
3.3	Summary of the parameters for the Clercx-Bruneau dipole collision with a no-slip wall [15].	67
3.4	Summary of the parameters for the impulsively started cylinder test case for $Re = 550$	71
6.1	Summary of the parameters for the Lamb-Oseen vortex evolution.	104
6.2	Summary of the parameters for the Clercx-Bruneau dipole convection problem.	114
6.3	Summary of the parameters for the Clercx-Bruneau dipole collision.	118
6.4	Summary of the parameters of the hybrid simulation for the impulsively started cylinder test case at $Re = 550$	123
6.5	Summary of the parameters of the hybrid simulation for the stalled elliptical airfoil test case.	130
A.1	Attributes of <code>Blobs</code> class and their description.	145
A.2	Attributes of <code>Panels</code> class and their description.	148
A.3	Attributes of <code>LagrangianSolver</code> class and their description.	149
A.4	Attributes of <code>EulerianSolver</code> class and their description.	152
A.5	Attributes of <code>HybridSolver</code> class and their description.	155

Nomenclature

Abbreviations

2-D	Two-Dimensional
AD	Actuator Disk
BEM	Blade Element Momentum
CFD	Computational Fluid Dynamics
CG	Continuous Galerkin
CSVP	Constant-Strength Vortex Panel
DOF	Degrees of Freedom
FDM	Finite Difference Method
FEM	Finite Element Method
FE	Forward Euler
FMM	Fast Multipole Method
FVM	Finite Volume Method
GPU	Graphical Processing Units
HELVPM	Hybrid Eulerian-Lagrangian Vortex Particle Method
ICNS	Incompressible Navier-Stokes
IPCS	Incremental Pressure Correction Scheme
ISC	Impulsively Started Cylinder
lhs	left hand side
LSTSQ	Least-Square solution method
MPI	Message Passing Interface
PC	Population Control

PIV	Particle Image Velocimetry
PSE	Particle Strength Exchange
RWM	Random Walk Method
SCS	Simple Coupling Strategy
VAWT	Vertical-Axis Wind Turbine
VPM	Vortex Particle Method
WRS	Wee-Ghoniem Remeshing Scheme

Chapter 1

Introduction

Conventional energy resources such as fossil fuels and nuclear energy are not only limited but also pose adverse effects on the environment. Therefore, we are striving to find a cheap and renewable source of energy. Wind energy is such source of energy, getting more popular and more affordable. Novel wind turbine designs such as Vertical-Axis Wind Turbine ([VAWT](#)) are now a promising research field that can satisfy this growing demand.

VAWTs are unlike the normal wind turbines, which are mounted on a mast away from the ground and generate energy by spinning perpendicular to the ground, figure [1.1](#), whereas the Horizontal-Axis Wind Turbine ([VAWT](#)), spins parallel to the ground with its hub located at the ground, figure [1.1b](#). The VAWT has it's generator located at the ground, allowing it to be easily accessible and maintained. However, the main advantage is the early wake dissipation of VAWTs. Near-wake experiments of Ferreira (2009) [\[55\]](#), and simulations of Vermeer (2003) [\[64\]](#) have shown that the fluid past the turbine is more turbulent. Due to this higher turbulence, the flow is able to recover much earlier than convectional wind turbines. This allows the turbines to be placed much closer, potentially



(a) VAWT: Darrieus wind turbine[\[17\]](#)



(b) HAWT: Offshore wind turbine [\[18\]](#)

Figure 1.1: VAWT vs. HAWT



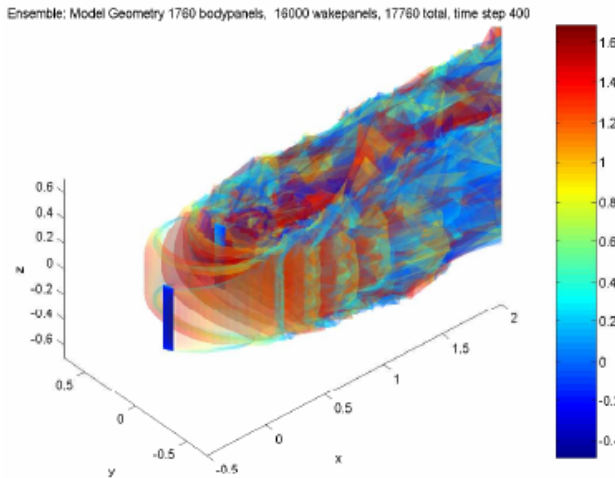


Figure 1.2: 3-D Unsteady Panel simulation of a Straight-bladed VAWT showing the strength of the shed vorticity. The VAWT blades interact with their own wake increasing the complexity of the wake geometry [26]

outputting more power per ground. Furthermore, VAWTs operate independently of the flow direction, and can operate at low wind speeds (i.e. at low tip-speed ratios).

However, there are some limitations that we must take into account. As the blades pass through their own wake, complex wake-body interactions take place, figure 1.2. These have adverse effects on the blade structure, making it more susceptible to fatigue. As the blade is constantly pitching, flow behaviors such as dynamic stall and constant vortex shedding take place [57]. These complex fluid behaviors makes it hard to predict the performance of a VAWTs and this is one of the reasons why VAWTs are not widely used.

In addition, a VAWT operates at a large Reynolds, number making accurate numerical methods computationally very expensive. So we see that we require a numerical method that can not only reproduce accurate results, but is also efficient at modeling the flow around the turbine.

1.1 Motivation and Goal

The goal of this research is to develop an efficient, reliable, and accurate numerical method for modeling the flow around a Two-Dimensional (2-D) VAWT, enabling to compute the correct performance characteristics. The two approaches of investigating the flow around a turbine are by either using a numerical method to model the flow, or by performing an experimental test, for example in a wind tunnel.

To understand the unsteady aerodynamic behavior, Particle Image Velocimetry (PIV) has been a useful tool to visualize the flow around the turbine. PIV was used by Ferreira et al. (2007) [56], showing that it is possible to measure the flow characteristics around the blade. The downside to experimental investigation is that it is very expensive to investigate all types of airfoil geometries, blade geometries and VAWT configurations. However, investigating this is vital in understanding the performance characteristics of

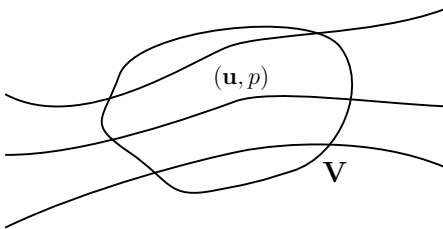


Figure 1.3: Eulerian formulation of the fluid. We observe a given volume \mathbf{V} and evaluate the change in properties of the fluid, velocity \mathbf{u} and pressure p at time passes.

VAWT. Furthermore, it is difficult to perform experiments on array of wind turbines in a wind tunnel.

Numerical methods are therefore a popular alternative as the cost of simulation is becoming progressively smaller, and the accuracy of the models are increasing day by day. Actuator Disk (AD) and Blade Element Momentum (BEM) models are the simplest models, built upon satisfying the momentum balance of the turbine with the fluid. The advantage is that they are very quick, however they lack the accuracy that are obtained by experimental simulation. Flow phenomena such as dynamic stalls and flow separations cannot be modeled by these methods, and therefore we must rely on more powerful tools.

To ensure more accuracy, one has to solve the Navier-Stokes equation of the flow around the turbine without large simplifications. Computational Fluid Dynamics (CFD) methods discretize the fluid into smaller cells (or volumes) and solve the Navier-Stokes equations. This type of formulation is known as an Eulerian formulation as we are evaluating the change in flow property in a given cell/volume, figure 1.3. In order to fully resolve the flow around the turbine, we would need a fine mesh near the blade where we have small scale vortices. However, far from the body, where these vortices dissipated into low frequency vortical structures, we can have lower mesh resolution. This means that at various regions of the flow, we require mesh resolutions of various magnitudes. This becomes a problem when we have moving boundaries as the mesh has to be adapted depending on the location of the body.

An alternative method is to use a Lagrangian formulation of the Navier-Stokes equations, known as vortex methods. These methods employ vorticity transport equations which makes them ideal for describing the evolution of the wake vorticity. Furthermore, they do not require cells/volumes to describe the domain. In addition, they use simulation acceleration methods such as Fast Multipole Method (FMM) and parallel computation in Graphical Processing Units (GPU) making them orders of magnitude faster than the typical CFD methods. However, vortex method cannot inherently take in account the solid body. They require additional methods that can describe the effect of the body in the fluid and the vorticity generated from the body.

We see that Eulerian method is accurate when describing the blade-wake interaction but not efficient when describing multi-scale domains. The Lagrangian method is very efficient in evolving the vorticity of the fluid. Due to auto-adaptive nature of the Lagrangian method, it is an ideal choice when describing the multi-scale flow characteristics. However, it is not efficient in resolving the near-body region, where the vorticity is generated. Therefore, in order to use the advantages of both methods, we have decided to use a



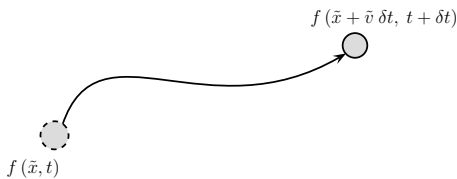


Figure 1.4: Lagrangian formulation of the fluid. We track the path of the individual fluid elements as time passes.

domain-decomposition method, referred to as Hybrid Eulerian-Lagrangian Vortex Particle Method ([HELVP](#)M).

For the HELVP, the Eulerian grid method will be used at the near-wall region of the blades, and the Lagrangian vortex method will be used in the wake region of the body. With proper coupling of these methods, we can ensure that this numerical method can capture not only the near-wake phenomena such as vortex shedding, dynamic stall, and the wake-body interaction, but also the large-scale flow structures such as the evolution of the VAWT wake.

1.2 Research Aim and Plan

We have formulated a research that can help us accomplish our goal. The research questions that are derived from the goal of the project is as follows:

Research Questions:

- *Is it possible to develop an efficient and accurate numerical method by an hybrid approach, with the vortex particle method solving the wake, and the Navier-Stokes grid solver solving the near-body region?*
- *Will it be able to predict similar performance characteristics and flow phenomena as observed from the experiments?*
- *Will it be capable of simulating the blade-wake interaction and the dynamic stall?*
- *Where are the errors and what are their sources?*

In order to answer the research questions, the goal of the project is to develop an efficient and accurate numerical method that is not only capable of capturing the small scale flow phenomena such as the dynamic stall and the vortex shedding, but is also efficient at modeling the evolution of the wake. Once the model have been developed, we will verify the approach and validate it against cases obtained from literature.

Research aim and plan:

- *Develop the hybrid method for capturing small-scale phenomena and large scale phenomena.*

- Verify the efficiency, reliability, and the accuracy of the model.
- Verify and validate the model with test cases from literature.

The innovativeness of this project is that such hybrid modeling has not been yet applied for the wind energy problem case. Through the parallelization of the vortex particle method in a GPU and employing solver acceleration techniques such as the FMM, this simulation could give an edge in the understanding the flow behavior of a VAWT.

1.3 Introduction to Hybrid Eulerian-Lagrangian Vortex Particle Method

The Hybrid Eulerian-Lagrangian Vortex Particle Method ([HELVPM](#)) is a domain decomposition method, where the Eulerian method and the Lagrangian method solves different regions of the fluid. The domain decomposition method simply splits the domain of interest and uses appropriate method in each domain. The Eulerian formulation will be used at the near-wall region, where we need proper description of the vorticity generation at the boundary, and the Lagrangian formulation is used away from the body, where we only need to evolve the vorticity field. Figure [1.5](#) shows the decomposition of the domain in the gridded and the non-gridded region.

Several studies have already been done: Cottet and Koumoutsakos (2000a)[\[21\]](#), Guermond and Lu (2000) [\[30\]](#) simulated the advection dominated flows; Ould-Salhi et al. (2001) [\[49\]](#) blended the finite difference and vortex method together; Winckelmans et al. (2005a) [\[66\]](#) investigated the trailing vortices; Daeninck (2006) [\[23\]](#) used a simplified coupling strategy, coupling Vortex Particle Method and Finite Diference Method; Stock (2010) [\[59\]](#) expanded Daeninck's strategy, coupling Vortex Particle Method and Finite Volume Method and modeled a 3-D rotor.

When evaluating the previous works, we see that not all domain decomposition methods are the same. The main difference between the methods is their coupling strategies. Most works employ the Schwartz alternating method to couple the vortex particle method and the grid solver. The Schwartz alternating method (or sometimes referred to as Schwartz iterative method), couples the vortex particle method and the grid solver by iteratively determining the boundary condition such that the stream functions in both domains, ψ_L and ψ_E in Ω_L and Ω_E respectively, match at the overlap region $\Omega_E - \Omega_L$, figure [1.5](#). The summary of a single iteration of the Schwartz alternating method is as follows:

- Determine the Eulerian boundary condition, the stream function ψ_{Γ_E} at the Eulerian boundary Γ_E , extracted from the Lagrangian stream function ψ_L in the Lagrangian subdomain Ω_L .
- Solve for the stream function ψ_E in the Eulerian subdomain Ω_E with the new boundary condition Γ_E .
- Determine the Lagrangian condition, the stream function ψ_{Γ_L} at the Lagrangian boundary Γ_L , extracted from the Eulerian stream function ψ_E in the Eulerian subdomain Ω_E .



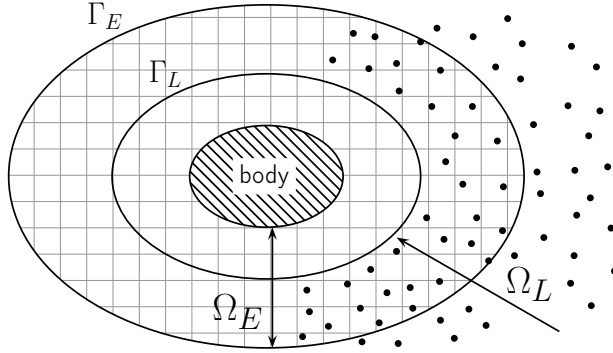


Figure 1.5: Standard domain decomposition using Schwartz iteration for coupling the two methods. Eulerian subdomain Ω_E (near the body), and Lagrangian subdomain Ω_L (away from the body). Figure is based on Guermond (2000) [30]

- Solve the stream function ψ_L in the Lagrangian subdomain with the boundary conditions ψ_{Γ_L} at the Lagrangian boundary Γ_L .

This procedure is iterated until the stream functions of both domains converge [49]. Once the stream function is determined in both the domains, the velocity field can be obtained. Using the velocity field, we can evolve the vorticity field in the Lagrangian subdomain.

As we realized now, the downside to this procedure is that we have to solve the stream function in both Ω_E and Ω_L iteratively, until we converge to a solution. This makes the computation very expensive, especially when we are dealing with large numbers of vortex particles. Therefore, for this project, we are using the coupling technique that is based on the research work of Daeninck (2006) [23] and Stock (2010) [59]. However we had to perform a correction to their scheme to ensure the conservation of circulation is satisfied.

1.3.1 Simple coupling strategy

This approach will be referred to as the Simple Coupling Strategy (SCS). It is simpler than the Schwartz iterative method, as no iteration is needed for the coupling procedure. The basic algorithm consists of solving the vortex method in the full fluid domain using a relatively coarse resolution on the near-wall region. Then we use the grid solver in the near-wall region to capture the detailed features of the boundary layer and transfer the vorticity field in this region to the vortex particles, figure 1.6. Therefore, the grid solver essentially acts as the correction for the under-resolved regions of the Lagrangian method. The functionality of this strategy has been demonstrated by Daeninck and was found to be significantly faster than the Schwartz coupling strategy. The features of the simple coupling strategy can summarized as follows:

- Eulerian method is used to resolve the near-wall region, at the Eulerian subdomain Ω_E , enabling it to capture important features of the boundary layer (such as flow separation) with great accuracy.
- Lagrangian method is used to capture the wake, at the Lagrangian subdomain Ω_L , and to efficiently evolve the wake.

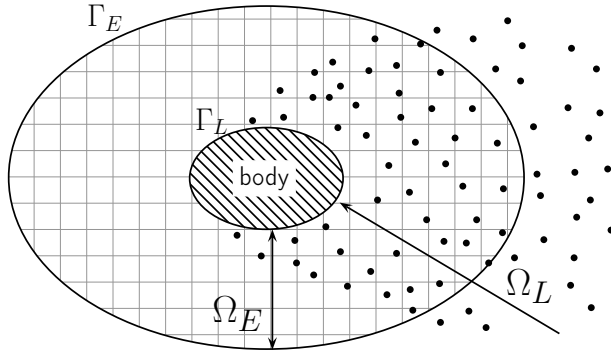


Figure 1.6: Modified domain decomposition without Schwartz alternating method. Lagrangian subdomain extends up to the surface of the body. Figure is based on Daeninck (2006) [23].

- The accurate solution of the Eulerian subdomain is transferred to the Lagrangian subdomain according to the coupling algorithm of Daeninck [23] and Stock [59]. In addition to their algorithm, a correction is done on the transfer to ensure conservation of circulation.
- The boundary conditions for the Eulerian subdomain are retrieved from the Lagrangian subdomain.

The algorithm to the Simple Coupling Strategy (SCS) follows from Daeninck's doctoral thesis, [23]. Figure 1.7 shows the overview to the algorithm and can be summarized as follows:

1. **Correct Lagrangian:** Use the solution of the Eulerian subdomain Ω_E (in the near-wall region) to correct the solution of the Lagrangian subdomain Ω_L , that is overlapping the Eulerian subdomain, ensuring that the *circulation is conserved*.
2. **Evolve Lagrangian:** With the modified solution, evolve the Lagrangian solution from time step t_n to next time step t_{n+1} .
3. **Determine Eulerian boundary conditions:** Use the Lagrangian solution of time t_{n+1} to determine the boundary conditions of the Eulerian subdomain at t_{n+1} .
4. **Evolve Eulerian:** With the boundary condition, evolve the Eulerian solution from t_n to t_{n+1} .

This is the basic approach for coupling the Eulerian method in the Eulerian subdomain Ω_E with the Lagrangian method in the Lagrangian subdomain Ω_L without the iterative Schwartz algorithm.

Furthermore, the SCS handles the Lagrangian boundary condition differently from the classic hybrid method. Typically during the evolution process of the Lagrangian subdomain, the shedding of the vorticity is also defined in the Lagrangian method. However, in our coupling strategy, the Lagrangian method is under-resolved at the boundary and cannot be used to resolve the vorticity flux at the body. Instead, we use the Eulerian



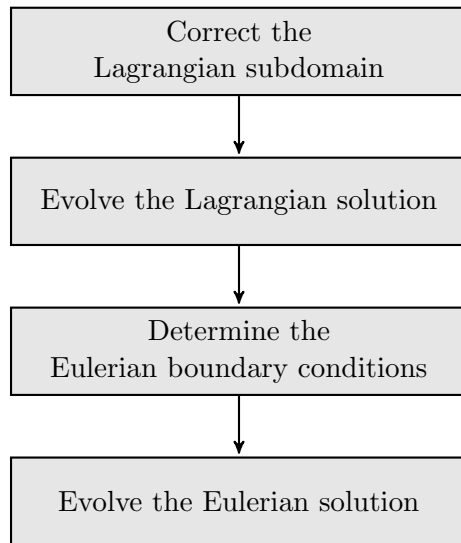


Figure 1.7: Flowchart of the simple coupling strategy. The flowchart shows the procedure to evolve both methods from t_n to t_{n+1} .

method to resolve the boundary, and the Eulerian method acts as the vorticity generator for the Lagrangian method. However, there are some assumptions that we must satisfy, for this coupling strategy to be valid:

- At t_n before the evolution of both method to t_{n+1} , the Lagrangian solution matches Eulerian solution at the boundary of the near-wall region.
- After the evolution to t_{n+1} , the deviation of the Lagrangian solution (due to lack of vorticity flux at Lagrangian boundary), should be minimal.
- Even though the Lagrangian subdomain is under-resolved in the near-wall region, it should be able to provide accurate boundary conditions for the Eulerian external boundary.

1.4 Verification and Validation Test Cases

In order to assess the accuracy of this hybrid formulation, the following test cases haven't been used:

Lamb-Oseen vortex [41] [61]

Lamb-Oseen vortex test case is an analytical solution derived from the NS equation, and is a test case for unbounded flow (without any wall). This is the first model that will be used to validate the Lagrangian method and Eulerian method separately. As it describes an unbounded flow, we do not need to concern with the vorticity generation problem. This helps us focus on just the evolution of the vorticity field.

Clercx-Bruneau dipole [15]

The Clercx-Bruneau dipole test case is the simple case of a colliding dipole with a wall. This test case will be used to verify and validate the coupling of the Eulerian and the Lagrangian method in the presence of a solid wall. This test cases focuses on the interaction of vorticity with the wall making it ideal to verify and validate the proper generation of vorticity and its transfer to the Lagrangian subdomain.

Impulsively started cylinder [39] [10] [6] [42]

The impulsively started cylinder test case is used to analyze the forces acting on the cylinder. This test case is used to verify and validate the lift and drag evolution of the cylinder exposed to free-stream flow.

Elliptic Airfoil [48]

The elliptic airfoil test case focuses on the flow separation past a lifting body. The elliptic airfoil is pitched at high angle of attack and the flow past the airfoil is comparatively unsteady and undergoes phenomena such as laminar separation bubble, flow separation and karman vortex shedding from the trailing edge of the airfoil. This helps us ensure the coupling strategy is accurate for complex flow phenomena.

1.5 Thesis Outline

Ch. 2 Lagrangian Subdomain: Vortex Particle Method

The chapter introduces the vortex particle method used to solve the Lagrangian subdomain of the hybrid method. The chapters introduces the concept of vortex blobs for discretizing the vorticity in the fluid and vortex panels for discretizing the wall-bounded vorticity. The chapter concludes with a verification and validation of the described Lagrangian method with the help of the Lamb-Oseen vortex test case.

Ch. 3 Eulerian Subdomain: Finite Element Method

The chapter introduces the finite element method used to solve the Eulerian subdomain of the hybrid method. We investigate the methodology for solving the incompressible Navier-Stokes equations using the finite element approach. The chapter concludes with a verification and validation of the described Eulerian method with the help of Lamb-Oseen vortex test case, impulsively started cylinder test case at $Re = 550$ of Koumoutsakos and Leonard [39], and the Clercx-Bruneau dipole collision of Clercx and Bruneau [15].

Ch. 4 Hybrid Eulerian-Lagrangian Vortex Particle Method

The chapter introduces the hybrid Eulerian-Lagrangian vortex particle method. We investigate the methodology for coupling the Eulerian subdomain and the Lagrangian subdomain. This chapter highlights the modification we implemented to the coupling strategy used by Daeninck [23] and Stock [59].

Ch. 5 Introduction to the Hybrid Solver: pHyFlow

The chapter introduces pHyFlow, the python based hybrid solver. The chapter gives an overview of the program structure and the class hierarchy.



Ch. 6 Verification and Validation of the Hybrid Method

The chapter focuses on the verification and the validation of the hybrid method. We use the test cases described in section 1.4, to achieve this.

Chapter 2

Lagrangian Subdomain: Vortex Particle Method

2.1 Introduction to the Vortex Particle Method

Vortex Particle Method ([VPM](#)) is a numerical method employed in computational fluid dynamics, dealing with the evolution of the vorticity in the fluid from a Lagrangian description. In an Eulerian formulation, the fluid is viewed at a fixed window where the change in the fluid properties are evaluated. However, the Lagrangian formulation, regards the fluid as a collection of particles (or elements) carrying properties of the fluid (such as vorticity, mass, etc.).

Efficient discretization of the fluid domain becomes a difficult task for cases such as Vertical-Axis Wind Turbine ([VAWT](#)), where the wake geometry is complex and unsteady. Discretizing such wake using Eulerian formulation becomes difficult as it requires the adaption of the mesh over time for efficient computation. The VPM only needs fluid elements where there is vorticity meaning that the method is inherently auto-adaptive. This is one of the advantage of the VPM. Furthermore, with computational acceleration methods such as Fast-Multipole Method ([FMM](#)) and parallel computation in Graphics Processing Units ([GPU](#)) enables an efficient evolution of the vorticity wake.

However, the key advantage of the VPM is that it is ideal for capturing the resolving the long-time characteristics of the unsteady compact vortical structures that are shed off from the VAWT blades, as described by Stock [59], providing the motivation for using VPM for modeling the rotor wake.

A summary of the advantage of the Lagrangian vortex method w.r.t the Eulerian method was provided by Wee and Ghoniem [65]:

- Eulerian methods introduce dissipation, even in flows with zero velocity gradient. However such error as minimized at the convection of the Lagrangian method.



- The numerical stability of the Lagrangian method is not restricted by the CFL condition.
- The support of the Lagrangian elements are a small fraction of the fluid domain. The support is confined to location of non-zero vorticity, making the method naturally grid adaptive.

The main literature on the VPM (the Lagrangian component of the hybrid method), is the book of Cottet and Koumoutsakos, Vortex Methods: Theory and Practice [21]. It gives an insight on the fundamentals of the vortex method (specifically VPM) and gives a summary on hybrid methods.

2.1.1 Vorticity

The vorticity ω is the governing element of the VPM. It is given by

$$\omega = \nabla \times \mathbf{u}, \quad (2.1)$$

where \mathbf{u} is the velocity vector field. In 2D, the circulation Γ is defined by Stokes' theorem as,

$$\Gamma = \int_L \mathbf{u} \cdot d\mathbf{s} = \int_A (\nabla \times \mathbf{u}) \cdot \mathbf{n} \, dA = \int_A \omega \cdot \mathbf{n} \, dA, \quad (2.2)$$

and represents the flux integral of vorticity across the surface A , contoured by the line s . Figure 2.1 depicts this relation of velocity \mathbf{u} , vorticity ω and the circulation Γ .

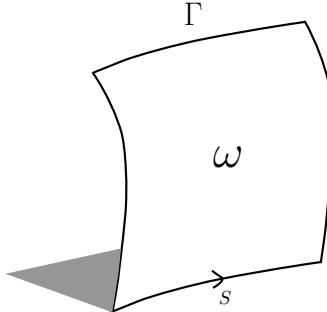


Figure 2.1: Definition of the circulation in the fluid.

2.1.2 Velocity-Vorticity Formulation of the Navier-Stokes Equations

The governing equation of the vortex particle method is the velocity-vorticity formulation $\mathbf{u} - \omega$ of the Navier-Stokes equations, as presented in Cottet and Koumoutsakos [21]. It is derived from the 2D incompressible Navier-Stokes momentum equation, given as,

$$\frac{\partial \mathbf{u}}{\partial t} + \mathbf{u} \cdot \nabla \mathbf{u} = -\frac{1}{\rho} \nabla p + \nu \nabla^2 \mathbf{u}, \quad (2.3)$$

relating the velocity field $\mathbf{u}(\mathbf{x}, t)$ to the pressure field $p(\mathbf{x}, t)$, the kinematic viscosity ν and density ρ , and satisfied the incompressibility constraint,

$$\nabla \cdot \mathbf{u} = 0, \quad (2.4)$$

The curl of the equation 2.3 is take to obtain the velocity-vorticity formulation,

$$\frac{\partial \omega}{\partial t} + \mathbf{u} \cdot \nabla \omega = \nu \nabla^2 \omega, \quad (2.5)$$

relating the vorticity ω to the velocity \mathbf{u} . Note that the pressure term p disappear from the equality.

2.1.3 Viscous Splitting Algorithm

The VPM was initially used to model the evolution of incompressible, inviscid flows. However, in order to simulate a real flow, we must also deal with the viscous behavior of the fluid. Chorin in 1973 [13], showed that using the viscous splitting algorithm, it is possible to take the viscous effects of the flow into account.

The viscous splitting algorithm is a fractional step method, where the viscous and the inviscid part of the vorticity transport equation, equation 2.5, are dealt with in two subsequent sub-steps,

1. **Convection** (sub-step 1):

$$\frac{\partial \omega}{\partial t} + \mathbf{u} \cdot \nabla \omega = 0; \quad (2.6)$$

2. **Diffusion** (sub-step 2):

$$\frac{\partial \omega}{\partial t} = \nu \nabla^2 \omega. \quad (2.7)$$

The first sub-step of the evolution deals with the convection of vorticity. The convection step is described in section 2.3. The diffusion of vorticity field is dealt with in the second sub-step. The diffusion of the vorticity field is dealt with in section 2.4

2.2 Spatial Discretization: Introduction to Vortex Blobs

The vorticity ω and the velocity \mathbf{u} in the vorticity transport equation, equation 2.5, describes a continuous field. However, these variables needs to be discretized to perform a numerical integration required for the numerical simulation.

2.2.1 Discrete Form of Vorticity Field

The vorticity field is discretized by representing the continuous vorticity field by a summation of particle-type elements, as described by Barba [1]. The discrete vorticity field ω^h is represented by a linear combination of N basis function, given as,

$$\omega(\mathbf{x}, t) \simeq \omega^h(\mathbf{x}, t) = \sum_p^N \alpha_p(t) \delta[\mathbf{x} - \mathbf{x}_p(t)], \quad (2.8)$$



where δ is the Dirac delta function, and α_p is the circulation carried by the particle at \mathbf{x}_p . We must note that ω^h is the discrete vorticity field and therefore an approximation of the continuous vorticity field ω .

The velocity \mathbf{u} is related to the vorticity ω using the Biot-Savart Law.

2.2.2 Biot-Savart Law

A velocity field \mathbf{u} that satisfies the incompressibility constraint, equation 2.4, can be decomposed using the Helmholtz decomposition,

$$\mathbf{u} = \mathbf{u}_\omega + \mathbf{u}_\phi + \mathbf{u}_\delta, \quad (2.9)$$

where \mathbf{u}_ω is the rotational (solenoidal) component of the velocity \mathbf{u} , \mathbf{u}_ϕ is the irrotational (potential) component, and \mathbf{u}_δ is the harmonic form. These components satisfying the following equality,

$$\nabla \cdot \mathbf{u}_\omega = \nabla \times \mathbf{u}_\phi = \nabla^2 \mathbf{u}_\delta = 0. \quad (2.10)$$

The divergence-free component \mathbf{u}_ω implies that there exists a stream function ψ , such that,

$$\mathbf{u}_\omega = \nabla \times \psi, \quad (2.11)$$

and therefore the vorticity ω of the velocity \mathbf{u} , is given as,

$$\omega = \nabla \times \mathbf{u} = -\Delta \psi \quad (2.12)$$

Similarly, there must exist a potential ϕ , such that,

$$\mathbf{u}_\phi = \nabla \phi. \quad (2.13)$$

For an incompressible and unbounded problem, the potential velocity \mathbf{u}_ϕ is simply the free-stream velocity \mathbf{u}_∞ and the harmonic form $\mathbf{u}_\delta = 0$. In the case of the bounded problem with solid boundaries, the presence of the body must be taken into account, see section 2.5. For now, we will discuss the unbounded problem.

From the Poisson equation 2.12, the velocity is related to the vorticity by the Biot-Savart law, given as,

$$\mathbf{u}_\omega = \mathbf{K} \star \omega, \quad (2.14)$$

where \star is the convolution of the vorticity with the 2-D Biot-Savart kernel \mathbf{K} given by,

$$\mathbf{K} = \frac{1}{2\pi |\mathbf{x}|^2} (-x_2, x_1). \quad (2.15)$$

From the kernel, we see that as the distance to the kernel center approaches zero ($\mathbf{x} \rightarrow 0$), the kernel goes to infinity. The singularity of the kernel \mathbf{K} is removed by mollifying the kernel distribution ensuring smooth velocity distribution.

2.2.3 Mollified Vortex Kernels

A mollified (or a regularized) vortex particle is called the vortex blob, and has a non-zero vortex core size σ . A smoothing function ζ is used to mollify the kernel \mathbf{K} , satisfying the constraint $\int \zeta = 1$, such that the circulation is conserved. An ideal choice for a smoothing function is the Gaussian distribution, given as,

$$\zeta_\sigma = \frac{1}{k\pi\sigma^2} \exp\left(-\frac{|\mathbf{x}|}{k\sigma^2}\right), \quad (2.16)$$

where typically k is either 1, 2 or 4, determining the width of the kernel, and σ being the core-size of the vortex blob.

Figure 2.2 depicts the smoothing function ζ_σ with $k = 2$ and $\sigma = 1$, showing that the function decays quickly away from the center of the core. The mollified Biot-Savart kernel \mathbf{K}_σ is given as,

$$\mathbf{K}_\sigma = \mathbf{K} \star \zeta_\sigma, \quad (2.17)$$

resulting in the discrete mollified vorticity field as,

$$\omega^h(\mathbf{x}, t) = \sum_p \alpha_p(t) \zeta_\sigma [\mathbf{x} - \mathbf{x}_p(t)], \quad (2.18)$$

and the discrete mollified velocity field as,

$$\mathbf{u}^h(\mathbf{x}, t) = \sum_p \mathbf{K}_\sigma [\mathbf{x} - \mathbf{x}_p(t)] \alpha_p(t). \quad (2.19)$$

Koumoutsakos and Chorin [21], explained that in order to ensure the smoothness of the velocity field, the vortex blobs need to have an overlap with each other. The overlap ratio λ is defined as,

$$\lambda = \frac{h}{\sigma}, \quad (2.20)$$

where h is the nominal particle spacing, and σ is the vortex blob core size. Figure 2.3 shows the visual representation of this definition.

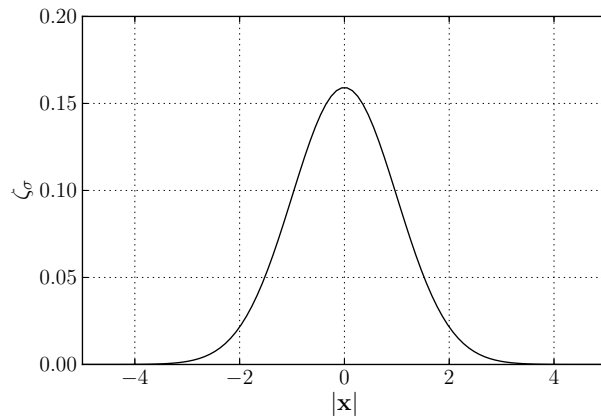


Figure 2.2: The smoothing function ζ_σ for a gaussian distribution with $k = 2$, $\sigma = 1$.



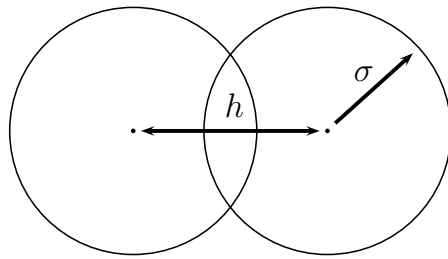


Figure 2.3: Vortex blob with an overlap ratio $\lambda = h/\sigma$

The overlap constraint is violated during the convection of the vortex blobs. Due to the strains in the flow, the vortex blobs cluster together at certain regions and disperse at others. This localized clustering effect is seen as a Lagrangian grid distortion, which is dealt with using a remeshing technique, section 2.3.1.

2.2.4 Vortex Blob Initialization

Now the question arises on how should we initialize the particle's circulation strengths α_p of equation 2.18. The common approach, that is used as a standard, is to estimate the particles strength by quadrature,

$$\alpha_p = \omega_p \cdot h^2, \quad (2.21)$$

meaning that the particle carries the circulation of its local area. This might seem like a valid assumption as the circulation of a given area is the integral of the vorticity in the area, given by equation 2.2, and therefore we will be conserving the circulation as all the circulation in the fluid is represented by the blobs.

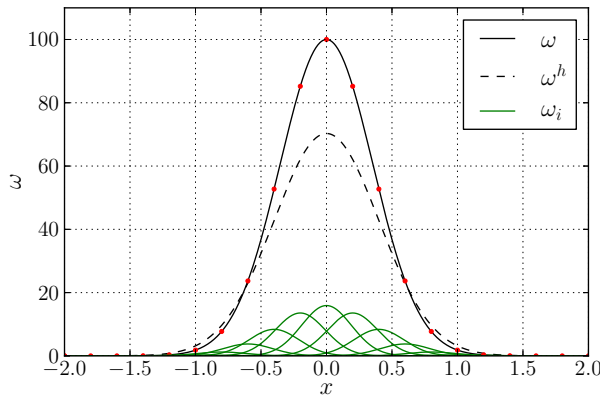


Figure 2.4: Mollified vorticity field of a Gaussian vorticity distribution by blobs with $\lambda = 1.0$, $\sigma = 0.19$, and $h = 0.19$. Vortex blob strengths were assigned using equation 2.21, sampling the exact vorticity [●, red dot]. Figure depicts the exact vorticity distribution ω [—, solid black], the vorticity distribution of each blob ω_i [—, solid green], and the mollified vorticity field from the blobs ω^h [- -, dashed black].

Figure 2.4 shows the initialization of the vorticity field using the equation 2.21. We observed that the mollified vorticity field ω^h , deviates from the original intended vorticity distribution ω . Barba and Rossi [1], have described this problem as Gaussian blurring of the original vorticity field due to use of mollified vortex kernel ζ_σ in equation 2.18. Even though the total circulation is conserved, locally we see that the circulation is not conserved.

This phenomenon causes issue during the coupling of the Lagrangian method and the Eulerian method, as particle in the overlap region are re-initialized at every step of the hybrid method. This error in initialization posses a challenge in the coupling of the method and is described in section 4.2.2.

A typical strategy for recovering the intended distribution is the Beale's Iterative Method [3], as used by Koumoutsakos and Cottet [21]. The method is particle circulation processing scheme where the circulation α_p of the particles are modified iteratively such that the mollified vorticity field ω^h matches the original distribution ω . However, the Beale's method required the correction of complete vorticity field in fluid domain and cannot be used to correct only part of the fluid domain, as required for our decomposed domain method. Therefore, an alternate method is required to minimized the error in particle initialization.

2.2.5 Minimization of Particle Discretization Error

An alternate method to reduce the Gaussian blurring of the vorticity field is to modify the overlap ratio λ , and the nominal particle spacing h . This approach does not remove the Gaussian blurring problem, but instead minimizes its discretization error.

Figure 2.5 shows mollified vorticity field results from modifying the spatial resolution parameters. Figure 2.5a shows the convergence of the mollified vorticity field ω^h to the exact vorticity field ω by reducing the nominal particle spacing h . The overlap ratio is set to overlap = 1, meaning that the blob core-size σ is equal to h . We see that by reducing blob core size, and simultaneously increasing the number of particles, the mollified vorticity converges to the exact vorticity.

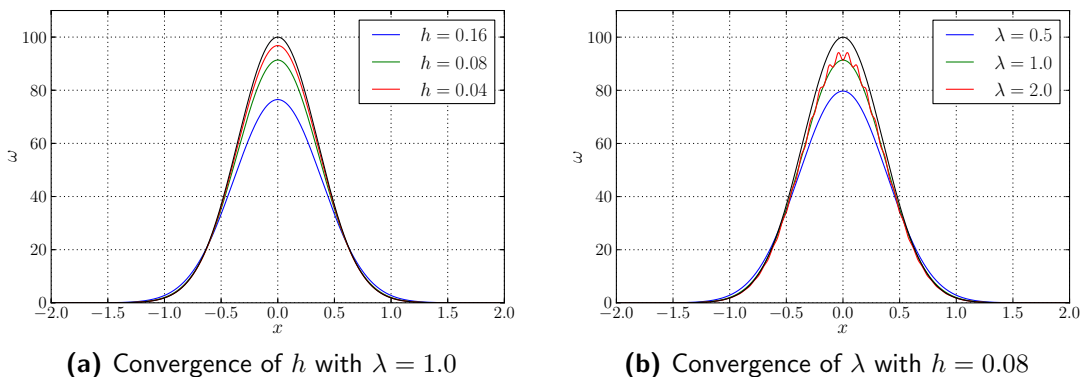


Figure 2.5: Convergence of the spatial discretization h and λ of the initial vorticity distribution. Figure depicts the exact vorticity field ω [—, solid black], and various discretized vorticity distributions.



The second parameter we can adjust is the overlap of the blobs, as seen in Figure 2.5b. The blob spacing h is set to $h = 0.08$, and we see that by increasing the overlap ratio λ , the mollified vorticity approaches the exact vorticity field. However, as shown by Koumoutsakos and Cottett [21], if the overlap is low, we lose the smooth reconstruction of the vorticity field. This can be seen for $\lambda = 2.0$. We see that the mollified vorticity field has a fluctuating solution, and will result in non-smooth velocity field.

Thus, to minimize the error in initializing the mollified vorticity ω^h from the vorticity ω , an overlap ratio of $\lambda = 1.0$, and a small nominal blob spacing h is required. In our hybrid method, this means that at the region where we initialize the vortex blobs (i.e inside the Eulerian subdomain), we require these conditions to be satisfied.

2.3 Convection in Vortex Particle Method

Convection of the vorticity is the first step of evolution of the vorticity from viscous splitting algorithm, from section 2.1.3. The convection of the vorticity is described by the first order hyperbolic equation, equation 2.6. The convection equation 2.6, is solved by the following system of ordinary differential equations,

$$\frac{d\mathbf{x}_p}{dt} = \mathbf{u}(\mathbf{x}_p), \quad (2.22a)$$

$$\frac{d\alpha_p}{dt} = 0, \quad (2.22b)$$

where the change in position of vortex blob \mathbf{x}_p is due to the induction velocity $\mathbf{u}(\mathbf{x}_p)$ acting on it, and the strengths of the particles α_p is conserved.

The Biot-Savart Law, equation 2.19, is used to determine the induced velocities acting on each particle, resulting in an N -body problem. The calculation of the N -body problem is optimized by parallelizing the calculations in GPU hardware. The calculation is further optimized by using a fast summation method, the Fast Multipole Method (**FMM**), reducing the problem from $\mathcal{O}(N^2)$ to $\mathcal{O}(N)$ (in the ideal case).

The time integration of equation 2.22 is performed using a 4th order explicit Runge-Kutta method. The higher-order time integration ensures an accurate convection of the vortex blobs, resulting in minimum dissipation. However, the downside to employing a multi-stage method is that we require multiple evaluation of the induced velocity $\mathbf{u}(\mathbf{x}_p)$, when stepping from a given time t_n to the next time t_{n+1} .

After several steps of the convection of the vortex blobs, the overlap ratio λ will no longer be satisfied due to strains in the fluid, as described by Koumoutsakos and Chorin [21]. In section 2.2.5, we determined that to have an accurate reconstruction of the vorticity field, the vortex blobs must satisfy the overlap ratio λ at all times t . This introduced the need for a remeshing (or a regridding) scheme that can reconstruct the vortex blobs distribution to the original overlap ratio λ .

2.3.1 Remeshing Scheme: Treating Lagrangian Grid Distortion

The distortion of the Lagrangian grid is due to the clustering and dispersion of the vortex blobs. This clustering and dispersing effect of the blobs is due to the high strains in

the flow. Figure 2.6 depicts the distortion of the Lagrangian grid after 100 convection steps. The final distribution shows gaps in vortex blob distribution and will result in an inaccurate representation of the vorticity field.

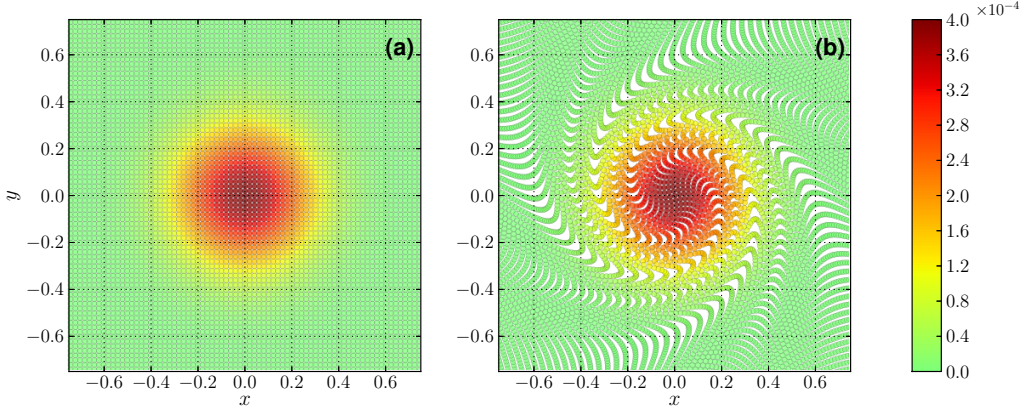


Figure 2.6: Lagrangian distortion of the vortex blobs after 100 time steps. The initial vorticity field is $\omega(\mathbf{x}, 0) = \exp(-12|\mathbf{x}|)$ with $\Delta t = 0.1$, $\sigma = 0.02$, and overlap = 1.0. Figure depicts (a) the initial distribution of the vortex blobs, and (b) the final distribution of the vortex blobs after 100 time steps.

A remeshing (or regridding) of this field is therefore required to retain proper distribution. It is done by interpolating the strengths of the vortex blobs from the distorted Lagrangian grid $\hat{\mathbf{x}}$ onto a uniform grid \mathbf{x} . The strengths of the blobs of the new uniform grid α_p is determined by,

$$\alpha_p = \sum_q \tilde{\alpha}_q W\left(\frac{x_p - \tilde{x}_q}{h}\right), \quad (2.23)$$

where the strengths of the blobs $\tilde{\alpha}_q$ of the distorted Lagrangian grid \tilde{x}_q are transferred to the regular Lagrangian grid x_p using the interpolation kernel W . Figure 2.7 shows an example of the remeshing of one vortex blob of the distorted grid on to the structured uniform grid with a kernel W with a 3×3 stencil. During this transfer, we must ensure

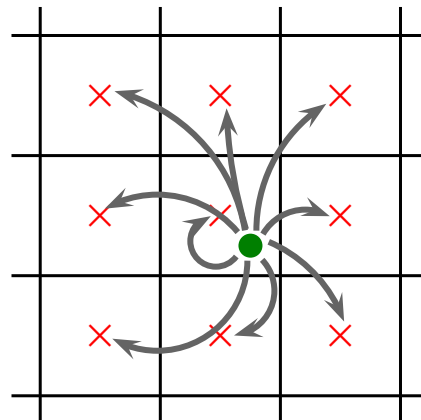


Figure 2.7: Remeshing of a single vortex blob [●, green dot] onto a uniform grid defined by the (3×3) 2-D stencil.



that the properties of the fluid are conserved. The interpolation kernel is constructed by ensuring that the total circulation, the linear impulse, and the angular impulse of the fluid are conserved.

For the present work, the widely used M'_4 interpolation kernel, such as by Koumoutsakos and Cottet [21], Speck [58], and Barba [2]. The kernel is continuously differentiable ensuring conservation of total circulation, linear and angular impulse.

M'_4 Interpolation Kernel

The M'_4 interpolation kernel is an efficient interpolation kernel that has been used to reconstruct a smooth distribution, and was introduced by Monaghan in 1985 [46]. For a 1D problem, the M'_4 interpolation kernel is defined as,

$$M'_4(\xi) = \begin{cases} 1 - \frac{5\xi^2}{2} + \frac{3|\xi|^3}{2} & |\xi| < 1, \\ \frac{1}{2}(2 - |\xi|)^2(1 - |\xi|) & 1 \leq |\xi| < 2, \\ 0 & 2 \leq |\xi|, \end{cases} \quad (2.24)$$

where

$$\xi = \frac{x_\nu - x_i}{h}, \quad (2.25)$$

is a non-dimensional parameter, relating the position of the particle x_ν to the position of the i^{th} interpolation node x_i . The M'_4 is a third-order accurate, piecewise smooth, B-spline kernel. The kernel with the $m = 4$, has a 4 support nodes in each dimension.

Figure 2.8 shows the distribution of the kernel. For the 2D problem, the 2D interpolation kernel is the tensor product of the 1D interpolation kernel, thus having a $4 = 16$ support nodes. The kernel has a compact support, making it ideal for an efficient $\mathcal{O}(N)$ remeshing.

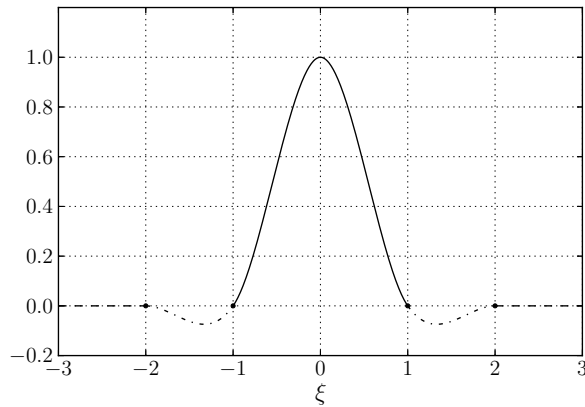


Figure 2.8: M'_4 interpolation kernel, a third-order, piecewise smooth, B-spline kernel by Monaghan [46]

2.4 Diffusion in Vortex Particle Method

Chorin [13], simulated the viscous flow using the viscous splitting algorithm, described in section 2.1.3. The viscous splitting algorithm segregated the vorticity transport equation, equation 2.5, to the inviscid and the viscous components, equation 2.6 and equation 2.7 respectively.

The flow is convected during the first sub-step, whereas in the second sub-step, we have to deal with the diffusion of the vorticity field, equation 2.7. The diffusion problem is solved using the following system of ODEs,

$$\frac{d\mathbf{x}_p}{dt} = 0, \quad (2.26a)$$

$$\frac{d\alpha_p}{dt} = \nu \Delta \alpha_p, \quad (2.26b)$$

where the position of the particles \mathbf{x}_p is fixed, whereas the change in strengths of the particles α_p as depended on the kinematic viscous ν . Thus the diffusion of the vortex blobs requires only the modification to the strengths α_p of the particles.

Chorin in 1973 [13], initially employed the Random Walk Method (RWM), which generates and disperses vorticity using a pseudo-random number algorithm. However, this method suffered some limitations in accuracy, and since then methods such as Particle Strength Exchange (PSE) method [25], and Vortex Redistribution Method (VRM) [53] become a popular choice for treating diffusion of the particles.

The VRM simulates the diffusion of the particles by redistributing fractions of circulations of the vortex blobs to each other, such that diffusion is appropriately modeled. These redistribution fractions f_{ij}^n are determined by solving a linear system of equations, that conserves the moments of the particles (such as the total circulation, linear and angular impulse) and the diffusion of the flow.

The redistribution fractions f_{ij}^n , transfers portion of circulation α_p of the particle p to others within the diffusion radius, defined as,

$$h_\nu = \sqrt{\nu \Delta t_d} \quad (2.27)$$

where h_ν is the diffusion distance and is directly related to the kinematic viscosity ν and the diffusive time step size Δt_d of the simulation.

For this work, we investigate two methods that employ this approach. The Wee-Ghoniem Remeshing Scheme [65] implemented the VRM into the remeshing process, section 2.4.1. The advantage was that diffusion and remeshing can be performed simultaneously in a single process. However for some flow cases, this approach had undesirable constraint on the diffusion time step size Δt_d . Therefore, the approach of Tutty [62], the Tutty Remeshing Scheme, was employed which had a desirable constraint on the diffusion time step size Δt_d , section 2.4.2. The scheme was used to perform diffusion at every step of the evolution, which is important for proper coupling of the Eulerian and the Lagrangian method.



2.4.1 Wee Remeshing Scheme

Ghoniem and Wee [65], observed the similarities between the VRM and the standard remeshing strategy described in section 2.3.1. They proposed to combine the remeshing and the diffusion of the vortex blobs together in one single process. The application of this methodology was later investigated by Speck [58]. This approach, referred to as the Wee-Ghoniem Remeshing Scheme (**WRS**), implements the diffusion of the vortex blobs in the interpolation kernel W of equation 2.23.

The key advantage of the WRS is that, now we are dealing with a uniform grid, and does not require a search algorithm to find the particles in the zone of influence, equation 2.27. This significantly reduces the computational cost, making this diffusion scheme practical for large scale simulations.

The modified M'_4 kernel for treating the diffusion is given as,

$$M'_4(\xi, c) = \begin{cases} 1 - \frac{5\xi^2}{2} + \frac{3|\xi|^3}{2} - c^2(2 - 9\xi^2 + 6|\xi|^3) & |\xi| < 1, \\ \frac{1}{2}(2 - |\xi|)^2(1 - |\xi|) - c^2(2 - |\xi|)^2(1 - 2|\xi|) & 1 \leq |\xi| < 2, \\ 0 & 2 \leq |\xi|, \end{cases} \quad (2.28)$$

where

$$c^2 = \frac{\nu \Delta t_d}{h^2}, \quad (2.29)$$

is a non-dimensional number that corresponds to the transfer weight for the diffusion. The constant c^2 is a function of the kinematic viscosity ν , diffusion time step size Δt_d and the remeshing grid spacing h . This additional term in the interpolation kernel accounts for the diffusion process. When $c \rightarrow 0$, the interpolation kernel simply turns into the standard remeshing kernel, equation 2.24.

Ghoniem and Wee also investigated the error growth and the stability properties of the interpolation kernel in the Fourier space and have determined that for a stable diffusion and remeshing, the following constraint has to be satisfied,

$$\frac{1}{6} \leq c^2 \leq \frac{1}{2}. \quad (2.30)$$

However, we see that this c^2 constraint imposes a direct constraint not only on the maximum diffusion time step size Δt_d , but also imposes a constraint on the minimum step size. This would mean that the diffusion time step size Δt_d will be sometimes larger than the convection step Δt_c ,

$$\Delta t_d = k_d \cdot \Delta t_c. \quad (2.31)$$

where $k_d \geq 1$ and is an integer. This is a problem for the hybrid method as the Lagrangian method and the Eulerian method are coupled at every step. If the Lagrangian method does not perform diffusion at every step, from the Eulerian method's point of view, it would seem that the Lagrangian vorticity diffuses in a discontinuous fashion. This discontinuous behavior of the Lagrangian method (w.r.t. the Eulerian method), can cause stability issues during the coupling process, and therefore should be avoided.

We could minimize this problem by modifying the Δt_c such that it matches the diffusion time step (i.e $\Delta t_c = \Delta t_d$), so that the diffusion is performed at every step. This was

a feasible solution for low Reynolds number flows, however for high Reynolds number Re flows, where the convection time step has to be small, we need a scheme that is not constrained by the minimum diffusion time step.

2.4.2 Tutty Remeshing Scheme

The Tutty Remeshing Scheme (TRS), developed by Tutty in 2010 [62], was based on the VRM of Shankar and Van Dommelen [53]. The scheme it possible to remesh and diffuse the vorticity after every convection step. The strengths of the particles after the remeshing and diffusion α_i^{n+1} , are given as,

$$\alpha_i^{n+1} = \sum_k \alpha_k^n W_{ki}^n, \quad (2.32)$$

where W_{ki}^n is the fraction of circulation transferred from vortex blob k (old) to the new vortex blob i (new), Figure 2.7. Tutty [62], explained that the fractions W_{ki}^n are calculated by imposing a conservation of vorticity, center of vorticity, linear, and angular momentum of the vortex blobs, given as,

$$\sum_k W_{ki}^n = 1, \quad (2.33a)$$

$$\sum_k W_{ki}^n (x_i - x_k) = \sum_k W_{ki}^n (y_i - y_k) = 0, \quad (2.33b)$$

$$\sum_k W_{ki}^n (x_i - x_k)^2 = \sum_k W_{ki}^n (y_i - y_k)^2 = 2h_\nu^2, \quad (2.33c)$$

$$\sum_k W_{ki}^n (x_i - x_k)(y_i - y_k) = 0, \quad (2.33d)$$

where h_ν is the characteristic diffusion distance associated to the time Δt_d ,

$$h_\nu = \sqrt{\Delta t_d \cdot \nu}. \quad (2.34)$$

Similar to the the TRS, described in section 2.4.1, the TRS transfers the strengths to known set of new nodes rather than the neighboring nodes (removing the requirement for a search algorithm). Figure 2.9 shows the 1D redistribution of the vortex blob $x_i \leq x_\nu \leq x_{i+1}$

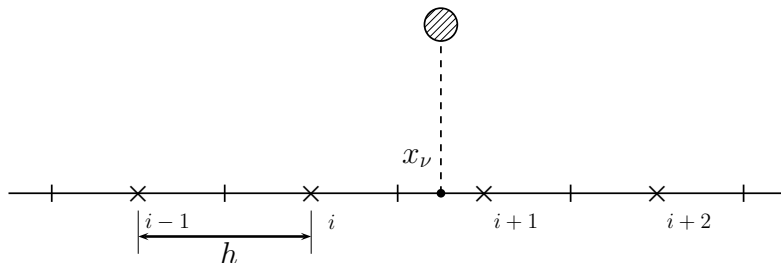


Figure 2.9: 1D Tutty Remeshing Scheme (TRS), diffusing the vortex blobs at $x_i \leq x_\nu \leq x_{i+1}$, onto the four stencil points $k = i - 1, \dots, i + 2$, with a grid spacing h .



x_{n+1} to the stencil nodes x_k , where $k = i-1, \dots, i+2$. The solution to the redistribution is given by the following equations,

$$f_{i-1} = \frac{1}{2} (1 - f_i - \Delta) \quad (2.35a)$$

$$f_i = 1 - 2 \left(\frac{h_\nu}{h} \right)^2 - \Delta^2 \quad (2.35b)$$

$$f_{i+1} = \frac{1}{2} (1 - f_i + \Delta) \quad (2.35c)$$

$$f_{i+2} = 0 \quad (2.35d)$$

and

$$g_{i-1} = 0 \quad (2.36a)$$

$$g_i = \frac{1}{2} (1 - g_{i+1} - \Delta_1) \quad (2.36b)$$

$$g_{i+1} = 1 - 2 \left(\frac{h_\nu}{h} \right)^2 - \Delta_1^2 \quad (2.36c)$$

$$g_{i+2} = \frac{1}{2} (1 - g_{i+1} + \Delta_1) \quad (2.36d)$$

where Δ is defined as,

$$\Delta = \frac{x_\nu - x_i}{h}, \quad (2.37)$$

as depicted in Figure 2.9. Note that $\xi_1 = \xi - 1$. The total redistribution fractions F_k , are the linear combinations of the functions f_k and g_k ,

$$F_k = (1 - \Delta) \cdot f_k + \Delta \cdot g_k, \quad k = i-1, \dots, i+2, \quad (2.38)$$

For the 2D, the redistribution fractions are simple tensors product of the x and y 1D redistribution fractions,

$$W_{kl} = F_k G_l, \quad k = i-1, \dots, i+2, \quad l = j-1, \dots, j+2, \quad (2.39)$$

with a 16 point stencil when $\xi = 1/2$.

The stability of the redistribution requires a positive redistribution fraction, $W_{kl}^n > 0$, imposing a direct constraint on the diffusive distance,

$$\frac{h_\nu}{h} < \frac{1}{\sqrt{2}}. \quad (2.40)$$

as explained by Tutty [62]. A resulting constraint is imposed on the maximum diffusion time step size Δt_d ,

$$\Delta t_d < \frac{h^2}{2\nu}. \quad (2.41)$$

Therefore, we observe that this scheme only poses a constraint on the maximum diffusion time step size Δt_d , enabling us to perform the diffusion at every step of the evolution, equation 2.31.

When employing the Tutty's scheme, we require diffusion and redistribution to be performed at every step, i.e the diffusion frequency $f_{diff} = 1$ and the redistribution frequency $f_{redis} = 1$. In addition to the redistribution, a common approach to minimize the number of vortex blobs is to perform a population control. A population control removes particles with strengths $|\alpha|$ less than pre-defined circulation threshold Γ_{loc} , and simultaneously ensuring that the total circulation removed is less than the pre-defined global threshold Γ_{glob} ,

$$\sum_i |\alpha_i| \leq \Gamma_{glob}, \quad (2.42)$$

where α_i is the strength of the removed particle i . Typically, the population control is performed in conjunction with the redistribution, i.e $f_{redis} = f_{pc} = 1$.

2.5 Boundary Conditions for Viscous Vortex Particle Method

For incompressible viscous flows, the solid boundary is the vorticity generator of the flow. So far, we have only dealt with unbounded flow. For bounded flow simulation, we must enforce the boundary condition of the flow. In 2D, the boundary condition for an immersed body, translating at velocity $\mathbf{u}_b(t)$ with an angular velocity $\Omega(t)$ about its center of mass \mathbf{x}_b is given as,

$$\mathbf{u}(\mathbf{x}_s) = \mathbf{u}_s \quad (2.43)$$

with,

$$\mathbf{u}_s = \mathbf{u}_b + \Omega(t) \times (\mathbf{x}_s - \mathbf{x}_b), \quad (2.44)$$

where \mathbf{u}_s is the velocity at the surface point \mathbf{x}_s . However, in the present work, we deal with stationary bodies and so $\mathbf{u}_b = 0$ and $\Omega(t) = 0$. The boundary condition, Equation 2.43, is usually expressed as,

$$\mathbf{u} \cdot \hat{\mathbf{s}} = \mathbf{u}_s \cdot \hat{\mathbf{s}}. \quad (2.45)$$

equating the tangential components $\hat{\mathbf{s}}$, and is referred to as the *no-slip* boundary condition. The paper of Koumoutsakos, Leonard and Pepin [40] stated that, by satisfying no-slip boundary condition directly satisfies the no-through boundary conditions, as these boundary conditions are linked (*Linked boundary condition*). This was also been stated by Shiels [54] and have been further employed by Cooper, Mar and Barba in 2009 [19].

Typically in an inviscid flow, the boundary condition is enforced after performing the Helmholtz decomposition of the velocity, equation 2.9. The rotational component \mathbf{u}_ω represents the velocity due to the vorticity in the flow, whereas the potential component \mathbf{u}_ϕ is used to taken in account of the presence of the body. However, Koumoutsakos, Leonard and Pepin in 1994 [40], used an alternate approach for enforcing the boundary condition. Instead of performing the Helmholtz decomposition, they considered an extended vorticity field that is divided into:

- the vorticity field in the fluid ω ,



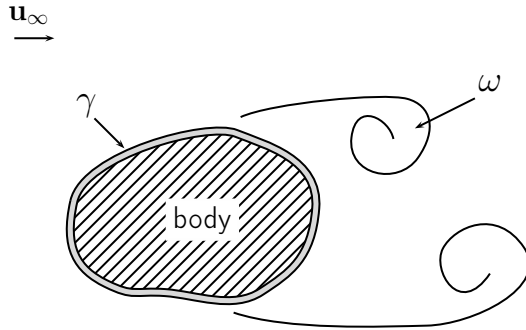


Figure 2.10: Extended vorticity field separated into vorticity in the fluid and the vortex sheet distribution confined to the body.

- the vortex sheet distribution on the boundary γ ,

Figure 2.10 depicts this extended vorticity and the division of the vorticity field to the two sub-categories. The resulting velocity field throughout the domain is given as,

$$\mathbf{u} = \mathbf{u}_\omega + \mathbf{u}_\gamma + \mathbf{u}_\infty \quad (2.46)$$

where \mathbf{u}_ω is velocity field induced by the vorticity in the flow, \mathbf{u}_γ is the velocity field induced by the vortex sheet and \mathbf{u}_∞ is the free-stream velocity.

The vortex sheet distribution γ on the boundary is defined by the boundary integral equations, which will be used to enforce the boundary condition.

2.5.1 Boundary Integral Equations

The Lagrangian method that we are using for the hybrid scheme, is modified according to Stock [59]. The Lagrangian method under-resolved the vorticity field in the near-wall region. Furthermore, the vorticity of the fluid is segregated between the vortex blob domain and the vortex sheet domain, as seen in Figure 2.11. The figure shows that, very near the wall the vorticity of the fluid is represented by the vortex sheet. In other words, the vortex sheet is an extension to the vorticity represented by the vortex blobs.

Enforcing the no-slip boundary conditions, equation 2.46, we have that,

$$(\mathbf{u}_{\text{ext}} + \mathbf{u}_\gamma) \cdot \hat{\mathbf{s}} = \mathbf{u}_s \cdot \hat{\mathbf{s}} \quad (2.47)$$

where $\mathbf{u}_{\text{ext}} = \mathbf{u}_\omega + \mathbf{u}_\infty$ is the velocity field induced from the vortex blob domain (i.e external to vortex sheet domain). The equation states that the tangential component of the total velocity acting on the body should be equal to the tangential velocity of the body. So the induced velocity of the vortex sheet is given as,

$$(\mathbf{u}_{\text{ext}} - \mathbf{u}_s) \cdot \hat{\mathbf{s}} = \mathbf{u}_\gamma \cdot \hat{\mathbf{s}}. \quad (2.48)$$

Koumoutsakos [38], expressed the relation of the vortex sheet strengths to the no-slip boundary condition at the surface of the body (inside the body) through the Fredholm integral equation of the second kind,

$$-\frac{\gamma(s)}{2} + \frac{1}{2\pi} \oint \frac{\partial}{\partial n} [\log |\mathbf{x}(s) - \mathbf{x}(s')|] \gamma(s') ds' = \mathbf{u}_{\text{slip}} \cdot \hat{\mathbf{s}}. \quad (2.49)$$

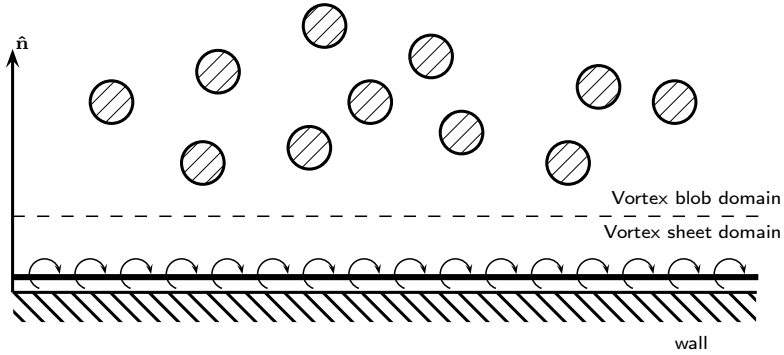


Figure 2.11: Extended vorticity field: Vortex sheet being an extension to the vorticity field (resolved by the vortex blobs), capable of capturing the body bounded vorticity distribution.

where $\gamma(s)$ is the strength of the vortex sheet, and $\mathbf{u}_{\text{slip}} = (\mathbf{u}_{\text{ext}} - \mathbf{u}_b)$, is the slip velocity that needs to be canceled. The left hand side ([lhs](#)) of the equation states that at the point \mathbf{x}_s , the velocity discontinuity is due to the vortex sheet of that point and integral of all the other vortex sheets on the body. However, equation [2.49](#) is singular and accepts non-unique solution.

An additional constraint is obtained from Kelvin's circulation theorem stating that the circulation must be conserved at all times. This imposed a direct constraint on the total circulation of the vortex sheet, defined as,

$$\Gamma_\gamma = \oint_S \gamma(s) \, ds. \quad (2.50)$$

where Γ_γ is the integral of the vortex sheet strengths γ . The total circulation of the vortex sheet Γ_γ is determined during the hybrid coupling of the Lagrangian method to the Eulerian method, see section [4.2.3](#).

2.5.2 Discretization of Integral Equations using Vortex Panels

The panel method approach, exposed by Katz and Plotkin [\[36\]](#), is used to solve the set of equations, equation [2.49](#) and equation [2.50](#). Katz and Plotkins have shown several types of panel distributions with various orders of accuracy; from 0th order point vortex or up to 2nd order linear vortex panel. For this work, we have used a constant-strength vortex distribution that discretizes the vortex sheet into straight segments, classified as Constant-Strength Vortex Panel ([CSV](#)P).

Equation [2.49](#) is solved by discretizing the body surface into M vortex panels, giving us a system of M equation to determine the M unknowns of the strength of the vortex panels.

The integral equation [2.49](#) is discretized and is given in the matrix form as,

$$\mathbf{A} \cdot \vec{\gamma} = \overrightarrow{\text{RHS}}, \quad (2.51)$$

where \mathbf{A} is an $M \times M$ matrix, containing the coefficients a_{ij} , the influence of vortex panel j on the vortex panel i . $\vec{\gamma}$ is an $M \times 1$ vector contains the strengths γ_i of the vortex panel



i and $\overrightarrow{\text{RHS}}$ contains,

$$\text{RHS}_i = \mathbf{u}_{\text{slip}} \cdot \hat{\mathbf{s}}_i. \quad (2.52)$$

The additional constraint 2.50, is similarly discretized and is given as,

$$\sum_i^M \gamma_i \Delta s_i = \Gamma_\gamma, \quad (2.53)$$

where Δs is the length of the vortex panel i . Combining the equations, we have a system of $M + 1$ equations with M unknowns, given in the matrix form as,

$$\underbrace{\begin{pmatrix} a_{11} & a_{12} & \cdots & a_{1M} \\ a_{21} & a_{22} & \cdots & a_{2M} \\ \vdots & \vdots & \ddots & \vdots \\ a_{M1} & a_{M2} & \cdots & a_{MM} \\ \Delta s_1 & \Delta s_2 & \cdots & \Delta s_M \end{pmatrix}}_{\mathbf{B}_{(M+1)M}} \underbrace{\begin{pmatrix} \gamma_1 \\ \gamma_2 \\ \vdots \\ \gamma_M \end{pmatrix}}_{\vec{\gamma}} = \underbrace{\begin{pmatrix} \text{RHS}_1 \\ \text{RHS}_2 \\ \vdots \\ \text{RHS}_M \\ \Gamma_\gamma \end{pmatrix}}_{\overrightarrow{\text{RHS}}}, \quad (2.54)$$

Since we now have a set of $M + 1$ equations with M unknowns, we have to solve the problem either by using a Least-Square solution method (**LSTSQ**), or by eliminating an equation as used by Katz, or by the spectral decomposition of the kernel in the Fredholm equation 2.49, as used by Koumoutsakos [21]. In this work, we opted for the LSTSQ method that the simplest to implement, however Koumoutsakos showed that to remove the singularity associated to the Fredholm equation 2.49, the spectral decomposition method should be used. The singularity becomes a problem with large number of panels, or thin panel geometries.

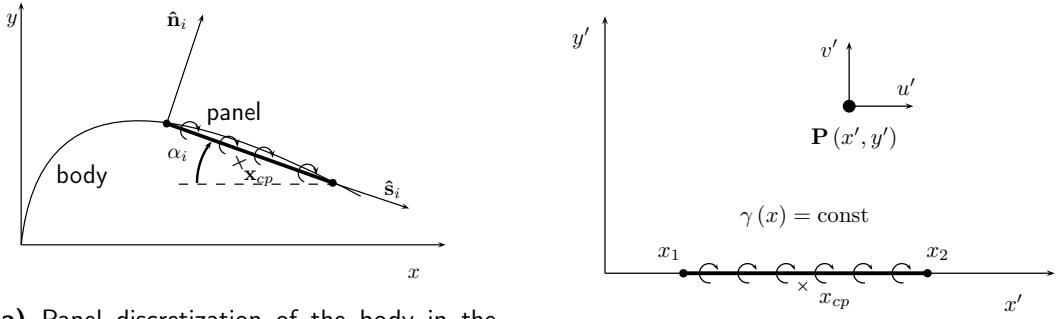
Constant-Strength Vortex Panel

The Constant-Strength vortex panel (**CSV**) is based on the flat (straight) discretization of the vortex sheet, where the panels have constant vortex strength. To solve the strengths of the panel problem, we enforce the Dirichlet velocity boundary conditions at the collocation points x_{cp} , that is located just below the vortex sheet, shown in Figure 2.12b. The coefficient a_{ij} of the influence matrix \mathbf{A} , equation 2.51, is defined as,

$$a_{ij} = \hat{\mathbf{u}}_{ij} \cdot \hat{\mathbf{t}}_i, \quad (2.55)$$

which represents the tangential influence coefficient of the j^{th} panel on the i^{th} panel. The influence coefficient is determined by prescribing the strengths of the vortex panels $\hat{\gamma}_i = 1$, resulting in an induced velocity $\hat{\mathbf{u}}_{ij} = (\hat{u}, \hat{v})_{ij}$ for a unit strength panel.

Figure 2.12a shows the discretization of the body into panels in the global coordinates system, defined by (x, y) , where each panel is rotated by an angle α_i w.r.t to the global coordinate system. Rotating the axis (x, y) by α_i , we arrive at the local panel coordinate system (x', y') , as shown in Figure 2.12b. Katz and Plotkin [36] showed that, the induced velocity of the vortex panels are calculated in the local panel coordinate system, where the



(a) Panel discretization of the body in the global cartesian coordinates system (x, y) with the local panel coordinates system rotated by α_i .

(b) Constant-Strength Vortex panel in the local panel coordinate system (x', y') inducing the velocity $\mathbf{u}' = (u', v')$ on the point P .

Figure 2.12: The two coordinate system of the panel method problem. The figure depicts **(a)** the global panel coordinate system, and **(b)** the local panel coordinate system, as defined by Katz and Plotkin [36].

induced velocity of the vortex panel j on the collocation point i (in the panel coordinate system) is given as,

$$u'_{ij} = \frac{\gamma_j}{2\pi} \left[\tan^{-1} \frac{y'_i - y'_{j,2}}{x'_i - x'_{j,2}} - \tan^{-1} \frac{y'_i - y'_{j,1}}{x'_i - x'_{j,1}} \right], \quad (2.56a)$$

$$v'_{ij} = -\frac{\gamma_j}{4\pi} \ln \frac{(x'_i - x'_{j,1})^2 + (y'_i - y'_{j,1})^2}{(x'_i - x'_{j,2})^2 + (y'_i - y'_{j,2})^2} \quad (2.56b)$$

where $(x'_1, y'_1)_j$ and $(x'_2, y'_2)_j$ are the coordinates of the panel start and end points in its local panel coordinate system, as shown in Figure 2.12b. The transformation of this vector (u'_{ij}, v'_{ij}) to the global coordinates is given as,

$$\begin{bmatrix} u_{ij} \\ v_{ij} \end{bmatrix} = \begin{bmatrix} \cos \alpha_j & \sin \alpha_j \\ -\sin \alpha_j & \cos \alpha_j \end{bmatrix} \cdot \begin{bmatrix} u'_{ij} \\ v'_{ij} \end{bmatrix} \quad (2.57)$$

corresponding to a rotation of α , as shown in Figure 2.12a.

If we are dealing with multiple panel bodies (i.e. multiple geometries), as seen in Figure



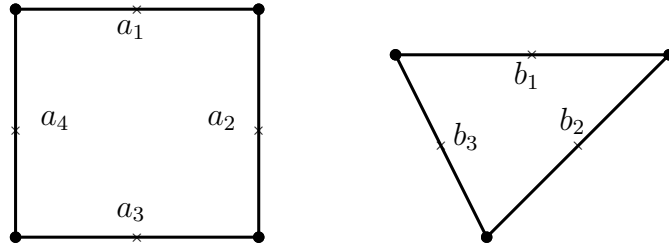


Figure 2.13: Multi-body panel problem: two bodies with different numbers of panels. The figure depicts a square body with 4 panels (a_1, a_2, a_3, a_4), and a triangular body with 3 panels (b_1, b_2, b_3).

2.13, the panel problem can be solved by constructing a global influence matrix,

$$\underbrace{\begin{pmatrix} c_{a_1 a_1} & \cdots & c_{a_1 a_N} & c_{a_1 b_1} & \cdots & c_{a_1 b_M} \\ \vdots & \ddots & \vdots & \vdots & \ddots & \vdots \\ c_{a_N a_1} & \cdots & c_{a_N a_N} & c_{a_N b_1} & \cdots & c_{a_N b_M} \\ c_{b_1 a_1} & \cdots & c_{b_1 a_N} & c_{b_1 b_1} & \cdots & c_{b_1 b_M} \\ \vdots & \ddots & \vdots & \vdots & \ddots & \vdots \\ c_{b_M a_1} & \cdots & c_{b_M a_N} & c_{b_M b_1} & \cdots & c_{b_M b_M} \\ \Delta s_{a_1} & \cdots & \Delta s_{a_N} & 0 & \cdots & 0 \\ 0 & \cdots & 0 & \Delta s_{b_1} & \cdots & \Delta s_{b_M} \end{pmatrix}}_{\left(\begin{matrix} C_{aa} & C_{ab} \\ C_{ba} & C_{bb} \\ \Delta s_a & 0 \\ 0 & \Delta s_b \end{matrix} \right)} \underbrace{\begin{pmatrix} \gamma_{a_1} \\ \vdots \\ \gamma_{a_N} \\ \gamma_{b_1} \\ \vdots \\ \gamma_{b_M} \end{pmatrix}}_{\left(\begin{matrix} \gamma_a \\ \gamma_b \end{matrix} \right)} = \underbrace{\begin{pmatrix} \text{RHS}_{a_1} \\ \vdots \\ \text{RHS}_{a_N} \\ \text{RHS}_{b_1} \\ \vdots \\ \text{RHS}_{b_M} \\ \Gamma_{\gamma,a} \\ \Gamma_{\gamma,b} \end{pmatrix}}_{\left(\begin{matrix} \text{RHS}_a \\ \text{RHS}_b \\ \Gamma_{\gamma,a} \\ \Gamma_{\gamma,b} \end{matrix} \right)} \quad (2.58)$$

where the matrices (C_{aa} , C_{bb}), are the self-induction matrices of each of the single vortex panel problem. The non-diagonal terms (C_{ab} , C_{ba}) are the inter-induction matrices containing the panel influence of body b on body a and body a on body b , respectively. The final two rows of the LHS matrix contain the circulation constraint for each body, defined by equation 2.53.

2.6 Evolution of the Lagrangian method

The algorithm of the full Lagrangian method is summarized in this section. The full or complete Lagrangian method is the coupled vortex blobs and the vortex panels. Note that for our hybrid scheme, the panel does not act as the source of the vorticity in the Lagrangian method (which is done by the Eulerian method), but instead simply enforces the *no-slip* boundary condition for the vortex blobs.

The flowchart of one time step of the Lagrangian method is given by Figure 2.14. The algorithm to the Lagrangian method can be summarized as follows:

1. **Solve for panels:** Determine the strengths of the vortex panels γ , such that the no-slip boundary condition at the collocation points of the vortex panels is enforced.

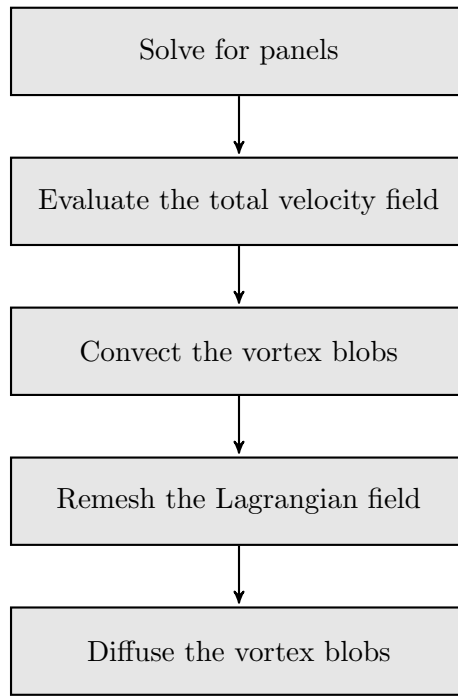


Figure 2.14: Flowchart of the Lagrangian method. The flowchart shows coupling between vortex panels and vortex blobs to evolve from t_n to t_{n+1} (without taking into account of the vorticity generation at the boundary).

When determining the strengths, we also have to ensure that the total circulation of the vortex panels satisfies the conservation of circulation, equation 2.50, which we investigate during the hybrid coupling, section 4.2.3.

2. **Evaluate the total velocity field:** Evaluate the total velocity field \mathbf{u} , which is the sum of velocity field induced by the vortex blobs \mathbf{u}_ω , the velocity field induced by the vortex panels \mathbf{u}_γ , and the free-stream velocity field \mathbf{u}_∞ .
3. **Convect the vortex blobs:** Use the velocity field to convect the vortex blobs from t_n to t_{n+1} to the new position.
4. **Remesh the Lagrangian field:** Remesh the vortex blobs onto a structured square lattice using the M'_4 interpolation kernel.
5. **Diffuse the vortex blobs:** Diffuse the vortex blobs using the Δt_d diffusion time step, by modifying the strengths of the vortex blobs according to Wee's WRS or Tutty's TRS method.

The generation of the vorticity is dealt with in the Eulerian subdomain, which is explained in chapter 3. The vorticity is then transferred into the Lagrangian domain using the Hybrid coupling scheme, which was summarized in the introduction, chapter 1, and fully elaborated in chapter 4.



2.7 Validation of Lagrangian method

In this chapter, we have investigated the Lagrangian component of the Hybrid method. The Lagrangian method is used to just evolve the vorticity field, whereas the Eulerian method is used to properly formulate the vorticity generation at the boundary. The resolved boundary solution of the Eulerian method is then transferred onto our Lagrangian method. Therefore, the Lagrangian method that is implemented here does not require the generation of the vorticity from the boundary.

Thus, during the validation of the Lagrangian method, we focus on two test cases: Potential flow around a cylinder and Lamb-Oseen vortex evolution. The potential flow around a cylinder test case is used to verify and validate the vortex panel solver that is used enforcing the no-through flow for the vortex blobs. The Lamb-Oseen vortex evolution test cases is used to verify and validate the convection method and the diffusion methods implemented for the evolution of the vortex blobs.

Note that to investigate the coupling of the vortex blobs and the vortex panels, we require the proper definition of the vorticity flux from the boundary, requiring the Eulerian method as well. Therefore, the handling of the vorticity flux is investigated in fully coupled method, in chapter 6.

2.7.1 Error Analysis of Vortex Panels

The vortex panels was verified and validated on the test case of the potential flow around a cylinder. To test the convergence of the solution of the vortex panels, a comparison was made with the analytical solution for the parameters in table 2.1.

An example of the numerical solution is shown in Figure 2.15. The figure shows the magnitude of the velocity $\|\mathbf{u}\|$, and it shows the velocity field of the potential flow solution, with an infinitely thin boundary layer, stagnating to zero velocity inside the body.

The jagged velocity field around the surface of the cylinder is simply due to the sampling resolution of the field. For a higher sampling resolution this will vanish. In order to determine the accuracy of the solution, the velocity field of the panel solution was compared with the analytical solution. The analytical velocity field around a cylinder is given in cylindrical coordinate centered in the cylinder as,

$$u_r = u_\infty \left(1 - \frac{R^2}{r^2} \right) \cos \theta, \quad (2.59a)$$

$$u_\theta = -u_\infty \left(1 + \frac{R^2}{r^2} \right) \cos \theta, \quad (2.59b)$$

Table 2.1: Panel study parameters

Parameters	Value	Description
R	1 m	Radius of cylinder
u_∞	1 m s ⁻¹	Free-stream velocity
N_{panels}	100	Number of panels

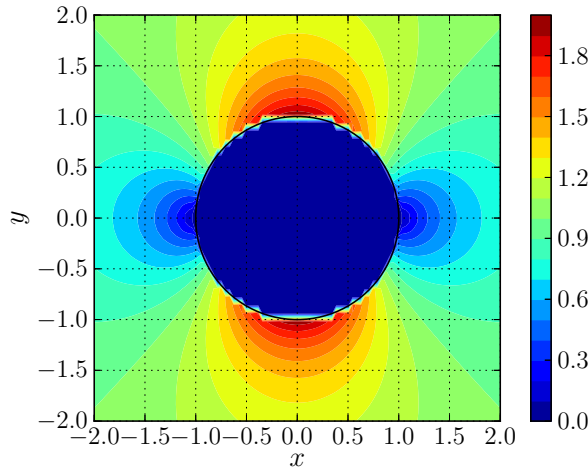
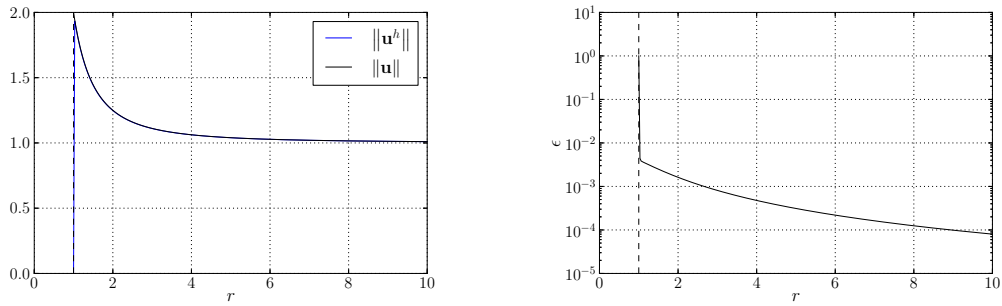


Figure 2.15: Panel method solution: the potential velocity field around a unit cylinder with $R = 1$, $\mathbf{u}_\infty = (1, 0)$, and $N_{\text{panels}} = 100$. The figure depicts the magnitude of velocity field $\|\mathbf{u}\|$, with a zero velocity inside the body.



(a) Comparison of the velocity field.

(b) Error in the velocity field

Figure 2.16: Comparison of the velocity field along the y -axis, $y = 0$ to $y = 10$. Figure (a) shows both the solutions, the numerical $\|\mathbf{u}^h\|$ [—, solid blue] and the analytical solution [—, solid black]. Figure (b) shows the relative error ϵ in velocity between the solution, given by equation 2.60.

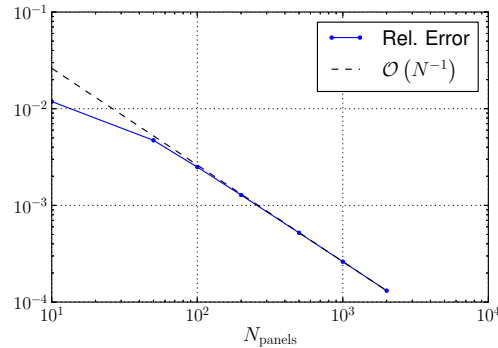


Figure 2.17: Convergence plot of the Constant-Strength Straight Vortex panels. The figures depicts the converges of the relative error ϵ at an $\mathcal{O}(N^{-1})$.



where u_r and u_θ are the radial and the angular velocity respectively for a given free-stream velocity u_∞ . Equation 2.59 is a function of the distance to the center of the cylinder r and the radius of the cylinder R and is valid for $r \geq R$

The velocity field of the vortex panel was compared with the analytical solution along the y-axis from $y = 0$ to $y = 10$. Figure 2.16a plots the magnitude of analytical velocity $\|\mathbf{u}\|$ and the vortex panel velocity field $\|\mathbf{u}^h\|$. Comparing the solutions of the plot we see that the solution of the vortex panels and the analytical potential flow solution matches everywhere except at the surface. This happens because the potential flow solution has a slip velocity (i.e non-zero velocity) at the surface of the body, whereas the vortex panels solves for a no-slip boundary condition at the collocation points of the surface. This explains the sudden drop of the velocity from $\|\mathbf{u}\| = 2$ to $\|\mathbf{u}\| = 0$ at the surface.

Figure 2.16b shows the relative error ϵ between the numerical and the analytical solutions,

$$\epsilon = \frac{\|\mathbf{u} - \mathbf{u}^h\|}{\|\mathbf{u}\|} \quad (2.60)$$

where \mathbf{u} is the analytical solution and the \mathbf{u}^h is the numerical solution. Ignoring the solution right at the surface ($r = R$), we see that the error between the numerical and the analytical solution reduces from $\epsilon = 5 \times 10^{-3}$ to $\epsilon = 8 \times 10^{-5}$ as we go from $r = 1$ to $r = 10$. This behavior of the error tells us that the solution of the constant-strength vortex panels gets more accurate as we go further away from the panels; right next to the panels, we have the largest error.

The convergence analysis of the vortex panels was done by determining the error of the vortex panel velocity field w.r.t to the analytical solution for the number of panels $N = 10$ to $N = 1000$, Figure 2.17. The error of the velocity field was computed at $(x = 0, y = 1.5)$, and we see that the error converges at with $\mathcal{O}(N)$. This validates that the vortex panel that we have used is a 1st order vortex panel.

2.7.2 Error Analysis of Vortex Blobs

In order to verify and validate the vortex blobs, we simulate the evolution of a Lamb-Oseen vortex. The results of the simulation were used to compare against the analytical ones, which we used to determine the accuracy of our vortex blobs.

The Lamb-Oseen vortex is a solution of the Navier-Stokes equation, corresponding to the viscous evolution of a laminar vortex core on an unbounded domain, first derived by Lamb and Oseen [61]. The vorticity distribution ω of the core at a given time is defined as,

$$\omega(\mathbf{x}, \tau) = \frac{\Gamma_c}{4\pi\nu(t + \tau)} \exp\left(-\frac{r^2}{4\pi\nu(t + \tau)}\right), \quad (2.61)$$

and is a function of core strength Γ_c , the simulation time $t \in [0, \infty[$ and distance from the core center r . The constant τ in the equation 2.61 defines to initial width of the Lamb-Oseen vortex, where if $\tau = 0$, we have Dirac delta distribution.

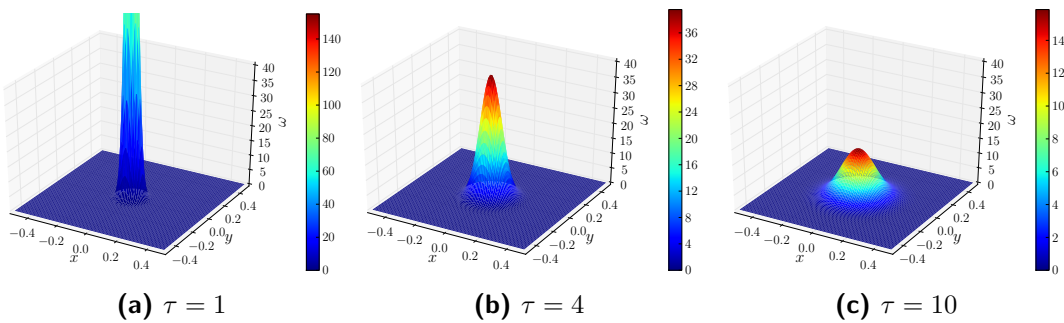


Figure 2.18: The vorticity ω distribution of the Lamb-Oseen vortex problem with $\Gamma_c = 1$ and $\nu = 5 \times 10^{-4}$ in the domain $[-0.5, 0.5] \times [-0.5, 0.5]$. The figure depicts distribution for various initial time constant τ , determining the peakiness of the distribution.

The velocity field, corresponding to equation 2.61, in cylindrical coordinate is defined as,

$$u_\theta = \frac{\Gamma_c}{2\pi r} \left[1 - \exp\left(-\frac{r^2}{4\pi\nu(t+\tau)}\right) \right] \quad (2.62a)$$

$$u_r = 0 \quad (2.62b)$$

where u_θ is the circumferential velocity, and u_r , the radial velocity is zero. Figure 2.18 shows the vorticity distribution ω for various initial time constant τ . We see that for small τ , the distribution approaches a Dirac delta distribution. Therefore, for this investigation we decided on $\tau = 4$ ensuring a non-peaky distribution, which was also investigated by Barba [2]. Therefore the literature of Barba [2] will serve as the validation data for our Lamb-Oseen investigation.

The Lagrangian method was applied to the Lamb-Oseen vortex test case with parameters tabulated in table 2.2. The vorticity field was discretized over the domain $[x, y]$ - domain $[-0.5, 0.5] \times [-0.5, 0.5]$. This was adequate as the circulation outside this domain was less than the threshold $\Gamma_{loc} \leq 10^{-14}$. The spatial discretization was performed according to the standard initialization method of vortex blobs, described in section 2.2.4.

However as explained in section 2.2.4, we have to take in account of the Gaussian blurring of the original vorticity field due to the initialization process. This poses a problem when evaluating the error between the numerical and the analytical solution. This problem has also been encountered by Barba [2], when investigating the Lamb-Oseen vortex. The solution to the problem was to apply a “time-shift correction”, to compensate for the Gaussian blurring, solving the problem of this very particular discretization of the Navier-Stokes equation. Therefore, this is a special method and this approach can only be used for the Lamb-Oseen vortex problem.

The “time-shift correction” is derived by determining the diffusion effect caused by the discretization of the diffusion equation using the Gaussian vortex blobs (with $k = 2$). Barba [2], determined that the discretization of the diffusion equation (i.e. the Lamb-Oseen vortex) reconstructs the vorticity field that has been diffused by a time $\sigma^2/2\nu$. So when initializing the particles with a certain strength, we will have to reverse the time



by $\sigma^2/2\nu$. Thus, the corrected initial particles strengths α_i^o of vortex blobs from the Lamb-Oseen vorticity field is given as,

$$\alpha_i^o = \omega_i^o \cdot h^2 = \left\{ \frac{\Gamma_c}{4\pi\nu(t + \tau - \sigma^2/2\nu)} \exp \left[-\frac{r_i^2}{4\nu(t + \tau - \sigma^2/2\nu)} \right] \right\} \cdot h^2. \quad (2.63)$$

This method was used to investigate the error evolution of the vortex blob method. The vortex blobs where convected according to the procedures in section 2.3. The diffusion of the vortex blobs was performed using the schemes described in section 2.4. We investigated the accuracy of the Tutty's scheme (TRS) and Wee-Ghoniem scheme (WRS) in section 2.7.2. For the general investigation however, we employed the Tutty's diffusion method. The advantage of this approach is that we can perform diffusion after every convection step. This makes the method less prone to time integration error and eliminates any discontinuous behavior in the evolution. We will see that when coupling the Lagrangian method and Eulerian method, discontinuity in the problem introduces additional errors.

The convection and diffusion was performed according to the time integration parameters tabulated in table 2.2. The vortex blobs where convected using a 4th-order Runge-Kutta method (RK4) for a high order time integration. After the convection sub-steps, the Lagrangian distortion was treated using the remeshing scheme discussed in section 2.3.1. Generally, the remeshing is typically done every 10 iterations [2]. However, as our diffusion scheme and hybrid method requires structured lattice of vortex blobs for efficient calculations, we will remesh after every step, $f_{redist} = 1$.

In addition to the evolution of the vortex blobs, we performed a population control to minimized the number of vortex blobs, as described by Barba [2]. The Population Control (PC) removes vortex blobs that have very small circulation strengths. After the diffusion

Table 2.2: Summary of the parameters for the Lamb-Oseen vortex evolution. This table shows also the parameters of Tutty's diffusion method

Parameters	Value	Unit	Description
Γ_c	1	$\text{m}^2 \text{s}^{-1}$	Core strength
Ω	$[-0.5, 0.5] \times [-0.5, 0.5]$	m	Initial particle domain
\mathbf{u}_∞	0	m s^{-1}	Free-stream velocity
ν	5×10^{-4}	$\text{kg s}^{-1} \text{m}^{-1}$	Kinematic viscosity
τ	4	s	Lamb-Oseen time constant
t	0 to 1	s	Simulation time
$\Delta t_c = \Delta t_d$	0.01	s	Diffusion and convection time step size
N_t	100	-	Number of time integration steps
σ	0.01	m	Vortex blob core size
λ	1	-	Overlap ratio
k	2	-	Gaussian kernel width spreading
f_{redis}	1	-	Redistribution frequency
f_{pc}	1	-	Population control frequency
$(\Gamma_{loc}, \Gamma_{glob})$	$(1 \times 10^{-14}, 1 \times 10^{-14})$	$\text{m}^2 \text{s}^{-1}$	Population control thresholds

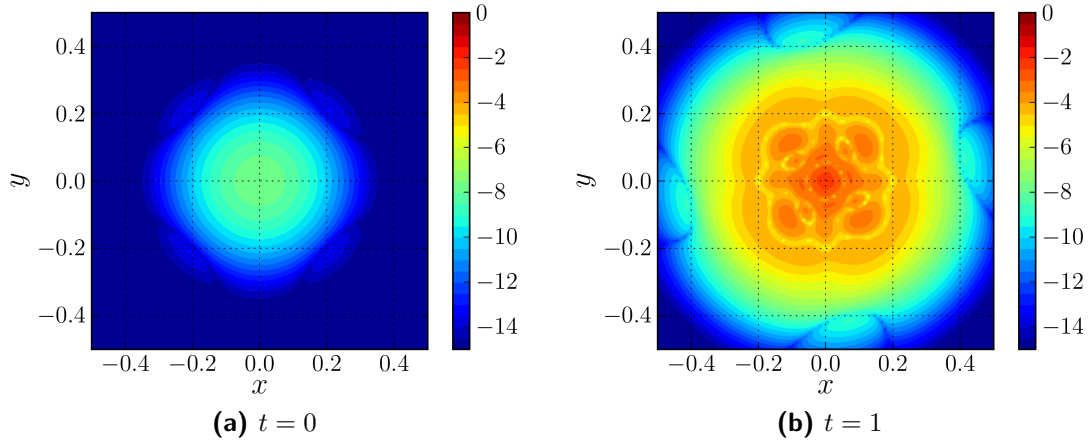


Figure 2.19: Relative error growth of Lamb-Oseen vorticity during the evolution (in logarithmic scale) using the parameters tabulated in table 2.2. The figure shows (a), the initial relative error at $t = 0$, and (b) the final relative error in vorticity at $t = 1$.

and remeshing, we will be left with vortex blobs with strengths close to the numerical precision, as they have minimal impact on the accuracy of the vorticity field, we can remove them. When performing population control, we need to ensure that the loss of total circulation is below the acceptable global threshold, Γ_{glob} . We used $\Gamma_{glob} = 10^{-14}$ as used by Barba [2] for the similar investigation.

To verify whether our Lagrangian scheme is performs according to theory, we evaluated the error evolution of the simulation. Figure 2.19, shows the initial and the final relative error in vorticity. We see that initially we have a maximum relative error around 10^{-8} , located at the center of the Lamb-Oseen core. After 100 time integration steps from $t = 0$ to $t = 1$, we see that the maximum relative error in vorticity increases from 10^{-8} to 10^{-2} . The errors of the vorticity are predominantly localized at the center of the core, where we have maximum vorticity, Figure 2.19.

Figure 2.20, shows the maximum relative error, equation 2.64, and the L^2 -norm, equation 2.65, error evolution of vorticity and velocity from $t = 0$ to $t = 1$. Similar investigation was performed by Barba [2] and Speck [58]. Due to the relation of the vorticity and the velocity, equation 2.1, the error of the vorticity is higher than the error in the velocity. The figure shows both the maximum relative error, and the error in the L^2 – norm. The maximum relative error (e.g. for vorticity), is defined as,

$$\|\omega^{\text{exact}} - \omega^{\text{discrete}}\|_{\infty} = \frac{\max\{|\omega^{\text{exact}} - \omega^{\text{discrete}}|\}}{\max\{|\omega^{\text{exact}}|\}}, \quad (2.64)$$

where ω^{exact} is the analytical vorticity field, equation 2.61, and ω^{discrete} is the numerical vorticity field from the vortex blobs. The error in the L^2 – norm of the vorticity is calculated as

$$\|\omega^{\text{exact}} - \omega^{\text{discrete}}\|_2 = \left(\sum_i^N |\omega^{\text{exact}} - \omega^{\text{discrete}}|^2 \cdot h^2 \right)^{\frac{1}{2}}, \quad (2.65)$$



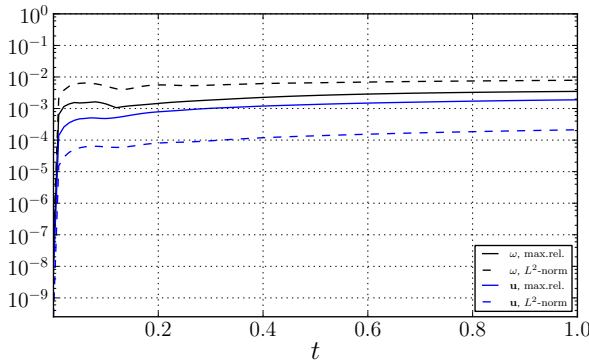


Figure 2.20: Relative error growth of Lamb-Oseen vortex during the evolution from $t = 0$ to $t = 1$ using the parameters in table 2.2. This figure depicts the error in vorticity: maximum relative error [—, solid **black**], and the error in L^2 – norm [- -, dashed **black**]; and error in velocity: maximum relative error [—, solid **blue**], and error in L^2 – norm [- -, dashed **blue**].

and the error in velocity is calculated using the same principle. Investigating the figure, we see that after the first iteration, there is a sudden increase in the error, but as time progresses the error growth reduces. From literature, we see that this trend has also been observed by Barba [2] and Speck [58]. For comparison, we used similar parameters, and we observe that the sudden jump in error is similar to the literature.

Comparison of Diffusion Schemes: WRS vs. TRS

To observe how both the diffusion schemes compare, we ran the same test case with both diffusion schemes. From the simulation, we were able to observe that Tutty’s diffusion scheme (TRS), produced less error than Wee’s approach (WRS).

Figure 2.21 shows the evolution of maximum relative error in vorticity, equation 2.64 for both diffusion schemes. Figure 2.21a shows the evolution of error for convective time step size $\Delta t_c = 0.01$. The diffusion scheme TRS enables us to perform diffusion in conjunction with the convection, $\Delta t_d = \Delta t_c = 0.01$. This was possible due to the favorable constraint on the diffusion time step, equation 2.41.

The Wee’s diffusion scheme WRS, however is constraint by equation 2.30 and equation 2.31. Therefore the diffusion time step Δt_d for the given convective time step $\Delta t_c = 0.01$ is $\Delta t_d = k_d \cdot \Delta t_c = 0.07$, where the diffusion frequency $k_d = 7$. We observe from the figure that performing diffusion at every other instant creates an oscillatory behavior. This behavior is not ideal when coupling with the Eulerian method as the oscillatory diffusion of the VPM will add additional error in coupling.

However, when modifying the convective time step to $\Delta t_c = 0.05$, Figure 2.21b, we observe that the error of WRS matches the TRS. At this convective time step Δt_c , the WRS has a diffusion time step size $\Delta t_d = k_d \cdot \Delta t_c = 0.05$, where the diffusion frequency $k_d = 1$ now. Therefore, the WRS performs diffusion at every step and we see that WRS performs similarly to TRS.

The conclusion to this investigation is that WRS is useful if we are able to match the convective time step Δt_c to the diffusion time step Δt_d . However, this may not be

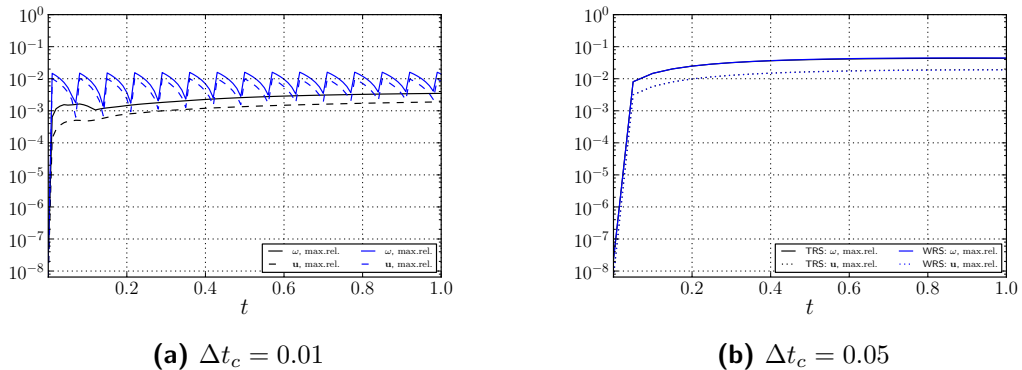


Figure 2.21: Comparison of Tutty's scheme TRS, and Wee-Ghoniem scheme WRS for treating diffusion, depicting the evolution of maximum relative error in vorticity, equation 2.64 from $t = 0$ to $t = 1$. The Figure (a) shows TRS performing diffusion at every step, $\Delta t_d = \Delta t_c = 0.01$ and WRS performing diffusion at every 7th step, $\Delta t_d = k_d \cdot \Delta t_c = 7 \times 0.01$; (b) shows TRS performing diffusion at every step, $\Delta t_d = \Delta t_c = 0.05$ and WRS performing diffusion at every step, $\Delta t_d = k_d \cdot \Delta t_c = 1 \times 0.05$.

possible for high Reynolds number flows where the convective time step is critical. The TRS outperforms WRS in this regard and should produce less error when coupling with the Eulerian method.

2.7.3 Convergence Study of the Viscous Vortex Method

Finally, we can perform a converge study, to validate that our scheme works according to the theory. For a scheme that is numerically stable, the error due to discretization must converge as the resolution of the discretization increases.

First, we investigate the convergence for spatial discretization. As we are dealing with vortex blobs, there are multiple ways of increasing the resolution. The straightforward method would be to increase the density of particles in a given area, i.e. reduce the blob spacing h and maintaining the core spreading σ . Figure 2.22a shows the convergence of

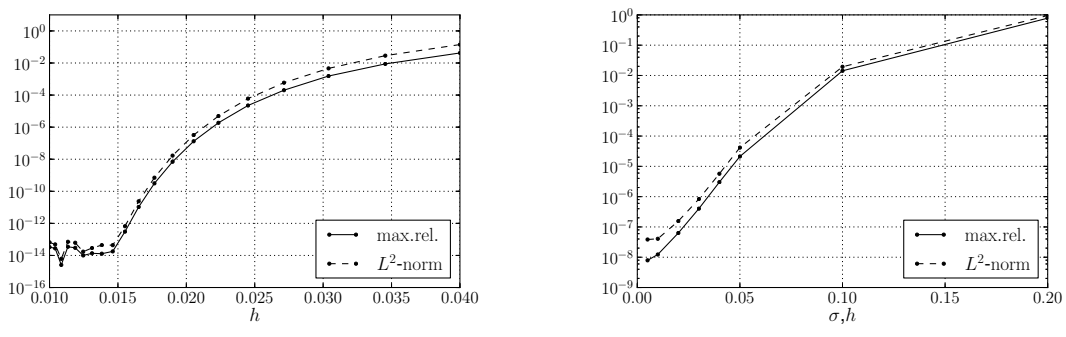


Figure 2.22: Convergence in spatial discretization of the vortex blobs. Figure (a) shows the convergence by fixing the core size σ and (b) shows the convergence when overlap ratio $\lambda = h/\sigma = 1$.



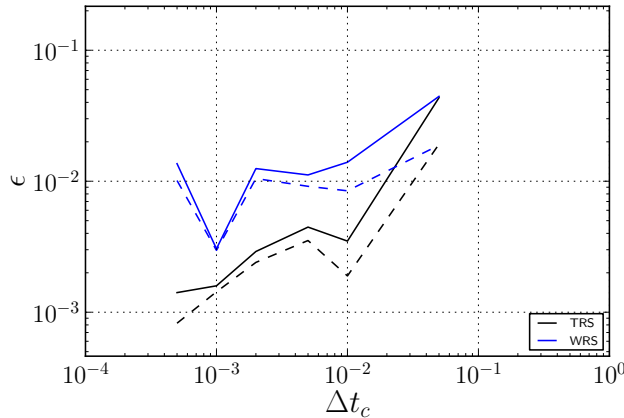


Figure 2.23: Convergence of the error in velocity [—, solid] and the error in vorticity [---, dashed] due to temporal discretization of the vortex blobs. The figure compares the convergence rate of TRS (black) vs. WRS (blue)

the spatial discretization when the core size σ is maintained at $\sigma = 0.02$. For this case, the overlap ratio changes with the blob spacing, described by equation 2.20. For small blob spacing h , the error in vorticity quickly drops to near machine precision. When investigating the order of convergence, we see that the error converges in a non-linear fashion and similar results have been obtained by Barba [2].

Figure 2.22b, shows the convergence of the error when the overlap ratio is fixed, $\lambda = 1$. In this test case, the core size scaled with the blob spacing, $h = \sigma$, and when increasing the spatial resolution, the error converges non-linearly.

To investigate the convergence in temporal discretization, we determined the evolution of the maximum relative error in vorticity, equation 2.64, at $t = 1$ for various convective time step sizes Δt_c , shown in Figure 2.23. At $t = 1$, we see that the error reduces as we increase the temporal resolution meaning that we have a convergent scheme. We also observe that the error produced by WRS is higher than TRS and that it converges at a lower order than TRS. This again validates that TRS performs better than the WRS as it produces less error.

2.8 Summary

In summary, we have investigated the Lagrangian subdomain of our hybrid method in this chapter. The Lagrangian method was used to described the evolution of the wake past the geometry. Vortex Particle Method (VPM) was an ideal choice to describe the wake, as we require only to evolve the wake, and the generation of the vorticity is dealt with in the Eulerian subdomain. Unlike the Eulerian method, VPM only required the fluid elements where there was vorticity, meaning that the VPM was inherently auto-adaptive. Using the Population Control method, we were able to remove vortex blobs where they were not needed. Furthermore, the computation of the these elements were accelerated using an FMM, and simultaneously was parallelized using a GPU hardware.

In section 2.1, an introduction to the VPM was given. We determined advantage of the

Lagrangian method w.r.t to the Eulerian method for resolving the wake for the VAWT. The velocity-vorticity formulation of the Navier-Stokes equations is the governing equation of the VPM and we investigated the viscous splitting algorithm in section 2.1.3.

The viscous splitting algorithm enabled to perform diffusion and convection of the fluid is segregated steps. The discretization of the fluid through vortex blobs was investigated in section 2.2. These fluid elements has non-zero core size, removing the singularity when performing Biot-Savart calculations.

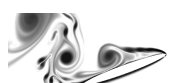
In section 2.2.4, we investigate the initialization of the vortex blobs. The proper initialization of the vortex blobs is a key factor for accurate coupling of Lagrangian method and the Eulerian method. The strengths of these particles is initialized by assigning the local circulation strength to the particle, as in equation 2.21. When the coupling is performed, it will be seen that the Gaussian blurring of the original vorticity field during the initialization is the fundamental source of error, section 4.2.2. Strategies such as Beale's iterative method, cannot be used as it is defined for an unbounded domain. The only approach found to minimize the Gaussian spreading initialization error is to increase the overlap ratio to $\lambda = 1$, and minimize the blob spacing h as much as possible, while keeping the computational effort to an acceptable level. The optimal strategy for the initialization of the vortex blob strengths is still an open question, and if solved can significantly improve the accuracy and the efficiency of the hybrid coupling.

In section 2.3, we investigated the convection of the vortex blobs. The convection is performed using a 4th-order Runge-Kutta time integration method. However, due to high strains in the fluid, the Lagrangian grid distortion of the vortex blob lattice has to be dealt with, section 2.3.1. For this reason, we used a M'_4 interpolation kernel that remeshed the particles onto a structured grid.

In section 2.4, we investigated two diffusion models for the vortex blobs. The WRS diffusion model developed by Wee and Ghoniem [65], integrated the diffusion process into the standard interpolation kernel. This reduces computation cost, however the model was unfavourable constraint on the diffusion time step size, equation 2.31. The constraint limits the minimum diffusion step size and results in a discontinuous diffusion in time, as shown in Figure 2.21a. To overcome this problem, we used the TRS diffusion model by Tutty [62], which enabled us to perform diffusion after every convection step, section 2.4.2. This also ensured that the diffusion process was continuous, which was important when performing the coupling algorithm.

In section 2.5, we investigated the handling of the *no-slip* boundary conditions for the viscous VPM. The boundary integral equations was used to enforces the wall boundary conditions in the Lagrangian method. We used the Constant-Strength Vortex panels, based on Katz [36], to discretize the integral equations. The panel method was then verified and validated with the analytical solution of a potential flow around a cylinder in section 2.7.

In section 2.7, we also verified and validated the implementation of the vortex blobs to analytical solution of the Lamb-Oseen vortex problem. We determined the evolution of the error for various spatial discretization and temporal discretization. The validation concluded that the implementation performed according to the literature, see example Barba [2].



2.9 Chapter Nomenclature

Latin Symbols

A	Vortex panel influence matrix	-
c^2	Diffusion parameter	-
\mathcal{E}	Enstrophy	$\text{m}^2 \text{s}^{-2}$
f_{pc}	Population control frequency	-
f_{redis}	Redistribution frequency	-
h	Nominal particle spacing	m
h_ν	Characteristic diffusion distance	m
k	Gaussian kernel width spreading	-
k_d	Frequency of vortex blob diffusion	-
K	Biot-Savart kernel	-
K_σ	Vortex blob kernel	-
$\hat{\mathbf{n}}$	Unit normal vector	-
N	Number of vortex blobs (particles)	-
λ	Overlap ratio	-
p	Pressure	Pa
r	Radial position	m
$\hat{\mathbf{s}}$	Unit tangent vector	-
t	Simulation time	s
u	Velocity	m s^{-1}
\mathbf{u}_b	Velocity of the body	m s^{-1}
\mathbf{u}_γ	Vortex sheet induced velocity	m s^{-1}
\mathbf{u}_{ext}	External induced velocity	m s^{-1}
\mathbf{u}^h	Discrete velocity	m s^{-1}
\mathbf{u}_∞	Free-stream velocity	m s^{-1}
\mathbf{u}_ϕ	Free-stream velocity	m s^{-1}
u_r	Radial velocity	m s^{-1}
u_θ	Angular velocity	m s^{-1}
\mathbf{u}_{slip}	Boundary slip velocity	m s^{-1}
\mathbf{u}_ω	Vorticity velocity	m s^{-1}
W	Interpolation kernel weight	-
\mathbf{x}	Position vector	m
\mathbf{x}_ν	Position vector of particle to be diffused	m
\mathbf{x}_p	Position vector of vortex blob (particle)	m

Greek Symbols

α_p	Circulation of the particle	$\text{m}^2 \text{s}^{-1}$
------------	-----------------------------	----------------------------

Δt_c	Convection time step size	s
Δt_d	Diffusion time step size	s
ϵ	Relative error	-
Γ	Circulation	$m^2 s^{-1}$
Γ_{glob}	Particle circulation threshold	$m^2 s^{-1}$
Γ_{glob}	Total circulation threshold	$m^2 s^{-1}$
ν	Kinematic viscosity	$m^2 s^{-1}$
ω	Vorticity	s^{-1}
$\tilde{\omega}$	Vortex blob cell vorticity	s^{-1}
ω^h	Discrete vorticity field	s^{-1}
Ω	Fluid domain	m
ρ	Density	$kg m^{-3}$
σ	Core size	m
τ	Lamb-Oseen time constant	s
ξ	Scale relative position of particle to stencil node	-
ζ_σ	Smooth cut-off function of the blobs	-



Chapter 3

Eulerian Subdomain: Finite Element Method

Standard Computation Fluid Dynamics ([CFD](#)) methods discretize the fluid into smaller grids, and solve the set of Navier-Stokes equations in these region. Eulerian methods uses this type of formulation.

For the hybrid method, we use the Navier-Stokes Eulerian formulation in the near-body region. The advantage of using this formulation in this region is that it is much more efficient in resolving boundary layers than the Vortex Particle Method ([VPM](#)). We can directly enforce the wall boundary condition at the wall boundary of the Eulerian subdomain, solving the problem of vorticity generation of the body.

The most common approaches to solve the fluid dynamics problem on an Eulerian reference frame are Finite Volume Method ([FVM](#)), Finite Difference Method ([FDM](#)), and Finite Element Method ([FEM](#)). FVM divides the domain into volumes where it enforces the conservation of mass and momentum in each grid. FDM divides the domain into nodes and uses local Taylor expansions to approximate the partial differential equations. FEM divides the domain into elements and solves the problem using variational calculus.

For the current study, we have decided to use the FEM package provided by the FEniCS project as it has implemented efficient, multi-threaded algorithms for setting up and solve a finite element problem. Furthermore, it provides extensive features for future developments such as adaptive mesh refinement, deformable meshes, and efficient computation of turbulent flow.

3.1 Introduction to the Finite Element Method

The Finite Element Method ([FEM](#)) is a numerical method to obtain approximations to partial differential equations. The equations are solved by writing them as a variational problem, giving us an approximate solution for the boundary value problem [7]. Therefore the FEM approximates the unknown functions and converts the partial differential



equations into a set of algebraic equations, which makes them suitable to be solved numerically. It was traditionally used for solid mechanics (e.g for the analysis of aircraft structures [50]), but have since been used to solve fluid dynamics problems [31, 34, 32].

3.1.1 Finite Element Discretization

The finite element method solves a problem by dividing the domain of interest into smaller cells known as *elements*. These *elements* are connected at the vertices which are called nodes or nodal points. We use these sets of nodes and elements to represent the variation in the field such as the displacement, the velocity, the pressure or the temperature using simple functions, known as basis functions. Thus, we have transformed the problem of interest into a finite number of Degrees of Freedom (DOF). We combined the set of equations of the elements into a global system of equations to solve for the unknowns.

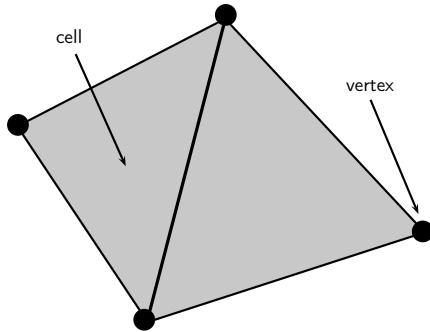


Figure 3.1: A two-dimensional finite element geometry. The cell represents the area of the element, and vertices are the edges of the cell.

A finite element discretization in 2D can be seen in Figure 3.1. The figure shows two connected elements, where the cells represent the area of the element, and the vertices of the cell represents the nodes of the element. The set of all the cells $\mathcal{T}_h = \{T\}$ in the fluid domain Ω , constitutes the mesh of the Eulerian domain. In Figure 3.1, the cells of the finite element in 2D, are made of simple triangles. There are two approaches to discretize the domain: structured or unstructured meshes. The structured mesh has cells oriented

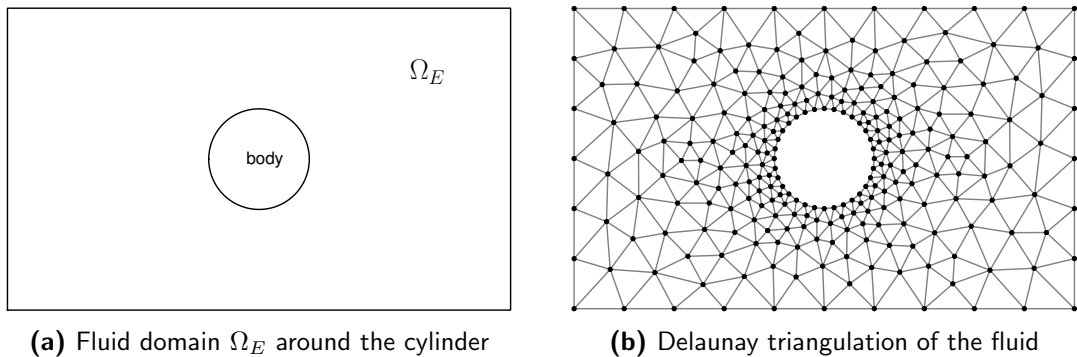


Figure 3.2: Delaunay triangulation of the fluid around a cylinder resulting in unstructured mesh with controllable cell sizes.

in a pattern, and is the simplest approach to construct the mesh. The advantage of such a discretization is that it is possible to make a simple data structure which can be used to perform efficient computations. The downside to such discretization is that it is very difficult to construct structured mesh in complex domains with several holes. However, the FEM enables us to perform an unstructured discretization of the domain, as shown in Figure 3.2. The figure shows the unstructured discretization of the fluid domain around the cylinder Ω_E , connecting the rectangular outer boundary of the fluid to the circular no-slip boundary of the body in a simple fashion. Although the unstructured approach gives rise to less efficient discretization, its geometrical flexibility has advantages that surpasses the disadvantage.

There are several algorithms for mesh generation. The standard approach is to employ the Delaunay triangulation method derived from the Voronoi diagram concept [9]. This divides the domain into a set of triangles, as shown in Figure 3.2. This type of mesh generation allows us to connect boundaries with difference shapes together.

3.1.2 Finite Element Functions and Function Spaces

The finite element is defined using a triplet $(T, \mathcal{V}, \mathcal{L})$, as defined in Ciarlet [14] and used in the FENiCS Project [44]. T is a tessellation of the domain Ω , the space $\mathcal{V} = \mathcal{V}(T)$ is a finite dimensional function space on T of dimension n , and $\mathcal{L} = \{\ell_1, \ell_2, \dots, \ell_n\}$ is the set of degrees of freedom forming the basis for the dual space \mathcal{V}' of \mathcal{V} .

Once we perform the tessellation, we can define the functions and the function spaces of the finite element problem. For each cell, a local function space \mathcal{V} can be defined to collectively construct the global function space V . Any given function $u \in V$ is expressed as a linear combination of basis functions $\{\phi_1, \phi_2, \dots, \phi_N\}$, of the function space V ,

$$u(x) = \sum_{j=1}^N U_j \phi_j(x). \quad (3.1)$$

There are several types of finite element families: the Brezzi-Douglas-Marini, the Crouzeix-Raviart, the Discontinuous Lagrange, the Hermite, and the Lagrange elements [44]. For the current study, we will rely on the Lagrange elements, also known as the Continuous Galerkin (CG), which are based on the Lagrange polynomials [11]. These elements are widely used and are the simplest to implement for our project.

Lagrange elements belong to the space H^1 , which is a Sobolev space containing functions u such that u^2 and $|\nabla u|^2$ have finite integral in the domain Ω [44]. The Lagrange element uses point evaluation for the degrees of freedom, where a DOF in (x_i, y_i) denotes the point evaluation of the function u , $\ell_i(u) = u(x_i, y_i)$. We can have Lagrange elements of various orders $q = 1, 2, \dots$, where q is the degree of the Lagrange polynomial \mathcal{P}_q . For the 2D case, the dimension n of the finite element is given as,

$$n(q) = \frac{1}{2}(q+1)(q+2). \quad (3.2)$$

For $q = 1$, we have a simple linear Lagrange element CG₁ or linear interpolant with 3 DOFs, known as the Courant triangle [22]. For a higher order finite element, we can set



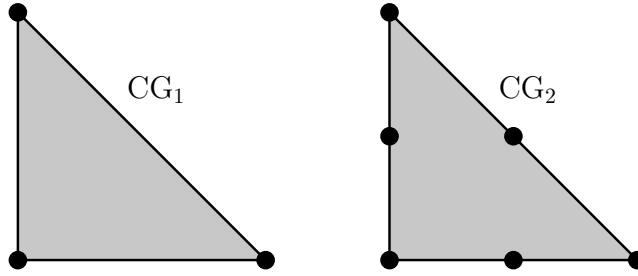


Figure 3.3: The Lagrange CG_q triangle for $q = 1, 2$. The triangles have 3 and 6 DOFs respectively (•, black dot).

$q = 2$, giving us a Lagrange element CG_2 with 6 DOFs per cell. Figure 3.3 shows the two Lagrange triangles CG_1 and CG_2 for $q = 1$ and $q = 2$ respectively. The Courant triangle has the DOFs located at the vertices of the cell, and the higher order CG_2 has 3 additional DOFs, all located midway between the vertices. Our Eulerian method of our hybrid scheme, is based on the CG_1 and CG_2 Lagrange elements.

Variational Formulation

To solve a problem such as the Poisson equation numerically with FE, we need to convert it into a variational problem. The methodology is followed from the FENICS tutorial provided by Langtangen [44]. A 1D Poisson problem is given as,

$$\begin{aligned} -\nabla^2 u(x) &= f(x), & x \text{ in } \Omega, \\ u(x) &= u_0(x), & x \text{ on } \partial\Omega. \end{aligned} \quad (3.3)$$

We can transform equation 3.3 into a variational form by multiplying it with a test function v , and integrating it over the domain Ω ,

$$-\int_{\Omega} (\nabla^2 u) v \, dx = \int_{\Omega} f v \, dx, \quad \forall v \in \hat{V}. \quad (3.4)$$

In equation 3.4, the function u is the trial function, and is what we are trying to approximate. The trial function u lies in the trial function space V , and the test function v lies in the test function space \hat{V} . When performing integration by parts, the test function v is required to be zero at regions where u is known. So, the additional terms cancel and we get,

$$-\int_{\Omega} \nabla u \nabla v \, dx = \int_{\Omega} f v \, dx \quad \forall v \in \hat{V} \quad (3.5)$$

This form is referred to as the *weak-form* of the original Poisson equation and is valid for all v in the trial space \hat{V} . An inner product of any two functions f and g in domain Ω is defined as,

$$\langle f, g \rangle = \int_{\Omega} f g \, dx, \quad (3.6)$$

so we can rewrite equation 3.5 as,

$$-\langle \nabla u, \nabla v \rangle = \langle f, v \rangle, \quad \forall v \in \hat{V}. \quad (3.7)$$

In order to solve this continuous problem numerically, we must transform it into a discrete variational problem,

$$-\langle \nabla u_h, \nabla v \rangle = \langle f, v \rangle \quad \forall v \in \hat{V}_h \subset \hat{V}, \quad (3.8)$$

where u_h is the approximate solution function belonging to the discrete function in the discrete space V_h which is a subset of V . Similarly the test discrete function space \hat{V}_h is a subset of \hat{V} . The linear triangular element, shown in Figure 3.3 is used as the function space, where \hat{V}_h and V_h are described by piecewise linear functions of the triangle. At the boundary, the functions in the test space are zero, whereas the functions in the trial space are equal to the boundary condition u_0 . In the Langtangen [44], u is used to denote/write the solution of the discrete problem, ignoring the subscript h of u_h . Therefore, to have a one-to-one relation with literature, we will employ the same notation from here on. The equation 3.8 can be simplified as,

$$a(u, v) = L(v), \quad (3.9)$$

where,

$$a(u, v) = -\langle \nabla u, \nabla v \rangle, \quad (3.10)$$

and

$$L(v) = \langle f, v \rangle. \quad (3.11)$$

The variable $a(u, v)$ and $L(v)$ is denoted as the bilinear and linear form, respectively. Since, $u \in V$, it can be written as a linear combination of the basis functions $\{\phi_i, \dots, \phi_N\}$ of V , with $\text{span}\{\phi_i, \dots, \phi_N\} = V$, we can express u as,

$$u = \sum_{j=1}^N U_j \phi_j. \quad (3.12)$$

Similarly, the test function v can be written as linear combination of basis functions $\{\hat{\phi}_i, \dots, \hat{\phi}_N\}$, with $\text{span}\{\hat{\phi}_i, \dots, \hat{\phi}_N\} = \hat{V}$,

$$v = \sum_{i=1}^N V_i \hat{\phi}_i. \quad (3.13)$$

Since equation 3.9 has to valid for all $v \in \hat{V}$, and \hat{V} can be written as a linear combination of the basis functions, equation 3.9 must be valid for each of the basis functions. Therefore, equation 3.9 can be expressed as,

$$a\left(\sum_{j=1}^N U_j \phi_j, \hat{\phi}_i\right) = L(\hat{\phi}_i), \quad \forall \phi_i, i = 1, \dots, N. \quad (3.14)$$

and simplifies to,

$$\sum_{j=1}^N U_j a(\phi_j, \hat{\phi}_i) = L(\hat{\phi}_i), \quad \forall \phi_i, i = 1, \dots, N. \quad (3.15)$$

This is an algebraic system of equations:

$$\mathbf{A}U = b, \quad (3.16)$$

where $\mathbf{A}_{ij} = a(\phi_j, \hat{\phi}_i)$ and the Right-Hand Side (RHS) b_i is given by $b_i = L(\hat{\phi}_i)$.



3.2 Solving the Finite Element Problem

To solve the finite element problem, we used DOLFIN , the finite element library of the FENiCS Project. This library uses high performance linear algebra kernels, and provide a scripting interface to PYTHON. The Python scripting environment helps us to focus on the development of the theory (i.e the high-level algorithms). In order to generate the mesh of the fluid domain, we used GMSH, a three-dimensional finite element mesh generator which proves a fast, light and user-friendly meshing tool.

3.2.1 Introduction to FEniCS Project

The FENiCS Project is a collaborative work of various universities that developed tools to perform automated finite element algorithms, which can be used to solve partial differential equations. It was a project originated in 2003 with the research collaboration of University of Chicago and Chalmers University of Technology from Logg, Mardal, and Wells [44]. Since then, several other groups have joined such as the Royal Institute of Technology, Simula Research Laboratory, University of Cambridge and Delft University of Technology.

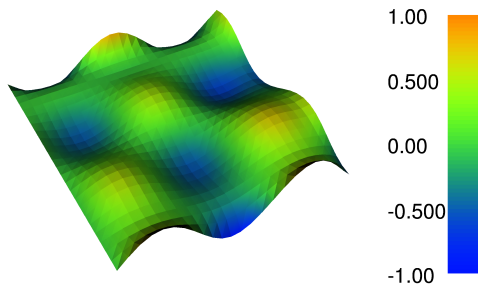


Figure 3.4: DOLFIN VTK plot of the Poisson solution, given by the problem, source code listing 3.1.

FENiCS consists of various libraries such as UFC, UFL, FIAT, INSTANT and DOLFIN. DOLFIN is the core library aimed at automating the solution of partial differential equations using the finite element method [45]. It uses automated code generation thus maintaining high-level mathematical expressions but still providing efficient, multi-threaded performance (with Message Passing Interface ([MPI](#))) internally.

We used the DOLFIN library wrapped in PYTHON to set up and solve the finite element problem. For example, we can demonstrate the procedures of solving the Poisson problem, equation 3.3. We can take $f = 2 \cdot \sin x \cdot \cos y$ with the boundary conditions,

$$u(x) = u_0(x) = \sin x \cdot \cos y, \quad (x, y) \in \partial\Omega. \quad (3.17)$$

The finite element code generation is automated with DOLFIN, leaving only the explicit expression of the problem in python, see source code listing 3.1. Figure 3.4 shows the VTK plot of the solution for the Poisson problem.

```

1 from dolfin import *
2
3 # Generate unit square mesh: 24 × 24
4 mesh = UnitSquareMesh(24, 24)
5
6 # Define Function space: 1st order, Continuous-Galerkin
7 V = FunctionSpace(mesh, "CG", 1)
8
9 # Define Dirichlet boundary conditions expression
10 #  $u_0 = \sin x \cdot \cos y$ 
11 u0 = Expression("sin(10*x[0])*cos(10*x[1])")
12
13 # Function that defines the boundary points
14 def u0_boundary(x, on_boundary):
15     return on_boundary
16
17 # Define the boundary condition
18 #  $u(x) = u_0(x)$ ,  $x$  on  $\partial\Omega$ 
19 bc = DirichletBC(V, u0, u0_boundary)
20
21 # Define the variational problem
22 u = TrialFunction(V) # Trial functions
23 v = TestFunction(V) # Test functions
24
25 #  $f = 100 \cdot \sin(x) \cdot \cos(y)$ 
26 f = Expression('100*sin(10*x[0])*cos(10*x[1])')
27
28 # LHS:  $a = - \int \nabla u \nabla v \, dx$ 
29 a = -inner(nabla_grad(u), nabla_grad(v))*dx
30
31 # RHS:  $L = \int fv \, dx$ 
32 L = f*v*dx
33
34 # Solve the Poisson problem
35 u = Function(V) # Define the solution
36 solve(a == L, u, bc) #  $a(u, v) = L(v)$ 
37
38 # Plot the result
39 plot(u, interactive=True)

```

Listing 3.1: A complete program for solving the Poisson problem and plotting the solution. The Poisson problem is given as $-\nabla^2 u = f$, where $u_0 = \sin x \cdot \cos y$ on the boundary and $f = 2 \cdot \sin(x) \cdot \cos(y)$. The code is written in PYTHON using DOLFIN 1.2 library



3.2.2 Mesh Generation using GMSH

The generation of the mesh is achieved by GMSH, an open-source software developed by Geuzaine & Remacle [28], which has implemented a user-friendly interface and fast algorithms. The GMSH implemented kernels use BLAS and LAPACK linear algebra packages in C++ for fast computation. Furthermore, it allows for scriptability making it ideal to integrate it with our current PYTHON code project for future automation.

3.3 Solving Incompressible Navier-Stokes Equations

Using the DOLFIN library for constructing the finite element problem, we can now solve the flow in the Eulerian subdomain of our hybrid scheme. The Eulerian method use the primitive variables velocity-pressure $\mathbf{u} - p$ to describe the flow.

3.3.1 Velocity-Pressure Formulation

The velocity-pressure $\mathbf{u} - p$ formulation of the fluid flow problem, is the standard formulation of the Navier-Stokes equations. The 2D incompressible Navier-Stokes equations of a fluid with unit density (i.e $\rho = 1$) is given as,

$$\frac{\partial \mathbf{u}}{\partial t} + \mathbf{u} \cdot \nabla \mathbf{u} - \nabla \cdot \sigma = f, \quad (3.18a)$$

$$\nabla \cdot \mathbf{u} = 0, \quad (3.18b)$$

where σ is the Cauchy stress tensor defined as,

$$\sigma(\mathbf{u}, p) = 2\nu\epsilon(\mathbf{u}) - p\mathbf{I}. \quad (3.19)$$

The Cauchy stress tensor is a function of pressure p , the fluid kinematic viscosity ν , and the symmetric gradient ϵ defined as,

$$\epsilon(\mathbf{u}) = \frac{1}{2} (\nabla \mathbf{u} + \nabla \mathbf{u}^T). \quad (3.20)$$

describing the stresses in the fluid due to the velocity gradient and the pressure. The incompressible 2D Navier-Stokes equations have two unknowns, the vector velocity field \mathbf{u} , that lies on the vector-valued function space V , and the scalar pressure field p , which lies on the scalar-valued function space Q . Once we compute these two quantities we can determine the vorticity field, which we then transfer to the Lagrangian subdomain.

3.3.2 Determining the Vorticity Field

The coupling between the Eulerian and the Lagrangian subdomain is done by transferring the vorticity field ω from the Eulerian subdomain to the Lagrangian vortex blobs. The vorticity field ω , is defined as:

$$\omega = \nabla \times \mathbf{u}, \quad (3.21)$$

where the vorticity ω lies on the scalar-valued function space X . However, as $\nabla \times \mathbf{u} \notin X$, because $\mathbf{u} \in V$, we require a projection from the velocity function space V onto the vorticity function space X . In variational formulation, this requires the following equality to be satisfied,

$$\int_{\Omega} \omega \cdot v \, dx = \int_{\Omega} (\nabla \times \mathbf{u}) \cdot v \, dx, \quad \forall v \in \hat{X}. \quad (3.22)$$

To determine the vorticity at every step of the simulation t_n, t_{n+1}, \dots , we have to perform this projection at every step. Thus, to solve this problem in an efficient manner, we can pre-assemble (i.e pre-calculated) the knowns of the problem using the `assemble` function of DOLFIN .

Using the inner product rule, defined by equation 3.6, equation 3.22 can be rewritten as,

$$-\langle \nabla \omega, \nabla v \rangle = \langle \nabla \times \mathbf{u}, v \rangle, \quad \forall v \in \hat{X}. \quad (3.23)$$

where \hat{X} is the test function space of the trial function space X . Equation 3.23 can also be written as,

$$a(\omega, v) = L(\mathbf{u}, v), \quad \forall v \in \hat{X}, \quad (3.24)$$

where $a(\omega, v) = -\langle \nabla \omega, \nabla v \rangle$, and $L(\mathbf{u}, v) = \langle \nabla \times \mathbf{u}, v \rangle$. Since ω can be written as a linear combination of basis functions $\{\psi_j, \dots, \psi_N\}$, with $\text{span}\{\psi_j, \dots, \psi_N\} = X$, we can express ω as,

$$\omega = \sum_{j=1}^N w_j \psi_j, \quad (3.25)$$

Similarly, v and \mathbf{u} can be expressed in the linear form as $v = \sum_{i=1}^N V_i \hat{\psi}_i$ and $\mathbf{u} = \sum_{j=1}^N U_j \phi_j$, respectively.

As described in section 3.1.2, since equation 3.24 is valid for all $v \in \hat{X}$, and as \hat{X} can be written as a linear combination of basis functions $\{\hat{\psi}_i, \dots, \hat{\psi}_N\}$, equation 3.24 must be valid for each of the basis functions. Therefore, equation 3.24 can be expresses in the linear form as,

$$a\left(\sum_{j=1}^N w_j \psi_j, \hat{\psi}_i\right) = L\left(\sum_{i=j}^N U_j \phi_j, \hat{\psi}_i\right), \quad \forall \hat{\psi}_i, i = 1, \dots, N, \quad (3.26)$$

and simplifying to,

$$\sum_{j=1}^N w_j \cdot a(\psi_j, \hat{\psi}_i) = \sum_{i=j}^N U_j \cdot L(\phi_j, \hat{\psi}_i), \quad \forall \hat{\psi}_i, i = 1, \dots, N, \quad (3.27)$$

resulting in an algebraic system of equations,

$$\mathbf{A}w = b, \quad (3.28)$$

where $\mathbf{A}_{ij} = a(\psi_j, \hat{\psi}_i)$, and the Right-Hand-Side (**RHS**) is given as $b_i = L(\phi_i, \hat{\psi}_i)$. Since \mathbf{A} does not change during the simulation, it can be pre-computed outside the time-marching loop, using the `assemble` function of DOLFIN , improving the efficiency of the vorticity calculation.



```

1 from dolfin import *
2
3 ...
4
5 # Define Function spaces
6 # X : scalar-valued vorticity function space W
7 X = FunctionSpace(mesh, 'CG', 1) # 1st order, Continuous-Galerkin
8
9 # Define the trial and test function
10 omega = TrialFunction(X) # vorticity  $\omega \in X$ 
11 v      = TestFunction(X) # test function  $v \in \hat{X}$ 
12
13 ...
14
15 # Define the variation problem for vorticity
16 a = inner(omega,v)*dx    #  $\langle \omega, v \rangle$ 
17 b = inner(curl(u),v)*dx  #  $\langle \nabla \times u, v \rangle$ 
18
19 # Pre-Assemble the LHS
20 A = assemble(a)
21
22 ...
23
24 # During the time-stepping
25 omega = Function(X) # Define the function
26 B = assemble(b)      # Assemble b
27 solve(A, omega.vector(), B) # Solve for vorticity

```

Listing 3.2: The PYTHON implementation of the vorticity calculation using DOLFIN 1.2 library. Line 24 shows the use of `assemble` function to pre-assemble the knowns of the problem.

The PYTHON implementation of the algorithm is show in listing 3.2. Using the DOLFIN library, we can used the `assemble` function to pre-calculated the LHS of the problem (line 24). So using the algorithms of the hybrid coupling scheme, we can transfer this vorticity field of the Eulerian subdomain on the vortex blobs.

3.3.3 Taylor-Hood Finite Element Family for Solving ICNS

To solve the Incompressible Navier-Stokes (**ICNS**) problem, we must choose appropriate finite element function spaces for the velocity \mathbf{u} and the pressure p by ensuring that we satisfy the Ladyzhenskaya-Babuška-Brezzi (LBB) compatibility condition, also known as the inf-sup compatibility condition, described in Brezzi and Fortin [8]. The Lagrange finite element space for velocity must be one order higher than the order of the pressure q_{pres} ,

$$q_{\text{vel}} = q_{\text{pres}} + 1, \quad (3.29)$$

for a stable problem. Therefore, we have decided to use the Taylor-Hood family, introduced by Taylor and Hood [60] and verified by Boffi [5], that satisfies the inf-sup compatibility condition by using $q_{\text{vel}} = 2$ and $q_{\text{pres}} = 1$. We decided to choose this method, as it is the most conventional method, that is simple, and shows a stable behavior.

In addition, we have to choose an appropriate function space for the vorticity. As vorticity is the curl of the velocity, to reduce interpolation error during the projection of the solution, we will use function space one order lower than the velocity, $q_{\text{vort}} = 1$. Table 3.1 shows the list of the function spaces, the finite element type and their orders. In addition, we have included the variable names of the function space, trial functions and the test functions, associated to the function element that we have chosen for the problem.

Table 3.1: Summary of the Lagrange element CG_q of order q , that was used for solving the incompressible Navier-Stokes problem. The variable names of the function space, the trial functions, and the test functions are tabulated together.

Variable	Finite element	Function space	Trial function	Test function
Velocity	CG_2	V	\mathbf{u}	\mathbf{v}
Pressure	CG_1	Q	p	q
Vorticity	CG_1	X	w	x

3.3.4 Incremental Pressure Correction Scheme

This algorithm to solve the NS problem was first demonstrated by Chorin in 1968 [12], and is referred to as Chorin's projection method or sometimes known as the non-incremental pressure correction scheme. The process relies in first computing a tentative velocity by initially neglecting the pressure in the momentum equation of the Navier-Stokes problem, equation 3.18. The velocity field is corrected by determining the pressure field satisfying a divergence free vector field. This method however does not satisfy the discrete incompressibility constraint exactly and so, Goda in 1979 [29], introduced an improved Incremental Pressure Correction Scheme (IPCS). The method computed the viscous term at the incremented time $(t_{n-1} + t_n)/2$, and used the stress formulation to determine the corrected pressure [44]. The detailed algorithms to the IPCS scheme, as presented in the FEniCS manual [44], can be summarized as follows:

1. **Compute the tentative velocity:** The tentative velocity \mathbf{u}^* is determined by solving,

$$\begin{aligned} \langle D_t^n \mathbf{u}^*, \mathbf{v} \rangle + \langle \mathbf{u}^{n-1} \cdot \nabla \mathbf{u}^{n-1}, \mathbf{v} \rangle + \langle \sigma(\mathbf{u}^{n-\frac{1}{2}}, p^{n-1}), \epsilon(\mathbf{v}) \rangle \\ + \langle p^{n-1} \hat{\mathbf{n}}, \mathbf{v} \rangle_{\partial\Omega} - \langle \mathbf{v} \cdot \hat{\mathbf{n}} \cdot (\nabla \mathbf{u}^{n-\frac{1}{2}})^T, \mathbf{v} \rangle_{\partial\Omega} = \langle f^n, \mathbf{v} \rangle, \end{aligned} \quad (3.30)$$

is valid for all $\mathbf{v} \in V$, where $\mathbf{u}^{n-\frac{1}{2}}$ is defined as,

$$\mathbf{u}^{n-\frac{1}{2}} = \frac{\mathbf{u}^* + \mathbf{u}^{n-1}}{2}, \quad (3.31)$$

With the Dirichlet velocity boundary conditions at the boundary $\partial\Omega$, we can solve equation 3.30. The additional term,

$$\langle \mathbf{v} \cdot \hat{\mathbf{n}} \cdot (\nabla \mathbf{u}^{n-\frac{1}{2}})^T, \mathbf{v} \rangle_{\partial\Omega}, \quad (3.32)$$



```

1 # Before the time-stepping:
2
3 # Define:  $\mathbf{u}^{n-1/2} = (\mathbf{u}^* + \mathbf{u}^{n-1})/2$ 
4 U = 0.5*(u0 + u)
5
6 # Formulate the tentative velocity problem
7 F1 = (1/k)*inner(v, u - u0)*dx \
8     + inner(v, grad(u0)*u0)*dx \
9     + inner(epsilon(v), sigma(U, p0, nu))*dx \
10    + inner(v, p0*n)*ds \
11    - beta*nu*inner(grad(U).T*n, v)*ds \
12    - inner(v, f)*dx
13
14 # Extract the LHS, and the RHS
15 a1 = lhs(F1)
16 L1 = rhs(F1)
17
18 # Pre-assemble the LHS
19 A1 = assemble(a1)
20
21 ...
22
23 # During the time-stepping:
24
25 # Assemble the RHS
26 b = assemble(L1)
27
28 # Apply the Dirichlet velocity boundary condition b.c
29 [bc.apply(A1, b) for bc in bcVelocity]
30
31 # Solve for the Tentative velocity
32 solve(A1, u1.vector(), b, "gmres", "default")

```

Listing 3.3: The source code for solving the tentative velocity \mathbf{u}^* , using the equation 3.30.

is results from integration by parts, when we evaluate the viscous term at $(t_{n-1} + t_n)/2$ and we use the stress formulation instead of the Laplacian formulation as done for the Chorin scheme. This difference ensures that the velocity profile at the inlet and the outlet of the domain is more accurate than the ones obtained for the Chorin scheme.

The source code for solving the tentative velocity problem is shown in listing 3.3. First, we pre-define all the terms needed for the tentative velocity problem formulation (lines 3 to 16). We can also pre-assemble the LHS of the problem (line 19) outside of the time-integration loop, since it remains constant. During time integration, we first assemble the RHS of the problem (line 26), then apply the Dirichlet velocity boundary condition (line 29) which consists of the wall boundary condition, and external Dirichlet velocity boundary condition (e.g. the free-stream). Finally, we can solve the problem using a GMRES solver for solving the system of linear equation (line 32).

2. **Determine the pressure:** The pressure p^n is determined by solving,

$$\langle \nabla p^n, \nabla q \rangle = \langle \nabla p^{n-1}, \nabla q \rangle - \langle \nabla \cdot \mathbf{u}^*, q \rangle / \Delta t_n \quad (3.33)$$

valid for all $q \in Q$. We use the previously calculated tentative velocity \mathbf{u}^* to determine the pressure. We can solve the problem using the Neumann pressure

```

1 # Before the time-stepping:
2
3 # Formulate the pressure correction problem
4 a2 = inner(grad(q), grad(p))*dx          # ⟨∇q, ∇pn⟩
5 L2 = inner(grad(q), grad(p0))*dx\        # ⟨∇ q, ∇ pn-1 ⟩ − ⟨ ∇ · u*, q ⟩/Δ tn
6     - (1/k)*q*div(u1)*dx
7
8 # Pre-assemble the LHS
9 A2 = assemble(a2)
10
11 ...
12
13 # During the time-stepping:
14
15 # Assemble the RHS
16 b = assemble(L2)
17
18 # Apply the Dirichlet velocity boundary condition b.c
19 if len(bcPressure) == 0: normalize(b)
20 [bc.apply(A2, b) for bc in bcPressure]
21
22 # Solve for the corrected pressure
23 solve(A2, p1.vector(), b)
24 if len(bcPressure) == 0: normalize(p1.vector())

```

Listing 3.4: The source code for solving the pressure p^n using the equation 3.33.

boundary condition at the pressure outlet of the domain. We define a boundary as the pressure outlet, if we do not know the velocity boundary condition at that boundary. This is true for the region where the exit flow is perturbed. However, for the coupled Eulerian method (that we will use), all the boundary conditions are available as a velocity boundary condition from the Lagrangian subdomain. This means that we do not have to assume any pressure boundary condition.

The source code for solving the pressure problem is shown in listing 3.4. As done for the tentative velocity, we can formulate and pre-assemble the problem before the time loop (lines 3 to 9). In the time loop, we only need to assemble the RHS (line 16), apply the boundary condition (if it exists, lines 18 to 20) and finally solve for the pressure (lines 22 to 24). Using the pressure, we can determine the corrected velocity field.

3. **Determine the corrected velocity:** The corrected velocity field u^n is determined by solving,

$$\langle \mathbf{u}^n, \mathbf{v} \rangle = \langle \mathbf{u}^*, \mathbf{v} \rangle - \Delta t_n \langle \nabla(p^n - p^{n-1}), \mathbf{v} \rangle, \quad (3.34)$$

which is valid for all $\mathbf{v} \in V$. We correct the tentative velocity \mathbf{u}^* by the pressure difference to determine the correct velocity field. We will have to apply the Dirichlet velocity boundary condition at the boundary again, to solve for the problem.

The source code for solving the corrected velocity problem is shown in listing 3.5. We first initialize the problem, by formulating the problem and assembling the LHS outside the time loop (line 3 to 8). In the time integration loop, we assemble the RHS (line 15), apply the velocity boundary condition (line 18) and finally solve for the corrected velocity field (line 21).



```

1 # Before the time-stepping:
2
3 # Formulate the velocity correction problem
4 a3 = inner(v, u)*dx      # <u^n, v>
5 L3 = inner(v, u1)*dx - k*inner(v, grad(p1 - p0))*dx # <u^*, v> - Δt_n <∇(p^n - p^{n-1}), v>
6
7 # Pre-assemble the LHS
8 A3 = assemble(a3)
9
10 ...
11
12 # During the time-stepping:
13
14 # Assemble the RHS
15 b = assemble(L3)
16
17 # Apply the Dirichlet velocity boundary condition b.c
18 [bc.apply(A3, b) for bc in bcVelocity]
19
20 # Solve for the corrected pressure
21 solve(A3, u1.vector(), b, "gmres", 'default')

```

Listing 3.5: The source code for solving the corrected velocity u^n using equation 3.34.

The algebraic system of equations resulting from this algorithm have been solved with DOLFIN's Krylov GMRES solver with an absolute and a relative error tolerance of 10^{-25} and 10^{-12} respectively. The program structure was based on the collection of benchmark solvers provided by the FENICS [43]. In the algorithm described above an explicit time marching scheme, Forward Euler (FE) has been used. Therefore, for the time marching scheme to be stable, we require the CFL number to satisfy the following condition:

$$\text{CFL} = \Delta t_{E,\max} \frac{\|\mathbf{u}\|_{\max}(\nu + \Delta h_{\min} \|\mathbf{u}\|_{\max})}{\Delta h_{\min}^2} \leq 1. \quad (3.35)$$

This gives us the direct constraint on the maximum Eulerian time step size $\Delta t_{E,\max}$ which is function of the CFL number, maximum fluid velocity in the Eulerian domain $\|\mathbf{u}\|_{\max}$, the fluid viscosity ν and the minimum mesh cell size Δh_{\min} .

3.3.5 Determining the Body Forces

After we determine the flow fields, we can compute the lift and the drag generated by the body. To determine these parameters, we first need to determine the forces acting on the no-slip boundary, which can be determined from the stress tensor σ acting on the surface of the body, equation 3.19. The lift coefficient and the drag coefficient are computed by:

$$L = \int_{\partial\Omega} [\sigma(\mathbf{u}, p) \cdot \hat{\mathbf{n}}] \cdot \hat{\mathbf{e}}_y \, ds, \quad (3.36a)$$

$$D = \int_{\partial\Omega} [\sigma(\mathbf{u}, p) \cdot \hat{\mathbf{n}}] \cdot \hat{\mathbf{e}}_x \, ds, \quad (3.36b)$$

where $\hat{\mathbf{e}}_x$ and $\hat{\mathbf{e}}_y$ are the 2D unit Cartesian vectors,

$$\hat{\mathbf{e}}_x = \begin{bmatrix} 1 \\ 0 \end{bmatrix}, \quad \hat{\mathbf{e}}_y = \begin{bmatrix} 0 \\ 1 \end{bmatrix}. \quad (3.37)$$

such that lift perpendicular to the free-stream and the drag is tangential to it. The lift coefficient C_l and the drag coefficient C_d , are obtained by normalizing the lift L and drag D forces with the dynamics pressure and reference length c (in 2D), where the lift perpendicular to the free-stream and the drag is tangential to it,

$$C_l = \frac{L}{\frac{1}{2}\|\mathbf{u}\|_\infty^2 c}, \quad C_d = \frac{D}{\frac{1}{2}\|\mathbf{u}\|_\infty^2 c}. \quad (3.38)$$

```

1 ...
2
3 def epsilon(u):
4     "Returns symmetric gradient"
5     return 0.5*(grad(u) + grad(u).T)
6
7 def sigma(u,p,nu):
8     "Returns stress tensor"
9     return 2*nu*epsilon(u) - p*Identity(u.cell().d)
10
11 # Define the normal function
12 n = FacetNormal(mesh)
13
14 # Define the unit vectors
15 eX = Constant((1.0, 0.0))
16 eY = Constant((0.0, 1.0))
17
18 # Define the line integrator
19 ds = Measure("ds")[boundaryDomains]
20 noSlip = 2 # No-slip boundary identification = 2
21
22 # Determine the forces
23 # Integrate the forces over the boundaryDomain == noSlip
24 L = assemble(inner(inner(sigma(u,p,nu), n), eY)*ds[noSlip]) # Lift
25 D = assemble(inner(inner(sigma(u,p,nu), n), eY)*ds[noSlip]) # Drag

```

Listing 3.6: The PYTHON implementation for calculating the lift force L and the drag force D acting on the no-slip boundary.

3.4 Evolution of the Eulerian method

The algorithm of evolving the Eulerian method is summarized in this section. The Eulerian method acts as the source of the vorticity for the Lagrangian method.

The flowchart of the Eulerian method is given by Figure 3.5. The algorithm to the Eulerian method can be summarized as follows:

1. **Mesh generation:** We generate the mesh of the fluid domain using GMSH before the iteration.
2. **Determine the boundary condition:** We determine the boundary conditions for the boundary domains: $\partial\Omega_E = [\Sigma_{wall}, \Sigma_d \Sigma_{pres}]$. If we have Dirichlet velocity



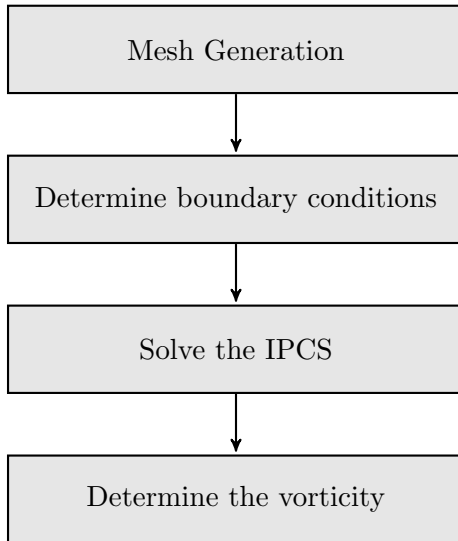


Figure 3.5: Flowchart of the Eulerian method.

boundary conditions for all the exterior boundaries, we do not have to apply any pressure boundary conditions at $\partial\Sigma_{pres}$, because $\Sigma_{pres} = \infty$ in that case.

3. **Solve the IPCS:** Using IPCS, time march from t_n to t_{n+1} to solve for the new velocity \mathbf{u} and pressure p field.
4. **Determine the vorticity:** Using the algorithm described in 3.3.2, solve for the vorticity field ω at the time t_{n+1} .

Once we have the well-resolved vorticity ω of the near-body region, the vorticity is then transferred into the Lagrangian subdomain using the Hybrid coupling scheme, which was summarized in the introduction, chapter 1, and fully elaborated in chapter 4.

3.5 Validation of Eulerian Method

To verify our Eulerian method, we first investigated the Lamb-Oseen vortex problem. The validation of the Eulerian method is done by investigating the Clercx-Bruneau dipole collision at $Re = 625$, comparing with the study of Clercx and Bruneau [15]. Furthermore, we investigated the problem of the impulsively started cylinder at $Re = 550$, where we verified and validated the lift and drag calculations with the literature of Koumoutsakos and Leonard [39], and Rosenfeld et al. [52].

3.5.1 Lamb-Oseen Vortex

The Lamb-Oseen vortex is an analytical solution by Lamb and Oseen, describing the diffusion of a vortex core [61]. The current investigation was performed similarly to the Lagrangian study in section 2.7.2.

Problem Definition

In section 2.7.2, the vortex blobs of the Lagrangian method required the vorticity formulation of the Lamb-Oseen vortex to set up the problem. However, as the Eulerian method use the primitive variables $\mathbf{u} - p$, we require the velocity formulation of the Lamb-Oseen vortex. The velocity field of the Lamb-Oseen vortex is defined as,

$$u_\theta = \frac{\Gamma_c}{2\pi r} \left[1 - \exp \left(-\frac{r^2}{4\pi\nu(t+\tau)} \right) \right] \quad (3.39a)$$

$$u_r = 0, \quad (3.39b)$$

where u_θ is the circumferential velocity, and u_r is the radial velocity. The velocity is a function of the vortex core strength Γ_c , the simulation time $t \in [0, \infty[$, the time constant τ , the kinematic viscosity ν , and the distance from the core center r .

The parameters used for the simulation are tabulated in table 3.2. To ensure a valid comparison of the present Eulerian method study with the Lagrangian method performed in section 2.7.2, we chose similar spatial discretization parameters.

Figure 3.6 depicts the domain for the present Lamb-Oseen vortex study. The fluid domain Ω_E is bounded by a Dirichlet boundary Σ_d such that $\partial\Omega_E = [\Sigma_d]$. The Dirichlet boundary Σ_d is used to prescribe the analytical Dirichlet velocity boundary conditions for the Lamb-Oseen vortex problem.

The Eulerian method is time marched using the time integration parameters tabulated in table 3.2. To ensure a stable time integration, we enforced the CFL conditions, equation 3.35. During the evolution of the solution, we evaluated the growth of the error in velocity, and the error in vorticity between the numerical and the analytical solutions.

Table 3.2: Summary of the parameters for the Lamb-Oseen vortex evolution.

Parameters	Value	Description
Γ_c	1	Core strength
Ω	$[-1, 1] \times [-1, 1]$	Eulerian domain bounds
\mathbf{u}_∞	0	Free-stream velocity
ν	5×10^{-4}	Kinematic viscosity
τ	4	Lamb-Oseen time offset
t	0 to 1	Simulation time span
Δt	0.001	Time step size
N_t	1000	Number of time integration steps
h_{grid}	≈ 0.01	Minimum mesh cell size
N_{cells}	161312	Number of mesh cells
CFL	0.95	CFL number
$\ \mathbf{u}\ _{max}$	1.5	Maximum magnitude of the velocity
Time integration	FE	Forward Euler time integration method



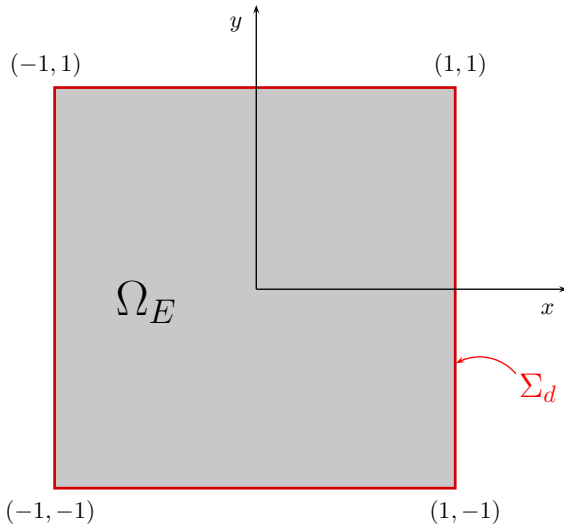


Figure 3.6: Eulerian domain Ω_E (gray) for the Lamb-Oseen vortex problem, bounded by the Dirichlet velocity boundary Σ_d (red), where the Dirichlet velocity boundary condition was applied. The parameters of the domain are tabulated in table 3.2.

Results and Discussion

We are interested in the evolution of error in vorticity, as this is the quantity which will be interpolated onto the Lagrangian subdomain. Figure 3.7 shows the initial and the final relative error in vorticity over the Eulerian domain. Opposed to the Lagrangian results, Figure 2.19, we see that initial relative error in the vorticity field is larger. This is so because the Eulerian solution was initialized using the velocity and the vorticity is obtained by projecting $\nabla \times \mathbf{u}$ (see section 3.3.2) onto the scalar-valued function space W , whereas the Lagrangian solution was initialized directly from vorticity. This process of initialization in the Eulerian domain introduces additional numerical error in the vorticity. However, the pattern of the relative error in vorticity is similar to the Lagrangian solution, with the highest error at the core center, where we have stronger vorticity.

As time progresses, we see that the error in the solution does not increase as observed for the Lagrangian method, Figure 3.7b. Figure 3.8 shows this change in the maximum relative error in velocity and vorticity. The maximum relative error in vorticity is at all times higher than the maximum relative error in velocity, due to the error in projection.

To determine the convergence with spatial resolution, the simulation was run for $h \approx 0.25$ to $h \approx 5 \times 10^{-3}$. Figure 3.9a shows the convergence of the relative error in vorticity. This validates that the scheme is 2nd-order in space, which is expectable due to the second order function space CG₂ for the primitive variable, velocity.

To determine convergence with time resolution, we ran the simulation with various time steps $\Delta t = 5 \times 10^{-3}$ to $\Delta t = 1 \times 10^{-4}$. As we performed the investigation, we saw that the error in the primitive variable \mathbf{u} , converged with order 1, Figure 3.9. This is expected, as have employed a 1st-order Forward Euler scheme. Thus, we have verified against the analytical solution of the Lamb-Oseen vortex that our Eulerian method is well implemented and performs in a robust manner.

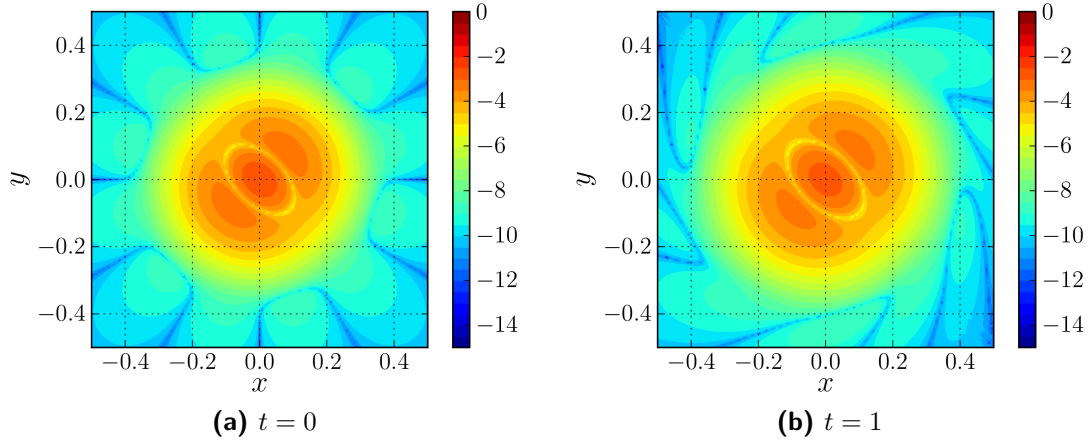


Figure 3.7: Relative error in vorticity (in logarithmic scale) using the parameters tabulated in table 3.2. The figure shows **(a)**, the initial relative error in vorticity at $t = 0$, and **(b)** the final relative error in vorticity at $t = 1$.

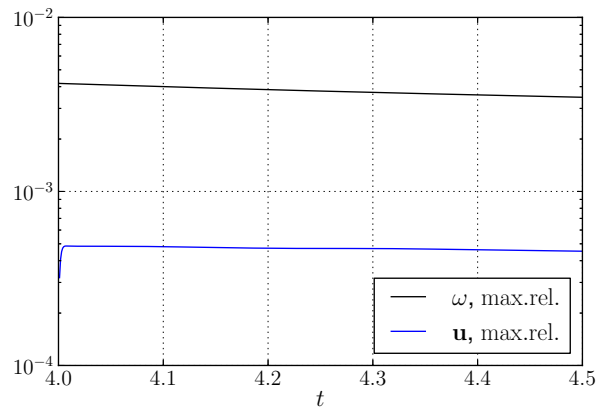


Figure 3.8: Evolution of the maximum relative errors from $t = 0$ to $t = 1$ using the parameters in table 3.2. The figure depicts maximum relative error in velocity [—, solid blue] and the maximum relative error in vorticity [—, solid black].

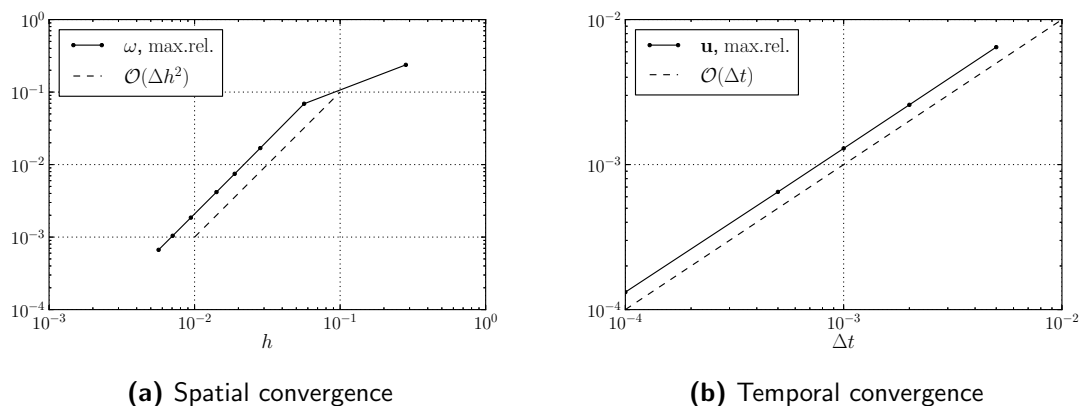


Figure 3.9: Convergence in space and time. The figure depicts **(a)** convergence in space of $\mathcal{O}(\Delta h^2)$ and **(b)** convergence in time of $\mathcal{O}(\Delta t)$. The control parameters are tabulated in table 3.2.



3.5.2 Clercx-Bruneau Dipole Collision at $Re = 625$

The Eulerian method that we have developed here is to be used as a wall-bounded Eulerian solver that can resolve the vorticity production at the boundary for the Hybrid method. Therefore it is vital that the vortex interaction with the no-slip boundary is handled properly.

To determine the proper handling of the no-slip boundary, it is common practice to use a simple test of dipole colliding with the wall. In these test cases, one could observe how the no-slip boundary handles the incoming vortex and can be used to determine if the system is formulated appropriately. Ould-Salihi et al. [49] used this case to validate their Hybrid method that couples vortex particles with finite-difference method. Cottet et al. [20] used this test case to validate the vortex method. Therefore in a similar fashion, we have decided to use the dipole collision study by Clercx and Bruneau [15], performed using a Chevyshev pseudo-spectral method, to verify and validate our Eulerian method.

Problem Definition

Unlike other dipole test cases, Clercx and Bruneau provide well-defined initial and boundary conditions for the dipole vorticity field. Furthermore, they used a vorticity distribution that was continuous, which ensures a smooth velocity field for our Eulerian method using the $\mathbf{u} - p$ formulation. The literature provided results for the collision that we are interested: a normal collision with the dipole traveling perpendicular to the wall.

For the present study, we have decided to use the simpler case of $Re = 625$, where Re is the integral-scale Reynolds number defined as,

$$Re = \frac{UW}{\nu}, \quad (3.40)$$

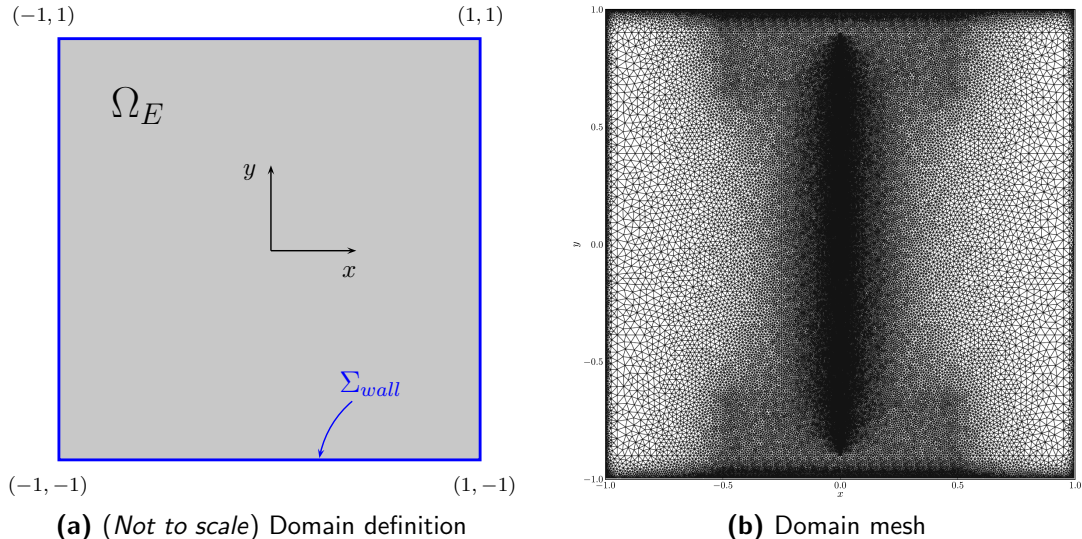


Figure 3.10: Domain of the Clercx-Bruneau dipole collision problem. The figure depicts **(a)** the definition of the domain with the fluid domain (gray) and the no-slip boundary (blue); and **(b)** the unstructured mesh of the domain with $N_{\text{vert}} = 48k$.

where U is the characteristic velocity of the flow, W is half width of domain, and ν is the kinematic viscosity and are chosen according to Clercx and Bruneau [15]. A low Reynolds number of $Re = 625$ is required as the Eulerian method currently only solves an incompressible laminar flow. However in future, an implementation of a turbulence method can enable a high Reynolds number investigation.

The domain Ω of the problem is square, $\Omega_E = [-1, 1] \times [-1, 1]$, as shown in Figure 3.10a. The problem is defined in a closed box, where the Eulerian domain is enclosed in a no-slip boundary $\partial\Omega = \Sigma_{wall}$ where dipole collides and interacts.

The initial condition of the Clercx-Bruneau dipole is a smooth dipole velocity distribution with a positive monopole at $(x_1, y_1) = (0.1, 0)$ and the negative monopole at $(x_2, y_2) = (-0.1, 0)$, with each having a core radius $R = 0.1$. The velocity distribution for the combined monopole at $t = 0$ is given as,

$$u(\mathbf{x}, 0) = -\frac{1}{2}\omega_e(y - y_1) \exp\left\{-\left(\frac{r_1}{R}\right)^2\right\} + \frac{1}{2}\omega_e(y - y_2) \exp\left\{-\left(\frac{r_2}{R}\right)^2\right\}, \quad (3.41a)$$

$$v(\mathbf{x}, 0) = +\frac{1}{2}\omega_e(x - x_1) \exp\left\{-\left(\frac{r_1}{R}\right)^2\right\} - \frac{1}{2}\omega_e(x - x_2) \exp\left\{-\left(\frac{r_2}{R}\right)^2\right\}, \quad (3.41b)$$

where u and v are the velocities in the x and y direction, respectively. The characteristic vorticity magnitude $\omega_e = 299.528385375226$ is obtained from Renac et. al [51]. The radii r_1 and r_2 are the radial distances to the point \mathbf{x} from the center of positive and the negative monopoles respectively. The corresponding vorticity distribution for the velocity distribution is given as,

$$\begin{aligned} \omega(\mathbf{x}, 0) = & \omega_e \left[1 - \left(\frac{r_1}{R} \right)^2 \right] \exp\left\{-\left(\frac{r_1}{R}\right)^2\right\} \\ & - \omega_e \left[1 - \left(\frac{r_2}{R} \right)^2 \right] \exp\left\{-\left(\frac{r_2}{R}\right)^2\right\}. \end{aligned} \quad (3.42)$$

The Eulerian domain was discretized using an unstructured meshing method in GMSH (section 3.2.2), as shown in Figure 3.10a. The velocity distribution, equation 3.41, shows that the maximum velocity in the fluid will be along the y -axis (i.e $x = 0$). Therefore, to satisfy the CFL condition, we need the minimum cell size at the location of the maximum velocity. The resolution of the mesh in the region where the dipole and the wall interacts (i.e $-0.5 \leq x \leq 0.5$ and $0.5 \leq |y| \leq 1$) was also increased. Furthermore, in the region where there is no vorticity, we do not need high resolution (i.e $0.5 \leq |x| \leq 1$ and $-0.5 \leq y \leq 0.5$).

After initializing the velocity field in the discretized domain, the problem was evolved from $t = 0$ to $t = 2$. The time integration parameters are tabulated in table 3.3.

Results and Discussion

Figure 3.11 shows the evolution of the vorticity field at various instances, $t = [0, 0.25, 0.5, 0.75, 1.25]$. During the initial stages of the simulation, the initialized dipole travels along the y -axis towards the bottom no-slip boundary.



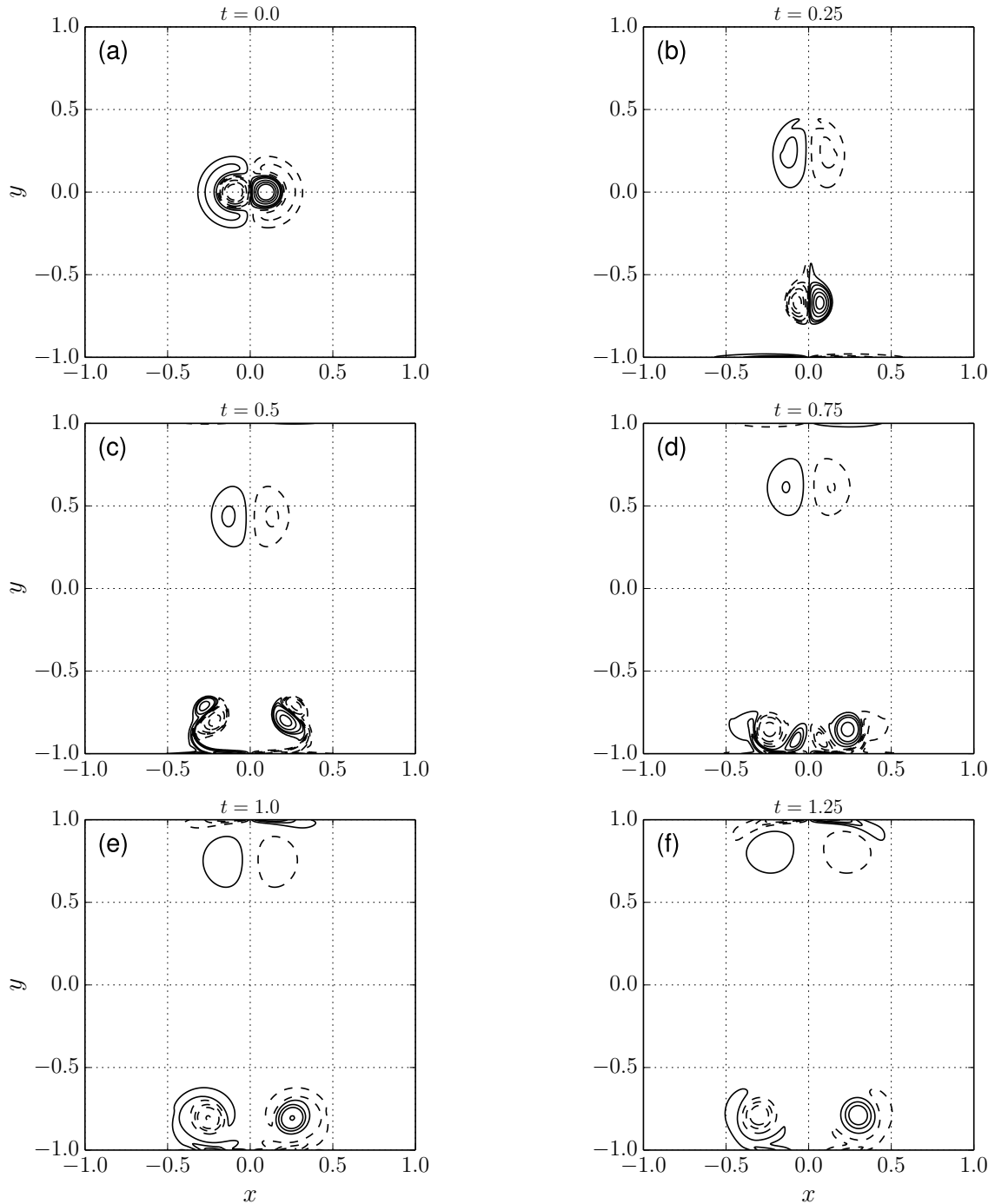


Figure 3.11: Vorticity contour plots of the Clercx-Bruneau dipole-wall collision at $Re = 625$ and $t = [0, 0.25, 0.5, 0.75, 1.0, 1.25]$ with vorticity contour levels at $[-320, -200, -100, -50, -10, 10, 50, 100, 200, 320]$. The figure depicts positive contours [—, solid **black**], and negative contours [- -, dashed **black**].

Table 3.3: Summary of the parameters for the Clercx-Bruneau dipole collision with a no-slip wall [15].

Parameters	Value	Description
Ω	$[-1, 1] \times [-1, 1]$	Eulerian domain bounds
Re	625	Reynolds number
U	1^a	Characteristic velocity
W	1^a	Half width of the domain
ν	1.6×10^{-3}	Kinematic viscosity
$(x, y)_{1,2}$	$(\pm 0.1, 0)$	Initial location of the monopoles
ω_e	299.5283853752226 ^b	Characteristic vorticity of the monopole
t	0 to 2	Simulation time span
CFL	0.95	CFL number
$\ \mathbf{u}\ _{\max}$	12	Maximum fluid velocity
Δt	1.25×10^{-5}	Time step size
N_{cells}	96142	Number of FE mesh cells
h_{grid}	3.6×10^{-3} to 5.1×10^{-2}	FE mesh cell size
N_t	160,000	Number of time integration steps

^a Obtained from Clercx and Bruneau [15]

^b Obtained from Renac et al. [51]

The dipole approaches the bottom boundary, where the no-slip boundary generates vorticity to ensure no-through flow, seen in Figure 3.11b. As the dipole approaches the wall, the vorticity filament at the wall rolls up and combines with the primary dipole forming two secondary dipoles, that is symmetric across the y -axis. Figure 3.11c shows the state of the vorticity field at $t = 0.5$ after the secondary dipoles are generated. This secondary dipole initially travels away from the bottom wall and later on approaches the wall again, colliding for a second time and creating a tertiary vortex, Figure 3.11d. The dipole stops convecting any further and diffuses as time progresses, as shown in Figure 3.11e and 3.11f, corresponding to $t = 1$ and $t = 1.25$.

Figure 3.12 compares the vorticity contours of the computational domain close to the bottom wall, $0 \leq x \leq 0.6$ and $-1 \leq y \leq -0.4$, at $t = 1$. The positive vortex (solid black) is surrounded by the negative vortex (dashed black). Comparing the present study, Figure 3.12b with the study of Clercx and Bruneau [15], Figure 3.12a, shows that the shows that the shape of the vorticity contours is indistinguishable. This means that the present study matches very well with the pseudo-spectral simulation of the Clercx and Bruneau.

To determine the variation of the fluid properties as time progresses, Clercx and Bruneau investigated the evolution of the total kinetic energy E , the total enstrophy Ω , and the total palinstrophy P of the flow field. The total kinetic energy E of the flow can be determined with,

$$E(t) = \frac{1}{2} \int \int \mathbf{u}^2(\mathbf{x}, t) \, dx dy, \quad (3.43)$$

and at $t = 0$, we have $E(0) = 2$. The total enstrophy of the flow is determined as,

$$\Omega(t) = \frac{1}{2} \int \int \omega^2(\mathbf{x}, t) \, dx dy. \quad (3.44)$$



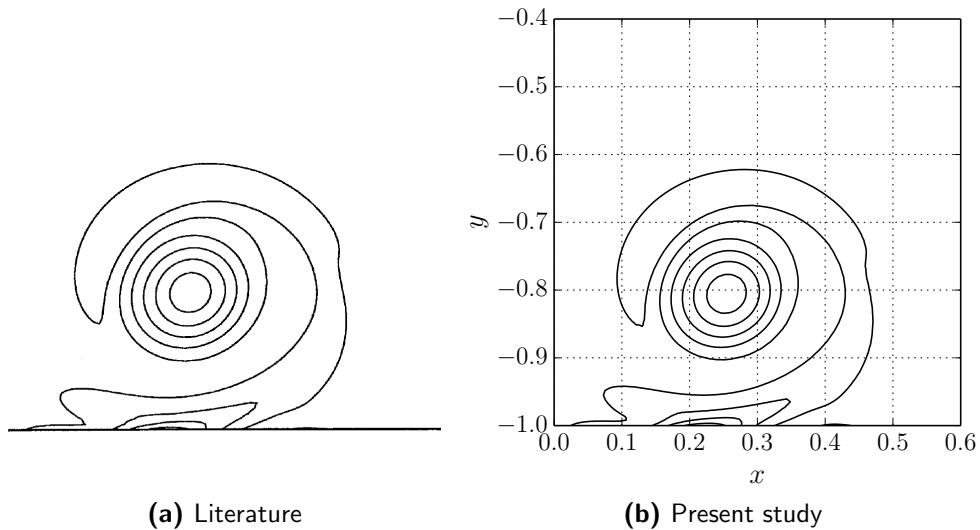


Figure 3.12: Comparison of the vorticity contours at $t = 1$ with contour levels $\{..., -50, -30, -10, 10, 30, 50, ...\}$. The figure compares the plot obtained by **(a)** literature of Clercx and Bruneau [15] and **(b)** the present study.

The change in enstrophy of the flow field can give an insight into the dissipation rate in the fluid. At $t = 0$, the total enstrophy of the fluid is $\Omega(0) = 800$. The total palinstrophy P of the flow measures the gradient of vorticity and is given by,

$$P(t) = \frac{1}{2} \int \int [\nabla \omega(\mathbf{x}, t)]^2 \, d\mathbf{x} dy, \quad (3.45)$$

and gives an insight into the generation of vorticity at the no-slip boundary. Figure 3.13 compares the evolution of these time dependent parameters with the reference data provided by Clercx and Bruneau. Clercx and Bruneau [15] provide the values of the parameters at $t = 0.25$, $t = 0.5$ and $t = 0.75$.

Figure 3.13a shows the evolution of the kinetic energy. The kinetic energy E reduced from $E(0) = 2$ to $E(2) \approx 0.3$. At $t = 0.4$, we have small kink representing the approach of the primary dipole at the wall. When plotting the reference data, we see that the variation in kinetic energy matches perfectly at $t = 0.25$, $t = 0.5$ and $t = 0.75$.

Figure 3.13b shows the evolution of enstrophy Ω in time. During the initial instants, enstrophy decreases linearly and at $t = 0.370$, there is sharp increase in the total enstrophy of the flow $\Omega(0.370) = 938.58$ (shown in blue). This indicates the initial impact of dipole with the no-slip wall. However, in literature [15], the initial peak occurs at $t = 0.371$ with a peak enstrophy of $\Omega(0.371) = 938.6$. Comparing these parameters we see that the enstrophy we calculate peaks earlier and with a larger values, meaning that our collision is slight early. However, the error in time of peaking is 0.3% with a 0.6% error in enstrophy, which is a significantly small error. We observe similar behaviour in the second collision, where the peak in our study is $\Omega(0.650) = 307.04$ (shown in blue), whereas in literature the peak is $\Omega(0.648) = 305.2$. Again the error is relatively small implying that our Eulerian method resolves the evolution of enstrophy very well.

Figure 3.13c shows the evolution of palinstrophy P in time. When the dipole collides, vorticity is generated from the wall to ensure no-through boundary condition, which

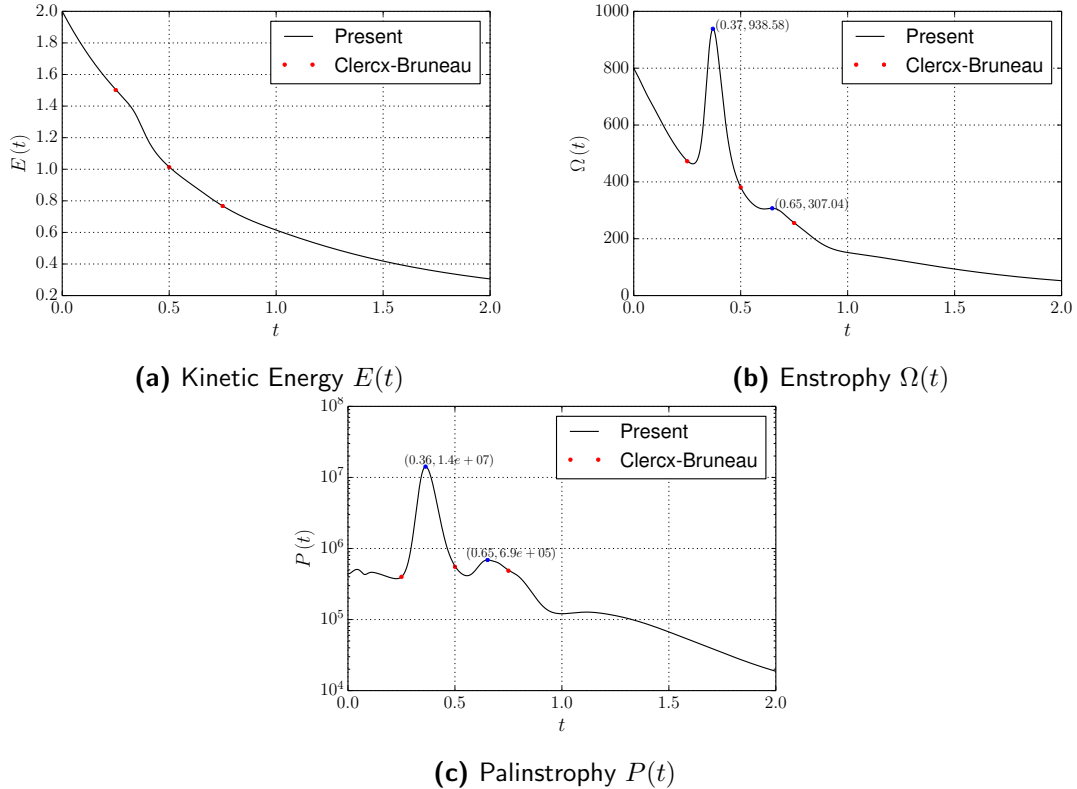


Figure 3.13: Comparison of the fluid parameters from $t = 0$ to $t = 2$ with reference data obtained from Clercx and Bruneau [15] [\bullet , red dot]. The figure shows the evolution of (a) the kinetic energy $E(t)$, (b) the enstrophy $\Omega(t)$, and (c) the palinstrophy $P(t)$.

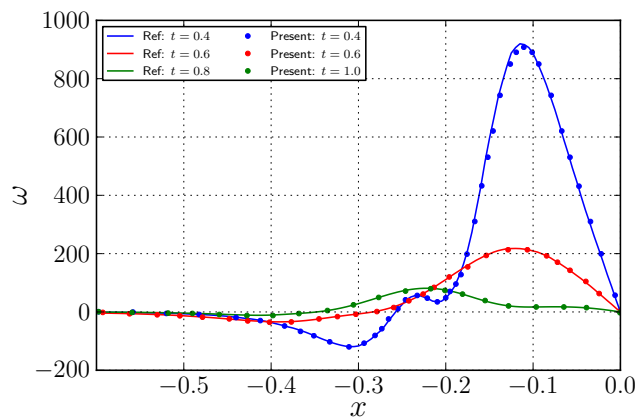


Figure 3.14: The vorticity generated at the bottom-left wall ($y = -1$, $-0.6 \leq x \leq 0$) at $t = 0.4$ [—, solid blue], $t = 0.6$ [—, solid red] and $t = 1$ [—, solid green]. The results are compared with Clercx and Bruneau [15] (dotted).



results in a sharp increase in the gradient of the vorticity. Similar to the evolution of enstrophy, we can observe to peaking at $t = 0.360$ and $t = 0.650$, with peak palinstrophy of $P(0.360) = 1.40 \times 10^7$ and $P(0.650) = 6.90 \times 10^5$, respectively (shown in blue). In literature however, the peak palinstrophy occurs at $P(0.361) = 1.39 \times 10^7$ and $P(0.652) = 6.78 \times 10^5$. This is an acceptable error and tells us the generation of vorticity in Eulerian method performs according to theory.

Figure 3.14 compares the vorticity along the boundary of the domain at $y = -1$ for $-0.6 \leq x \leq 0$. The solid lines represent the present data, and is compared with the dotted data obtained from Clercx and Bruneau [15]. The comparison is done for various time instances $t = 0.4$, $t = 0.6$ and $t = 1.0$ and we can finally validate that the Eulerian method accurately represents vorticity generation from the wall.

3.5.3 Impulsively started cylinder at $Re = 550$

Finally, we an impulsively started cylinder at $Re = 550$. This validation test ensured that we are able to determine correct forces acting on the body.

Problem Definition

The Impulsively Started Cylinder (ISC) test case simulates an impulsively started freestream flow around a cylinder. The test case focuses on the unsteady behavior of the separated flow past the cylinder. Various experimental and numerical investigations have been performed to study the flow characteristics. For this project we relied on the widely used and validated results of Koumoutsakos and Leonard [39]. They investigated the flow around the ISC using vortex method and provided extensive data on the vorticity profile behind the cylinder and the evolution of the lift and drag coefficients.

Figure 3.15 shows the domain of the ISC problem, where Figure 3.15a shows the definitions of the Eulerian domain Ω_E . The Eulerian domain Ω_E has the following boundary conditions: the no-slip wall boundary condition at Σ_{wall} (solid blue) $\mathbf{u} = 0$, the freestream Dirichlet velocity boundary condition at Σ_d (solid red) $\mathbf{u}_\infty = [1, 0]$, and the pressure outlet Σ_{pres} (solid green). Unlike the previous test cases we now require a pressure outlet boundary condition $\partial p / \partial \mathbf{n} = 0$, as the velocity field behind the cylinder perturbed and therefore free-stream boundary condition cannot be applied there. The boundaries of the Eulerian domain Ω_E are $\partial\Omega_E = [\Sigma_{wall}, \Sigma_d, \Sigma_{pres}]$.

The Reynolds number Re of the flow dependent is defined as,

$$Re = \frac{UD}{\nu}, \quad (3.46)$$

and is a function of the freestream velocity U , the diameter of the cylinder D , and the kinematic viscosity ν . The normalized simulation time T is defined as,

$$T = \frac{U}{R} t, \quad (3.47)$$

where R is the radius of the cylinder.

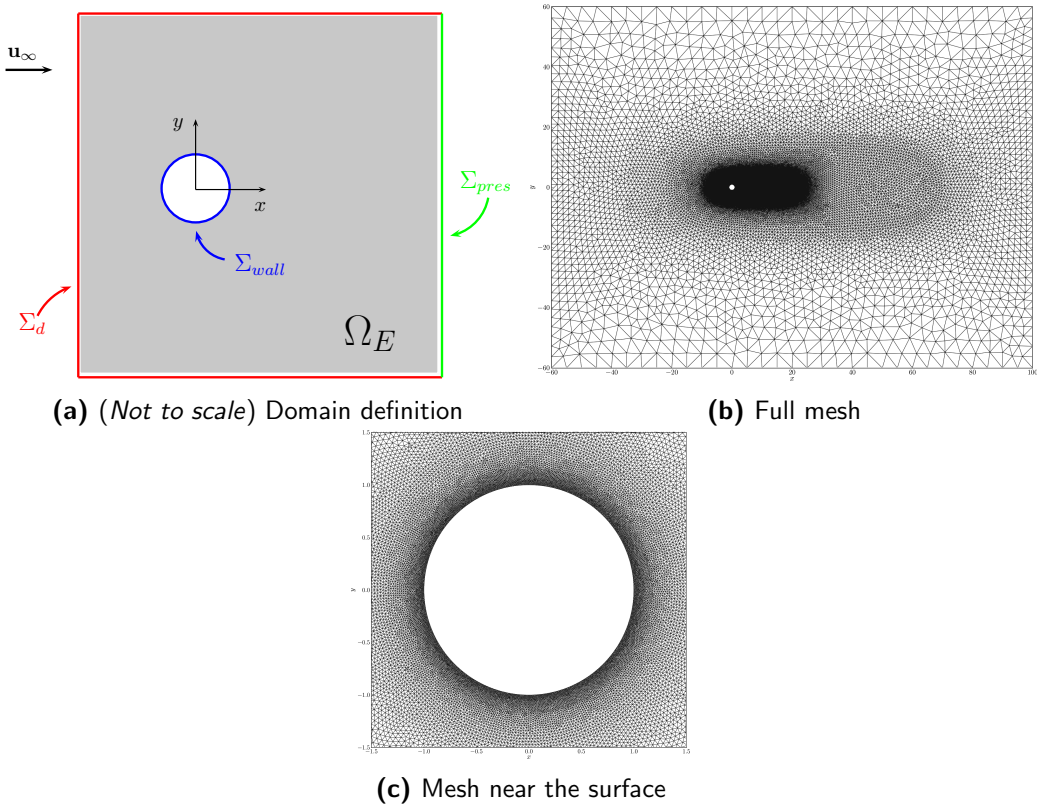


Figure 3.15: Domain of the ISC problem. The figure depicts (a) the definition, (b) the full domain mesh, and (c) the mesh near the surface.

Table 3.4: Summary of the parameters for the impulsively started cylinder test case for $Re = 550$.

Parameters	Value	Description
Ω	$[-60, 100] \times [-60, 60]$	Eulerian domain bounds
Re	550	Reynolds number
U	$1\hat{\mathbf{e}}_x$	Free-stream velocity
R	1	Radius of cylinder
D	2	Diameter of cylinder
ν	3.6×10^{-3}	Kinematic viscosity
T	0 to 40	Normalized simulation time
CFL	0.95	CFL number
$\ \mathbf{u}\ _{\max}$	2.5	Maximum fluid velocity
ΔT	1×10^{-3}	Time step size
N_{cells}	94352	Number of mesh cells
h_{grid}	9.7×10^{-3} to 7.4	FE mesh cell size
N_t	40,000	Number of time integration steps



The domain discretized with the highest mesh resolutions near the surface of the body, and in the near-wake region of the body, as shown in Figure 3.15b and Figure 3.15c. The discretization parameters are tabulated in table 3.4.

The simulation was started with an impulsively started free-stream boundary condition at the Dirichlet boundary Σ_d . The problem was evolved from $T = 0$ to $T = 40$ for $N_t = 40,000$ time steps. To validate the method against the reference data of Koumoutsakos and Leonard [39], we investigated the evolution of the vorticity field and the evolution of the forces acting on the body.

Results and Discussion

Figure 3.16 depicts the evolution of the vorticity at $T = [1, 3, 5, 7]$. The iso-vorticity contours of the present study are compared with the reference data obtained from Koumoutsakos and Leonard [39]. At $T = 1$, negative and positive vorticity is generated at the top and bottom of the cylinder, respectively. This results from satisfying the no-slip boundary condition. As time progresses, two primary vortices are formed behind the cylinder, increasing in shape as time advances. Comparing the vorticity contours, we can say that the contour lines match with the literature.

Using equations 3.36 to 3.38, we were able to calculate the lift and the drag force acting on the cylinder as time progresses, which we used to validate against the literature. Figure 3.17 shows the components of the drag force (friction drag $C_{d\text{fric}}$, pressure drag $C_{d\text{pres}}$) acting on the surface of the body. At $T = 0$, we have a singularity in the total drag C_d acting on the body due to the impulsive start of the flow. It then plunges to $C_d = 0.75$ at $T = 0.8$ and peaks again near $T = 3$ with $C_d = 1.3$. The dotted line is the data obtained from literature [39] and we see that the results of the simulation match well with the literature.

A final comparison was done for the evolution of the lift and the drag coefficients for a larger period ($T = 0$ to $T = 40$), which was used to determine the oscillatory behavior of the forces. For lower Reynolds number, the vorticity field is symmetric across the x -axis for a long time. This meant that the oscillatory behavior of the forces starts at a much later time. Therefore, we prescribed an artificial perturbation to the problem to create an asymmetry in the vorticity field which trips the wake. The perturbation was performed according to Leocointe and Piquet [42],

$$u_{\text{wall}} = \begin{cases} 0.15 & 3 \leq T \leq 3.5, \\ -0.25 & 3.5 \leq T \leq 5. \end{cases} \quad (3.48)$$

With this, we could ensure that we have a controlled behavior for the lift and drag, which we used to determine the amplitude and the frequency of the oscillation. Figure 3.18 compares the evolution of the lift and drag for $T = 0$ to $T = 40$. We see that our numerical scheme performs very similar to the literature [52]. However, there is a slight difference, which is due to the under-resolution of the Eulerian domain downstream of the cylinder, making the wake our Eulerian method more dissipative than the Lagrangian reference method used by Koumoutsakos and Leonard [39].

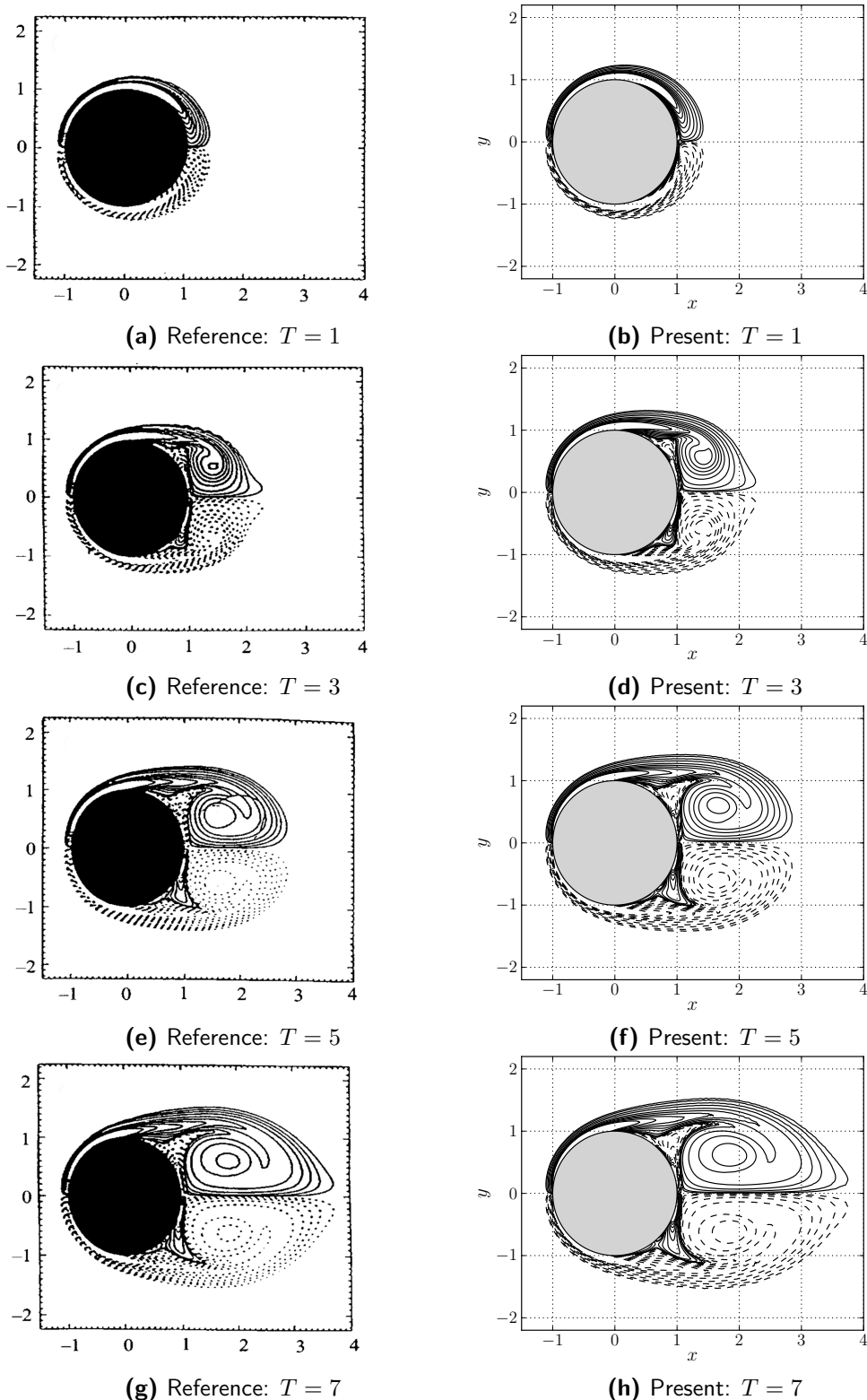


Figure 3.16: Comparison of the vorticity contours for $T = [1, 3, 5, 7]$ with contour levels $[-7, \dots, -2, -1, -0.5, -0.2, -0.1, 0.1, 0.2, 0.5, 1, 2, \dots, 7]$, showing negative vorticity (solid) and positive vorticity (dotted). The present study (right) is compared with plots obtained from Koumoutsakos and Leonard [39] (left).



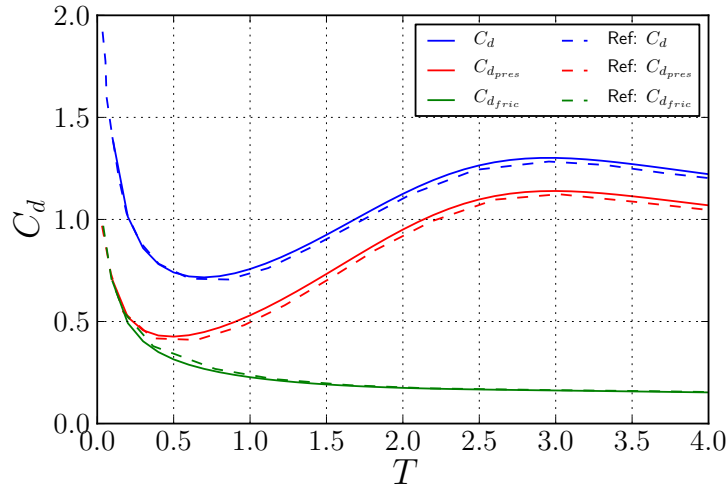


Figure 3.17: Evolution of drag force. The figure depicts the total drag coefficient C_d [—, solid blue], the pressure drag coefficient $C_{d,\text{pres}}$ [—, solid red] and the friction drag coefficient $C_{d,\text{fric}}$ [—, solid green]. The dotted lines indicate the data obtained from literature, Koumoutsakos and Leonard [39].

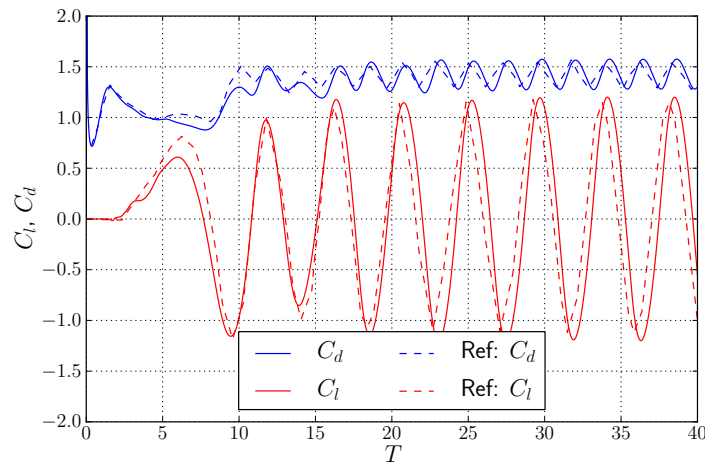


Figure 3.18: Evolution of the lift coefficient C_l and the drag coefficient C_d from $T = 0$ to $T = 40$ with artificial perturbation [42]. The dotted lines represent the data obtained from literature, Rosenfeld et al. [52].

3.6 Summary

In summary, we have investigated the Eulerian domain of our hybrid method in this chapter. The Eulerian method was used to resolve the near-body region where generation of vorticity from the *no-slip* boundary was of concern. The advantage of an Eulerian formulation is that it is much more efficient in resolving the boundary layer than the VPM described in chapter 2. We decided to use a Finite Element Method (**FEM**) to solve the incompressible laminar Navier-Stokes problem of the near-wall region.

In section 3.1, an introduced to the FEM was given. We investigated the theory of finite element discretization, and introduced the concept of functions and function spaces of a finite elements. Finally, we introduced the variational formulation for solving the PDE.

In section 3.2, we introduced FENICS project, a collaborative work of various universities that developed tools to perform automated finite element algorithms. The DOLFIN library of FENICS project provided the finite element library for set up and solve the finite element problem. We used the DOLFIN library wrapped in PYTHON . It uses automated code generation thus maintaining high-level mathematic expressions but still provided an efficient, a multi-threaded performance. GMSH mesh generation tool was used to generate the unstructured mesh of the fluid domain.

In section 3.3, we investigated the Incremental Pressure Correction Scheme (**IPCS**) for solving the incompressible Navier-Stokes equations. The scheme allows us to decouple the velocity \mathbf{u} and pressure p from the momentum equation. Furthermore, we determined an approach for solving the vorticity field, which was computationally efficient.

In section 3.5, we verified and validated our implementation of the Eulerian method. A Lamb-Oseen Vortex test case was used to verify the implementation of the Eulerian method, and concluded that the method had a 1st-order convergence in time and 2nd-order convergence in space. To validate the calculation of vorticity and the vorticity production of the no-slip boundary, we used the high-fidelity numerical test case of Clercx and Bruneau [15]. The literature studied the collision of dipole with the wall, investigating the change in kinetic energy E , enstrophy Ω , and Palinstrophy P over time. Furthermore, we compared the generation of vorticity at the boundary, validating a consistent result.

The final test case involved simulating an impulsively started cylinder at $Re = 550$. We investigated the shedding of vorticity in time progress and observed that it matched the reference data provided by Koumoutsakos and Leonard [39]. We also investigated the long term evolution of the lift and drag of the cylinder, and observed that the frequency and the amplitude of the oscillation was similar to literature study of Rosenfeld et al. [52].

3.7 Chapter Nomenclature

Latin Symbols

A	Coefficient matrix	-
<i>b</i>	Right-Hand-Side	-



c	Reference length (chord)	m
C_d	Drag coefficient	-
C_l	Lift coefficient	-
CFL	CFL number	-
$\hat{\mathbf{e}}$	Cartesian unit vector	-
E	Kinetic Energy	J
f	Source terms	-
\mathbf{I}	Identity matrix	-
$\hat{\mathbf{n}}$	Unit normal vector	-
N_{cells}	Number of FE mesh cells	-
N_t	Number of time integration steps	-
p	Pressure	Pa
	Trial function for pressure	-
\mathcal{P}	Lagrange polynomial	-
q	Degree of Lagrange polynomial \mathcal{P}_q	-
	Test function for pressure	-
Q	Scalar-valued function space for pressure p	-
Re	Reynolds number	-
t_n	Simulation time at n^{th} step	s
\mathcal{T}_h	Finite Element mesh	-
T	Cell of Finite Element mesh	-
\mathbf{u}	Velocity	m s^{-1}
	Trial function for velocity	-
\mathbf{u}^*	Tentative velocity	m s^{-1}
v	Test function for velocity	-
V	Trial vector function space for velocity	-
\hat{V}	Test vector function space for velocity	-
w	Trial function for vorticity	-
x	Test function for vorticity	-
X	Scalar-valued function space for vorticity ω	-

Greek Symbols

Γ	Circulation	$\text{m}^2 \text{s}^{-1}$
Δh	Mesh cell size	m
Δt_E	Eulerian time step size	s
ϵ	Symmetric gradient	-
ν	Kinematic viscosity	$\text{kg s}^{-1} \text{m}^{-1}$
ρ	Fluid density	kg m^{-3}
σ	Cauchy stress tensor	Pa
Σ_d	Dirichlet velocity boundary	-

Σ_{pres}	Pressure outlet boundary	-
Σ_{wall}	No-slip wall boundary	-
ψ	Basis function	-
ψ	Basis function	-
ω	Vorticity	s^{-1}
Ω	Fluid domain	-
Ω_E	Eulerian fluid domain	-
$\partial\Omega$	Boundary of the domain Ω	-



Chapter 4

Hybrid Eulerian-Lagrangian Vortex Particle Method

Chapter 1 introduces the Hybrid Eulerian-Lagrangian Vortex Particle Method ([HELVPMP](#)), a domain decomposition method, where the Eulerian solver and the Lagrangian solver are used to solve different domains of the fluid. The algorithm that we use to couple the two solver is a modified version of approach used by Stock [59] and Daeninck [23]. The algorithm that we employ is summarized as follows:

1. **Correct Lagrangian:** Use the solutions of the Eulerian solver in the near-wall domain Ω_E to correct the solution of the Lagrangian solver, with key requirement that circulation is conserved.
2. **Evolve Lagrangian:** Evolve the newly adjusted Lagrangian solution from time t_n to t_{n+1} . The procedures of the Lagrangian solver is elaborated in Chapter 2.
3. **Determine Eulerian boundary conditions:** Use the Lagrangian solution at time t_{n+1} to determine the boundary conditions for time marching the Eulerian solver from t_n to t_{n+1} .
4. **Evolve Eulerian:** Evolve the Eulerian solver with the newly acquired boundary condition from t_n to t_{n+1} . The procedures of the Eulerian solver is elaborated in Chapter 3.

The coupling of the Eulerian and the Lagrangian solver is done at steps 1 and 3. In step 1, the Eulerian solution is transferred to the Lagrangian solver, whereas in step 3, we use the Lagrangian solution back to time-march the Eulerian solver. This chapter will be dedicated to elaborate the procedures of step 1 and step 3.



4.1 Decomposition of the domain

The hybrid solver decomposes the fluid domain into two subdomains: the near-body region, referred to as the Eulerian domain Ω_E where the Eulerian solution of the Eulerian solver is valid; and the wake region, referred to as the Lagrangian domain Ω_L where the Lagrangian solution of the Lagrangian solver is valid. Figure 4.1 shows this segregation of the fluid into these two regions. To ensure that the two solvers are coupled, where steps 1 and 3 can be performed correctly, the Lagrangian domain Ω_L is overlapped with the Eulerian domain Ω_E completely, such that $\Omega_E \subset \Omega_L$.

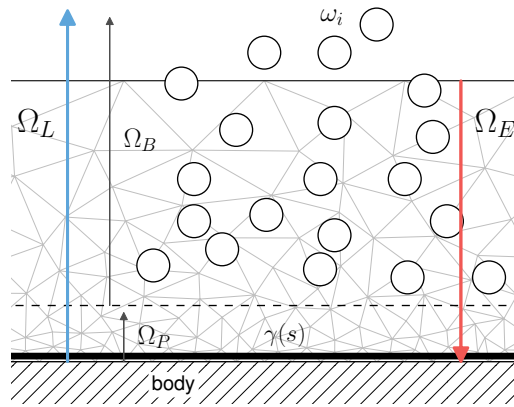


Figure 4.1: Schematic of the domain decomposition. The two subdomain are the Lagrangian domain $\Omega_L : \Omega_p \cup \Omega_b$ and the Eulerian domain Ω_E where $\Omega_E \subset \Omega_L$.

The Lagrangian domain Ω_L is further divided into two subdomains: the vortex blob domain Ω_b where the vortex blobs $\mathbf{x}_i \in \Omega_B$ resolve the vorticity ω ; and the vortex panel domain Ω_p consisting of the wall-bounded vorticity resolved by the vortex panel at the surface $\mathbf{s} \in \partial\Omega_{body}$. This division of the Lagrangian domain Ω_L to Ω_b and Ω_p such that $\Omega_L = \Omega_p \cup \Omega_b$ is elaborated in section 2.5. The vortex panel was required to efficiently represent the singular vorticity distribution of the wall-bounded vortex sheet and further was necessary to enforce the wall boundary condition for the Lagrangian solver.

Therefore, the decomposition of the fluid domain is as follows:

$$\text{fluid} : \quad \begin{cases} \Omega_E & \{ \text{Eulerian domain} \}, \\ \Omega_L = \Omega_p \cup \Omega_b & \{ \text{Lagrangian domain} \}, \end{cases} \quad (4.1)$$

and should satisfy the following requirements:

- Eulerian domain belongs to the near-wall region of the Lagrangian domain, $\Omega_E : \Omega_E \subset \Omega_L$, bounded by the wall $\partial\Omega_{body}$ and the exterior Eulerian boundary $\partial\Omega_E$ such that $\Omega_E : \Omega_E \in [\partial\Omega_{body}, \partial\Omega_E]$.
- Vortex panel domain Ω_p belongs to the near-wall region of the Eulerian domain, $\Omega_p : \Omega_p \subset \Omega_E$, bounded by the wall $\partial\Omega_{body}$ and the boundary $\partial\Omega_p$ such that $\Omega_p : \Omega_p \in [\partial\Omega_{body}, \partial\Omega_p]$.

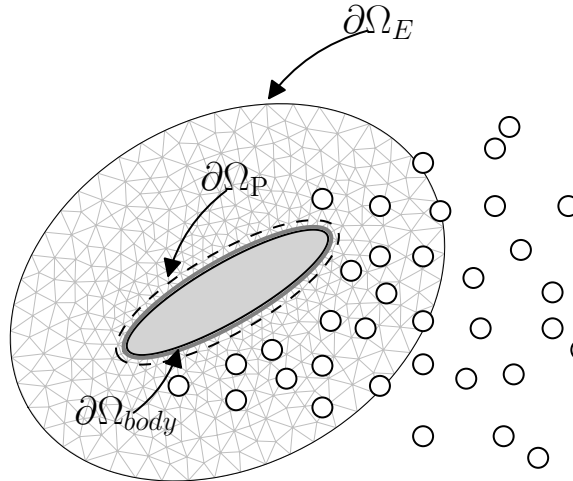


Figure 4.2: Boundaries of the decomposed domains. No-slip boundary $\partial\Omega_{body}$, exterior vortex panel boundary $\partial\Omega_p$, exterior Eulerian boundary $\partial\Omega_E$.

- Vortex blob domain Ω_b resolves the off-wall region of the Lagrangian domain $\Omega_b = \Omega_L \setminus \Omega_p$, overlaps with the Eulerian domain $\Omega_b \cap \Omega_E \neq \emptyset$. The vortex vortex blob domains starts from panel exterior boundary $\partial\Omega_p$ and continuous to full fluid domain, $\Omega_b : \Omega_b \in [\partial\Omega_p, \infty)$.

During the decomposition of the domain, we defined three boundaries, figure 4.2:

- $\partial\Omega_{body}$: No-slip wall boundary of the Eulerian domain Ω_E and the vortex panel domain Ω_p .
- $\partial\Omega_p$: External boundary of the vortex panel domain Ω_p .
- $\partial\Omega_E$: External boundary of the Eulerian domain $\partial\Omega_E$ where the Dirichlet velocity boundary condition will be prescribed.

The solutions in the overlap region $\Omega_E \cap \Omega_L$ will be used to couple the Eulerian and the Lagrangian solver, based on the procedures of Stock [59] and the Daeninck [23].

4.1.1 Local to Global Transformation

The geometries in the simulation are defined in their respective local coordinate system $[x, y]'$. Figure 4.3a shows an elliptical geometry defined in its local coordinate system about its origin $[x_o, y_o]'$. The origin point is defined such that it is the center of rotation and any rotation will be prescribed about the origin point.

The body is then transformed to the global coordinate system $[x, y]$ by the displacement vector $[x_o, y_o]$ and a local rotation by θ_{loc} about the local origin $[x_o, y_o]$.

The Eulerian solver defines the body mesh in the local coordinate system is then transformed to global position using these parameters. Similarly, the panel geometry for the Lagrangian solver is defined in the same fashion. For a moving problems, the displacement vector and the local rotation angle can be updated to prescribe the motion.



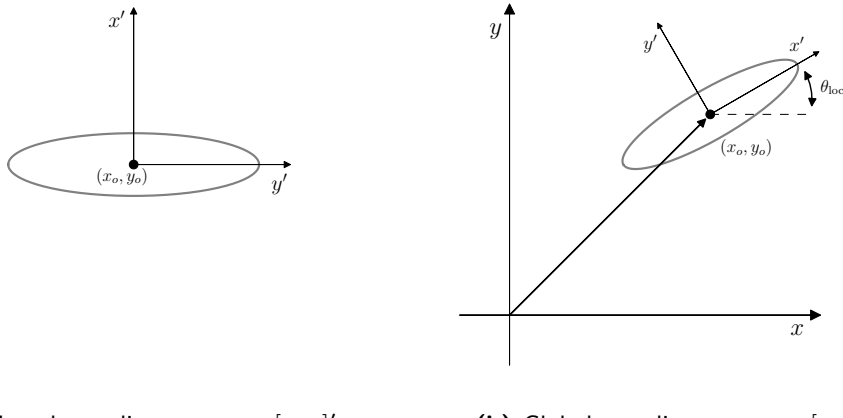
(a) Local coordinate system $[x, y]'$ (b) Global coordinate system $[x, y]$

Figure 4.3: Elliptical geometry in (a) the local coordinate system and (b) the global coordinate system. The geometry is positioned using the displacement vector $[x_o, y_o]$ and rotated by θ_0 about the local origin point.

4.2 Correction of Lagrangian domain

The first step of the hybrid coupling scheme is to transfer the highly resolved Eulerian solution from the Eulerian solver to the Lagrangian solver. The vorticity in the domain Ω_E is transferred from the grid of the Eulerian solver onto the vortex blobs.

4.2.1 Approach from literature

This is the approach used by Stock [59] and is based on the assumption that the Eulerian solution is correct from the body up to ‘somewhat inside of the outer Eulerian domain’, and the Lagrangian solution is correct outside the outer Eulerian boundary. Figure 4.4 shows Daeninck’s [23] result of hybrid coupling. It shows the vorticity field behind a cylinder and at the outer boundary $\partial\Omega_E$ one can observe a slight mismatch in the vorticity, and some artificial vorticity. Daeninck has observed this and stated that this is due to the slight difference in the solution of the two solvers.

Stock solution to this problem was to interpolate only part of the Eulerian domain of the Eulerian solver onto the Lagrangian solver ignoring the regions of incorrect vorticity field. This introduces the definition of the interpolation region Ω_{int} , as shown in figure 4.5a. In addition to the outer boundary region, Stock also proposed to ignore the boundary layer region during interpolation to the vortex blobs. His reasoning for ignoring this region during the correction process was that because the boundary layer has very strong vorticity gradient, they cannot be efficiently represented using the Gaussian vortex kernels. To resolve this singular vorticity distribution, we have to use boundary elements such as the vortex panel kernels, which can efficiently represent such distribution. Therefore, the interpolation region Ω_{int} , figure 4.5, has the following properties:

- The region is within the overlap region $\Omega_E \cap \Omega_b$ such that $\Omega_{int} : \Omega_{int} \subset \Omega_E \cap \Omega_b$.

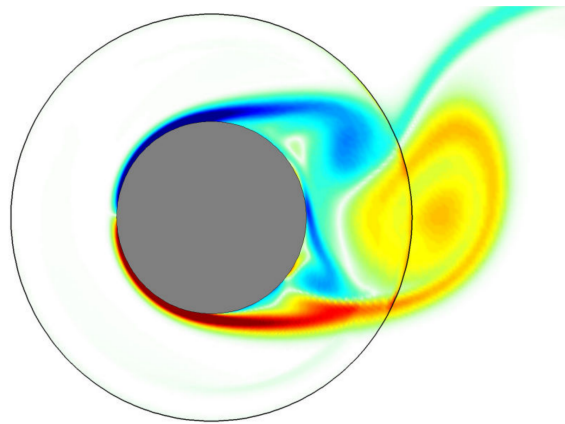


Figure 4.4: Result of hybrid coupling by Daeninck [23]. The figure shows artificial vorticity at the boundary of the Eulerian domain.

- The region starts from the outer vortex panel boundary $\partial\Omega_p$. All the vorticity of the vortex panel boundary is represented using the vortex panels. The interpolation region ends at $\partial\Omega_{int}$, slight distance away from the outer Eulerian boundary $\partial\Omega_E$ ignoring the region of incorrect vorticity, as shown in figure 4.4.
- The offset of the interpolation region boundaries are in the order of the nominal vortex blobs spacing h . The boundary $\partial\Omega_p$ is offset by $d_{surf} \cdot h$ from the surface $\partial\Omega_{body}$, where Stock used $d_{surf} = 3$. The boundary $\partial\Omega_{int}$ is offset by $d_{bdry} \cdot h$ from the outer Eulerian boundary $\partial\Omega_E$, where Stock used $d_{bdry} = 2$.
- For an M'_4 interpolation kernel and for high Re flows, Stock [59], stated that $d_{surf} = 3$ and $d_{bdry} = 2$ will ensure proper interpolation of the solutions.

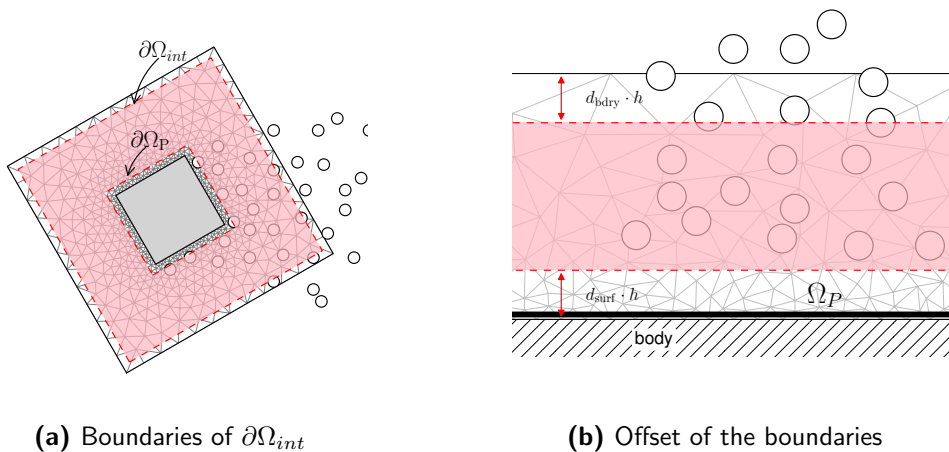


Figure 4.5: Definition of the interpolation region $\partial\Omega_{int}$ with the boundaries: $\partial\Omega_p$ and $\partial\Omega_{int}$.



The summary of the interpolation algorithm used by Stock [59] based on the works of Daeninck [23] and Guermond and Lu [30] for interpolation the Eulerian solution onto the vortex blobs is as follows:

1. Interpolate the solution from Eulerian domain onto a temporary structured grid. The temporary structured grid has $\Delta x = \Delta y = h$, the nominal particle spacing and covers the entire Eulerian domain.
2. Identify the particles inside the interpolation region Ω_{int} . Fill gaps in the region with zero-strength particles, so that we can interpolate the Eulerian solution onto them.
3. Reset the strengths of the particles \mathbf{x}_i inside the interpolation region Ω_{int} , figure 4.5a, using the local particle volume and the vorticity interpolated from the grid (i.e $\alpha_i = \omega_i \cdot h^2$).

However, during our research we have determined that this approach suffers from some issues and mainly does not guarantee that the circulation is conserved.

4.2.2 Issues with the correction algorithm

The two main issues with the above approach is as follows:

- The vorticity bounded to the solid wall was not interpolated to the vortex blobs.
- The particle strength initialization using the cell circulation equation, $\alpha_i = \omega \cdot h^2$, does not ensure the local conservation of circulation.

Vorticity at the solid wall

The first problem that we are concerned is that the vorticity bounded at the solid wall of the Eulerian solver was not transferred to the Lagrangian solver. Stock [59] use a Lagrangian solver with BEM that diffuses the vortex sheet to the vortex blobs. However, we implemented the approach of Daeninck [23], that requires the Eulerian solver to introduce the vorticity generated at the wall to the Lagrangian solver.

To ensure that all the vorticity in fluid is represented, we will use the vortex panels to represent the vorticity of the boundary layer region Ω_p . Furthermore, if the body is in motion, the body will contain circulation due to the motion,

$$\Gamma_{body} = \iint_{body} \nabla \times \mathbf{u}_b \, dA. \quad (4.2)$$

To ensure that all the vorticity is transferred from the Eulerian solver to the Lagrangian solver, we propose to modify Stock's algorithm to transfer the circulation of the domain Ω_p and the circulation in the body Γ_{body} to the vortex panels such that we do not violate the conservation of circulation.

Vorticity Field interpolation error

The second issue we must tackle is the interpolation error that arises due to the standard approach of initializing the particles using the local particle volume and the local vorticity,

$$\alpha_i = \omega_i \cdot h^2, \quad (4.3)$$

where i corresponds to the vortex blobs $\mathbf{x}_i \in \Omega_{int}$. We summarized this issue in the section 2.2.4 of the Lagrangian chapter which was extensively investigated by Barba and Rossi [1]. To solve the wake domain of the fluid, we used a vortex particle method that discretizes the vorticity field using N quadrature points,

$$\omega \approx \omega^h(\mathbf{x}_j) = \sum_{i=1}^N \alpha_i \delta(\mathbf{x}_j - \mathbf{x}_i). \quad (4.4)$$

To remove the singularity of the kernel δ , we used a smooth Gaussian kernel ζ_σ . This approach of using vortex blobs is common in the research of vortex particle method and ensures continuous vorticity distribution. However, the downside to this approach is that on top of the discretization error, we now introduce the “smoothing error” or the “regularization error” due to the use of gaussian kernel. This is equivalent to blurring the vorticity field, as explained by Barba and Rossi [1], and the cumulative error in the initialization error is given as:

$$\text{Error} = \text{Smoothing Error} + \text{Discretization Error}$$

To perform accurate interpolation of the vorticity ω inside the interpolation domain Ω_{int} onto the particles $\mathbf{x}_j \in \Omega_{int}$, we must satisfy the following interpolation problem:

$$\omega(\mathbf{x})|_{\text{Eulerian Solver}} = \hat{\omega}(\mathbf{x})|_{\text{Lagrangian Solver}}, \quad (4.5)$$

where the $\omega(x)|_{\text{Eulerian Solver}}$ is the Eulerian solution from the Eulerian solver, and the smoothed Lagrangian vorticity from the Lagrangian solver is given as,

$$\hat{\omega}(\mathbf{x}) = \sum_{i=1}^N \alpha_i \zeta_\sigma(\mathbf{x} - \mathbf{x}_i). \quad (4.6)$$

The discrete vorticity field is represented by the linear combinations of the Gaussian basis function ζ_σ with the vortex blob strength α_i . Therefore taking that $\alpha_i = \omega(\mathbf{x}_i) \cdot h^2$ is mathematically incorrect and does not ensure the interpolated vorticity field matches the original vorticity distribution from the Eulerian solver.

We discussed the Beale’s iterative method for retaining the original vorticity distribution in section ???. ??, however this approach cannot be employed for decomposed domains. The Beale’s method uses equation 4.6 to construct a linear system of equation to directly solve for the particle strengths α_i :

$$\mathbf{A}_{ij} \alpha_i = \omega_i, \quad (4.7)$$

where the coefficient matrix \mathbf{A} is given as,

$$\mathbf{A}_{ij} = \zeta_\sigma(\mathbf{x}_j - \mathbf{x}_i). \quad (4.8)$$



However inverting the matrix \mathbf{A} is still an open question, as stated by Koumoutsakos and Cottet [21], and was the primary investigation of Barba and Rossi [1]. The problem is that the matrix \mathbf{A} is full and badly condition for direct inversion. For a global field interpolation (i.e for unbounded domain), one could use the Beale's iterative method which uses a successive over-relaxation (**SOR**) for solving the equation 4.8. This method relies on iterative correction of all the particles $\mathbf{x}_i \in \Omega_L$, in the full Lagrangian domain. However, in our case of initializing the strengths of the particles \mathbf{x}_i in the sub-domain Ω_{int} of the Lagrangian domain Ω_L , it would require us to modify the strength of only the particles \mathbf{x}_i in Ω_b . In such case, the Beale's iterative method is not valid and cannot be used. Therefore, the Beale's method cannot be used to solve the problem of the smoothing error.

In future, the key to solving this smoothing error might be in the research works of Barba and Rossi [1], where they try to reverse the blurring of the vorticity field by reversing the “diffusion” caused by the smoothing kernel. However, currently for our investigation the best possible way of ensure minimal interpolation error from Eulerian domain onto vortex blobs is to perform the following steps:

- Minimize the smoothing and discretization error by maximizing the particle resolution, achieved by setting $Ov = 1$ and reducing σ such that the relative error $\epsilon \leq 5\%$. The convergence of the overlap Ov and the core spreading σ was investigated in section 2.2.5.
- A vital requirement for vortex particle method is the conservation of circulation. Therefore, to ensure that the Hybrid method is valid, we ensure that the interpolation of the vorticity from the Eulerian solver to the Lagrangian solver satisfies the conservation of circulation.

Thus, we will modified the approach of Stock [59] to ensure that all the vorticity is transferred from the Eulerian solver to the Lagrangian solver and that we satisfy the conservation of circulation.

4.2.3 Modified correction strategy

The modified version of the correction can be divided into five steps

1. **Probe vorticity:** Interpolate the vorticity from the unstructured Eulerian mesh onto a uniform structured grid.
2. **Remove particles:** Remove particles that are inside the interpolation domain Ω_{int} .
3. **Generate particles:** Generate zero-strength particle inside the interpolation domain Ω_{int} .
4. **Assign strengths:** Use the standard particle initialization approach, $\alpha_i = \omega_i \cdot h^2$ to assign the particles \mathbf{x}_i .
5. **Conserve circulation:** Determine the mismatch in the total circulation of the Lagrangian field as determine the strength of the panels such that circulation is conserved.

Probe vorticity

The first sub-step of the correction step is to interpolate the vorticity from the unstructured Eulerian grid onto a uniform structured grid. The purpose of the structured grid is to perform fast and efficient interpolation of vorticity from the Eulerian domain onto the vortex blobs.

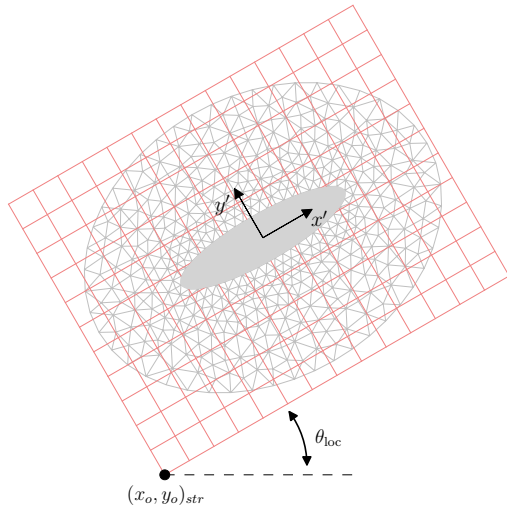


Figure 4.6: Structured interpolation grid \mathbf{x}_{str} (pink) covering the entire Eulerian mesh (gray).

The structured grid \mathbf{x}_{str} is defined in the local coordinates system of the geometry $[x, y]'$ where the grid covers the entire Eulerian domain Ω_E . Figure 4.6 shows the structured grid bounded to the Eulerian domain in the global coordinate system. The vorticity function ω of the function space X of the Eulerian solver is interpolated from the unstructured mesh \mathbf{x}_{unstr} onto the structured uniform grid \mathbf{x}_{str} ,

$$\hat{\omega}_i = \sum_k \omega_k W_{ki} \quad (4.9)$$

using the interpolation weight W , where $\hat{\omega}$ is the interpolated vorticity. Figure 4.7 shows a depiction of the transfer of the vorticity from the unstructured grid to the structured grid. As the structured grid \mathbf{x}_{str} that does not move w.r.t to the unstructured mesh \mathbf{x}_{unstr} , the interpolation weight W only needs to be calculated once, ensuring fast interpolation. We used the `Probe` function, a C++ implementation developed by Mortensen [47], to probe the vorticity function space X for the structured vorticity $\hat{\omega}$ at the nodes of the structured grid \mathbf{x}_{str} .

Once we have determined $\hat{\omega}$, we can assign the strengths of the particles using an efficient index search algorithm to find the location of the particle in the structured grid. If we had not used this approach and directly transferred the vorticity from the unstructured mesh \mathbf{x}_{unstr} onto the vortex blobs \mathbf{x}_i , at each iteration we would require an expensive search algorithm to determine the position of the blob w.r.t to the nodes of the unstructured grid. This would mean that we would have to construct the interpolation matrix at each iteration, drastically reducing the efficiency of interpolation.



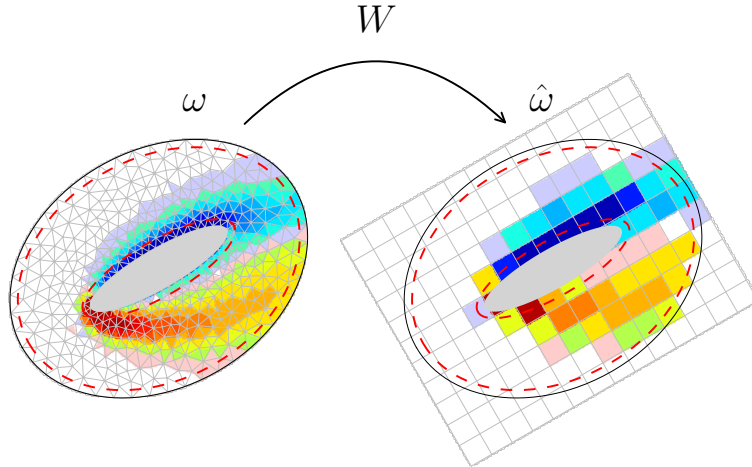
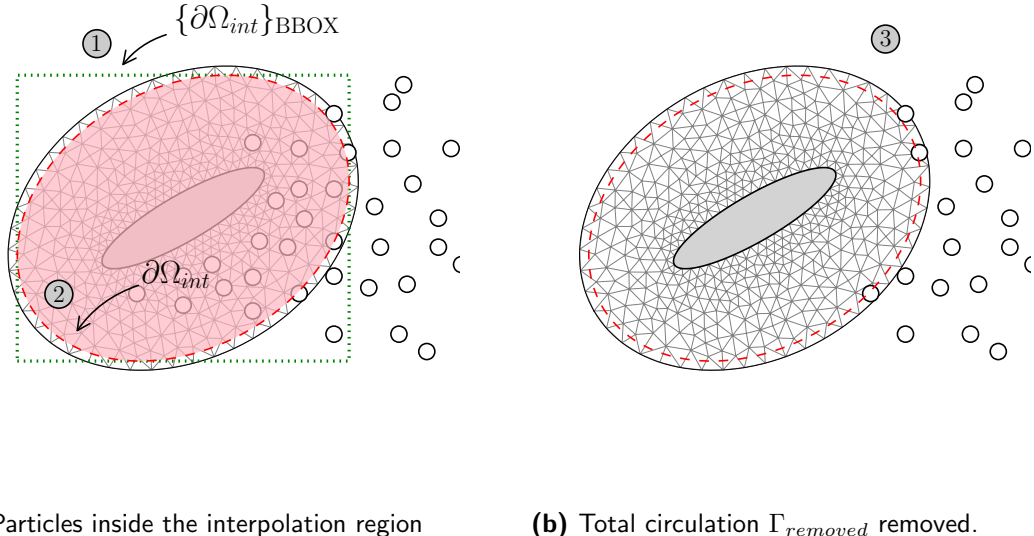


Figure 4.7: Interpolated vorticity $\hat{\omega}$ on the structured grid x_{str} from interpolating ω of the unstructured grid x_{unstr} with the interpolation weights W .

Remove particles

The second sub-step of the correction step is remove the particles that are inside the interpolation region Ω_{int} and the vortex panel domain Ω_p . The purpose of this step is that we want to ultimately correct the Lagrangian solution in these regions with the more refined Eulerian solution of the domain Ω_E . To perform the coupling, we first need to remove the particles in the region of correction Ω_{int} and Ω_p . Figure 4.8a shows the vortex blobs x_i inside the boundary $\partial\Omega_{int}$ that needs to be removed. To see which particles are inside, we need to perform a “Point inclusion in polygon” test to determine which



(a) Particles inside the interpolation region

(b) Total circulation $\Gamma_{removed}$ removed.

Figure 4.8: The interpolation region Ω_{int} , bounded by the boundary polygons: panel region boundary $\partial\Omega_P$ near the wall, and exterior boundary $\partial\Omega_{int}$ near the outer region.

particles \mathbf{x}_i are within the boundary polygon $\partial\Omega_{int}$. However, this point-in-polygon search is computationally expensive but can be simplified by neglecting the particles outside the minimum bounding box of the polygon. Thus the steps to remove the vortex blobs inside the interpolation region is as follows:

1. Determine which particles inside the bounding box of the polygon $\partial\Omega_{int}$.
2. Perform a point-in-polygon test for only the particles $\mathbf{x}_i \in \text{BBOX}\{\partial\Omega_{int}\}$.
3. Remove the particles \mathbf{x}_i from the total set of particles, resulting in a total circulation change of $\Gamma_{removed}$.

To perform the point-in-polygon test, we used the `pnpoly` function of `matplotlib`, the python 2D plotting library created by Hunter [33]. The function implemented the “point inclusion in polygon” test algorithm developed by Franklin [27]. The algorithm is based on the crossings test, which determines whether the point is inside the polygon by determining the number of the times a semi-infinite ray originating from the point intersects with the polygon.

Generate particles

The third sub-step of the correction step is generate zero-strength particles inside interpolation region Ω_{int} , figure 4.9. These zero-strength particles will later be corrected with the strengths obtained from the structured grid \mathbf{x}_{str} .

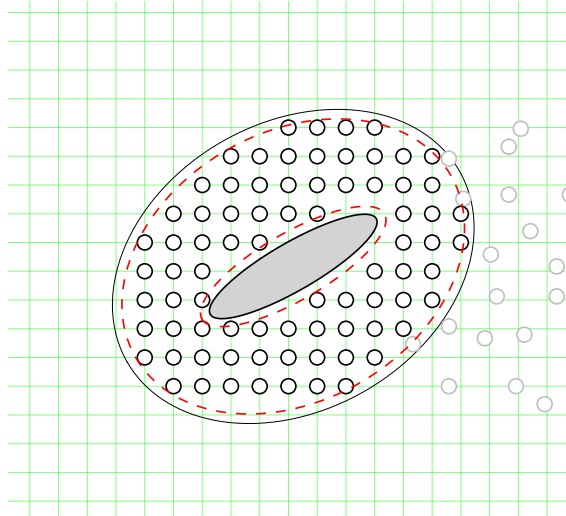


Figure 4.9: Particles inside the interpolation domain Ω_{int} located at \mathbf{x}_i coinciding the Lagrangian remeshing grid.

The procedures of generating zero-strength particles are as follows:

1. Generate zero-strength particles \mathbf{x}_i inside the bounding box of the boundary polygon $\partial\Omega_{int}$, $\mathbf{x}_i \in \text{BBOX}\{\partial\Omega_{int}\}$. The position of the particles \mathbf{x}_i coincides with the global Lagrangian remeshing grid (shown in green), such that particles are equally spaced.



2. Perform a point-in-polygon test for the particles \mathbf{x}_i , so that we can neglect the particles outside of the interpolation boundary $\partial\Omega_{int}$, the particles inside the body Ω_{body} , and the particles inside the vortex panel domain Ω_p , leaving us only the particles $\mathbf{x}_i \in \Omega_{int}$.

Figure 4.9 shows the newly generated particles (in black) and the pre-existing set of particles (in gray). Once we have uniformly distributed particles covering all the regions of the interpolation region Ω_{int} , we can transfer the solution from the Eulerian solver to the Lagrangian solver.

Assign strengths

The fourth sub-step of the correction is to assign the strengths to the newly generated particles in the interpolation domain Ω_{int} . The strengths of the particles α_i is determined using the standard method,

$$\alpha(\mathbf{x}_i) = \hat{\omega}(\mathbf{x}_i) \cdot h^2, \quad (4.10)$$

where the local circulation inside the area h^2 is assigned to the particle. We have minimized the h^2 interpolation area such that the smoothing error caused the Gaussian kernel is acceptable, see section 2.2.5. Therefore, to determine the strength of the particles inside the interpolation region, we simply require the vorticity $\hat{\omega}(\mathbf{x}_i)$ at the local \mathbf{x}_i . We have interpolated the vorticity from the unstructured finite element grid nodes onto a structure grid \mathbf{x}_{str} . We can transfer the vorticity from the structured grid onto to vortex blobs using an efficient Bilinear interpolation algorithm.

Figure 4.10 shows the schematic representation of the Bilinear interpolation of vorticity. The vortex blob (in blue) is located inside the one of the cells of the structured grid (in

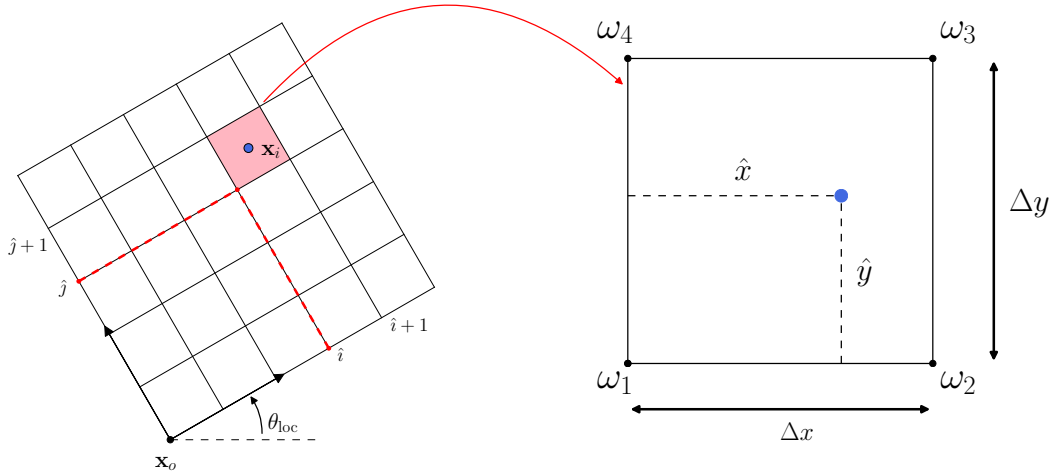


Figure 4.10: Interpolating the strengths from the structured grid \mathbf{x}_{str} onto the vortex blobs \mathbf{x}_i using a bilinear interpolation

pink), bounded by 4 grid nodes:

$$\begin{aligned} p_1 &= \mathbf{x}_{i,j}, \\ p_2 &= \mathbf{x}_{i+1,j}, \\ p_3 &= \mathbf{x}_{i+1,j+1}, \\ p_4 &= \mathbf{x}_{i,j+1}. \end{aligned} \quad (4.11)$$

The four nodes p_1, \dots, p_4 are defined in the anti-clockwise direction. The bilinear interpolation of the vorticity becomes,

$$\hat{\omega}(\mathbf{x}_i) = \sum_{k=1}^4 W_k \cdot \omega_k \quad (4.12)$$

where $\{\omega_k, W_k\} \mapsto p_k$. The interpolation weights W_k are defined as

$$\begin{aligned} W_1 &= \frac{(\hat{x} - \Delta x)(\hat{y} - \Delta y)}{\Delta x \Delta y} \\ W_2 &= \frac{-\hat{x}(\hat{y} - \Delta y)}{\Delta x \Delta y} \\ W_3 &= \frac{\hat{x}\hat{y}}{\Delta x \Delta y} \\ W_4 &= \frac{-\hat{y}(\hat{x} - \Delta x)}{\Delta x \Delta y} \end{aligned} \quad (4.13)$$

where the cell of the structured grid has dimension $[\Delta x, \Delta y]$, with $\Delta x = \Delta y$. The coordinates of the blobs are normalized such that, the vortex blobs is located at $0 \leq \hat{x} \leq \Delta x$ and $0 \leq \hat{y} \leq \Delta y$. Figure 4.11 shows the results of the assigning the strengths of the particles from the structured grid.

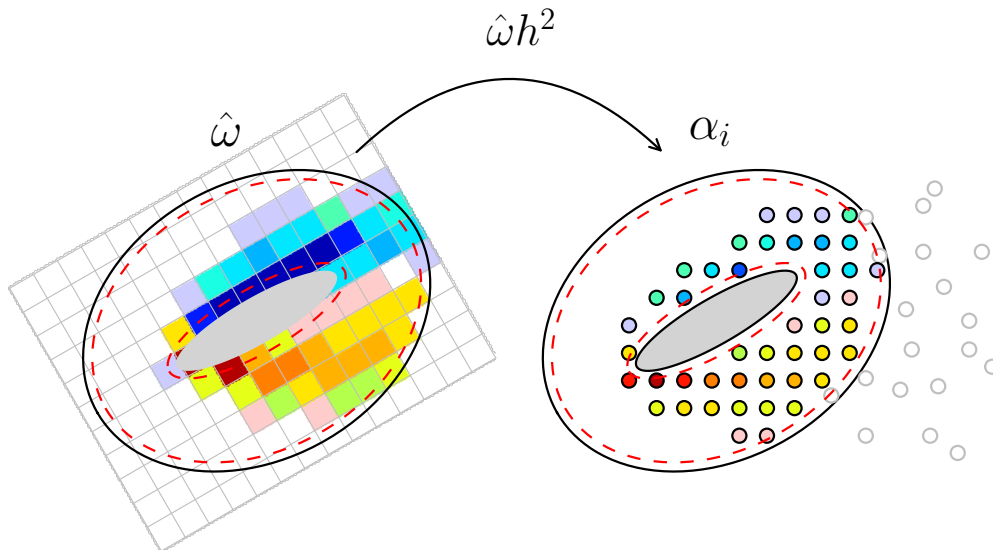


Figure 4.11: Interpolated strengths α_i from the structured grid \mathbf{x}_{str} using bilinear interpolation.



Conserve circulation

The fifth and the final step of correcting the Lagrangian field is to ensure that the we have to ensure that circulation is conserved. Two main source of errors for the conservation of circulation is the vorticity at the solid wall, and the vorticity field interpolation error.

The vorticity at the solid was not transferred to particles because the Gaussian kernels cannot efficiently represent the singular distribution. However, we cannot simply neglect this distribution and therefore we use the vortex panels to represent these. To ensure that the conservation of circulation is satisfied in the Lagrangian solver, we will prescribe the integral strengths of the panels (i.e the total circulation).

The second error is the vorticity field interpolation error. The correction algorithm so far does satisfy the conservation of circulation, so we will employ Kelvin's circulation theorem to ensure circulation is conserved. If we are dealing with fluid flow with initial total circulation $\Gamma_0 = 0$, then according to Kelvin's circulation theorem, we require that at all times t ,

$$\Gamma_{\text{panels}} + \Gamma_{\text{blobs}} = 0. \quad (4.14)$$

Thus, to ensure that the circulation is conserved, we have to solve for the no-slip panels such that the total circulation is zero. However, in a general case (especially when we are dealing with multiple bodies), we have to formulate the equality in a different manner. We have to define two regions of the flow, domain where Eulerian solution is valid,

$$\Omega_{\text{inside}} = \Omega_{\text{body}} \cup \Omega_p \cup \Omega_{\text{int}}, \quad (4.15)$$

and domain where Lagrangian solution is valid,

$$\Omega_{\text{outside}} = \Omega_L \setminus \Omega_{\text{inside}}. \quad (4.16)$$

The total circulation of the Lagrangian solver now becomes,

$$\Gamma_b^{\text{outside}} + \Gamma_b^{\text{inside}} + \Gamma_p = 0 \quad (4.17)$$

where $\Gamma_b^{\text{outside}}$ is the total circulation in the domain Ω_{outside} , and $\Gamma_b^{\text{inside}} + \Gamma_p$ is the total circulation in the domain Ω_{inside} from the Lagrangian solver. Due to the correction algorithm, we require that the Lagrangian solutions in the domain Ω_{inside} matches the Eulerian solution, therefore we have equality:

$$\Gamma^{\text{inside}} \Big|_{\text{Eulerian Solver}} = \Gamma_b^{\text{inside}} + \Gamma_p \Big|_{\text{Lagrangian Solver}}, \quad (4.18)$$

where Γ^{inside} total circulation from the Eulerian solution in the domain Ω_{inside} . From the equality, we can derived the net circulation of the vortex panels,

$$\Gamma_p = \Gamma^{\text{inside}} \Big|_{\text{Eulerian}} - \Gamma_b^{\text{inside}}. \quad (4.19)$$

Section 2.5 summarized the methodology for solving the no-slip boundary condition using the vortex panel using this prescribed net strengths Γ_p . Due to the slight error in coupling, we have an error in the total circulation ϵ_Γ ,

$$\Gamma_b^{\text{outside}} + \Gamma_b^{\text{inside}} + \Gamma_p = \epsilon_\Gamma. \quad (4.20)$$

To remove this mismatch in total circulation, we will have to modify the strengths of the newly generated vortex blobs such that the total circulation is conserved. The mismatch in total circulation ϵ_Γ is correctly uniformly with all the vortex blobs such that:

$$\hat{\alpha}_i^{inside} = \alpha_i^{inside} - \frac{\epsilon_\Gamma}{N^{inside}}, \quad (4.21)$$

where $\hat{\alpha}_i^{inside}$ is the corrected vortex blob strengths, α_i^{inside} is the previous strengths of the vortex blobs, and N^{inside} is the number of vortex blobs $\mathbf{x}_i \in \Omega_{int}$.

4.3 Evolution of the Lagrangian solution

We have corrected the near-region solution of the Lagrangian domain $\Omega_L \cap \Omega_E$ with solution obtained from the Eulerian solver. Furthermore, we have solved the vortex panels such that: (a) it conserves the total circulation, and (b) it ensure the no-through/no-slip boundary condition. With the initial conditions provided at t_n , we can use the algorithms described in chapter 2, to evolve the Lagrangian solution from t_n to t_{n+1} . We can summarize the several features of the Lagrangian solver as follows:

- A 4th-order Runge-Kutta method is used to time march the vorticity field from t_n to $t_n + 1$.
- The Lagrangian solver has a convection time step size $\Delta t_c = t_{n+1} - t_n$.
- We use Tutty's diffusion scheme such that the diffusion time step size $\Delta t_d = \Delta t_c$. Tutty's diffusion scheme is used in the majority of the cases as it is more versatile as it enables us to diffuse with convection ensure well represented vorticity field at every time t .
- The strengths of the vortex panels γ_i remains constant during t_n and t_{n+1} . This is derived from the assumption that the change in the total circulation in domain Ω_p is small during t_n and t_{n+1} .

Chapter 2 gives a detailed analysis on procedures of the Lagrangian solver.

4.4 Evolution of the Eulerian solution

Once we have evolved the Lagrangian solution from t_n to t_{n+1} , we can determine the boundary conditions for the Eulerian domain for t_{n+1} . In chapter 3, we have determined that to evolve the Eulerian solution, we require: (a) the initial velocity \mathbf{u} distribution at t_n , and (b) the Dirichlet velocity boundary condition \mathbf{u} at the boundary $\partial\Omega_E$ at the final step t_{n+1} .



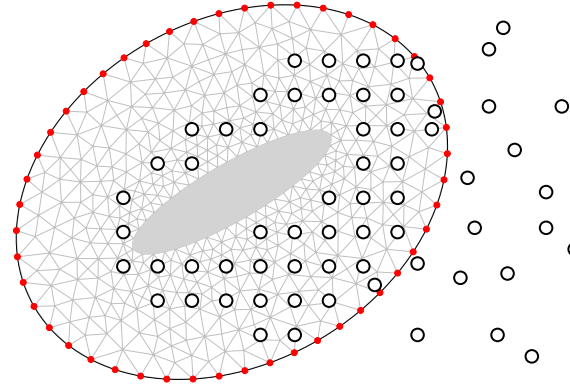


Figure 4.12: Dirichlet boundary conditions at boundary of Eulerian domain $\mathbf{u} \in \partial\Omega_E$. We evaluate the induced velocities from the Lagrangian solution at the nodes of the boundary [•, red dot].

4.4.1 Dirichlet boundary conditions

We can determine the Dirichlet velocity boundary condition at the Eulerian boundary $\partial\Omega_E$ from the Lagrangian vorticity field ω at t_{n+1} . In section 2.2.1, we derived that the discrete mollified velocity field of the vortex blobs. So, the velocity at the Eulerian boundary \mathbf{x}_{bdry} is given an,

$$\mathbf{u}(\mathbf{x}_{bdry}, t_{n+1}) = \sum_p \mathbf{K}_\sigma [\mathbf{x}_{bdry} - \mathbf{x}_p(t_{n+1})] \alpha_p(t_{n+1}), \quad (4.22)$$

where \mathbf{x}_{bdry} are the nodal coordinates of the Eulerian dirichlet boundary $\partial\Omega_E$, as shown in figure 4.12.

4.4.2 Multi-step evolution

When coupling the Eulerian solver with the Lagrangian solver, we will see that the Eulerian time step size $\Delta t_E \leq \Delta t_L$. This is also the main benefit of the domain decomposition such that the wake region can be evolved with much larger step size. So we will have to perform k_E Eulerian sub-steps to reach the Lagrangian step t_{n+1} ,

$$t_k = t_n + k\Delta t_E, \quad (4.23)$$

where $k = 0, \dots, k_E$ and k_E is given as

$$k_E = \frac{t_{n+1} - t_n}{\Delta t_E} = \frac{\Delta t_L}{\Delta t_E}. \quad (4.24)$$

When $k = 0$, we have $t_k = t_n$ and for $k = k_E$, we have $t_k = t_{n+1}$. We have a criterion that Δt_L must be multiple of Δt_E for an integer k_E . Figure 4.13 depicts the multi-stepping of the Eulerian solution from t_n to t_{n+1} to match the Lagrangian time. As the Eulerian solver requires boundary condition at each sub-step, we have to perform a interpolation of the boundary conditions for each sub-step t_k . We can perform a linear interpolation of the boundary condition for determines the boundary conditions at each sub-step,

$$\mathbf{u}(t_k) = \mathbf{u}(t_n) + k\Delta \mathbf{u}, \quad (4.25)$$

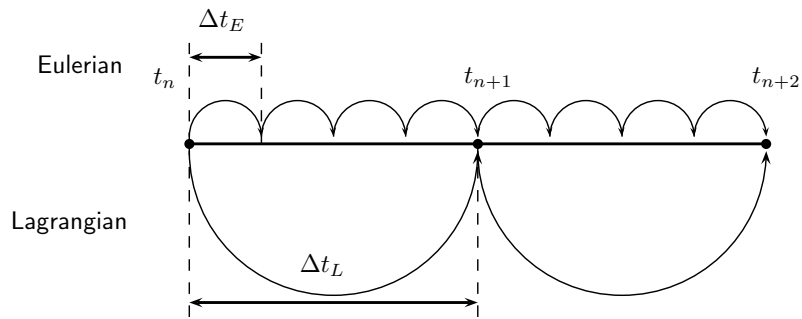


Figure 4.13: Eulerian multi-stepping to match the Lagrangian Δt_L . The figure shows $\Delta t_L = 4\Delta t_E$ and required $k_E = 4$ iterations to time march from t_n to t_{n+1} .

where $\Delta \mathbf{u}$ is given as

$$\Delta \mathbf{u} = \frac{\mathbf{u}(t_{n+1}) - \mathbf{u}(t_n)}{k_E}, \quad (4.26)$$

and is the gradient in velocity between each sub-step. We can summarize the feature of the evolution of the Eulerian solution as follows:

- The Eulerian solver uses a 1st order Forward Euler time-marching scheme to evolution the solution from t_n to t_k .
- The solution is evolved k_E steps to reach t_{n+1} .
- We use velocity-pressure $\mathbf{u} - p$ formulation for the solution in the Eulerian solver.
- At the end of the time-step t_{n+1} , the Eulerian solver will have a higher resolved solution of the wall-region in comparison to the Lagrangian solver.

The modified correction strategy is iterated until we reach the desired time t .

Chapter 3 gives a detailed analysis on procedures of the Eulerian solver.



Chapter 5

Introduction to the Hybrid Solver: pHyFlow

We have implemented the algorithms described in chapter 2, 3, and 4 into pHyFlow, an acronym for **p**ython **H**ybrid **F**low solver. pHyFlow functions a fluid dynamics computational library in python, that has implemented the Eulerian solver, the Lagrangian solver (without vorticity diffusion of panels). These solver can used as a standalone solver (for test purposes), or can be coupled together to make the Hybrid solver.

The features of pHyFlow can be summarized as follows:

- pHyFlow is a hybrid flow solver that uses Hybrid Eulerian-Lagrangian Vortex Particle Method to couple the Navier-Stokes grid solver and a vortex blob solver.
- The algorithms are written in PYTHON , CYTHON [4], C, C++, and CUDA C/C++ for efficiency. All the high-level algorithms such as definition of the problem, coupling of the solver, convection and diffusion of the problem is implemented in PYTHON . The low-level algorithms such as remeshing kernel and saving routine calculations are written in the computationally efficient languages: CYTHON, C, and C++. The parallelizable routine such as calculation of the induced velocity of the vortex blobs is written in CUDA C/C++ for the NVIDIA GPU hardware.
- pHyFlow uses several open-source libraries: FEniCS [44], Fenicstools [47], Scipy [35], Numpy [63], mpi4py [24], pyUblas [37], for performing the calculations; and PyVTK [37], H5py [16], Matplotlib [33] for plotting and efficient data storage.
- pHyFlow is maintained, and is available at the bitbucket online repository <https://bitbucket.org/apalha/phyflow2.0>.

5.1 Program structure

The pHyFlow library serves as a computing environment for PYTHON programming language, where one could solve the hybrid flow problems. To achieve this, we have im-



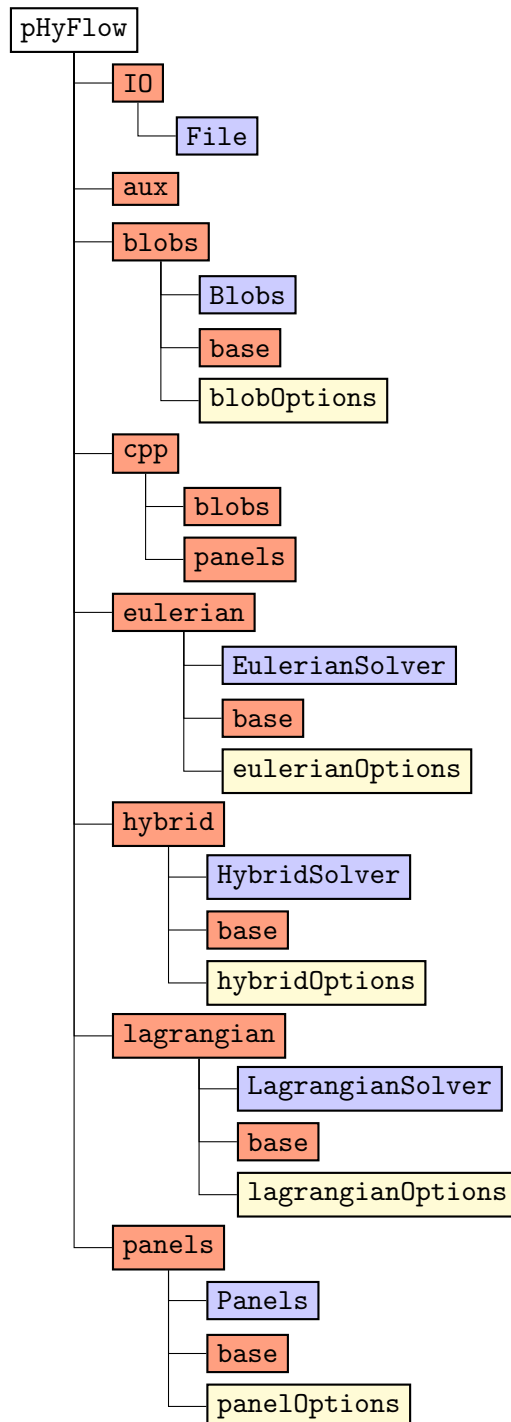


Figure 5.1: Flowchart of the pHyFlow library structured into modules, option script files, and classes.

plemented an Eulerian solver, and a Lagrangian solver (without panel diffusion scheme), which can be used as a standalone solver for verification and validation. The `pHyFlow` library is structured into several modules, categorized by their purposes. In each `module`, we defined a `class` that handles the functions in the module. To add flexibility in computation, we added an `option` file where the user change the solver options. Figure 5.1 shows the structure of the `pHyFlow` library, classified using a color code. The structure of the `pHyFlow` is as follows:

- **IO:** This module contains all the input/output function for saving and plotting data. The `File` class handles the functions of the `IO` module.
- **aux:** This module contains all the auxiliary function of the library that does not belong to the fluid dynamics computation.
- **cpp:** The module that contains all the low-level compiled function that has been wrapped using binding generator for the use in python. The module contains the two main low-level algorithms for performing the induced velocity calculations for vortex blobs and vortex panels, and the remeshing algorithm for the vortex blobs.
- **blobs:** This module contains all the vortex blob operations. The module contains the class `Blobs`, an the vortex blob solver object handling the all the vortex blobs operations. Algorithms of the vortex blobs defined in chapter 2 is implemented in this module.
- **panels:** This module contains all the vortex panel operations and is wrapped in the class `Panels`, an the Panel method solver object. Algorithms of the vortex panel defined in chapter 2 is implemented in this module
- **lagrangian:** This module contains all the vortex blob and vortex panel coupling function and wrapped in the `LagrangianSolver` class and containing all the high-level function for managing the Lagrangian solver. THe vortex panel, vortex blob coupling algorithm described in chapter 2 is implemented in this module.
- **eulerian:** This module contains all the Navier-Stokes grid operations and wrapped in the `EulerianSolver` class, that containing all the high-level function for defining and managing the Eulerian solver. Algorithms explained in chapter 3 is implemented in this module.
- **hybrid:** This module contains all the functions related to coupling of the Lagrangian and the Eulerian solver, summarized in section 4.2, 4.3, and 4.4. The functions are wrapped in the `HybridSolver` class and manages the global coupling process.

Figure 5.1 shows the structure of the `pHyFlow` library and is categorized into several modules of different purposes. It is structured in this manner such that one could employ the library for any general simulation purposes such as for hybrid case, or for non-hybrid cases (e.g. potential flow using vortex panels, full Eulerian grid simulation using Eulerian solver). This means that one could use a single module of `pHyFlow` library for the desired test case.



5.2 Hybrid class Hierarchy

However, the hybrid module relies on the functions of the Lagrangian module and the Eulerian module. Moreover, the Lagrangian module requires the function of vortex blob module and the vortex panel module. Therefore, the hierarchy of the hybrid class is defined in a different manner, as shown in figure 5.2.

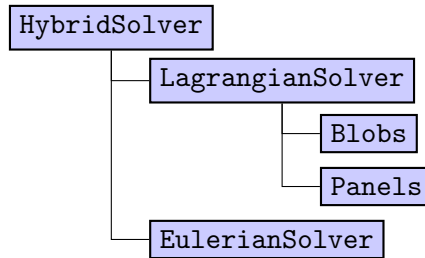


Figure 5.2: Flowchart of the `HybridSolver` hierarchy. The `HybridSolver` couples the `LagrangianSolver` class and the `EulerianSolver` class using the hybrid coupling schemes.

We use a bottom-up approach to construct the `HybridSolver` object, starting the lower-level objects: `Blobs`, `Panels` and then constructing the mid-level object: `LagrangianSolver`, and `EulerianSolver`, and finally constructing the highest-level object: `HybridSolver`. The procedure of constructing the hybrid class is as follows:

1. Construct the lowest-level objects:
 - (a) Construct the `Blobs` object using the vorticity field parameters, the vortex blob parameters, time step parameters, and population control parameters.
 - (b) Construct the `Panels` object using panel geometry parameters.
2. Construct the mid-level solvers:
 - (a) Construct `LagrangianSolver` object using the vortex blob object `Blobs` and the vortex panel object `Panels`.
 - (b) Construct `EulerianSolver` object using the geometry mesh file, interpolation probe grid parameters, and the fluid parameters.
3. Construct the hybrid solver:
 - (a) Construct `HybridSolver` object using the Lagrangian solver object `LagrangianSolver`, the Eulerian solver object `EulerianSolver`, and the interpolation parameters.

A detailed description of the parameters required for the construction of the objects, and the schematic of these objects are given in appendix A.

Chapter 6

Verification and Validation of Hybrid Method

The verification and validation of the hybrid method focuses on 4 aspects:

- Lamb-Oseen vortex evolution at $Re = 1000$ (section 6.1)
- Clercx-Bruneau dipole convection at $Re = 625$ (section 6.2)
- Clercx-Bruneau dipole collision at $Re = 550$ (section 6.3)
- Stalled elliptical airfoil at $Re = 5000$ (section 6.5)
- Multi-body problem at $Re = 550$ (section 6.6)

This chapter focuses on the verification and the validation of the hybrid method. We investigated several test-cases: the Lamb-Oseen vortex problem, the Clercx-Bruneau dipole collision by Clercx and Bruneau [15], the impulsively started cylinder test case, an elliptical airfoil at $Re = 5000$ and a multi-body problem.

The implementation of the hybrid method was verified using the analytical solutions of the Lamb-Oseen vortex problem. The analytical solution of the problem enabled us to quantify the error in the scheme.

The validation of the hybrid solver was performed using the test cases provided from literature. The Clercx-Bruneau dipole collision problem of Clercx and Bruneau [15], provide a detailed analysis on the evolution of the vorticity field and the generation of vorticity from the boundary. The impulsively started cylinder problem investigated by Koumoutsakos and Leonard [39], and Rosenfeld et al. [52] showed the evolution of the forces acting on an immersed cylinder in a free-stream flow.

With a proper verification and validation of the hybrid solver, we were able to perform simulation of more complex problems. We were able to perform simulation of a stalled flow past a thin airfoil using an elliptical airfoil at $Re = 5000$. Furthermore, a simulation



of two cylinder in tandem showed the feasibility of simulation a multi-body problem. Both these simulations served as a proof of concept for a simulation of a full VAWT in future research.

6.1 Lamb-Oseen Vortex Evolution

The Lamb-Oseen vortex test case simulates the evolution of a laminar vortex core in an unbounded domain. In section 2.7.2, we used this test case to verify and validate the implementation of the vortex blobs of the Lagrangian solver and in section 3.5.1, we used it to verify the implementation of the Eulerian solver. Therefore, in a similar fashion we employed this test case to verify the coupling of the hybrid solver.

The unbounded nature of the problem helps us to neglect the influence of the solid boundary (i.e the wall). Therefore, this test case did not require the panel solver in the Lagrangian solver as we are only concerned with the coupling of the vortex blobs to the Eulerian solver. Thus, we primarily focused on the vorticity field interpolation error discussed in section 4.2.2. Furthermore, with the analytical solution, we were able to quantitatively present the importance of ensuring conservation of circulation.

Moreover, we were able to quantify the influences of the discretization on the accuracy of the coupling. A parameter sensitivity analysis was therefore performed to determine their effects on the coupling error. The parameters that determine the spatial discretization of the vortex blobs are the nominal particle spacing h , and the overlap ratio λ (see figure 2.3). The spatial discretization of the Eulerian solver is regarded as a control variable for this test case as its impact was concluded in section 3.5.1. The parameters that determine the temporal discretization of the hybrid method are the time step size of the Eulerian solver Δt_E , and the time step size of the Lagrangian solver Δt_L . These are depended according to equation 4.24, with k_E being the number of Eulerian sub-steps.

The coupling error was quantified by determining the growth of maximum relative error in vorticity ϵ_ω given by equation 2.64, the approach used in section 2.7.2 and in section 3.5.1.

6.1.1 Problem Definition

The Lamb-Oseen Vortex problem is defined by the vorticity field and the velocity field, equations 2.61 and 2.62, respectively. The hybrid solver is initialized by first assigning the strengths of the vortex blobs using equation 2.63. The Eulerian domain Ω_E is then initialized using the solution of the Lagrangian solver. Daeninck [23] used this approach to enhance the coupling between the methods ensuring minimum interpolation error.

Figure 6.1 shows the hybrid domain configuration for the Lamb-Oseen vortex problem with the Lagrangian domain Ω_L spanning the full fluid domain. The Eulerian domain Ω_E only resolves the center of the Lamb-Oseen core, $\Omega_E \subseteq \Omega_L$, bounding $[-0.5, -0.5] \times [-0.5, -0.5]$. The boundary of the Eulerian domain $\partial\Omega_E$ is a Dirichlet velocity boundary $\partial\Omega_E = [\Sigma_d]$ where the velocity boundary condition is applied, as described in section 4.4.1. The correction of the Lagrangian domain is performed in the interpolation domain Ω_{int} according to the procedures described in section 4.2. The boundary of the interpolation

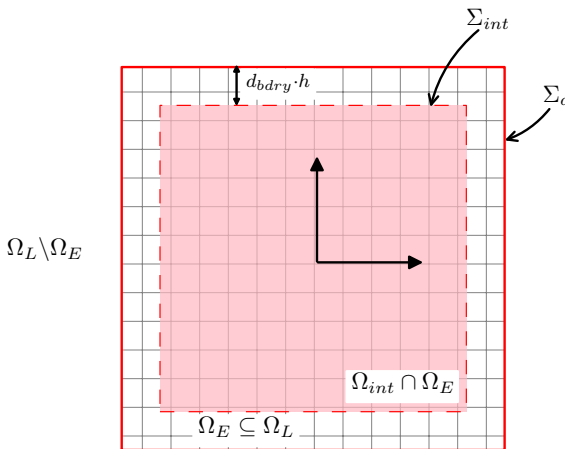


Figure 6.1: (Not to scale) The domain decomposition for the Lamb-Oseen vortex problem, $\Omega_E \subseteq \Omega_L$. The Eulerian domain is defined as $\Omega_E = [-0.5, 0.5] \times [-0.5, 0.5]$ with Dirichlet boundary $\partial\Omega_{dirichlet}$ [—, solid red]. The parameters of the discretization are tabulated in table 6.1.

domain Σ_{int} is defined with an offset d_{bdry} from the Eulerian boundary Σ_d by a distance $d_{bdry} = 2 \cdot h$, where h is the nominal blob spacing. Similar choice was made by Stock [59], and ensures that the potential inaccuracies at the outer Eulerian boundary is ignored during the interpolation procedure.

The spatial discretization of the Eulerian domain Ω_E is regarded as a control (i.e fixed) variable. Therefore, the parameter sensitivity analysis is performed by varying the discretization of the Lagrangian method only. The Eulerian domain is discretized with an unstructured mesh formulation using GMSH (see section 3.2.2) having $N_{cells} = 26448$ unstructured cells and grid size h_{grid} ranging from 0.007 to 0.0016.

The Lamb-Oseen vortex problem is defined according to the parameters tabulated in table 6.1. The center of the core is located at $(x, y) = (0, 0)$, where the Eulerian domain Ω_E is also centered. The parameters are chosen such that vorticity ω and velocity \mathbf{u} is non-zero at the boundary of the Eulerian domain Σ_d , figure 6.1. With the Lamb-Oseen time constant $\tau = 100$, this can be ensured.

The evolution of the Lagrangian solver and the Eulerian solver is performed according to sections 4.3 and 4.4 respectively. The Lagrangian solver performs TRS for diffusion of the vortex blobs, see section 2.4.2. The scheme requires vortex blob redistribution at every step, $f_{redis} = 1$. In conjunction with the redistribution, the population control is also performed at every step, $f_{pc} = 1$ with $(\Gamma_{loc}, \Gamma_{glob})$ as tabulated in table 6.1.

6.1.2 Results and Discussion

The investigation of the Lamb-Oseen vortex problem is divided into three parts. The first part of the investigation concerns with comparing several stages of the hybrid coupling, defined in section 6.1.2. We compared the uncoupled scheme with the one-way coupled scheme and with the fully coupled scheme. These successive coupling investigation helped us determine the source of the error, and furthermore quantify the errors in the coupling



Table 6.1: Summary of the parameters for the Lamb-Oseen vortex evolution.

Parameters	Value	Unit	Description
Γ_c	1	$\text{m}^2 \text{s}^{-1}$	Core strength
Ω	$[-0.5, 0.5] \times [-0.5, 0.5]$	m	Eulerian domain bounds
ν	0.001	$\text{kg s}^{-1} \text{m}^{-1}$	Kinematic viscosity
τ	100	s	Lamb-Oseen time constant
λ	1	-	Overlap ratio
h	0.01	m	Nominal blob spacing
$(\Gamma_{loc}, \Gamma_{glob})$	$(1 \times 10^{-14}, 1 \times 10^{-14})$	-	Population control threshold
h_{grid}	0.007 to 0.016	m	FE cell diameter span
N_{cells}	26448	-	Number of mesh cells
Δt_L	0.001	s	Lagrangian time step size
Δt_E	0.001	s	Eulerian time step size
k_E	1	-	Eulerian sub-steps
$N_{\text{t-steps}}$	1000	-	Number of time integration steps
t	0 to 1	s	Simulation time span
d_{bdry}	$2 \cdot h$	m	Interpolation boundary offset

process. The second part of the investigation, section 6.1.2 focuses on importance of conservation of circulation that was discussed in section 4.2.3. The results of the non-conserved and conserved scheme are compared to conclude the importance of conservation of circulation. During these two investigations, the parameters tabulated in table 6.1 are used.

The third and final investigation is dedicated to the parameter sensitivity analysis, section 6.1.2. The parameters that determine the spatial and temporal discretization of the scheme is investigated to verify the convergence of scheme.

Uncoupled vs. One-way Coupled vs. Fully Coupled

The several stages of the hybrid coupling with the fully Eulerian test case, to verify the implementation of the hybrid algorithm. The three stages of the coupling are as follows:

- **Uncoupled:** The uncoupled test case involves only the Eulerian solver and serves as a benchmark to quantify the error in the coupling. The boundary conditions are determined directly from the analytical formulation, equation 3.39.
- **One-way coupled:** The one-way coupled test case is a partially coupled hybrid test case where the Eulerian method is evolved using the Lagrangian solution. The correction of the Lagrangian solution is not performed in this scenario. Thus, this case helped us determine the error in the evolution of the Eulerian method using the Lagrangian solution.
- **Fully coupled:** The fully coupled test case performs the full coupling strategy described in section 4.2.3. The Eulerian method is evolved using the Lagrangian

solution. At the end of each time step, the Lagrangian solution inside the interpolation domain Ω_{int} , figure 6.1, is corrected. This test case helped us quantify the error in transferring the Eulerian solution to the Lagrangian method.

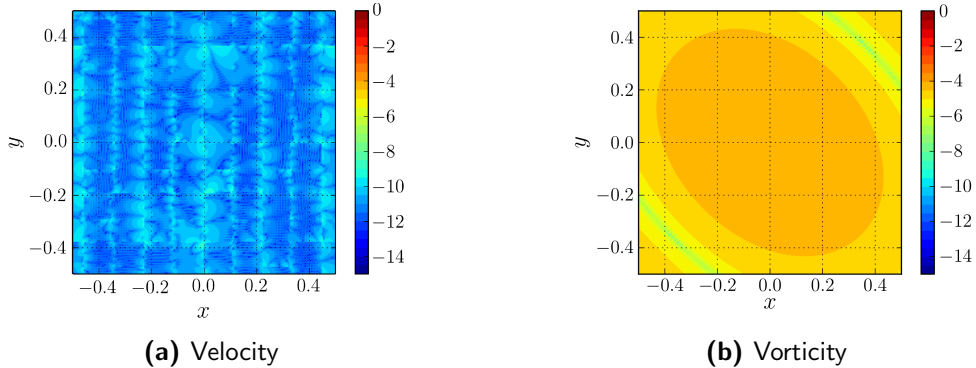


Figure 6.2: Initial relative error at $t = 0$ inside the Eulerian domain Ω_E . The figure depicts (a) the relative error in velocity \mathbf{u} , and (b) the relative error in vorticity ω .

Figure 6.2 depicts the initial relative error in velocity and vorticity inside the Eulerian domain Ω_E . The relative error in velocity is near machine epsilon $\epsilon \leq 10^{-10}$, but the error in vorticity is in the order of 10^{-5} . A similar observation was made in section 3.5.1, and it concluded that the source of the error is the projection error of the finite element when determining the vorticity ω from velocity \mathbf{u} , described in section 3.3.2.

The simulation was evolved from $t = 0$ to $t = 1$ with $N_{t\text{-steps}} = 1000$ Lagrangian time steps with $k_E = 1$ Eulerian sub-steps. A detailed summary of the time step parameters is tabulated in table 6.1. Figure 6.3 shows the evolution of maximum relative error in vorticity ω and velocity \mathbf{u} of the uncoupled, one-way coupled and the fully coupled cases inside the Eulerian domain Ω_E w.r.t. the analytical solution, equation 2.61. The initial observation shows that the error in velocity is two to three orders of magnitude lower than

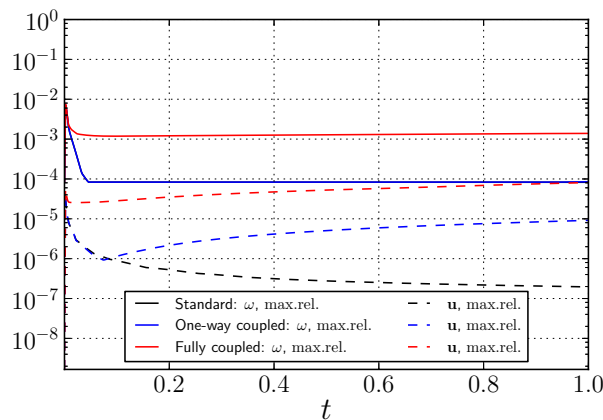


Figure 6.3: Evolution of the maximum relative error in velocity (dashed) and the maximum relative error in vorticity (solid), equation 2.64, from $t = 0$ to $t = 1$, using the parameters tabulated in table 6.1. The figure compares uncoupled case (black) vs. the one-way coupled case (blue) vs. the fully coupled case (red).



the error in vorticity (due to the projection error). The figure shows that the uncoupled scheme has the lowest error in vorticity and velocity. As the boundary condition is directly obtained from the analytical solution, the error only arises from the FE discretization of the Eulerian method. As the time progresses, the error in velocity converges near 10^{-7} and the error in vorticity converges near 10^{-4} .

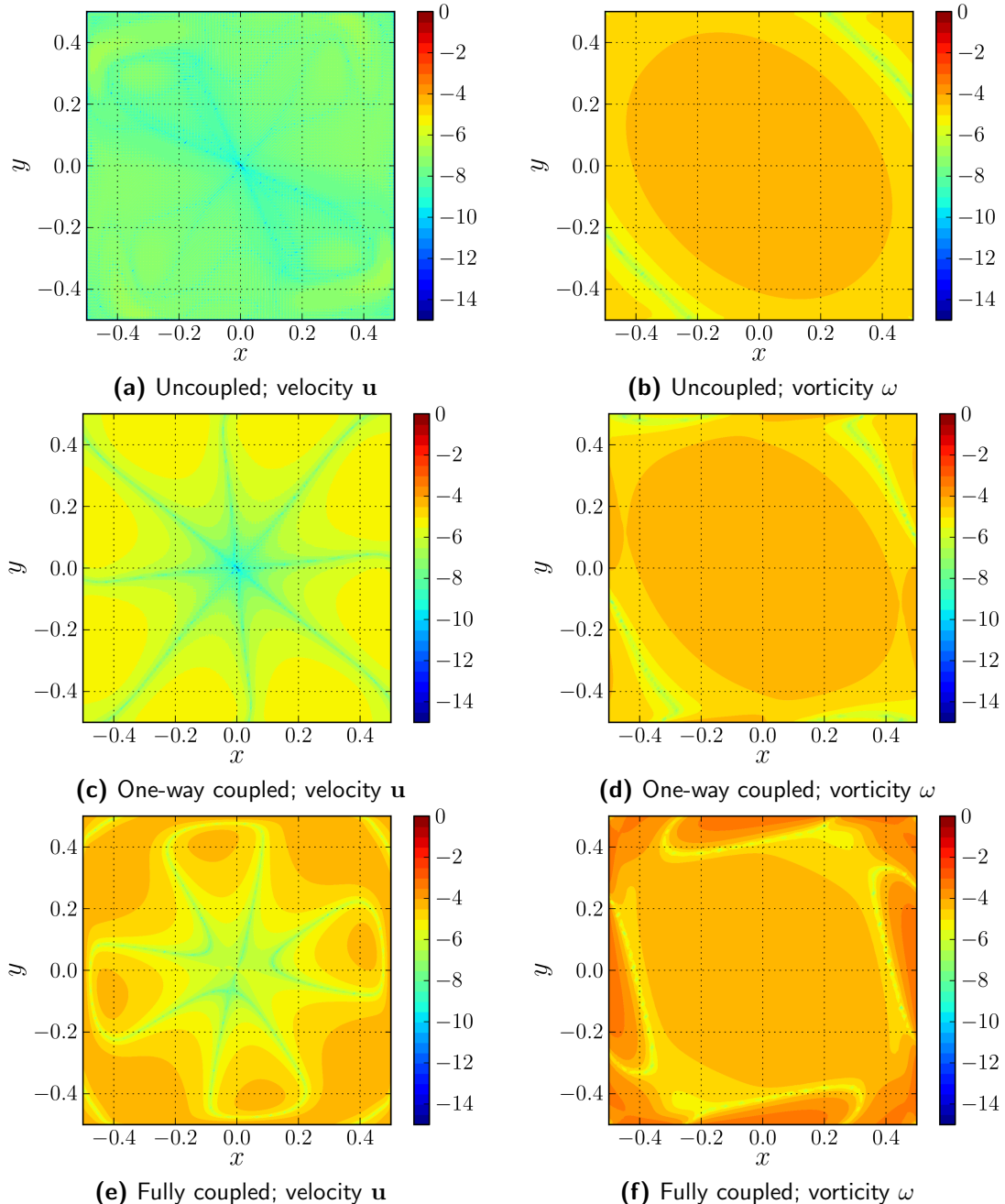


Figure 6.4: Plot of the relative error in velocity (left) and relative error in vorticity (right) in the Eulerian domain Ω_E at $t = 1$. The figure compares the error between (a)(b) the uncoupled, (c)(d) the one-way coupled, and (e)(f) the fully coupled cases.

The one-way coupled case shows an increase in the relative error in velocity field \mathbf{u} inside the Eulerian domain Ω_E . However, the difference is negligible at the initial stages of the simulation. This states that the analytical solution was well represented by the vortex blobs with a small discretization error. However by $t = 1$, the error in velocity increases by two orders of magnitude from 10^{-7} to 10^{-5} , w.r.t to the uncoupled scheme. This implies that the source of the error is due to the time integration error of the Lagrangian method. In section 2.7.2, we observed similar trend of growth in error due to time-marching of the vortex blobs.

The fully coupled case demonstrates that there is an additional increase in the error. Unlike the one-way coupled case, the increase in the error is observed from the start of the simulation, implying that the increase in the error is due to the correction of the strengths of the vortex blobs. In section 4.2.2, we discussed that the re-initialization of the vortex blobs introduces smoothing error in the vorticity field (i.e the Gaussian blurring of the vorticity field). This causes the Lagrangian solution to further deviate from the analytical solution of the Lamb-Oseen vortex. The consequence of this was that at $t = 1$, the error in vorticity ϵ_ω increased from 10^{-4} to 10^{-3} and the error in velocity increased from 10^{-5} to 10^{-4} , w.r.t the one-way coupled case.

Figure 6.4 shows the relative error in velocity and vorticity inside the Eulerian domain Ω_E at $t = 1$, for the three stages of coupling. We observe that there is an increase in error when going from the uncoupled scheme to the one-way coupled scheme to the fully coupled. Comparing the uncoupled scheme to the one-way coupled scheme, an increase in error is observed at the boundary of the Eulerian domain Σ_d . Comparing the one-way coupled to fully coupled case, we see that there is an additional increase in the error from the boundary. Therefore, the artificial vorticity generated from the boundary is due to the mismatch in the solutions of the Eulerian and the Lagrangian method. A larger mismatch in the solution will introduce strong artificial vorticity from the boundary.

The strength of the artificial vorticity at the boundary is proportional to the error in the coupling and to ensure an accurate coupling scheme, we have ensure this vorticity does not corrupt the characteristics of the original vorticity field. Therefore, we modified the discretization of the Lagrangian field such that the artificial vorticity generated from the boundary is less the threshold of influence (i.e $< 1\%$ of the maximum vorticity $\max\{\omega\}$).

Conservation of circulation

The approach for ensuring conservation of circulation during the coupling process was discussed in section 4.2.3. To validate the importance of conservation of circulation, we ran two simulation with and without the conservation of circulation during the transfer of vorticity from the Eulerian method to the Lagrangian method. The control variables of the simulation are the parameters tabulated in table 6.1.

Figure 6.5 compares the error in the Eulerian domain Ω_E of the coupling approach without the conservation circulation against the approach satisfying the conservation of circulation, at $t = 1$. We see that the scheme without the conservation has significantly larger error than the scheme with conservation. The maximum error is near the Eulerian boundary Σ_d and shows an increase in the artificial vorticity emanating from the bound-



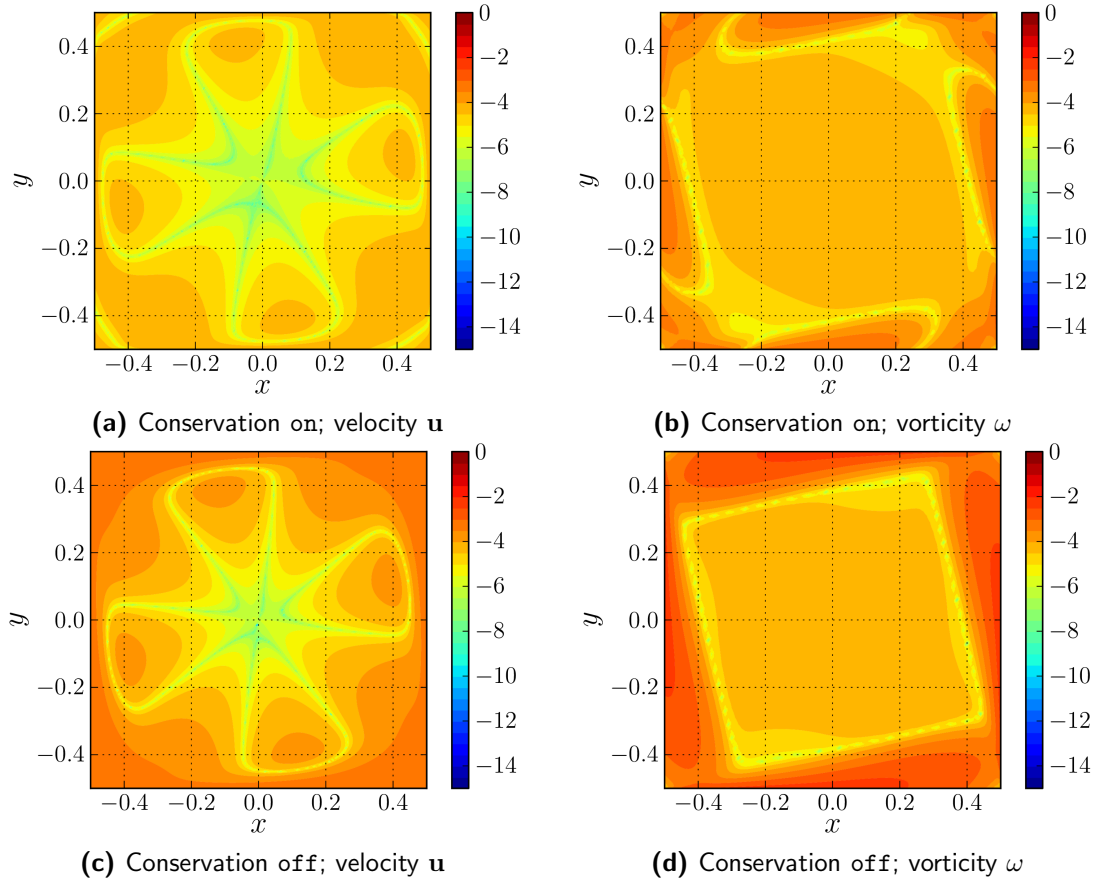


Figure 6.5: Plot of the relative error in velocity (left) and the relative error in vorticity (right) in the Eulerian domain Ω_E at $t = 1$. The figure compares the error between (a)(b) without conservation of circulation, and (c)(d) with the conservation of circulation.

ary due to the larger mismatch in the solutions, figure 6.5d. However, when we ensure that circulation is conserved, figure 6.5b, the boundary produces significantly less error.

Figure 6.6 shows the evolution of the maximum relative error from $t = 0$ to $t = 1$, comparing the results of with and without the conservation of circulation. Observing the difference in the relative error in velocity and vorticity, we see that the scheme without the conservation of circulation produces larger error at all times t . At $t = 1$, we observe that scheme without the conservation of circulation has a relative error in vorticity near 10^{-2} , whereas with the conservation of circulation, the relative error is an order of magnitude lower, reaching only 10^{-3} . Similarly for velocity, the scheme without the conservation of circulation has the relative error approaching 10^{-3} , whereas with the conservation enabled, the error only reaches 10^{-4} .

Figure 6.7 shows the change in total circulation from $t = 0$ to $t = 1$ for the non-conserved and conserved scheme. It is apparent that without the conservation of circulation, the error in total circulation is significantly larger and approaches 10^{-3} . If the circulation is not conserved explicitly, the transfer of vorticity from the Eulerian method to the Lagrangian method introduces additional error in total circulation. By ensuring conservation of circulation, as described in section 4.2.3, we see that the error in total circulation

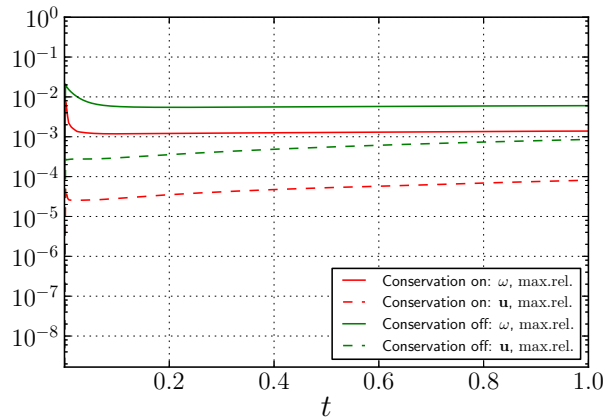


Figure 6.6: Plot of the maximum relative error in vorticity ϵ_ω [- -, dashed] and maximum relative error in vorticity ϵ_u [—, solid], equation 2.64, from $t = 0$ to $t = 1$, using the parameters tabulated in table 6.1. The figure compares the coupling scheme with conservation of circulation (red) vs. the coupling scheme without conservation of circulation (green).

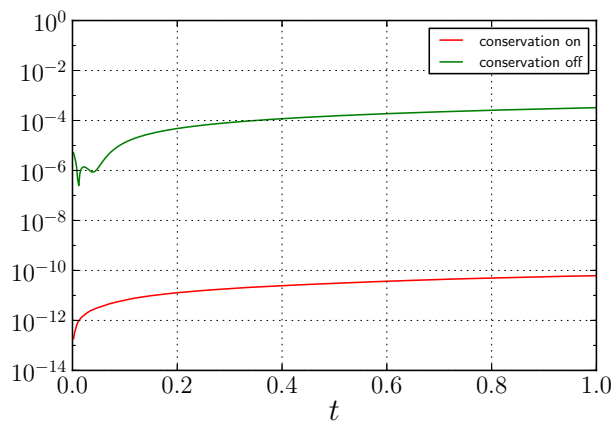


Figure 6.7: Plot of the error in total circulation ϵ_Γ of the Lagrangian method from $t = 0$ to $t = 1$. The figure compares the scheme with conservation of circulation [—, solid red], and the scheme without conservation of circulation [—, solid green].



is significantly smaller, near 10^{-10} .

In summary, we have determined that to ensure minimum error during the transfer of Eulerian solution to the Lagrangian solution, we have to ensure that the total circulation of the Lagrangian method is conserved.

Parameter sensitivity analysis

The parameter sensitivity analysis is the last stage of the Lamb-Oseen vortex investigation. The Lamb-Oseen vortex test case was ideal to determining the effects of the temporal and the spatial discretization of the hybrid method on the accuracy of the coupling.

To investigate the effects of the spatial discretization on the accuracy of the coupling, we ran several test cases varying the nominal blob spacing h , and test cases varying the overlap ratio λ . To investigate the effects of temporal discretization, we modified the Lagrangian time step size Δt_L w.r.t the Eulerian time step size Δt_E . The control variables of the simulations are the ones tabulated in table 6.1.

Figure 6.8 shows the impact of varying the nominal blob spacing h on the coupling. The maximum relative error in vorticity and the maximum relative error in velocity is plotted from $t = 0$ to $t = 1$ for nominal blob spacing $h = [0.01, 0.02, 0.05, 0.1]$. The figure shows that increasing the spatial resolution of the Lagrangian method reduces the error. At $t = 1$, the minimum error is observed for $h = 0.01$ with the relative error in velocity at 10^{-4} and the relative error in vorticity at 10^{-3} . The maximum relative error is observed for $h = 0.1$, with 10^{-3} for relative error in velocity and 10^{-2} for relative error in vorticity. This implies that the growth in error is of order one. Figure 6.9 shows the variation in the maximum relative error in vorticity at $t = 1$ for various nominal blob spacing h . The figure indeed shows that the change in error due to the spatial discretization is of order one.

Figure 6.10 compares the evolution of the maximum relative error for various overlap ratios, $\lambda = [0.5, 0.75, 1.0, 1.5]$. We see that the minimum error in velocity and vorticity

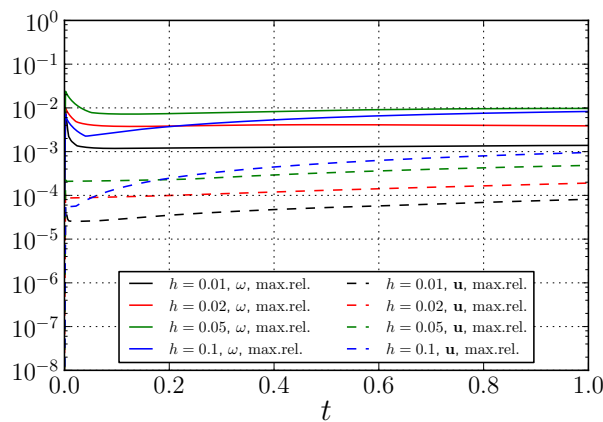


Figure 6.8: Evolution of the maximum relative error for various nominal blob spacing $h = [0.01, 0.02, 0.05, 0.1]$ from $t = 0$ to $t = 1$. The figures shows the maximum relative error in vorticity [--, dashed] and maximum relative error in vorticity [—, solid].

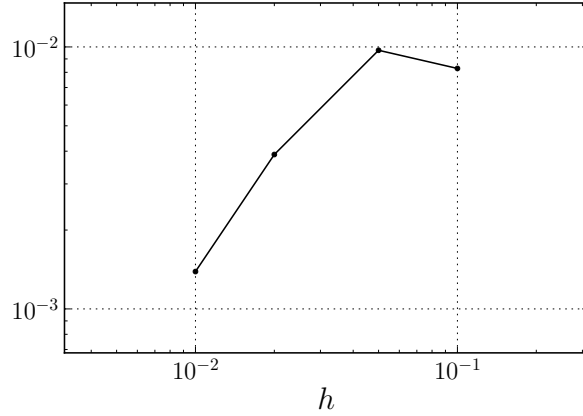


Figure 6.9: Convergence of the maximum relative error in vorticity due to the nominal blob spacing $h = [0.01, 0.02, 0.05, 0.1]$.

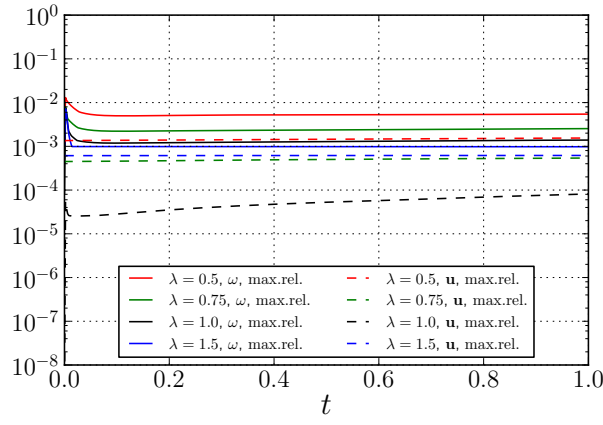
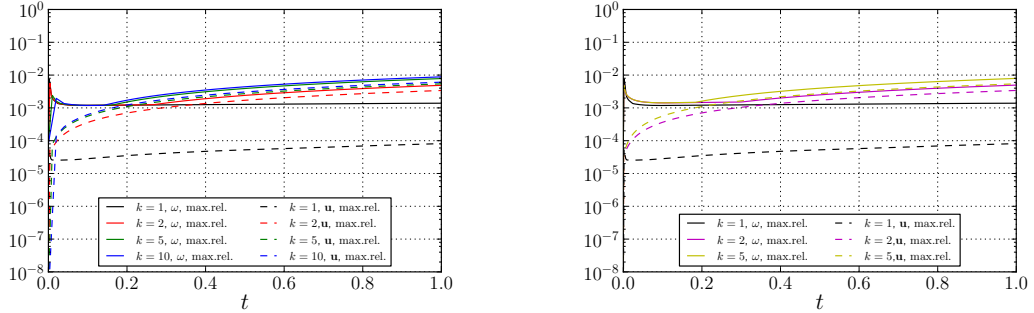


Figure 6.10: Evolution of the maximum relative error for various overlap ratios $\lambda = [0.5, 0.75, 1.0, 1.5]$ from $t = 0$ to $t = 1$. The figures shows the maximum relative error in vorticity [- -, dashed] and the maximum relative error in vorticity [—, solid].



(a) $\Delta t_L = [0.001, 0.002, 0.005, 0.01]$, $\Delta t_E = 0.001$ (b) $\Delta t_E = [0.001, 0.0005, 0.0002]$, $\Delta t_L = 0.001$

Figure 6.11: Evolution of the maximum relative error from $t = 0$ to $t = 1$ for various number of Eulerian sub-steps $k_E = [1, 2, 5, 10]$, modifying (a) the Lagrangian time step Δt_L , and (b) the Eulerian time step Δt_E . The figures shows the maximum relative error in vorticity [- -, dashed] and maximum relative error in vorticity [—, solid].



is observed for the overlap ratio $\lambda = 1$. As we move from this value, an increase in the error is observable. In section 2.2.5, we determined that to reduce the Gaussian blurring of the vorticity field from the Gaussian vortex kernels, we require an overlap ratio $\lambda = 1$ and a small nominal blob spacing h . The parameter sensitivity analysis on the spatial discretization validates this observation and states that to ensure minimum error in coupling, these criteria has to be satisfied.

Figure 6.11 shows the impact of varying the temporal discretization of the Lagrangian method and the Eulerian method w.r.t each other. The relation of the Eulerian time step size Δt_E to the Lagrangian time step size Δt_L is described in section 4.4.2. Figure 6.11a shows the effect of modifying the Lagrangian time step size Δt_L w.r.t to a fixed Eulerian time step size. With $\Delta t_E = 0.001$ and the number of Eulerian sub-steps $k_E = [1, 2, 5, 10]$, we have $\Delta t_L = k_E \cdot \Delta t_E = [0.001, 0.002, 0.005, 0.01]$. Similarly, figure 6.11b shows the effect of modifying the Eulerian time step size Δt_E w.r.t to the Lagrangian time step. With $\Delta t_L = 0.001$ and $k_E = [1, 2, 5]$, we have $\Delta t_E = \Delta t_L/k_E = [0.001, 0.0005, 0.0002]$. We see that the minimum error occurs when the time steps match (i.e $\Delta t_L = \Delta t_E$). However if increase the number of Eulerian time steps from $k_E = 1$ to $k_E = 2$, there an substantial increase in the relative error in velocity. This observation states that the linear interpolation used for sub-stepping process, has potential for improvement. A possible solution might be to employ a higher-order interpolation method for determining the Eulerian Dirichlet boundary condition at the sub-steps.

6.1.3 Conclusion

In section 6.1.2, we observed that moving from uncoupled to one-way coupled case, increases the relative error in velocity. The growth in error was mainly due to the time integration error of the Lagrangian method. When moving from one-way coupled to fully coupled scheme, there is a tangible increase in the relative error in vorticity and an additional increase in the error in velocity. The increase in this error was due to the re-initialization of the vortex blobs introducing an additional smoothing error at each correction step.

In section 6.1.2, we observed that conservation of circulation is vital in ensuring an accurate coupling strategy. The transfer of vorticity from the Eulerian method to the Lagrangian method, must be performed with a focus on the conservation of circulation, to ensure that the artificial vorticity at the Eulerian Dirichlet boundary Σ_d is minimal.

In section 6.1.2, we investigated the impact of varying the spatial and temporal discretization on the accuracy of the coupling. We determined there is an increase in error, if the Lagrangian method is spatially under-resolved w.r.t to the Eulerian method. An overlap ratio of $\lambda = 1$ was shown to have the minimum error during the coupling, as it ensures minimum Gaussian blurring. Varying the number of Eulerian sub-steps k_E , showed that the linear interpolation for the Dirichlet boundary condition is potential source of improvement.

6.2 Clercx-Bruneau Dipole Convection

In section 6.1, we determine the effects of transferring the Lagrangian solution to the Eulerian method, and transferring the Eulerian solution back to the Lagrangian method on an Lamb-Oseen vortex test case. However, an important aspect of domain decomposition method is the entering and the exiting of a vortex core in the Eulerian domain Ω_E . We used the Clercx-Bruneau dipole [15] to simulate the convection of vortex an Eulerian domain Ω_E .

6.2.1 Problem Definition

The hybrid domain decomposition of this investigation is depicted in figure 6.12. The Eulerian domain Ω_E is finite with bounds $[-0.25, 0.25] \times [-0.5, 0.5]$. The Clercx-Bruneau dipole, defined by equation 6.12, is initialized outside the Eulerian domain $\Omega_L \setminus \Omega_E$ at $(x_1, y_1) = (-1, 0.1)$ and $(x_2, y_2) = (-1, -0.1)$, corresponding to the positive and negative cores, respectively. As the simulation progresses, the dipole convects along the x -axis, passing through the Eulerian domain.

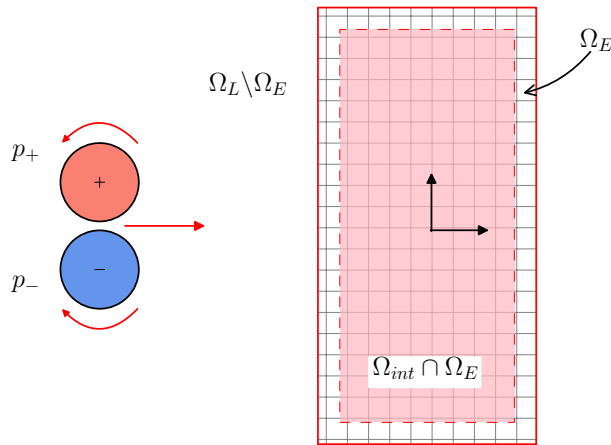


Figure 6.12: (Not to Scale) The domain decomposition for the Clercx-Bruneau convection problem, with the positive pole located at $p_+ = (x_1, y_1) = (-1, 0.1)$ and negative pole located at $p_- = (x_2, y_2) = (-1, -0.1)$. The parameters of the simulation are tabulated in table 6.2.

The Eulerian and the Lagrangian domain is discretized according to the parameters shown in table 6.2. The focus of this simulation is the entry and the exit of vorticity from in and out of the Eulerian domain and its impact on the solution. The simulation was first benchmarked using a Finite Element (FE) only simulation, and a Vortex Particle Method (VPM) only simulation, providing an basis for hybrid simulation. We can assume that the FE and VPM simulation are valid as we have already verified and validated their implementation in section 2.7 and 3.5, respectively.

To ensure that FE only simulation was valid, the Eulerian domain Ω_E stretched up to the far-field of the dipole, where the vorticity and the induced velocity is zero. The Eulerian domain Ω_E of the FE only simulation spanned $[-3, 3] \times [-2, 2]$. For a valid comparison,



Table 6.2: Summary of the parameters for the Clercx-Bruneau dipole convection problem.

Parameters	Value	Unit	Description
Ω_E	$[-0.25, 0.25] \times [-0.5, 0.5]$	m	Eulerian domain bounds
Re	625	-	Reynolds number
U	1	m s^{-1}	Characteristic velocity
W	1	m	Characteristic Length
ν	1.6×10^{-3}	$\text{kg s}^{-1} \text{ m}^{-1}$	Kinematic viscosity
$(x, y)_{1,2}$	$(-1, \pm 0.1)$	m	Initial location of the monopoles
ω_e	299.528385375226 ^a	-	Characteristic vorticity of the monopole
λ	1	-	Overlap ratio
h	0.005	m	Nominal blob spacing
h_{grid}	≈ 0.007	m	FE cell diameter
N_{cells}	40000	-	Number of mesh cells
Δt_L	2.5×10^{-4}	s	Lagrangian time step size
Δt_E	2.5×10^{-5}	s	Eulerian time step size
k_E	10	-	Eulerian sub-steps
$N_{\text{t-steps}}$	2800	-	Number of time integration steps
t	0 to 0.7	-	Simulation time
d_{bdry}	$2 \cdot h$	m	Interpolation boundary offset

^a Obtained from Renac et al. [51]

these benchmark simulations followed similar parameters as the ones tabulated in table 6.2.

6.2.2 Results and Discussion

Figure 6.13 compares the vorticity field of the FE simulation and the hybrid simulation at various instances, $t = [0, 0.2, 0.4, 0.6]$. The top half of each subplot belongs to the hybrid simulation, whereas the bottom half to the FE only simulation. It was determined that the cores of the dipole enters the Eulerian domain at $t = 0.26$ and exits the domain at $t = 0.45$. The figure shows that solution of both simulation matches up to the entry of the dipole, figure 6.13a and figure 6.13b. However in figure 6.13c, the solutions start to deviate, and at $t = 0.7$, figure 6.13d, it is apparent that the dipole in the hybrid method is lagging w.r.t to the FE only simulation. This would imply that the passage of the vortex through the domain has a stalling influence on the vorticity evolution.

To investigate further on this influence of the passage, we analyzed variation in maximum vorticity ω_{max} . Figure 6.14a shows evolution of the maximum vorticity ω_{max} from $t = 0$ to $t = 0.7$ in the Eulerian and the Lagrangian sub-domain of the hybrid simulation, the FE only simulation, and the VPM only simulation. We observe there is a slight difference in the maximum vorticity for the FE only and the VPM only simulation, which increases as the time progresses.

At $t = 0.26$, the maximum vorticity in the Eulerian sub-domain starts to increase, signifying the entering of the vortex core. Similarly, at $t = 0.45$, the maximum vorticity starts to decrease, signifying the exiting of the vortex core. As the dipole enters the sub-domain,

there is slight drop in the maximum vorticity. Similarly, as the dipole exits, there is a slight peak in the solution of the Eulerian sub-domain. The explanation to the increases in the vorticity in the Eulerian domain is the generation of the artificial vorticity. When the core of the dipole is right next to the Eulerian boundary Σ_d , the influence of the vorticity on the boundary is larger. However, with the implementation of Stocks interpolation tolerance at the boundary, this artificial vorticity is somewhat neglected.

Figure 6.15a shows a vorticity contour plot of the Lagrangian method and the Eulerian method, at $t = 0.28$ when the dipole has just entered the Eulerian domain. We see that there is a mismatch in the vorticity at the boundary of the Eulerian domain. Similarly, there is a slight mismatch in the vorticity field when the dipole leaves the Eulerian domain,

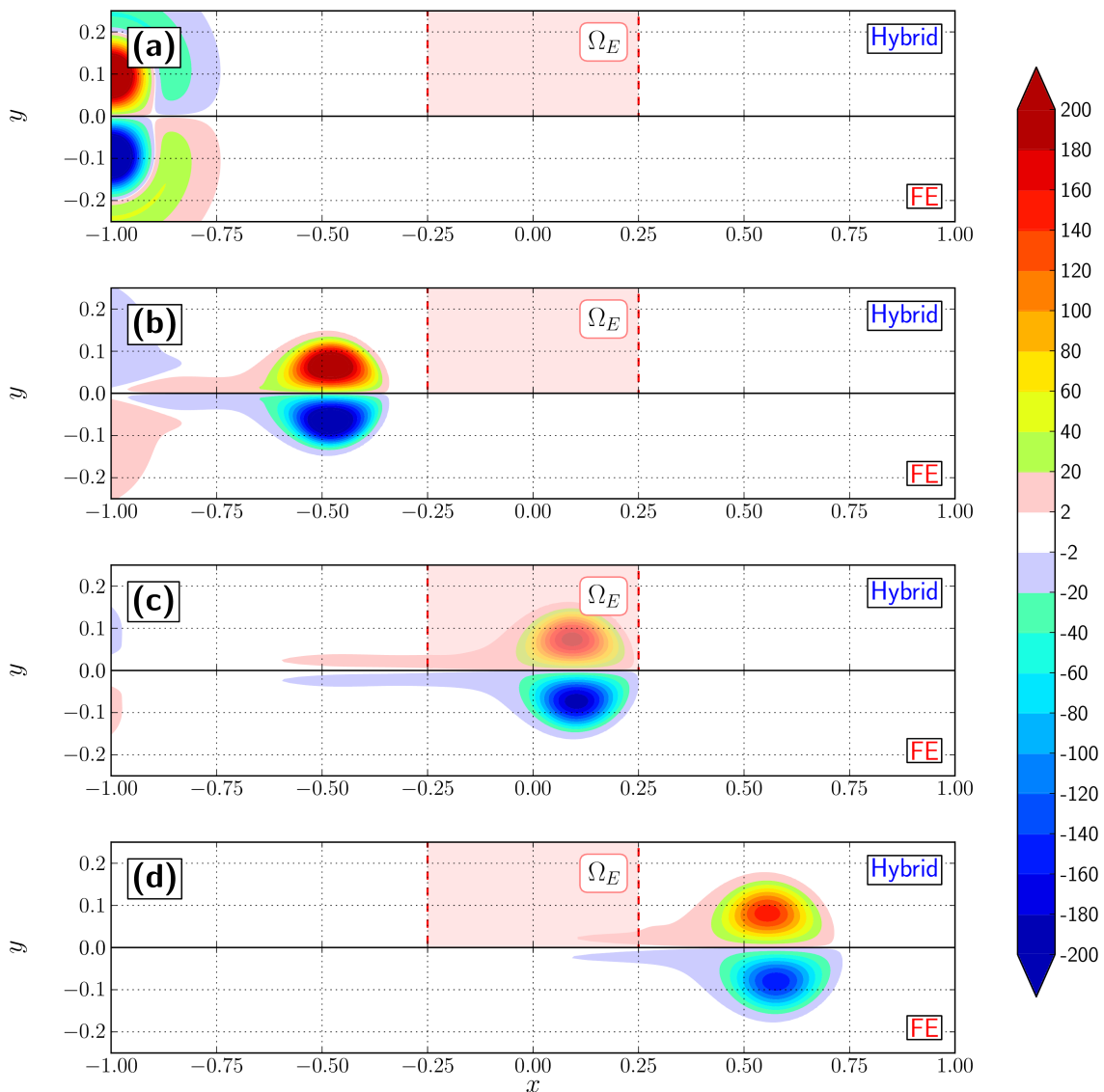


Figure 6.13: Plot of the Clercx-Bruneau dipole at $t = [0, 0.2, 0.4, 0.7]$ using parameters tabulated in table 6.2. The figure compares the hybrid simulation (top halves) against the FE only simulation (bottom halves).



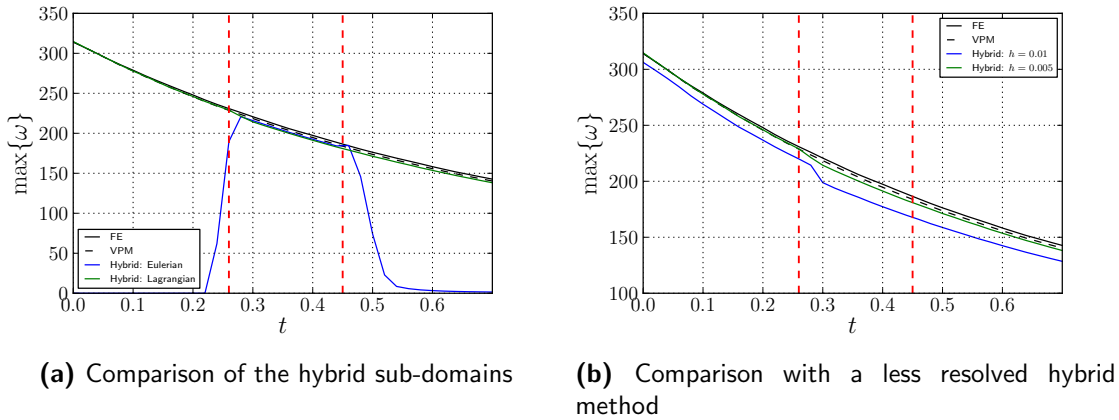


Figure 6.14: Evolution of the maximum vorticity $\max\{\omega\}$ from $t = 0$ to $t = 0.7$. The solutions are compared with the benchmark results of FE only [—, solid black], and VPM only [- -, dashed black] simulations. The figure depicts (a) the maximum vorticity in the Eulerian and the Lagrangian sub-domain of the hybrid method, and (b) the maximum vorticity of hybrid method with nominal blob spacing $h = 0.01$ and $h = 0.005$.

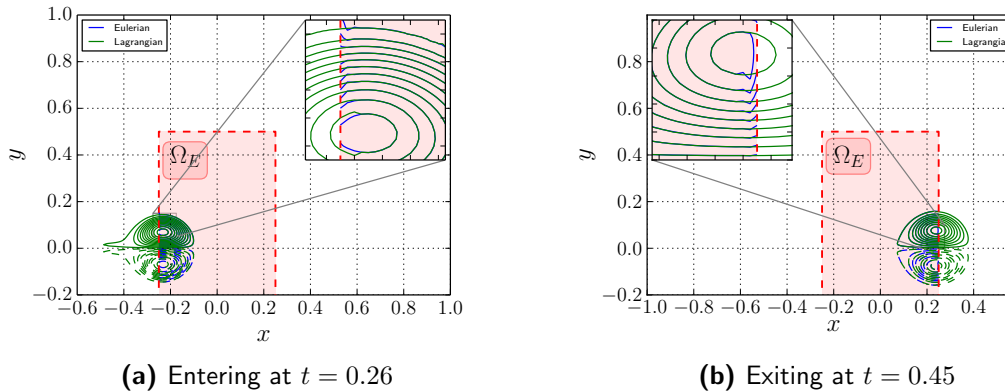


Figure 6.15: Vorticity contour plots of the dipole with levels $\dots, -50, -30, -10, 10, 30, 50, \dots$ of the Eulerian and the Lagrangian sub-domains. The figure highlights the effect of the artificial vorticity at the boundary of the Eulerian domain.

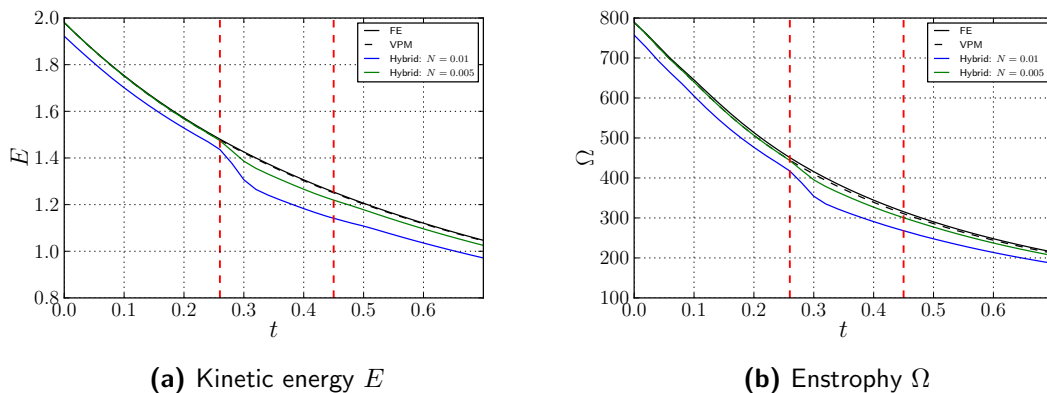


Figure 6.16: Evolution of the (a) kinetic energy E and (b) enstrophy for the nominal blob spacing $h = 0.01$ and $h = 0.005$.

figure 6.15b.

A simulation with lower Lagrangian resolution was ran to verify this theory. Figure 6.14b compares the evolution of maximum vorticity ω_{max} for nominal blob spacing $h = 0.01$ and $h = 0.005$. The less resolved simulation shows a larger drop in maximum vorticity during the entry of the dipole. However, at $t = 0.45$, the exiting of the dipole seems has no effect on the maximum vorticity, due to the interpolation tolerance from the boundary.

The evolution of the kinetic energy E and the enstrophy Ω shows the same behavior, figures 6.16a and 6.16b, respectively. It shows that during the entry there is larger change in the kinetic energy and the enstrophy of the flow. The artificial vorticity causes an increased diffusion of the dipole. With the reduced strength of the vortex core, the dipole is weaker in energy and travels a shorter distance, as observed in figure 6.13. The effect is more sever for a lower resolved Lagrangian method, as seen for the simulation with $h = 0.01$.

6.2.3 Conclusion

In conclusion, we see that a high resolution discretization of the Lagrangian method inside the Eulerian domain $\Omega_L \cap \Omega_E$ is paramount for accurate transfer of information to and from the Eulerian method. For a lower resolved Lagrangian method in this region introduces artificial vorticity at the boundary of the Eulerian domain Σ_d , corrupting the solution of the coupling.

6.3 Clercx-Bruneau Dipole Collision

In this section, we study the Clercx-Bruneau dipole colliding with a solid wall. A Finite Element (FE) only investigate was first performed in section 3.5.2 to form a benchmark for further investigation, validated against the study of Clercx and Bruneau [15]. The main goal of the Clercx-Bruneau dipole collision test case was to investigate how the hybrid method deal with a wall bounded problem.

6.3.1 Problem Definition

A detailed description of the Clercx-Bruneau dipole collision problem is given in section 3.5.2. Figure 6.17 shows the step-up of the hybrid simulation, with the Eulerian sub-domain Ω_E resolving the near-wall region, and the Lagrangian sub-domain domain resolving the complete fluid domain. The fluid domain is bounded by the no-slip wall Σ_{wall} (shown in blue). The Eulerian domain Ω_E extends from the wall Σ_{wall} to the boundary Σ_d , where the velocity boundary condition from the Lagrangian method is prescribed. The parameters of the simulation are tabulated in table 6.3.

As we are dealing with the wall-bounded problem, we require the vortex panel method to enforce the boundary condition in the Lagrangian method. In section 4.1, we described the decomposition of the Lagrangian domain Ω_L to the vortex blob domain Ω_b and the vortex panel domain Ω_p . Therefore, this decomposition was applied to this problem.



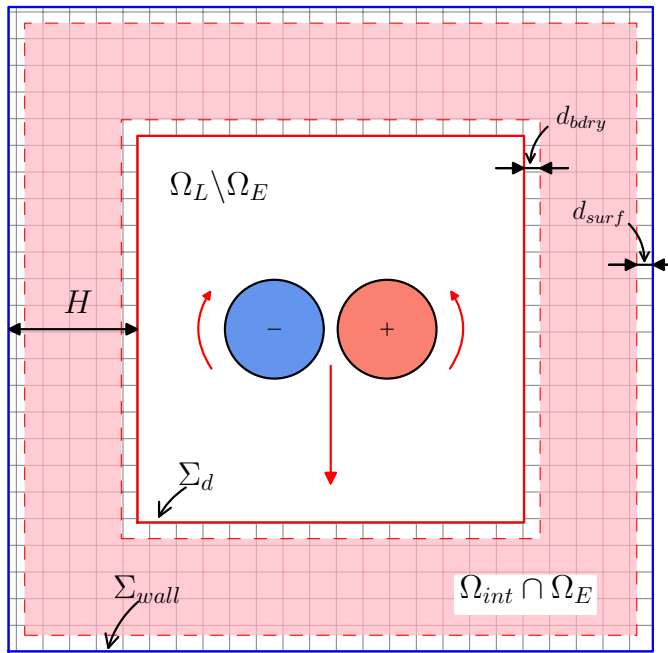


Figure 6.17: [Not to Scale] The domain decomposition for the Clercx-Bruneau dipole collision problem, with the positive pole at $p_+ = (x_1, y_1) = (0.1, 0)$ and negative pole at $p_- = (x_2, y_2) = (-0.1, 0)$. The parameters of the simulation are tabulated in table 6.3.

Table 6.3: Summary of the parameters for the Clercx-Bruneau dipole collision.

Parameters	Value	Unit	Description
Ω	$[-1, 1]^2$	m	Extend of Eulerian domain from wall Σ_d
H	0.2	m	Eulerian domain width
Re	625	-	Reynolds number
U	1	m s^{-1}	Characteristic velocity
W	1	m	Characteristic Length
ν	1.6×10^{-3}	$\text{kg s}^{-1} \text{m}^{-1}$	Kinematic viscosity
$(x, y)_{1,2}$	$(\pm 0.1, 0)$	m	Initial location of the dipole
ω_e	299.528385375226 ^a	-	Characteristic vorticity of the monopole
λ	1	-	Overlap ratio
h	0.003	m	Nominal blob spacing
N_{panels}	400	-	Number of panels
h_{grid}	0.005 to 0.01	m	FE cell diameter
N_{cells}	58272	-	Number of mesh cells
Δt_L	2.5×10^{-4}	s	Lagrangian time step size
Δt_E	2.5×10^{-5}	s	Eulerian time step size
k_E	10	-	Eulerian sub-steps
$N_{\text{t-steps}}$	4000	-	Number of time integration steps
t	0 to 1	-	Simulation time
d_{bdry}	$2 \cdot h$	m	Interpolation domain offset from Σ_d
d_{surf}	$3 \cdot h$	m	Interpolation domain offset from Σ_{wall}

^a Obtained from Renac et al. [51]

The dipole is initialized in the center of the domain, in the Lagrangian only domain $\Omega_L \setminus \Omega_E$ at the locations $(x, y)_{1,2}$. As the simulation progresses, the dipole travels along the negative y -axis, entering the Eulerian domain Ω and colliding with the no-slip wall Σ_{wall} .

6.3.2 Results and Discussion

Figure 6.18 shows the state of the dipole at $t = [0, 0.2, 0.4, 0.6, 0.8, 1]$. The figure compares the hybrid simulation (left half) with the FE only simulation (right half), investigated in section 3.5.2. Once the dipole enters the Eulerian domain, at $t = 0.4$, we observe that there is a slight difference in the solution. We observe a slight artificial vorticity emanating from the Eulerian boundary Σ_d , corrupting the vorticity field. The corruption of the vorticity field is apparent when observing the hybrid plot at $t = 0.4$, at the location $x = -0.2$ and $y = -0.8$. The artificial vorticity is in order of $< \pm 5$. Note that with the maximum vorticity in the fluid near $\max\{\omega\} = 300$ is near 2% of the maximum vorticity.

Figure 6.19 compares the vorticity contour at $t = 1$ against the FE only simulation. We see there is a slight difference in the vorticity contour lines of hybrid solution, figure 6.19b. The shape of the contour lines near the wall is slightly different, and furthermore, the location of the core is also shifted slightly.

To investigate further on the cause of this difference, we studied the change in maximum vorticity ω_{max} , the kinetic energy E and the enstrophy Ω , and the palinstrophy P , shown in figure 6.20d. The variation in maximum vorticity, figure 6.20a, shows that the first peak in the hybrid is slightly lower than the FE only simulation, at $t \approx 0.35$. However, the second peak in vorticity, at $t \approx 0.65$ is higher than the standard simulation. Between $t = 0.4$ and $t = 0.6$, the dipole exits and re-enters the Eulerian domain, as seen in figure 6.18. The artificial vorticity generated during this time, causes a detrimental effect on overall solution.

Figure 6.20b shows that, as the dipole leaves the Eulerian domain Ω_E from $t = 0.4$, the kinetic energy E reduces less, and is higher than the FE only simulation at $t \leq 0.4$. Therefore, the core that is leaving and re-entering the Eulerian domain Ω_E has a higher kinetic energy E . This could be cause of deviation seen at $t = 1$, figure 6.19.

Figure 6.20c shows that the enstrophy Ω matches reasonable well with the FE only simulation and we see that there is a slight difference at the peaks. Similarly, figure 6.20d, shows the variation in palinstrophy P . The solution stars to deviate from $t \approx 0.5$, after the vortex core re-enters the domain.

Figure 6.21 shows the vorticity at the boundary, along $y = -1$. We observe that for $t = 0.4$ the solution matches, at $t = 0.6$ the peak in vorticity is larger for the hybrid simulation, and for $t = 1$, the peak has a larger span. The increased kinetic energy E of the vortex could provide a possible explanation for this. With a higher kinetic energy, the wall generates stronger vorticity to repel the dipole.

We investigated further with a higher resolved Lagrangian method, with a smaller nominal blob spacing h , a larger number of panels N_{panels} , and a smaller Lagrangian time step size Δt_L . However, these simulation did not provide significant improvement to the present results.



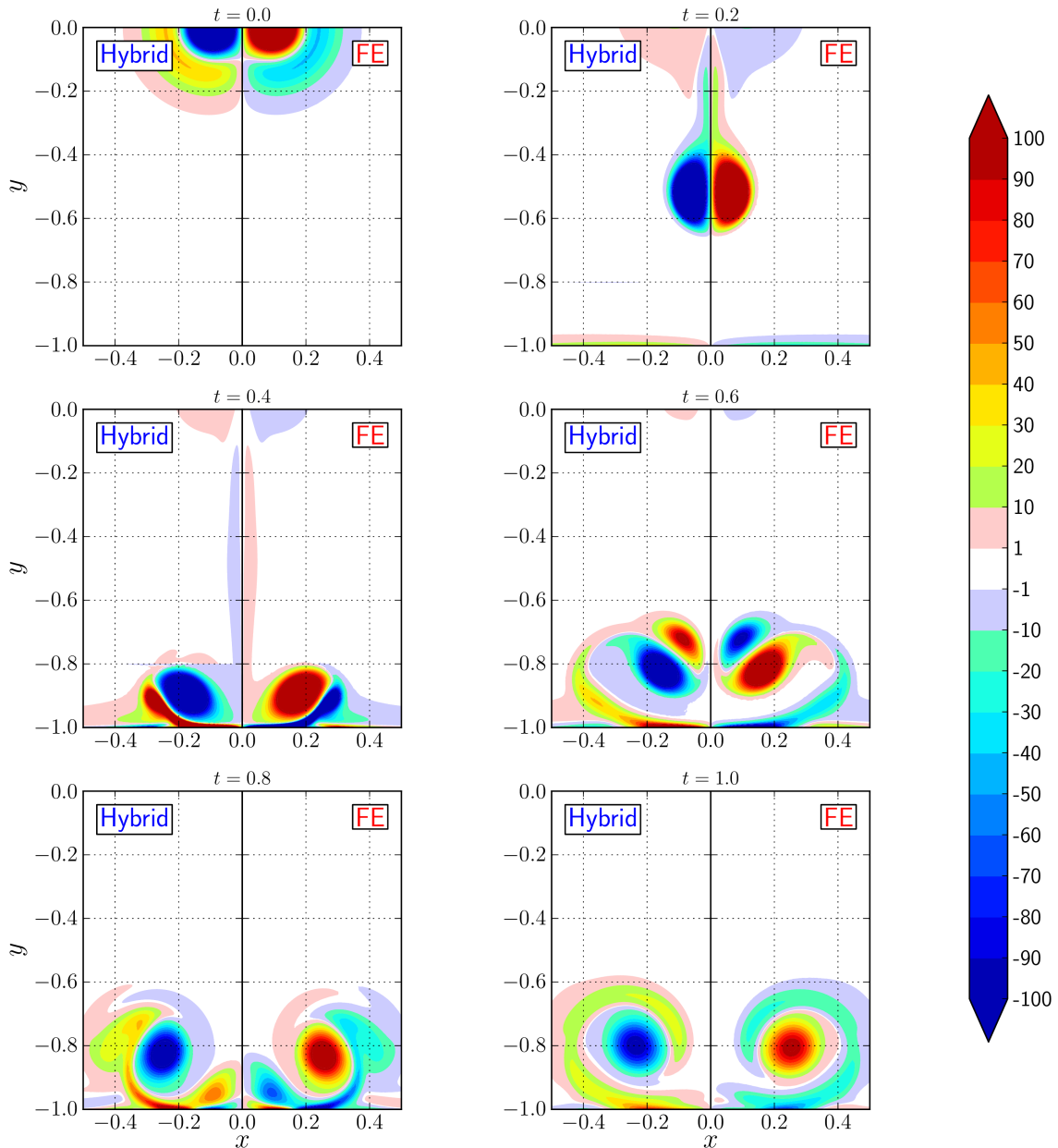


Figure 6.18: Plot of the dipole at $t = [0, 0.2, 0.4, 0.6, 0.8, 1]$, comparing the hybrid simulation (left half) and FE only simulation (right half).

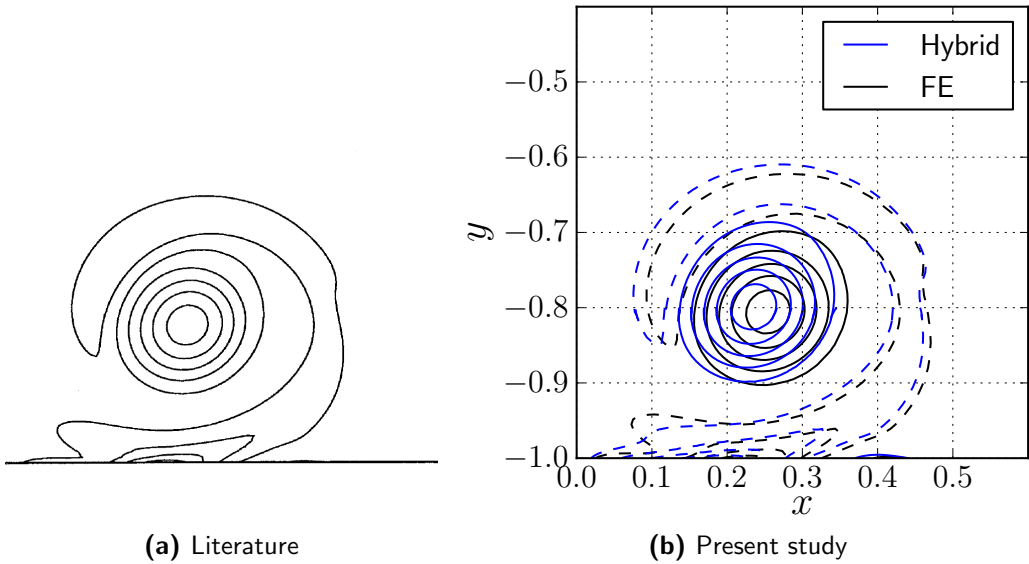


Figure 6.19: Comparison of the vorticity contours at $t = 1$. The figure compares the plot obtained by **(a)** literature, Clercx and Bruneau [15], and **(b)** the present study, the hybrid and FE only simulation.

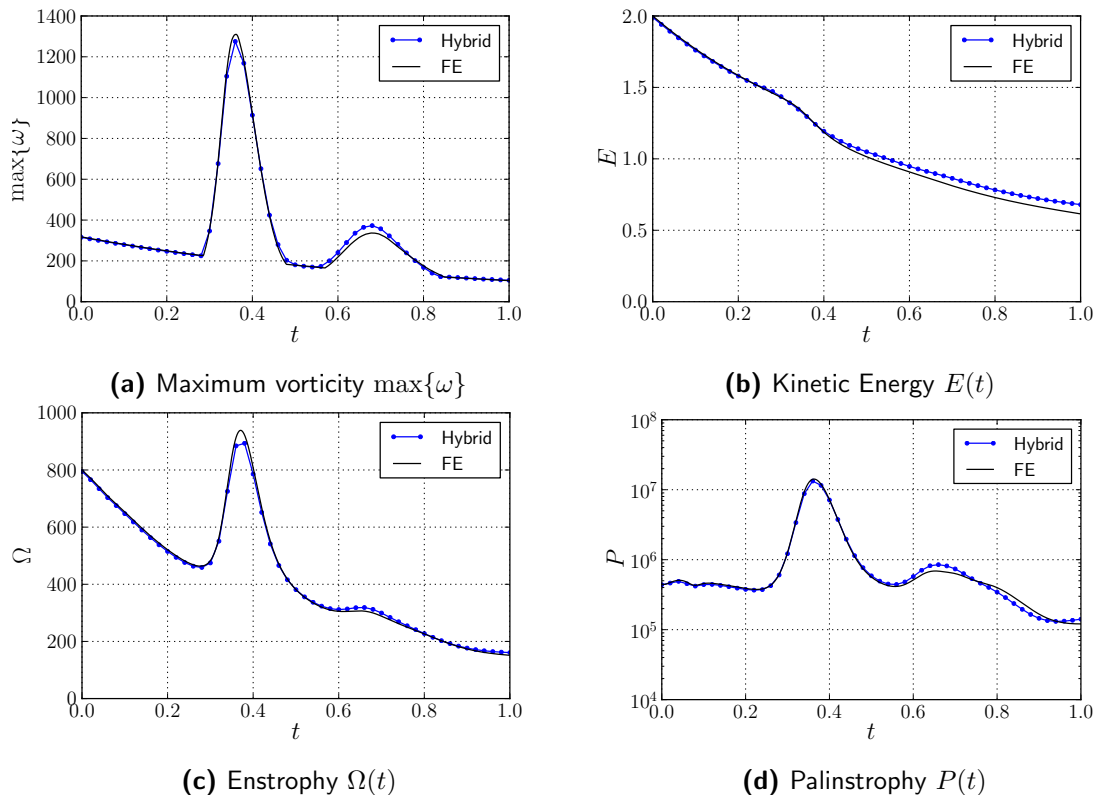


Figure 6.20: Variation in the fluid parameters from $t = 0$ to $t = 1$. The figure compares the hybrid results [—, solid blue] with the FE only [—, solid black] results.



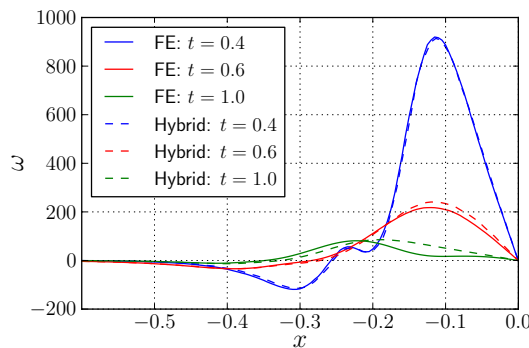


Figure 6.21: Compares the vorticity generated at the bottom-left wall ($y = -1$, $-0.6 \leq x \leq 0$) at $t = 0.4$ [—, solid blue], $t = 0.6$ [—, solid red] and $t = 1$ [—, solid green].

6.3.3 Conclusion

In conclusion, we determined that the exists a slight difference in the geometry of the vorticity contours and the location of the dipole at the end of the simulation. The deviation of the dipole stars as the dipole enters the Eulerian domain. The entering and the re-entering process of the dipole introduces artificial vorticity from the Dirichlet boundary Σ_d , increasing the overall kinetic energy E of the problem. This intern has an influence on the position of the dipole at $t = 1$. Increasing the resolution of the Lagrangian solution only minimally increases the accuracy of the results.

It is recommended that a further focused study should be performed on the artificial vorticity generated from the boundary of Eulerian domain Σ_d . If this artificial vorticity can be further minimized, we could potential attain more accurate results.

6.4 Impulsively Started Cylinder at $Re = 550$

In this section, we will study the flow around an impulsively started cylinder (ISC) at $Re = 550$. The purpose of this test case is ensure that we are able to correctly predict the lift and drag forces acting on a body. In section 3.5.3, the FE only simulation was validated against the study of Koumoutsakos and Leonard [39], and the study of Rosenfeld et al. [52]. The FE only investigation will be therefore be used a benchmark for the current hybrid study.

6.4.1 Problem Definition

The description of the impulsively started test case was initially introduced in section 3.5.3. For the hybrid simulation, we performed similar investigation and the compared the results with the benchmark study and the aforementioned literature. The parameters of the simulation are tabulated in table 6.4.

Figure 6.22 shows the domain decomposition of the hybrid simulation, performed according to section 4.1. The Lagrangian domain Ω_L resolves the full fluid domain, with an Eulerian domain Ω_E resolving the near-wall region of the cylinder. The Eulerian domain

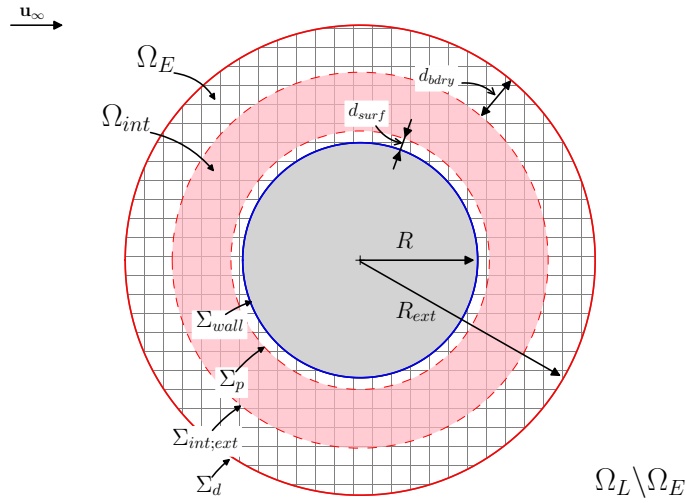


Figure 6.22: (Not to Scale) The domain decomposition for the impulsively started cylinder. The parameters of the domain are tabulated in table 6.4.

Table 6.4: Summary of the parameters of the hybrid simulation for the impulsively started cylinder test case at $Re = 550$.

Parameters	Value	Unit	Description
Re	550	-	Reynolds number
\mathbf{u}_∞	[1, 0]	m s^{-1}	Freestream velocity
R	1	m	Radius to Eulerian boundary Σ_{wall}
R_{ext}	1.5	m	Radius to Eulerian boundary Σ_d
ν	3.6×10^{-3}	$\text{kg s}^{-1} \text{ m}^{-1}$	Kinematic viscosity
λ	1	-	Overlap ratio
h	0.008	m	Nominal blob spacing
h_{grid}	0.008 to 0.04	m	FE cell diameter
N_{cells}	32138	-	Number of mesh cells
N_{panels}	100	-	Number of panels
Δt_L	0.005	s	Lagrangian time step size
Δt_E	0.001	s	Eulerian time step size
k_E	5	-	Number of Eulerian sub-steps
$N_{t\text{-steps}}$	40000	-	Number of time integration steps
t	0 to 40	-	Simulation time
d_{bdry}	$0.1 \cdot R$	m	Interpolation domain offset from boundary Σ_d
d_{surf}	$3 \cdot h$	m	Interpolation domain offset from boundary Σ_{wall}



Ω_E is bounded by boundary $\partial\Omega_E = \Sigma_d \cup \Sigma_{wall}$, where Σ_d is the external Dirichlet boundary and Σ_{wall} is the no-slip wall of the cylinder. The interpolation region Ω_{int} , where we correct the particle strengths, is within the Eulerian domain Ω_E , i.e $\Omega_{int} \subset \Omega_E$. The interpolation region Ω_{int} is bounded by $\partial\Omega_{int} = \Sigma_p \cup \Sigma_{int;ext}$, where Σ_p is the vortex panel domain boundary, and $\Sigma_{int;ext}$ is the external boundary of the interpolation domain. The vortex panel domain boundary Σ_p , is defined with an offset $d_{surf} = 3 \cdot h$ from the cylinder wall Σ_{wall} . The exterior boundary $\Sigma_{int;ext}$ of the interpolation region Ω_{int} is defined with a larger offset $d_{bdry} = 0.1 \cdot R$ for the boundary Σ_d . We observed in the previous test cases that the main error of the hybrid scheme is the artificial vorticity generated at the Σ_d and therefore to minimize this error, we have chosen a larger offset than used by Stock [59].

We investigated two aspects of the impulsively started cylinder problem. The first study focused on the impact of coupling parameters on the accuracy of the lift and the drag forces. The parameters of interest are the number of vortex panels N_{panels} , nominal blob spacing h , and time step size of the Lagrangian method Δt_L .

The second study focused on the long run performance of the forces acting of the cylinder. Artificial perturbation was induced, as described in section 3.5.3, to induce vortex shedding at a smaller simulation time t .

6.4.2 Results and Discussion

Figure 6.23 shows the vorticity contour at $t = [1, 3, 5, 7]$. The plot compares the hybrid simulation (top halves) with the FE only simulation (bottom halves). The hybrid halves of the plot depicts the Eulerian sub-domain Ω_E in pink. After studying the figure, we observe that the vorticity contours of the hybrid simulation matches with the FE only simulation. The only difference between both simulations is the artificial vorticity emanating from the Dirichlet boundary Σ_d . This magnitude of this artificial vorticity is in the range $|\omega| \leq 0.2$, and with the maximum vorticity in the domain $\max\{\omega\} = 32$, we have that the strength of the artificial vorticity is less than 1% of the maximum vorticity in the fluid.

To investigate the effect of the artificial vorticity, we determined the error in drag during the initial stages of the simulation, for times $t < 4$. Figure 6.24 shows the evolution of the drag coefficient C_d , the friction drag $C_{d_{fric}}$, and the pressure drag $C_{d_{pres}}$. The results are compared with the FE only simulation and the reference data obtained from Koumoutsakos and Leonard [39]. Observing the figure, we see that the hybrid simulation has a larger drag coefficient, due to the increased pressure drag $C_{d_{pres}}$. Moreover, the drag coefficient is under-estimated at the first few time instances. To investigate further on the causes of this trends, we performed a parameter sensitivity analysis.

Figure 6.25 shows the impact of varying the resolution of the Lagrangian method w.r.t to the Eulerian method on the accuracy of the drag coefficient calculated. To reduce the artificial vorticity, we modified the Lagrangian time step size Δt_L , the nominal blob spacing h , and the number of vortex panels N_{panels} .

Figure 6.25a investigates the effect of changing the Lagrangian time step size Δt_L on the drag coefficient. The Lagrangian time step was varied with setting the number of Eulerian

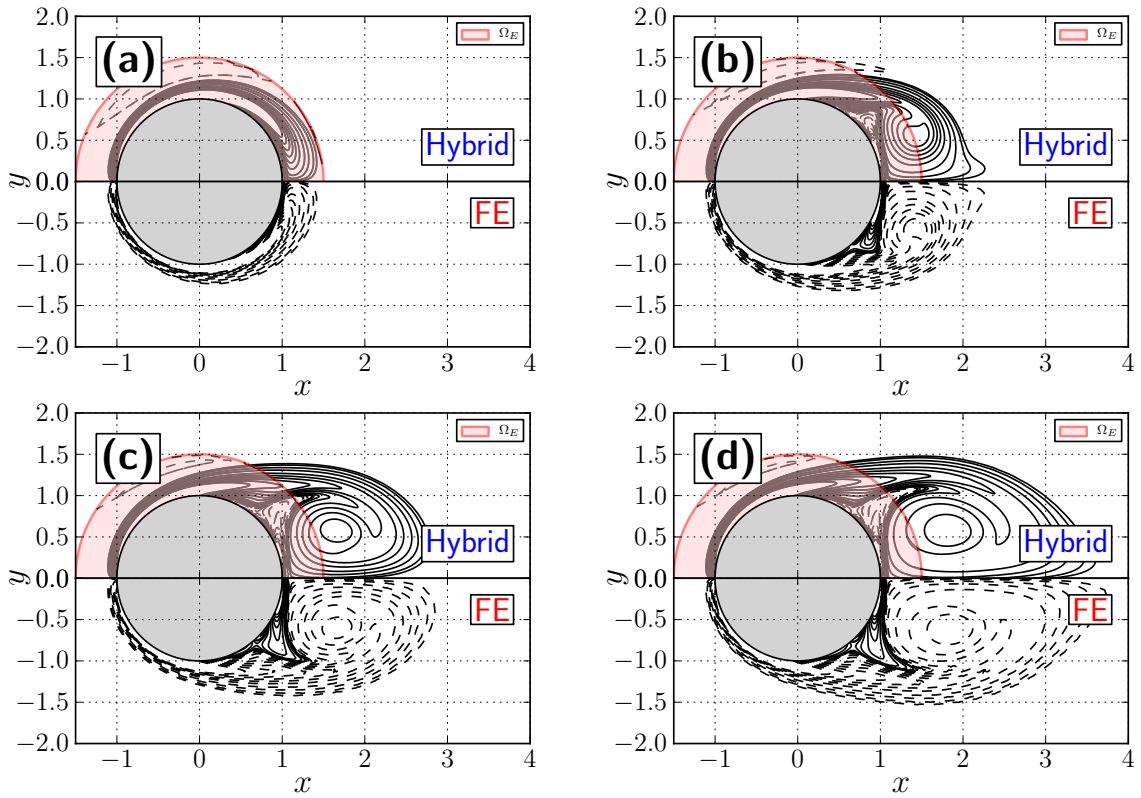


Figure 6.23: Comparison of the vorticity contours for (a) $t = 1$, (b) $t = 3$, (c) $t = 5$ and (d) $t = 7$ with contour levels $[-7, \dots, -3, -2, -1, 0.5, -0.2, -0.1, 0.1, 0.2, 0.5, 1, 2, 3, \dots, 7]$. The figures compares the hybrid simulation (top half) with FE only simulation (bottom half).

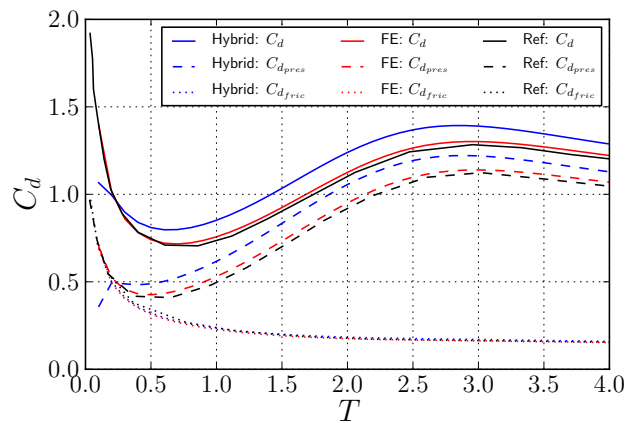


Figure 6.24: Evolution of the drag coefficient during the initial stages $t = 0$ to $t = 4$ with total drag coefficient C_d (solid), pressure drag coefficient $C_{d_{pres}}$ (dashed) and friction drag coefficient $C_{d_{fric}}$ (dotted). The figure compares results of hybrid simulation (blue), FE only simulation (red) and reference data (black) of Koumoutsakos and Leonard [39].



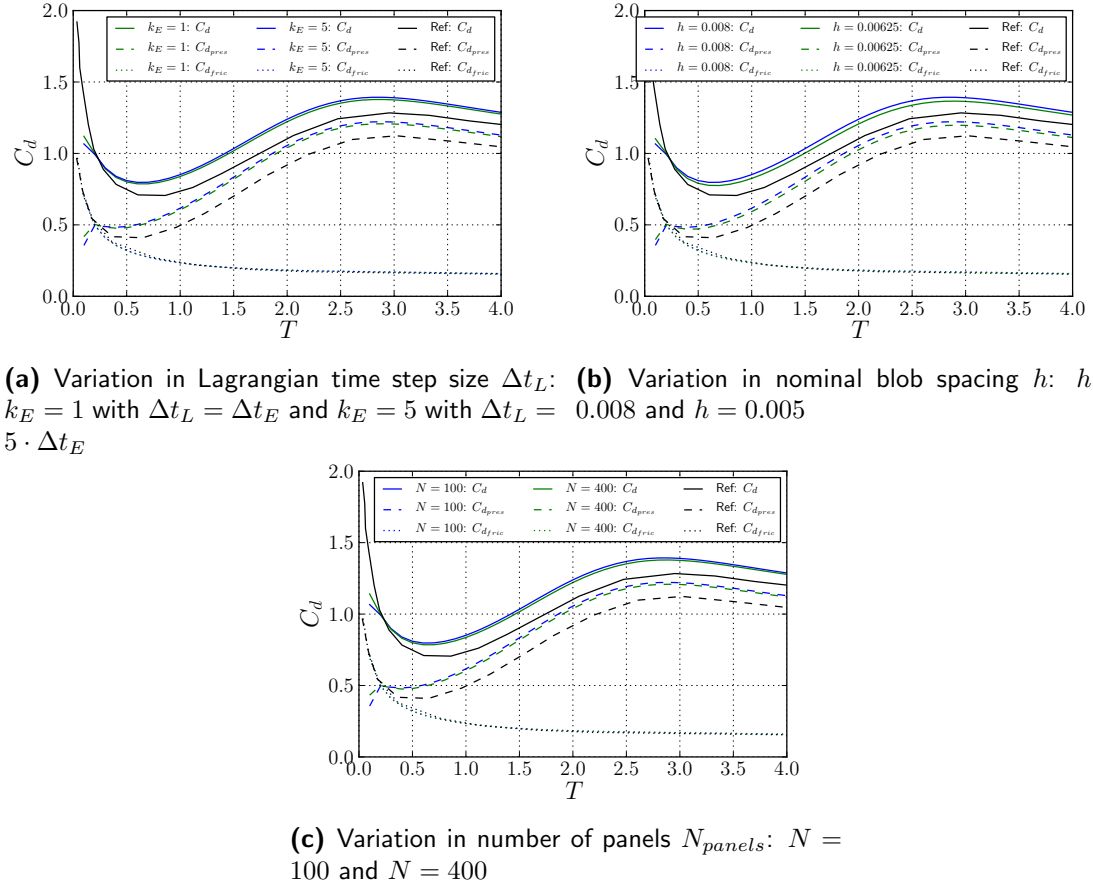


Figure 6.25: Parameters sensitivity analysis on the drag evolution of the cylinder from $t = 0$ to $t = 4$, compared with literature data (**black**) obtained from Koumoutsakos and Leonard [39]

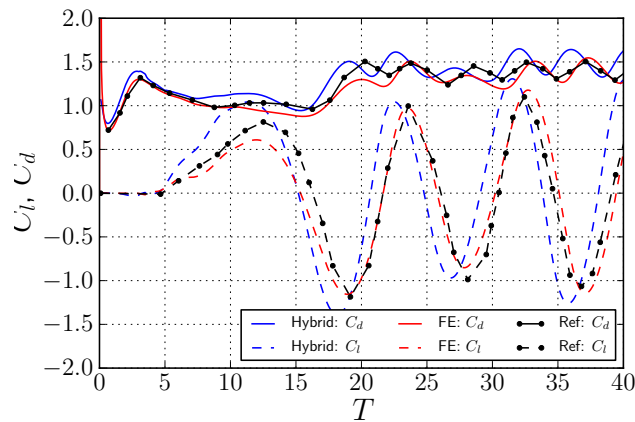


Figure 6.26: Evolution of the lift and drag coefficient from $t = 0$ to $t = 40$ with artificial perturbation [42]. The figure compares hybrid (**blue**), FE only (**red**), and the reference data (**black**) from Rosenfeld et al. [52].

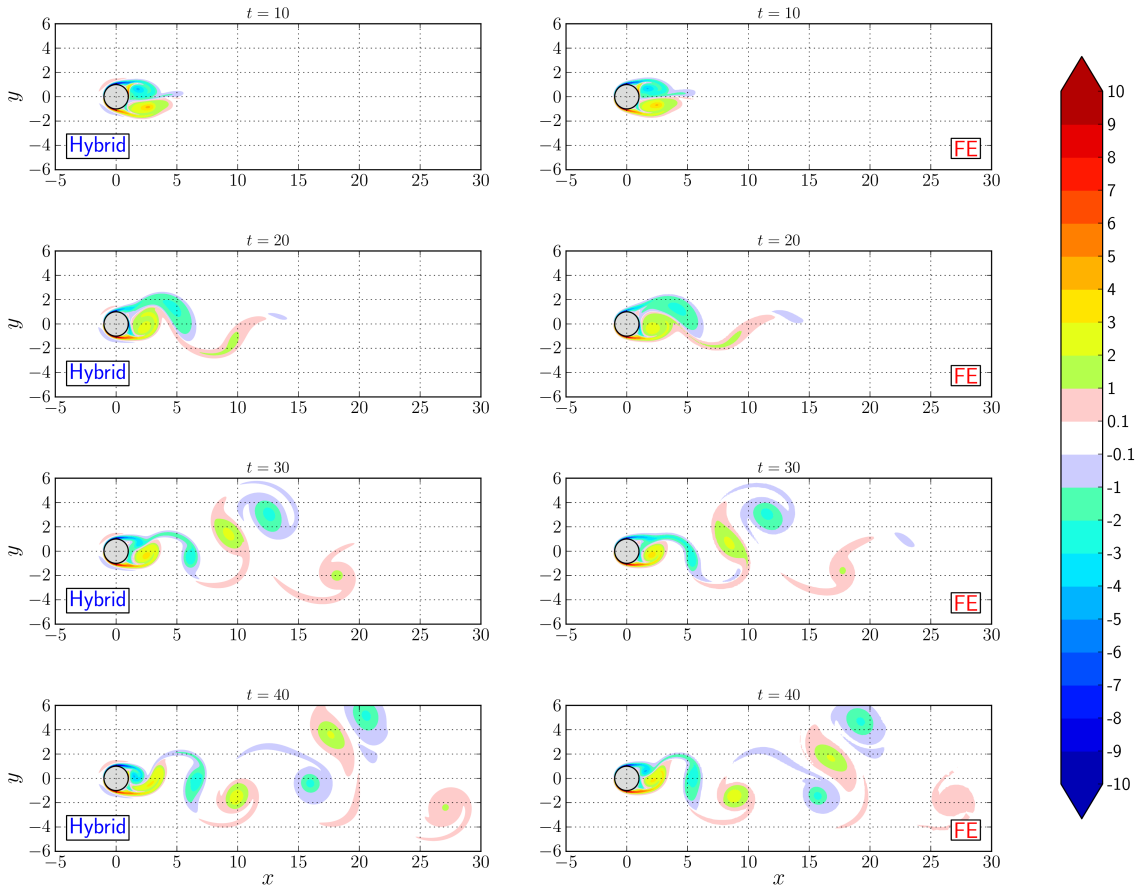


Figure 6.27: Plot of the vorticity field at $t = [10, 20, 30, 40]$, comparing the hybrid simulation (left) with the FE only simulation (right).

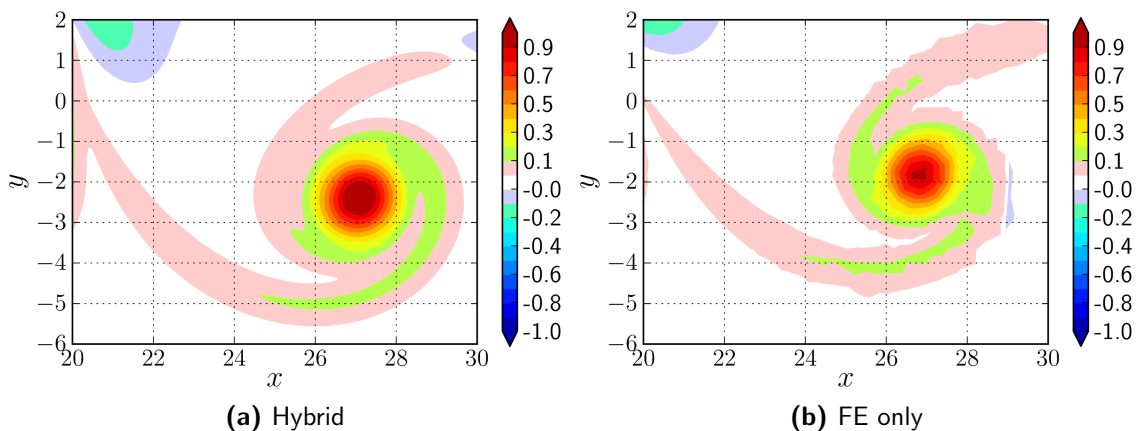


Figure 6.28: Plot of the first shed vortex at $t = 40$, comparing (a) the hybrid simulation, and (b) the FE only simulation.



sub-steps k_E to $k_E = 1$ and $k_E = 5$. With fixed Eulerian time step size $\Delta t_E = 0.001$, the Lagrangian time step sizes were $\Delta t_L = 0.001$ and $\Delta t_L = 0.005$, respectively. The figure shows that reducing the Lagrangian time-step size by a 5th, only reduces the error slightly. Therefore, varying the Lagrangian time-step size has only a minimal improvement.

Figure 6.25b shows the effect of varying the nominal blob spacing h from $h = 0.008$ to $h = 0.00625$. The figure shows that by a small increase in resolution of the blobs as a larger improvement on the drag coefficient, than varying the Lagrangian time step size. Therefore, to improve the coupling, it is more ideal to increase the spatial resolution of the Lagrangian method than the temporal resolution.

Figure 6.25c shows the effect of varying the number of vortex panels N_{panels} from $N = 100$ to $N = 400$. Increasing the number of panels by 4 times, has a smaller effect than the improvement of varying the resolution of the vortex blobs.

The second focus of the impulsively started cylinder is the long run evolution of the lift and the drag of the cylinder, from $t = 0$ to $t = 40$. We performed similar comparison as done in section 3.5.3. An artificial perturbation was induced according to Leocointe and Piquet [42]. Figure 6.26 compares the evolution of the lift coefficient C_l , and the drag coefficient C_d of hybrid simulation, with the FE only simulation, and the reference data from Rosenfeld et al. [52].

Investigating the evolution of drag shows that the hybrid simulation has higher drag. After $t = 5$, there is slight mismatch in the oscillation of the drag. However observing the amplitude fluctuation, we see that the simulation tends to fluctuate around $C_d = 1.4$. Observing the evolution of lift shows that the hybrid simulation has a larger initial amplitude. Furthermore, there exist a negative phase shift in the amplitude. However, at time progress, $t > 20$, we see that the frequency and the amplitude of the oscillation is similar to the reference data. A thorough investigation of the oscillation requires a longer simulation where the amplitude of the oscillation would become fixed. However, due to the lack of computational resources, a longer simulation than $t = 40$ with the current simulation parameters was not feasible.

Figure 6.27 compares the vorticity field of the hybrid simulation (left), and the FE only simulation (right) at time instances $t = [10, 20, 30, 40]$. The differences in the both the vorticity plots is minimal. The main difference between the simulations, at $t = 40$, is not the strength of shed vortex, but its location. A possible reason for this difference might be the small artificial vorticity emanating from the Eulerian boundary Σ_d . With a higher resolved hybrid scheme, their effects should be further minimized.

Figure 6.28 shows the state of the first shed vortex at $t = 40$, for the hybrid simulation and the FE only simulation. For an efficient FE only simulation, we had to under-resolve the mesh, away from the cylinder. However, with the auto-adaptive nature of the Lagrangian method, the hybrid simulation has a well defined first vortex core. Furthermore, we see that the dipole sustains its strength, unlike the FE only simulation which is more diffusive, when under-resolved. This highlights the main advantage of employing the hybrid method.

6.4.3 Conclusion

In conclusion, we observed that the hybrid simulation provided a relative similar performance as the benchmark simulation and the literature of Koumoutsakos and Leonard [39] and Rosenfeld et al. [52]. However, when the hybrid scheme is under-resolved, the artificial vorticity due to the mismatch increases the amplitude of the drag and the lift.

We were also able to observe the auto-adaptive nature of our hybrid scheme. The first vortex shed from the cylinder, was still well-resolved at $t = 40$ in the hybrid scheme, whereas the FE only simulation failed to sustain the structure and the strength of the vortex.

6.5 Stalled Elliptic Airfoil at $Re = 5000$

The purpose of investigating the stalled elliptical airfoil at $Re = 5000$ is to demonstrate the feasibility of using the hybrid method to simulate a complex problem, such as a flow around a thin stalled airfoil. The FE only simulation is as a benchmark for the current study.

6.5.1 Problem Definition

The study of the stalled elliptical airfoil at $RE = 5000$, is performed similar to the study of the impulsively started cylinder at $Re = 550$, see section 6.4. The main difference now is the mesh geometry (now representing a thin stalled airfoil), and a higher Reynolds number.

Figure 6.29 depicts the configuration of the hybrid simulation. We studied the flow around a thin airfoil with thickness to chord ratio t/c of 12%, having a chord length $L = 1$, and a maximum thickness $W = 0.12$. As we have a elliptical airfoil, the

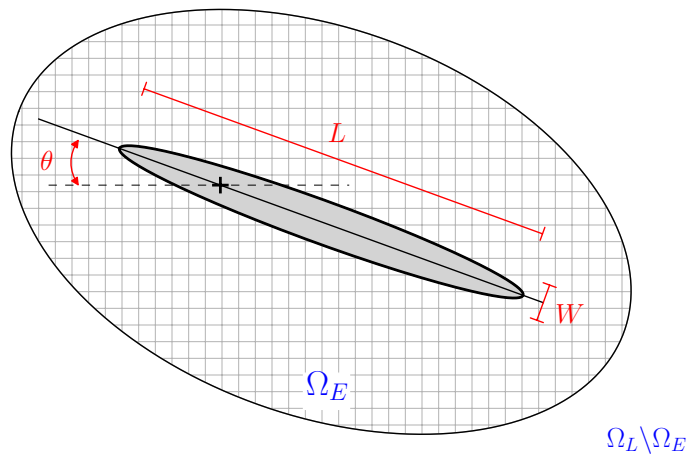


Figure 6.29: (Not to scale) The domain decomposition for the stalled elliptical airfoil. The parameters of the domain are tabulated in table 6.5.



Table 6.5: Summary of the parameters of the hybrid simulation for the stalled elliptical airfoil test case.

Parameters	Value	Unit	Description
Re	5000	-	Reynolds number
\mathbf{u}_∞	[1, 0]	m s^{-1}	Freestream velocity
L	1	m	Chord length
W	0.12	m	Maximum thickness
ν	2×10^{-4}	$\text{kg s}^{-1} \text{m}^{-1}$	Kinematic viscosity
λ	1	-	Overlap ratio
h	1.67×10^{-3}	m	Nominal blob spacing
h_{grid}	0.0014 to 0.008	m	FE cell diameter
N_{cells}	118196	-	Number of mesh cells
N_{panels}	400	-	Number of panels
Δt_L	1×10^{-4}	s	Lagrangian time step size
Δt_E	1×10^{-3}	s	Eulerian time step size
k_E	10	-	Number of Eulerian sub-steps
$N_{\text{t-steps}}$	10000	-	Number of time integration steps
t	0 to 10	-	Simulation time
d_{bdry}	$0.1 \cdot L$	m	Interpolation domain offset from boundary Σ_d
d_{surf}	$3 \cdot h$	m	Interpolation domain offset from boundary Σ_{wall}

maximum thickness is located at $0.5L$. Furthermore, the airfoil is pitched to 20° about center of rotation $0.25L$, to create a stalled flow.

The parameters of the simulation are summarized in table 6.5.

6.5.2 Results and Discussion

Figure 6.30 compares the vorticity plot of hybrid and the FE only simulation at time instances $t = [1, 2, 3, 4]$. It is apparent that from $t = 3$, the structure of the shed vorticity is different. For higher Reynolds number flows, the error in the coupling, seemed to have a greater impact on the evolution of the vorticity field.

To further investigate the effect of the artificial vorticity, we investigated the evolution of the lift and the drag forces, depicted in figure 6.31. The lift and the drag forces determined by the hybrid method matches upto $t = 2$. The oscillation of the lift after $t = 3$ is fundamentally different, which peaks occurring at different time instances. Similarly, the peak drag occurs at different time instances, however we can see that the maximum and minimum drag coefficient during is similar.

Figure 6.32 shows the plot of vorticity field at $t = [1, 2, 3, \dots, 10]$. We see that thanks to adaptive nature of the scheme, the shed vortices are well-defined. Furthermore, in the near-wall region, the Eulerian region is able to capture the complex stalled structure of the airfoil.

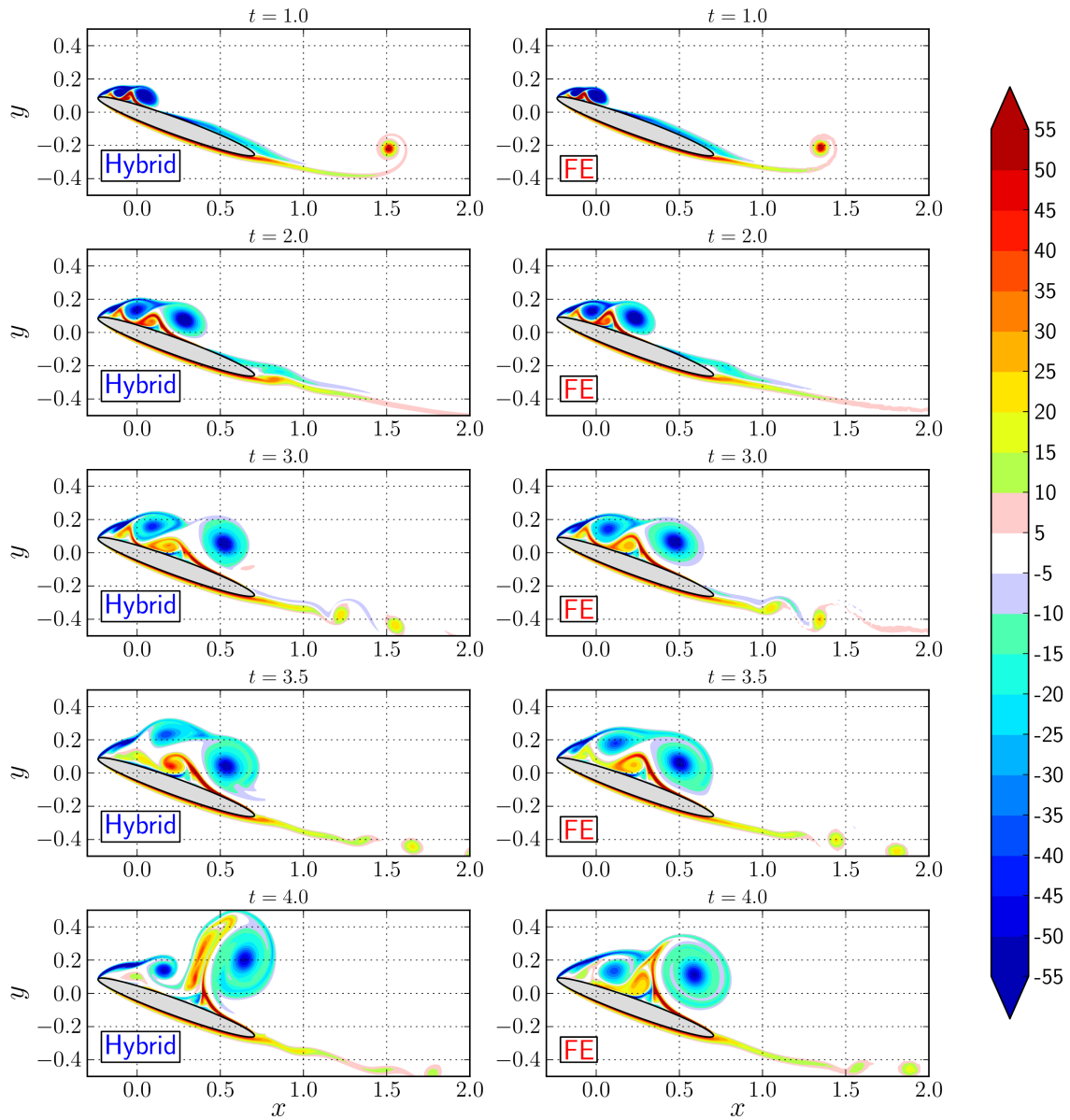
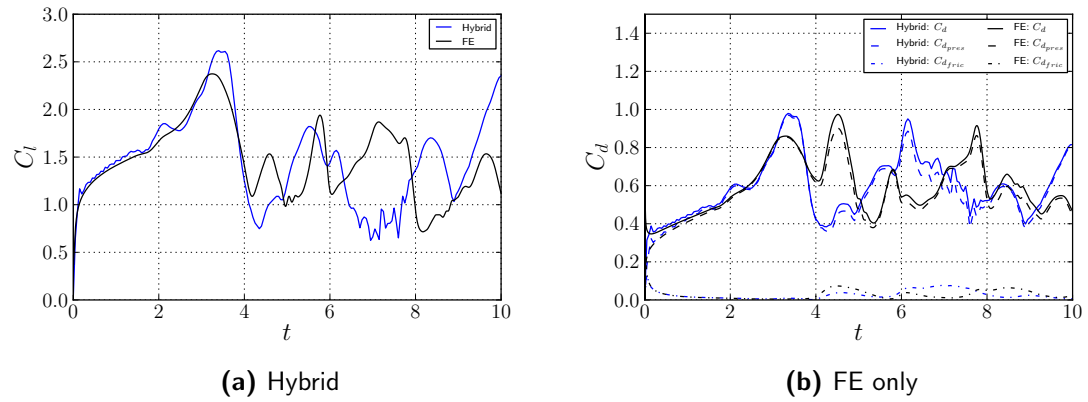
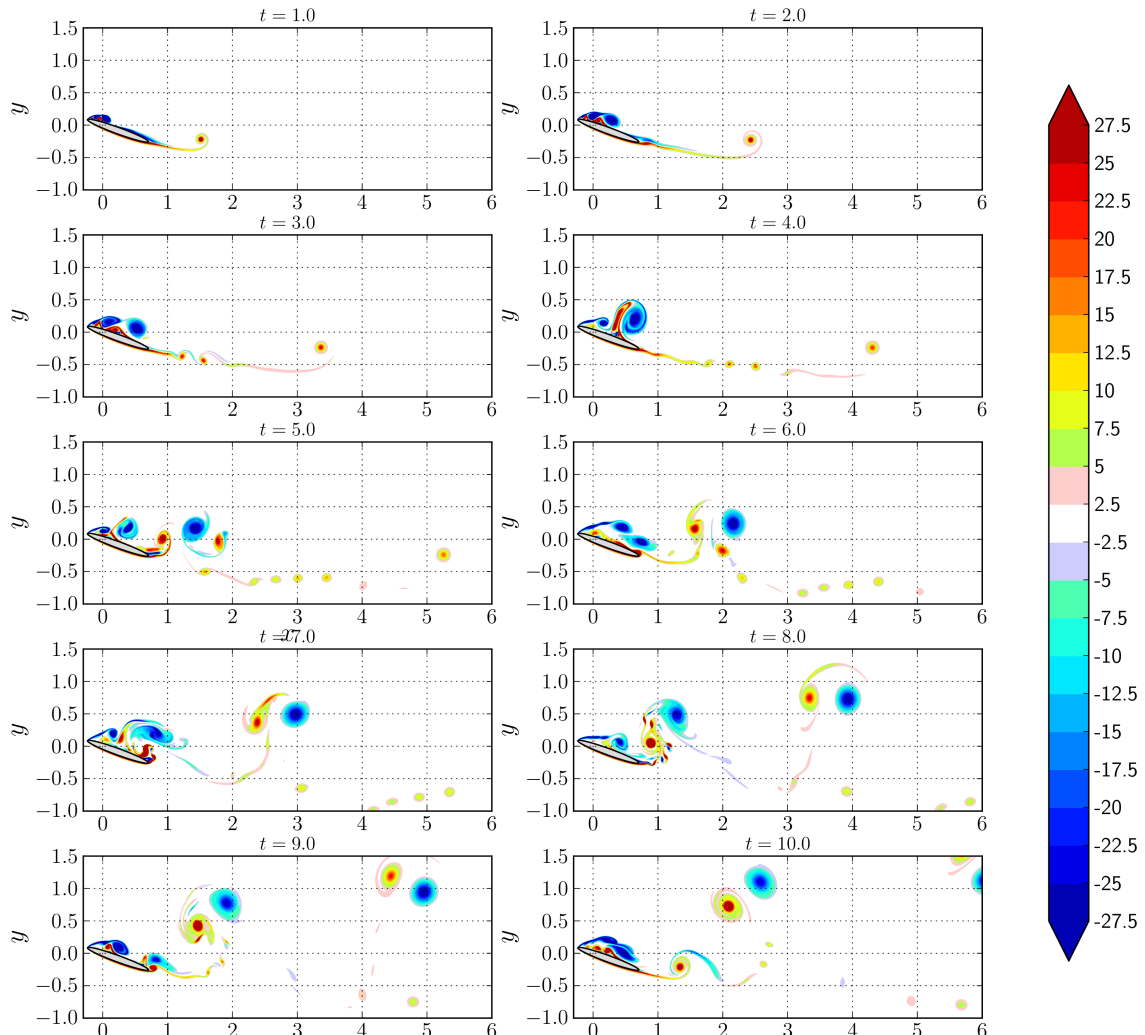


Figure 6.30: hybrid ellipse HybridvsFE contourDeviation



**Figure 6.31:** Forces**Figure 6.32:** hybrid ellipse Hybrid contours

6.6 Multi-body problem

To demonstrate the feasibility of simulating a multi-body problem with the hybrid method, we simulated the flow around two impulsively started cylinders. The simulation is performed similarly to the single cylinder configuration, section 6.4, where here we use two cylinders instead of one.

6.6.1 Problem Definition

As the simulation is performed similar to the single cylinder setup, the parameters of the simulation are according to table 6.4. However, now with the two cylinder configuration, we have two Eulerian sub-domains, Ω_{E_A} and Ω_{E_B} , belonging to cylinder A and cylinder B respectively. The configuration of the two cylinder is depicted in figure 6.33. The locations of the cylinder A and B are at $(x_A, y_A) = (-R_{ext}, 0)$ and $(x_B, y_B) = (R_{ext}, R)$, respectively. These positions ensure that the Eulerian sub-domains do not overlap, $\Omega_{E_A} \cap \Omega_{E_B} = \emptyset$, and the Lagrangian method is used to communicate between theses sub-domains.

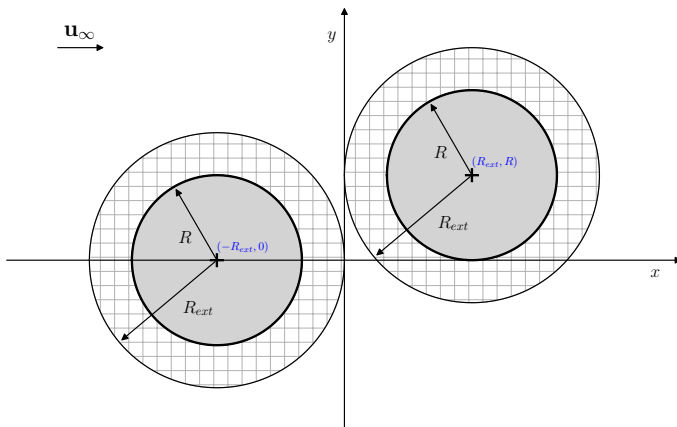


Figure 6.33: (Not to Scale) The hybrid domain decomposition configuration of two impulsively started cylinder test case.

6.6.2 Results and Discussion

The simulation of multi-body problem was ran upto $t = 22$, reaching the limit of the computational resource. Figure 6.34 shows the plot of the vorticity at various time instances, at $t = [1, 4, 7, 10, 13, 16, 19, 22]$. The plot shows the transfer of vorticity from cylinder A to cylinder B with the help of the Lagrangian method. The Lagrangian method serves as the global communication tool for transferring the information between various Eulerian sub-domains.

Therefore, by extending the current hybrid method implementation to take in account of the moving body, it should be feasible to simulate a VAWT simulation.



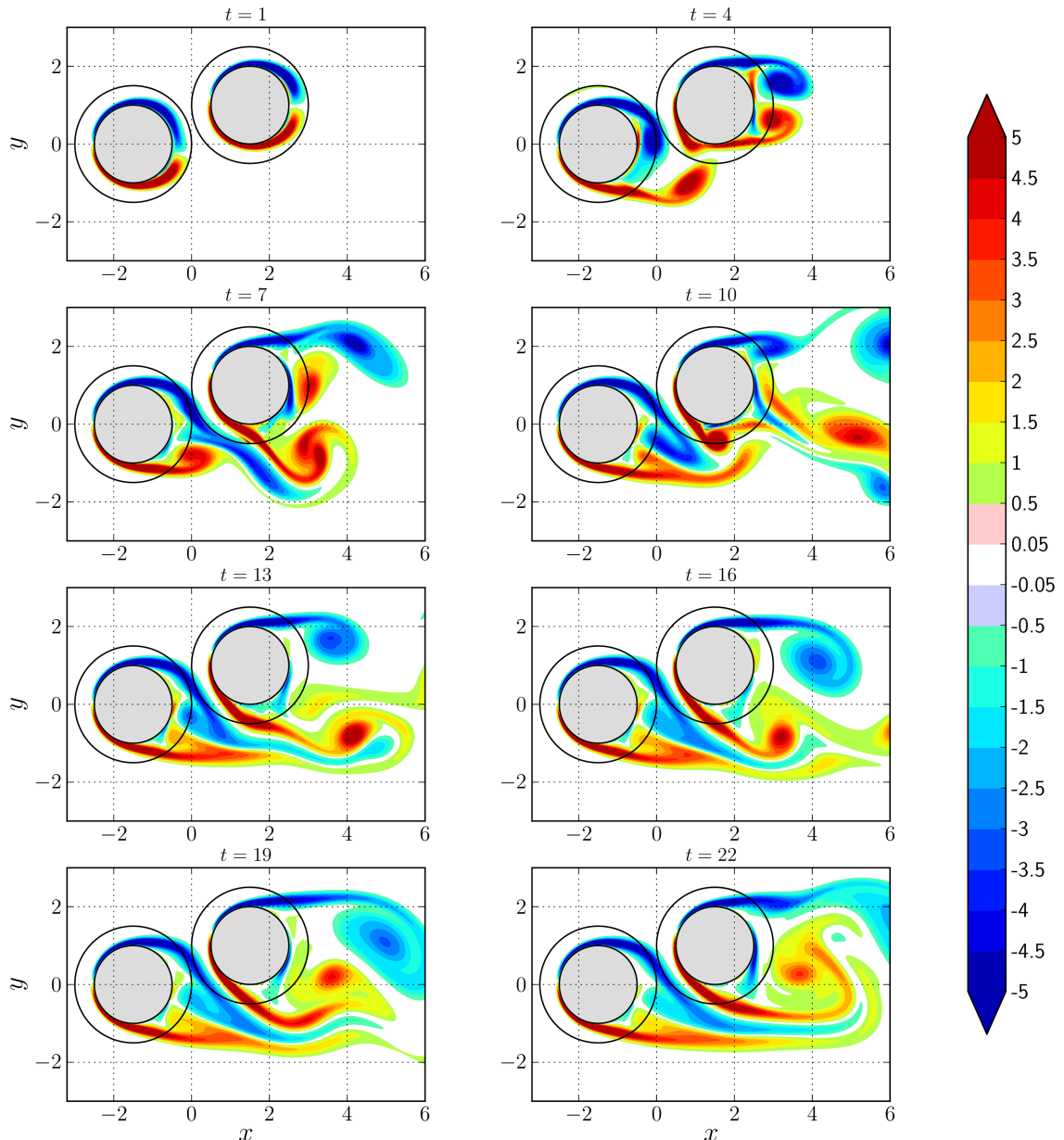


Figure 6.34: hybrid ellipse Hybrid contours

Chapter 7

Conclusion and Recommendation

7.1 Conclusion

7.1.1 Lagrangian domain

7.1.2 Eulerian domain

7.1.3 Hybrid method

7.2 Recommendations

7.2.1 Lagrangian domain

7.2.2 Eulerian domain

7.2.3 Hybrid method



References

- [1] BARBA, L. A., AND ROSSI, L. F. Global field interpolation for particle methods. *Journal of Computational Physics* 229, 4 (2010), 1292–1310.
- [2] BARBA, L. A. L. Vortex method for computing high-Reynolds number flows: Increased accuracy with a fully mesh-less formulation.
- [3] BEALE, J. On the Accuracy of Vortex Methods at Large Times. In *Computational Fluid Dynamics and Reacting Gas Flows SE - 2*, B. Engquist, A. Majda, and M. Luskin, Eds., vol. 12 of *The IMA Volumes in Mathematics and Its Applications*. Springer New York, 1988, pp. 19–32.
- [4] BEHNEL, S., BRADSHAW, R., CITRO, C., DALCIN, L., SELJEBOTN, D. S., AND SMITH, K. Cython: The best of both worlds. *Computing in Science and Engineering* 13, 2 (2011), 31–39.
- [5] BOFFI, D. Three-Dimensional Finite Element Methods for the Stokes Problem. *SIAM Journal on Numerical Analysis* 34, 2 (Apr. 1997), 664–670.
- [6] BRAZA, M., CHASSAING, P., AND HA MINH, H. Numerical Study and Physical Analysis of the Pressure and Velocity Fields in the Near Wake of a Circular Cylinder. *Journal of Fluid Mechanics* 165 (1986), 79–130.
- [7] BRENNER, S. C., AND SCOTT, L. R. *The Mathematical Theory of Finite Element Methods*. Texts in applied mathematics. Springer-Verlag, 2002.
- [8] BREZZI, F., AND FORTIN, M. *Mixed and hybrid finite elements methods*. Springer series in computational mathematics. Springer-Verlag, 1991.
- [9] CAREY, G. F. *Computational Grids: Generations, Adaptation & Solution Strategies*. CRC Press, 1997.
- [10] CHANG, C. C., AND CHERN, R. L. Numerical study of flow around an impulsively started circular cylinder by a deterministic vortex method. *Journal of Fluid Mechanics* 233 (1991), 243–263.



- [11] CHEN, Z. *The Finite Element Method: Its Fundamentals and Applications in Engineering*. World Scientific, 2011.
- [12] CHORIN, A. J. Numerical solution of the Navier-Stokes equations. *Mathematics of computation* 22, 104 (1968), 745–762.
- [13] CHORIN, A. J. Numerical Study of Slightly Viscous Flow. *Journal of Fluid Mechanics* 57, Part 4 (1973), 785–796.
- [14] CIARLET, P. G., AND RAVIART, P. A. General Lagrange and Hermite interpolation in \mathbf{R}^n with applications to finite element methods. *Archive for Rational Mechanics and Analysis* 46, 3 (1972), 177–199.
- [15] CLERCX, H., AND BRUNEAU, C.-H. The normal and oblique collision of a dipole with a no-slip boundary. *Computers & Fluids* 35, 3 (Mar. 2006), 245–279.
- [16] COLLETTE, A. *Python and HDF5*. O'Reilly Media, 2013.
- [17] COMMONS, W. Darrieus windmill, 2007.
- [18] COMMONS, W. Windmills d1-d4 (thornton bank), 2008.
- [19] COOPER, C. D., AND BARBA, L. A. Panel-free boundary conditions for viscous vortex methods. In *19th AIAA Computational Fluid Dynamics Conference* (Dept. of Mechanical Engineering, Universidad Técnica F. Santa María, Casilla 110-V, Valparaíso, Chile, 2009).
- [20] COTTET, G.-H., KOUMOUTSAKOS, P., AND SALIHI, M. L. O. Vortex Methods with Spatially Varying Cores. *Journal of Computational Physics* 162, 1 (July 2000), 164–185.
- [21] COTTET, G. H., AND KOUMOUTSAKOS, P. D. *Vortex Methods: Theory and Practice*, vol. 12. Cambridge University Press, 2000.
- [22] COURANT, R. Variational methods for the solution of problems of equilibrium and vibrations. *Bull. Amer. Math. Soc* 49, 1 (1943), 1–23.
- [23] DAENINCK, G. *Developments in Hybrid Approaches: Vortex Method with Known Separation Location; Vortex Method with Near-Wall Eulerian Solver; RANS-LES Coupling*. PhD thesis, Université Catholique de Louvain, Belgium, 2006.
- [24] DALCÍN, L., PAZ, R., STORTI, M., AND D'ELÍA, J. MPI for Python: Performance improvements and MPI-2 extensions. *Journal of Parallel and Distributed Computing* 68, 5 (2008), 655–662.
- [25] DEGOND, P., AND MAS-GALIC, S. The Weighted Particle Method for Convection-Diffusion Equations. Part 1: The Case of an Isotropic Viscosity. *Mathematics of Computation* 53, 188 (Oct. 1989), 485–507.
- [26] DIXON, K., SIMÃO FERREIRA, C. J., HOFEMANN, C., VAN BUSSEL, G., AND VAN KUIK, G. A 3D unsteady panel method for vertical axis wind turbines. In *European Wind Energy Conference and Exhibition 2008* (2008), vol. 6, pp. 2981–2990.

- [27] FRANKLIN, W. R. Pnpoly-point inclusion in polygon test. http://www.ecse.rpi.edu/Homepages/wrf/Research/Short_Notes/pnpoly.html, 2006.
- [28] GEUZAIN, C., AND REMACLE, J.-F. Gmsh: A 3-D finite element mesh generator with built-in pre- and post-processing facilities. *International Journal for Numerical Methods in Engineering* 79, 11 (2009), 1309–1331.
- [29] GODA, K. A multistep technique with implicit difference schemes for calculating two- or three-dimensional cavity flows. *Journal of Computational Physics* 30, 1 (1979), 76–95.
- [30] GUERMOND, J. L., AND LU, H. A domain decomposition method for simulating advection dominated, external incompressible viscous flows. *Computers & Fluids* 29, 5 (June 2000), 525–546.
- [31] GUERMOND, J. L., MINEV, P., AND SHEN, J. An overview of projection methods for incompressible flows. *Computer Methods in Applied Mechanics and Engineering* 195, 44-47 (2006), 6011–6045.
- [32] GUERMOND, J. L., AND SHEN, J. A new class of truly consistent splitting schemes for incompressible flows. *Journal of Computational Physics* 192, 1 (2003), 262–276.
- [33] HUNTER, J. D. Matplotlib: A 2d graphics environment. *Computing In Science & Engineering* 9, 3 (2007), 90–95.
- [34] JOHNSTON, H., AND LIU, J.-G. Accurate, stable and efficient Navier-Stokes solvers based on explicit treatment of the pressure term. *Journal of Computational Physics* 199, 1 (2004), 221–259.
- [35] JONES, E., OLIPHANT, T., PETERSON, P., ET AL. SciPy: Open source scientific tools for Python, 2001–. [Online; accessed 2014-07-16].
- [36] KATZ, J., AND PLOTKIN, A. *Low-speed aerodynamics*. Cambridge Aerospace Series. Cambridge University Press, 2001.
- [37] KLOECKNE, A. PyUblas: Hybrid numerical codes in Python and C++ integrate numpy and Boost.Ublas, 2008–. [Online; accessed 2014-07-16].
- [38] KOUMOUTSAKOS, P. *Direct numerical simulations of unsteady separated flows using vortex methods*. PhD thesis, California Institute of Technology, USA, 1993.
- [39] KOUMOUTSAKOS, P., AND LEONARD, A. High-resolution simulations of the flow around an impulsively started cylinder using vortex methods. *Journal of Fluid Mechanics* 296 (1995), 1–38.
- [40] KOUMOUTSAKOS, P., LEONARD, A., AND PÉPIN, F. Boundary Conditions for Viscous Vortex Methods. *Journal of Computational Physics* 113, 1 (July 1994), 52–61.
- [41] LAMB, H. *Hydrodynamics*. Cambridge university press, 1993.



- [42] LECOINTE, Y., AND PIQUET, J. On the use of several compact methods for the study of unsteady incompressible viscous flow round a circular cylinder. *Computers and Fluids* 12, 4 (1984), 255–280.
- [43] LOGG, A. NSBench in Launchpad. <https://launchpad.net/nsbench>, 2014.
- [44] LOGG, A., MARDAL, K.-A., WELLS, G. N., ET AL. *Automated Solution of Differential Equations by the Finite Element Method*, vol. 84. Springer, 2012.
- [45] LOGG, A., AND WELLS, G. N. DOLFIN: Automated finite element computing. *ACM Transactions on Mathematical Software* 37, 2 (2010).
- [46] MONAGHAN, J. Extrapolating B-splines for interpolation. *Journal of Computational Physics* 60, 2 (Sept. 1985), 253–262.
- [47] MORTENSEN, M. Fenicstools. <https://github.com/mikaem/fenicstools>, 2014.
- [48] NAIR, M. T., AND SENGUPTA, T. K. Unsteady flow past elliptic cylinders. *Journal of Fluids and Structures* 11, 6 (1997), 555–595.
- [49] OULD-SALIHI, M. L., COTTET, G. H., AND EL HAMRAOUI, M. Blending Finite-Difference and Vortex Methods for Incompressible Flow Computations. *SIAM Journal on Scientific Computing* 22, 5 (Jan. 2001), 1655–1674.
- [50] RAO, S. S. *The Finite Element Method in Engineering*. Elsevier Science, 2011.
- [51] RENAC, F., GÉRALD, S., MARMIGNON, C., AND COQUEL, F. Fast time implicit-explicit discontinuous Galerkin method for the compressible NavierStokes equations. *Journal of Computational Physics* 251 (Oct. 2013), 272–291.
- [52] ROSENFIELD, M., KWAK, D., AND VINOKUR, M. A fractional step solution method for the unsteady incompressible Navier-Stokes equations in generalized coordinate systems. *Journal of Computational Physics* 137 (1991), 102–137.
- [53] SHANKAR, S., AND DOMMELEN, L. A New Diffusion Procedure for Vortex Methods. *Journal of Computational Physics* 127, 1 (Aug. 1996), 88–109.
- [54] SHIELS, D. *Simulation of controlled bluff body flow with a viscous vortex method*. PhD thesis, California Institute of Technology, USA, 1998.
- [55] SIMÃO FERREIRA, C. J. *The near wake of the VAWT: 2D and 3D views of the VAWT aerodynamics*. PhD thesis, Delft University of Technology, Netherlands, 2009.
- [56] SIMÃO FERREIRA, C. J., BIJL, H., VAN BUSSEL, G., AND VAN KUIK, G. Simulating Dynamic Stall in a 2D VAWT: Modeling strategy, verification and validation with Particle Image Velocimetry data. *Journal of Physics: Conference Series* 75, 1 (July 2007), 012023.
- [57] SIMÃO FERREIRA, C. J., KUIK, G., VAN BUSSEL, G., AND SCARANO, F. Visualization by PIV of dynamic stall on a vertical axis wind turbine. *Experiments in Fluids* 46, 1 (Aug. 2008), 97–108.

- [58] SPECK, R. *Generalized Algebraic Kernels and Multipole Expansions for massively parallel Vortex Particle Methods*. PhD thesis, University of Wuppertal, Germany, 2011.
- [59] STOCK, M. J., GHARAKHANI, A., AND STONE, C. P. Modeling rotor wakes with a hybrid OVERFLOW-vortex method on a GPU cluster. In *28th AIAA Applied Aerodynamics Conference* (2010).
- [60] TAYLOR, C., AND HOOD, P. A numerical solution of the Navier-Stokes equations using the finite element technique. *Computers & Fluids* 1, 1 (Jan. 1973), 73–100.
- [61] TRYGGESON, H. *Analytical Vortex Solutions to the Navier-Stokes Equation*. PhD thesis, Växjö University, Sweden, 2007.
- [62] TUTTY, O. R. A Simple Redistribution Vortex Method (with Accurate Body Forces). *ArXiv e-prints* (Sept. 2010).
- [63] VAN DER WALT, S., COLBERT, S. C., AND VAROQUAUX, G. The NumPy array: A structure for efficient numerical computation. *Computing in Science and Engineering* 13, 2 (2011), 22–30.
- [64] VERMEER, L., SØ RENSEN, J., AND CRESPO, A. Wind turbine wake aerodynamics. *Progress in Aerospace Sciences* 39, 6-7 (Aug. 2003), 467–510.
- [65] WEE, D., AND GHONIEM, A. F. Modified interpolation kernels for treating diffusion and remeshing in vortex methods. *Journal of Computational Physics* 213, 1 (2006), 239–263.
- [66] WINCKELMANS, G., COCLE, R., DUFRESNE, L., AND CAPART, R. Vortex methods and their application to trailing wake vortex simulations. *Comptes Rendus Physique* 6, 4-5 (May 2005), 467–486.

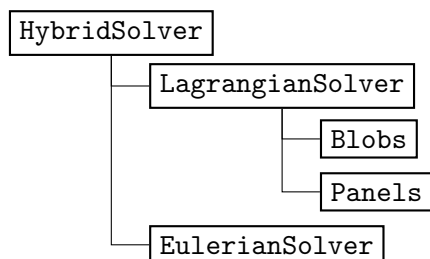


Appendix A

pHyFlow Code Structure

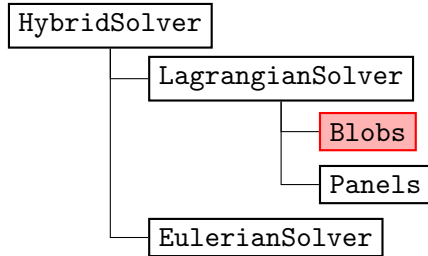
The document outlines the pHyFlow code structure. The pHyFlow functions are organized into several classes. The functions related to the vortex particles are placed inside the `Blobs` class. The functions related to the panel problem are inside `Panels` class. The `LagrangianSolver` class is made to couple the functions of the vortex blobs and the vortex panel together. The functions of the Eulerian domain are placed inside the `EulerianSolver` class, where the Navier-stokes grid problem is solved. Finally, coupling of all the problems are done with the `HybridSolver` class. Note, all the classes are capable of handling multi-body / multi-domain problem within them and `LagrangianSolver` class and the `HybridSolver` class only couples methods together.

pHyFlow Structure:

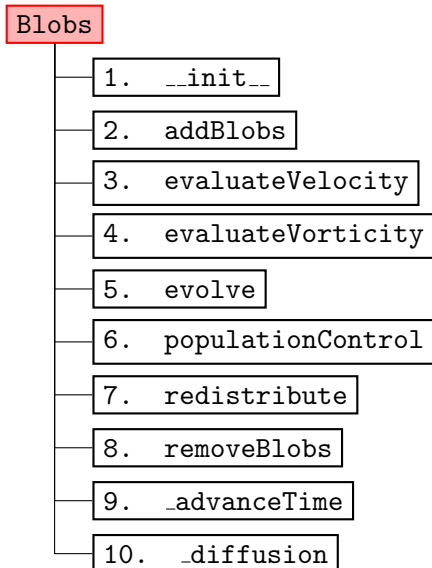


Blobs Class

The main structure of the `Blobs` class. This class contains all the function related to the calculation of the vortex blobs.



Class structure:



Attributes:

Attributes	Description
<code>blobControlParams</code>	The diffusion parameters. It is a dictionary containing all the parameters of the diffusion method used for the simulation. Contains: <code>stepRedistribution</code> , <code>stepPopulationControl</code> , <code>gThresholdLocal</code> , <code>gThresholdGlobal</code> .
<code>computationMethod</code>	<code>computationMethod</code> (tuple) with the type of Biot-Savart solver (<code>direct</code> , <code>fmm</code>) and the type of hardware to use (<code>cpu</code> , <code>gpu</code>).
<code>deltaTc</code>	The size of the convective time step Δt_c
<code>deltaTd</code>	The size of the convective time step Δt_d
<code>diffusionParams</code>	A dictionary containing all the parameters related to the computation of the diffusion step. Specifies the diffusion scheme and other specific parameters. Contains: <code>method</code> , <code>c2</code> .

<code>g</code>	The strength of the vortex blobs α .
<code>gThresholdGlobal</code>	Maximum value of variation of total vorticity due to the removal of blobs during population control.
<code>gThresholdLocal</code>	Minimum value of circulation to consider for each vortex blob when selecting blobs to remove during population control.
<code>h</code>	The size of the cell associated to the vortex blobs. Corresponds to the minimum spacing between the core of two neighboring cells. It is related to the core size of the blob, σ , and to the spacing h by the expression $Ov = h/\sigma$.
<code>integrationMethod</code>	<code>integrationMethod (fe, rk4)</code> the type of time integrator used: <code>fe</code> forward Euler, <code>rk4</code> Runge-Kutta 4 th order.
<code>nu</code>	The fluid kinematic viscosity, used to calculate the diffusion coefficient: c_2 and diffusion time step <code>deltaTd</code> , Δt_d .
<code>numBlobs</code>	The number of blobs.
<code>overlap</code>	The overlap ratio between neighboring blobs.
<code>plotVelocity</code>	A flag that defines if velocity is to be plotted or not.
<code>sigma</code>	The core size of the vortex blobs.
<code>stepDiffusion</code>	The frequency of diffusion steps.
<code>stepPopulationControl</code>	The frequency of population control.
<code>stepRedistribution</code>	The frequency of redistribution of blobs.
<code>timeIntegrationParams</code>	A dictionary containing all time integration parameters of the simulation. Contains the definition of the time integration scheme possibly additional parameters specific to the scheme.
<code>t</code>	The current time of the simulation.
<code>tStep</code>	The current time step of the simulation.
<code>velocityComputationParams</code>	A dictionary containing all the parameters related to the computation of induced velocities. Specifies computation scheme (direct or fmm) and hardware to use (cpu or gpu).
<code>vInf</code>	The free stream velocity.
<code>x</code>	The x coordinates of the vortex blobs.
<code>y</code>	The y coordinates of the vortex blobs.

Table A.1: Attributes of `Blobs` class and their description.`--init--`

Description: Initialize the `Blobs` class with either the given input parameters or by a reading a file containing all the necessary parameters.

Input Parameters

<code>File Name</code>	Containing all the parameters to re-initialize the class.
— or —	
<code>Parameters</code>	
Vorticity Field	: { <code>xBlob</code> , <code>yBlob</code> , <code>gBlob</code> } or { <code>wFunction</code> , <code>xBounds</code> , <code>yBounds</code> }
Blob parameters	: <code>overlap</code> , <code>h</code>
Time Step parameters	: <code>deltaTc</code> , <code>nu</code> , <code>stepRedistribution</code> , <code>integrationMethod</code> , <code>computationMethod</code>
Population control parameters	: <code>stepPopulationControl</code> , <code>gThreshold</code>

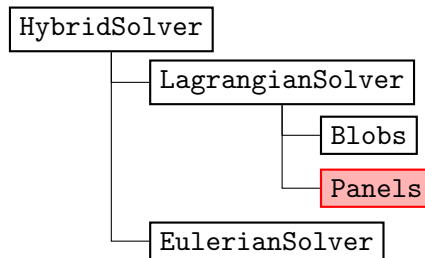


Descriptions of the parameters:

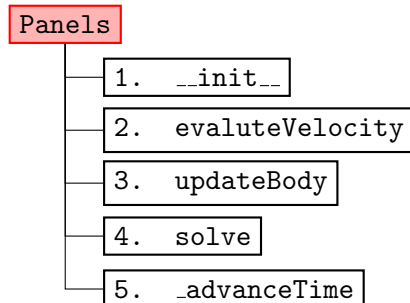
<i>Vorticity field</i>		<i>Default</i>
xBlob,yBlob	: the x, y blob coordinates.	-
gBlob	: the circulation Γ_i associated to each of the vortex blobs.	-
— or —		
wExactFunction	: the function that returns the exact value of vorticity ω at any given x, y coordinates. Input parameters : xEval,yEval Assigns : - Returns : wEval	1.0
xBounds, yBounds	: the x, y bounds of the domain where the particles was originally distributed.	-
<i>Blob parameters</i>		<i>Default</i>
overlap	: the overlap ratio h/σ .	1.0
h	: the size of the cell h associated to the blobs. <i>Note:</i> Cells are square.	-
<i>Time step parameters</i>		<i>Default</i>
deltaTc	: the size of the convective time step Δt_c .	-
nu	: the fluid kinematic viscosity ν , used to calculate the diffusion coefficient c^2 and diffusion time step size ΔT_d .	-
stepRedistribution	: the redistribution step frequency.	1
integrationMethod	: the time integration method (FE: Forward euler , RK4: 4 th order Runge-Kutta).	RK4
computationMethod	: the calculation method to evolve the blobs, (Direct: Direct Method, FMM: Fast-Multipole Method) using (CPU, GPU).	{FMM, GPU}.
<i>Population control parameters</i>		<i>Default</i>
stepPopulationControl	: population control step frequency	1.
gThreshold	: the tuple with minimum and maximum value of the circulation Γ_{min} .	-
<i>Free stream velocity</i>		<i>Default</i>
vInf	: The free-stream velocity function, returning the velocity action on the vortex blobs. Input parameters : t Assigns : - Returns : vx,vy	-

Panels class

The main structure of the panel method class **Panels**. This class contains all the functions related to the calculation of panels.



Class structure:



Attributes:

Attributes	Description
A	The inter-induction matrix A , the LHS of the problem.
cmGlobal	The global position vector for each of the N body, refining the position of the local panel (0, 0) in the global coordinate system.
deltaT	The simulation time step size ΔT
geometryKeys	The dictionary containing all the parameters of the geometry. Contains: xPanel (the <i>x</i> coordinate of the M panel corners.), yPanel (The <i>y</i> coordinate of the M panel corners), cmGlobal , thetaLocal , dPanel (The off-set of the panel collocation point from the panel mid-point).
nBodies	The number of panel bodies.
norm	The <i>x</i> , <i>y</i> normal vector of each panel.
normCat	The global concatenated <i>x</i> , <i>y</i> component of the panel normal vector at each collocation points.
nPanels	The number of panels in each body/geometry.
nPanelsTotal	The total number of panels.
panelKernel	A string defining panel kernel type.
problemType	A string defining the panel problem is of a moving type or of a fixed type.
solverCompParams	The dictionary containing solver computation parameters.
sPanel	The vortex sheet strengths γ of M panels.
t	The current time <i>t</i> of the simulation.
tang	The <i>x</i> , <i>y</i> tangent vector of each panel.



<code>tangCat</code>	The global concatenated x, y component of the panel normal vector at each collocation points.
<code>thetaLocal</code>	The local rotation angle θ w.r.t to the local coordinate system. The rotational will be performed around the local reference point $(0, 0)$, i.e around the global center of rotation point <code>cmGlobal</code> .
<code>tStep</code>	The current step of the simulation.
<code>velCompParams</code>	A dictionary containing the velocity computation parameters, method and hardware.
<code>xyCPGlobal</code>	The global x, y coordinate of the panel collocation points.
<code>xyCPGlobalCat</code>	The global concatenated x, y coordinate of the panel collocation points.
<code>xyPanelGlobal</code>	The global x, y coordinate of the panel bodies.
<code>xyPanelGlobalCat</code>	The global concatenated x, y coordinate of the panel bodies.
<code>xyPanelLocal</code>	The local x, y coordinate of the panel bodies.

Table A.2: Attributes of `Panels` class and their description.`--init--`**Input Parameters**

<i>File Name</i>	Containing all the parameters to re-initialize the class.
<i>Parameters</i>	Panel coordinates : { <code>xCP</code> , <code>yCP</code> , <code>xPanel</code> , <code>yPanel</code> , <code>cmGlobal</code> , <code>thetaLocal</code> }
	External velocity : <code>externVel</code>

Description: Initialize the `Panels` class with the given input parameters. In the case of a multibody problem, a list of panel coordinates can be given and internally it takes care of the inter-coupling.

Panel coordinates

<code>xCP</code> , <code>yCP</code>	: the local x, y -coordinates of the panel collocation points.
<code>xPanel</code> , <code>yPanel</code>	: the local coordinate of the panel edges. <i>Note:</i> Should have a closed loop (end with initial point coordinates).
<code>cmGlobal</code>	: the position of reference points of a given panel body.
<code>thetaLocal</code>	: the rotational angles of the panel body axes w.r.t to the global x -axis.

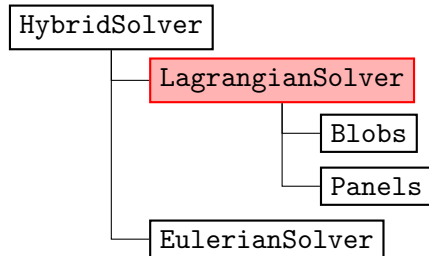
External velocity

<code>externVel</code>	: Reference to an external velocity function acting of the panels. For the panel case, the external velocity will be the induced velocity of the blobs + freestream <code>vortexBlob.evaluateVelocity</code> .
------------------------	---

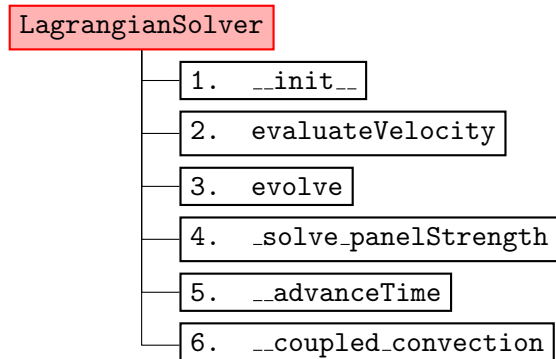
Input parameters : `xCP`, `yCP`**Assigns** : -**Returns** : `vxCP`, `vyCP`

LagrangianSolver Class

The main structure of the **Blobs + Panels** (LagrangianSolver) class. This class contains all the function related to the calculations of panel with vortex blobs.



Class structure:



Attributes:

Attributes	Description
<code>deltaT</code>	The inter-induction matrix \mathbf{A} , the LHS of the problem.
<code>gTotal</code>	The total circulation of the Lagrangian domain.
<code>t</code>	The current time t of the simulation.
<code>tStep</code>	The current step of the simulation.
<code>vInf</code>	The x, y component of the free-stream velocity.
<code>Blobs</code>	The vortex blobs class <code>Blobs</code> .
<code>Panels</code>	The vortex panels class <code>Panels</code> .

Table A.3: Attributes of LagrangianSolver class and their description.

`__init__`

Input Parameters

<i>File Name</i>	Containing all the parameters to re-initialize the class.
<i>Parameters</i>	<code>vortexBlobs</code> : {vortexBlobs} class. <code>panels</code> : panels class.



Description: Initialize the `vortexMethod` class using `vortexBlob+panelMethod` classes.

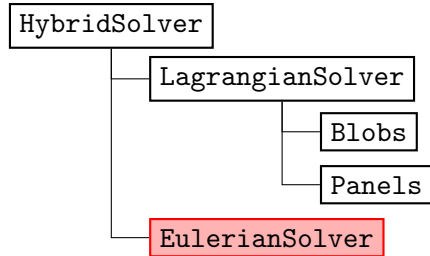
Input parameters:

`Blobs`: vortex particle class

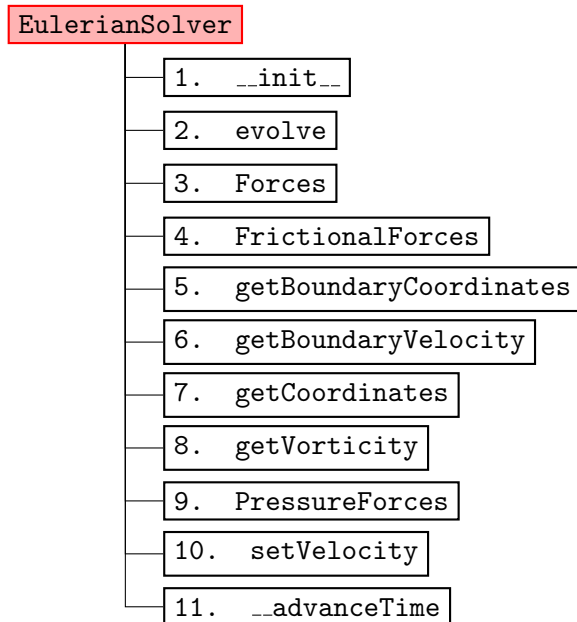
`Panels`: panel method class

EulerianSolver

The main structure for the Navier-stokes class `EulerianSolver`. This class contains all the functions related to computation of the Navier-stokes problem. Below is set of functions that acts as the interface to the class.



Class structure:



Attributes:

Attributes	Description
<code>deltaT</code>	The time step size Δt .
<code>deltaTMax</code>	The maximum allowable time step size $\max\{\Delta t\}$.
<code>cfl</code>	The CourantFriedrichsLowy condition stability number CFL.
<code>cmGlobal</code>	The x, y position of the mesh local reference point $(0, 0)$ in the global coordinates.
<code>hMin</code>	The minimum mesh cell size.
<code>nu</code>	The fluid kinematic viscosity ν .
<code>probeGridMesh</code>	The local x, y coordinates of the probe grid mesh.



<code>probeGridParams</code>	The dictionary containing all the parameters of the probe grid for extracting the vorticity data.
<code>solverParams</code>	The dictionary file containing all the solver parameters.
<code>t</code>	The current time of the simulation.
<code>thetaLocal</code>	The local rotational angle θ of the mesh domain. Therefore, the rotation will be done about local reference point $(0, 0)$, i.e <code>cmGlobal</code> in the global coordinate system.
<code>tStep</code>	The current step of the simulation.
<code>uMax</code>	The maximum fluid velocity $\max\{\mathbf{u}\}$.

Table A.4: Attributes of EulerianSolver class and their description.`--init--`

Description: Initialize the `navierStokes` class either using a `fileName` containing all the necessary parameter for initialization or by explicitly inputting the parameters.

Input Parameters

<i>File Name</i>	Containing all the parameters to re-initialize the class.
– or –	
<i>Parameters</i>	Mesh data : <code>mesh</code> , <code>boundaryDomains</code>
	Geometry position : <code>cmGlobal</code> , <code>thetaLocal</code>
	Fluid parameters : <code>uMax</code> , <code>nu</code>
	Solver options : <code>cfl</code>
	Probe grid parameters : <code>x0</code> , <code>y0</code> , <code>Lx</code> , <code>Ly</code> , <code>hx</code> , <code>hy</code>

Description of the parameters:

Mesh data

- `mesh` : the mesh data file.
`boundaryDomains` : the boundary mesh domain data file.

Geometry position

- `cmGlobal` : the x, y position of the geometry in global coordinates.
`thetaGlobal` : the rotation angle (in rad) of the geometry in global coordinate system.

Fluid parameters

- `uMax` : the maximum fluid velocity U_{max} . Used to determine the maximum time step size Δt_{max} .
`nu` : the fluid kinematic viscosity ν , for incompressible navier-stokes problem.

Solver options

- `cfl` : the *CFL* stability parameter. If explicit time marching scheme, $CFL < 1$.

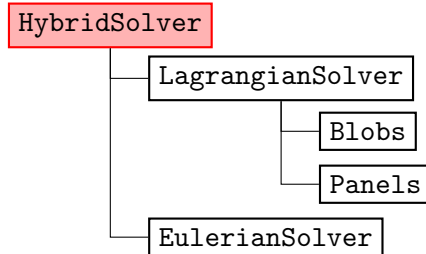
Probe grid parameters

-
- x0,y0 : the x, y coordinate of the origin of the probe grid.
 - Lx,Ly : the x, y size (width and height) of the probing grid.
 - hx,hy : the x, y spacing of the probe grid cell.

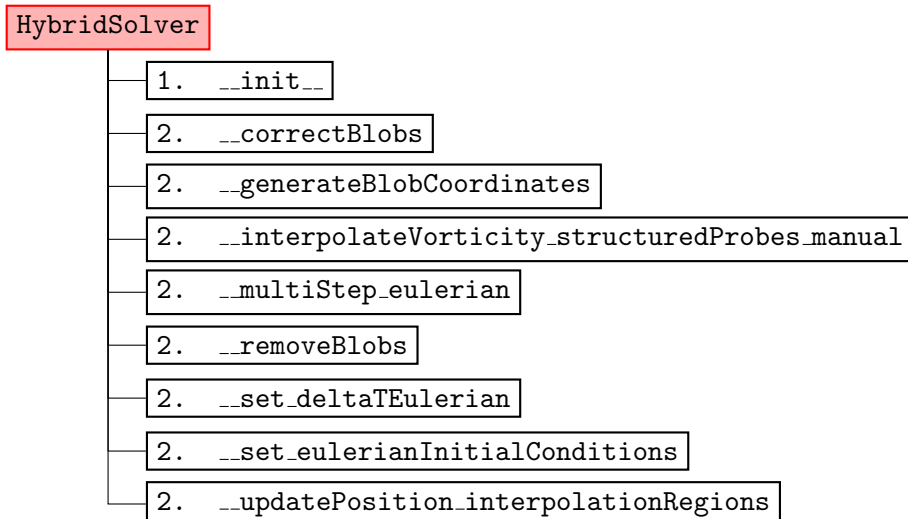


HybridSolver Class

The main structure for the hybrid class `HybridSolver`. This class contains all the functions related to computation of the hybrid problem.



Class structure:



Attributes:

Attributes	Description
<code>deltaTEulerian</code>	The time step size of the Eulerian sub-domain Δt_E .
<code>deltaTLagrangian</code>	The time step size of the Lagrangian sub-domain Δt_L .
<code>nu</code>	The fluid kinematic viscosity ν .
<code>t</code>	The current time t of the simulation.
<code>tStep</code>	The current step of the simulation.
<code>vInf</code>	The x, y component of the free-stream velocity.
<code>interpolationRegion</code>	The dictionary containing the <code>surfacePolygon</code> and <code>boundaryPolygon</code> defining the boundaries of the interpolation region for each Eulerian sub-domains. The geometry is identified by the keys of the Eulerian sub-domain found in <code>multiEulerian</code> . The coordinates are defined in local coordinate system of the Eulerian grid and will be transformed (rotated + moved) during the evolution step.

<code>lagrangian</code>	The Lagrangian solver class contains all the parameters related to simulation the flow in lagrangian sub-domain.
<code>multiEulerian</code>	The <code>multiEulerian</code> is solver class containing all the Eulerian sub-domains of the hybrid problem.

Table A.5: Attributes of `HybridSolver` class and their description.`--init--`**Input Parameters**

<i>File Name</i>	Containing all the parameters to re-initialize the class.
<i>Parameters</i>	<code>vortexMethod</code> : { <code>vortexMethod</code> } class.
	<code>navierStokes</code> : <code>navierStokes</code> class.
	Interpolation region : <code>xPolygon</code> , <code>yPolygon</code>
	Motion functions : <code>T</code> , <code>cmGlobal</code> , <code>thetaGlobal</code> , <code>cmDotGlobal</code> , <code>thetaDotGlobal</code>

Description: Initialize the `hybrid` class using `LagrangianSolver` + `EulerianSolver` classes.

Input parameters:

LagrangianSolver: The vortex method containing `Blobs` and **Panels** classes which can already handle the multi-body problem.

EulerianSolver: The Navier-Stokes grid solver class (if multiple: list of `EulerianSolver` classes). The number of navier-stokes class has to be same as the number of vortex panels.

Interpolation Region: the Navier-Stokes class (if multiple: list of `EulerianSolver` classes). Should be equal to number of Navier-Stokes classes. The interpolation region should be defined as list of x, y coordinates of the polygon of the interpolation region.

Motion function: the function describing the motion of all the geometries in the hybrid class.

Interpolation Regions

xPolygon, yPolygon: the new x, y coordinate of the polygons description the interpolation region. The polygon should have a closed loop (end with starting coordinates) before continuing to the next polygon. In the case of multiple polygons, a list of `xPolygon`,`yPolygon` should be given and should be as many as the number of navier-stokes domain.



Motion function

T	: the current time.
cmGlobal	: a list of new positions of the geometries in the hybrid problem.
thetaGlobal	: a list of new rotational angle of the geometries in the hybrid problem.
cmDotGlobal	: a list of current displacement velocity of the geometries in the hybrid problem.
thetaDotGlobal	: a list of current rotational velocity of the geometries in the hybrid problem.

Input parameters : T

Assigns : -

Returns : cmGlobal,thetaGlobal,cmDotGlobal,thetaDotGlobal